

DOUTORAMENTO

BIOTECNOLOGIA MOLECULAR E CELULAR APLICADA ÀS CIÊNCIAS DA SAÚDE

# Novel insights into axonal physiology through the development and use of new microelectrode array technologies

José Carlos Barreiro Mateus

D  
2021



**José Carlos Barreiro Mateus.** Novel insights into axonal physiology through the development and use of new microelectrode array technologies



**Novel insights into axonal physiology through the development and use of new microelectrode array technologies**

José Carlos Barreiro Mateus



JOSÉ CARLOS BARREIRO MATEUS

## **Novel insights into axonal physiology through the development and use of new microelectrode array technologies**

Tese de Candidatura ao grau de Doutor em Biotecnologia Molecular e Celular Aplicada às Ciências da Saúde;  
Programa Doutoral da Universidade do porto (Instituto de Ciências Biomédicas Abel Salazar)

Orientador – Doutor Paulo Aguiar

Categoria – Investigador Principal

Afiliação – i3S - Instituto de Investigação e Inovação em Saúde, INEB - Instituto Nacional de Engenharia Biomédica, FMUP - Faculdade de Medicina da Universidade do Porto.

Coorientadora – Doutora Mónica Sousa

Categoria – Investigadora Principal com Agregação

Afiliação – i3S - Instituto de Investigação e Inovação em Saúde, IBMC - Instituto de Biologia Molecular e Celular, ICBAS - Instituto de Ciências Biomédicas Abel Salazar.



**The work presented in this thesis was developed at:**

Neuroengineering and Computational Neuroscience Group

i3S - Instituto de Investigação e Inovação em Saúde

INEB - Instituto Nacional de Engenharia Biomédica

Universidade do Porto, Porto, Portugal

Rua Alfredo Allen, 208

4200-135 Porto, Portugal

[www.i3s.up.pt](http://www.i3s.up.pt) | [www.ineb.up.pt](http://www.ineb.up.pt)





*“The history of electrophysiology has been decided  
by the history of electrical recording instruments”*

Edgar Adrian, electrophysiologist and recipient  
of the 1932 Nobel Prize for Physiology



## Financial Support

José Carlos Barreiro Mateus was the recipient of a PhD grant (PD/BD/135491/2018) from Fundação para a Ciência e Tecnologia (FCT) in the scope of the BiotechHealth PhD Program (Doctoral Program on Cellular and Molecular Biotechnology Applied to Health Sciences).

This work was partially financed by FEDER - Fundo Europeu de Desenvolvimento Regional funds through the COMPETE 2020 - Operacional Programme for Competitiveness and Internationalisation (POCI), Portugal 2020, and by Portuguese funds through FCT - Fundação para a Ciência e a Tecnologia/Ministério da Ciência, Tecnologia e Ensino Superior in the framework of the financed projects PTDC/CTM-NAN/3146/2014 (POCI-01-0145-FEDER-007274) and PTDC/EMD-EMD/31540/2017 (POCI-01-0145-FEDER-031540).





## Declaração

*Declaro que a presente tese é de minha autoria e não foi utilizada previamente noutro curso ou unidade curricular, desta ou de outra instituição. As referências a outros autores (afirmações, ideias, pensamentos) respeitam escrupulosamente as regras da atribuição, e encontram-se devidamente indicadas no texto e nas referências bibliográficas, de acordo com as normas de referenciação. Tenho consciência de que a prática de plágio e auto-plágio constitui um ilícito académico.*



José Carlos Barreiro Mateus

The work developed in this doctoral thesis is published in peer-reviewed scientific journals (complying with the terms of n.º 2, alínea a) do artigo 31.º do Decreto-Lei n.º 230/2009), or in preparation for publication.



## Acknowledgements

Em parte, o doutoramento é um caminho solitário, difícil e extenuante. Felizmente, eu tive a *sorte* de estar acompanhado pelas melhores pessoas possíveis para me ajudar nesta caminhada. O resultado é  $\approx 4.5$  anos de muitos bons momentos, muito entusiasmo, muita aprendizagem, muitas colaborações interessantes e a certeza de que fazer esta caminhada foi a melhor decisão que já tomei. Aqui, tento fazer justiça a quem tornou isto possível:

Em primeiro lugar, o meu agradecimento especial ao **Paulo**. Obrigado por seres muito mais do que um *supervisor*, ou até *orientador*. Foste (e serás) para mim um *mentor* que me influenciou, além de cientificamente, pessoalmente. Obrigado pela oportunidade de fazer Neuroengenharia, pelo suporte contínuo, pela confiança nas minhas capacidades e pela grande amizade que criámos. Não me podia ter *calhado* melhor mentor, muito obrigado.

Quero também agradecer a todos os membros que fazem, e fizeram, parte do *Neuroengineering and Computational Neuroscience (NCN)*. Desde que éramos apenas 3 até à versão atual (e mais alargada) sempre senti que estava no sítio e grupo certo, muito graças a vocês. Foram todos de um suporte e amizade fantásticos e acho que conseguimos sempre manter um excelente espírito, mesmo com uma pandemia pelo meio! **Ana**, obrigado por tudo, mesmo. Desde o 1º dia que foste uma amiga, confidente e ajuda preciosa no Matlab (para além de em muitos outros “problemas”). **Cátia**, igualmente, obrigado pela amizade, confiança, mentoria e ajuda preciosa em tantas experiências. **Miguel**, obrigado por seres sempre um 2º orientador dentro do lab, manteres tudo em ordem (!) e seres um grande amigo. Vocês foram o “núcleo duro” do NCN nesta caminhada e não consigo dissociar a minha contribuição, da vossa, neste trabalho. Um obrigado especial também à **Andreia**, ao **Domingos**, à **Sara** e à **Kristine** pela vossa amizade e contribuição a tantos níveis. Um desejo muito grande de boa sorte à “nova geração” de alunos de doutoramento do NCN – nunca se esqueçam da *sorte* que vos *calhou* e mantenham este espírito do São Neurão & Glião em alta!

**Mónica**, o meu agradecimento por teres sido minha co-orientadora, me teres dado suporte sempre que precisei e teres sido uma fonte de inspiração (mais do que imaginas) para grande parte deste trabalho. Um obrigado também às pessoas do *Nerve Regeneration*, em particular à **Ana Rita Costa**, pela ajuda, colaboração e bons momentos ao longo deste percurso. (Rita, aquelas longas noites no STED só reforçaram o meu fascínio por axónios, obrigado!).

I would also like to show my gratitude to Prof. **János Vörös** for giving me the opportunity (twice!) to work in such a stimulating environment as is the *Laboratory of Biosensors and Bioelectronics* (LBB). I am very grateful for all the support and confidence you deposited in me and all the enthusiastic discussions we had. I felt “at home” in ETH Zurich, thanks to you and all the LBB members. I would like to thank my *Neuronies*’ friends in particular – a big thank you to **Sophie, Nako, Stephan** and **Jens** for all the nice moments together and for always making me feel as part of LBB. Finally, a special word to **Sean** for being my companion in so many interesting experiments, experiences and discussions. I wish you all the best!

O meu agradecimento a vários elementos do **INEB/i3S** pela minha integração científica e pessoal no instituto, que se tornou fácil. Em particular, aos grupos **nBTT**, **GCB** e **NESK** com quem colaborei e/ou partilhei laboratório durante estes anos. O meu obrigado especial à **Estrela** pela boa disposição constante, entusiasmo em fazer ciência juntos e amizade. O meu obrigado e reconhecimento aos responsáveis do programa doutoral **BiotechHealth** por acreditarem em mim para a realização deste doutoramento - estou extremamente agradecido por esta oportunidade. Um obrigado, também, aos meus companheiros da **4ª edição** do Biotech por todos os bons momentos, conversas e companheirismo.

Ao **Luís, Ana, Chico, Cláudia, Andreia, Patrícia, Rita, Tiago, Elsa** e malta das **Segundas-Mágicas** por toda a vida dentro e fora do i3S. Aos meus amigos de sempre por todo o apoio, preocupação e amizade, mesmo quando eu passo anos (!) sem dar sinal de vida. Em especial, ao **David, Alex, Tiago, Miguel, Dave, Bea, Bi, Manteigas, Sérgio, Márcio, Diana, Duarte e Mariana**. À minha “família adoptiva” na Suíça - **Licínia e Toino**, que foram o meu maior apoio durante 6 meses desta caminhada. Obrigado a todos, por tudo!

À **Cátia**, por seres o meu porto de abrigo, de amor e de cumplicidade. Foste também tu, que no meio da minha fase de desânimo, me encorajou a candidatar ao BiotechHealth e iniciar esta caminhada (juntos). O meu muito obrigado por isso e por muito mais ♥. O meu muito obrigado também à família da Cátia, em especial, à **Rosa, Vítor e Çalo** pelo apoio constante e bons momentos juntos.

Por fim, à minha **família**, em especial, à minha **mãe Dalila, pai Carlos** e **irmão Luís** pelo amor, apoio, exemplo, preocupação e suporte incondicional. Obrigado por acreditarem em mim, terem-me dado todas as condições para fazer esta caminhada e terem estado sempre ao meu lado, mesmo quando longe. A vocês dedico esta Tese - foi um privilégio ter a oportunidade de a fazer. Muito obrigado por tudo ♥.

## Thesis Publications

### First-Author Publications:

**Mateus JC**, Lopes CD, Cerquido M, Leitão L, Leitão DC, Cardoso S, Ventura J, Aguiar P. *Improved in vitro electrophysiology using 3D-structured microelectrode arrays with a micro-mushrooms islets architecture capable of promoting topotaxis*. **Journal of Neural Engineering** (16), 036012, doi:[10.1088/1741-2552/ab0b86](https://doi.org/10.1088/1741-2552/ab0b86) (2019). (IF = 4.141, CI\* = 7)

**Mateus JC**, Lopes CDF, Aroso M, Costa AR, Gerós A, Meneses J, Faria P, Lamghari M, Sousa MM, Aguiar P. *Bidirectional flow of action potentials in axons drives activity dynamics in neuronal cultures*. **Journal of Neural Engineering**, doi:[10.1088/1741-2552/ac41db](https://doi.org/10.1088/1741-2552/ac41db) (2021). (IF = 5.379#) (#IF for 2020)

### Additional Related Publications:

Lopes CD, **Mateus JC**, Aguiar P. *Interfacing Microfluidics with Microelectrode Arrays for Studying Neuronal Communication and Axonal Signal Propagation*. **JoVE** (142), e58878, doi:[10.3791/58878](https://doi.org/10.3791/58878) (2018). (IF = 1.14, CI\* = 7)

Heiney K, **Mateus JC**, Lopes CD, Neto E, Lamghari M, Aguiar P.  *$\mu$ SpikeHunter: An advanced computational tool for the analysis of neuronal communication and action potential propagation in microfluidic platforms*. **Scientific Reports** (9), 5777, doi:[10.1038/s41598-019-42148-3](https://doi.org/10.1038/s41598-019-42148-3) (2019). (IF = 3.998, CI\* = 5)

Costa AR, Sousa SC, Pinto-Costa R, **Mateus JC**, Lopes CD, Costa AC, Rosa D, Machado D, Pajuelo L, Wang X, Zhou F, Pereira AJ, Sampaio P, Rubinstein BY, Pinto IM, Lampe M, Aguiar P, Sousa MM. *The membrane periodic skeleton is an actomyosin network that regulates axonal diameter and conduction*. **eLife** (9), doi:[10.7554/eLife.55471](https://doi.org/10.7554/eLife.55471) (2020). (IF = 8.14, CI\* = 24)

Neto E, Leitão L, **Mateus J**, Sousa D, Conceição F, Alves CJ, Oreffo ROC, West J, Aguiar P, Lamghari M. *Sensory neurons sprouting is dependent on osteoclast-derived extracellular vesicles involving the activation of epidermal growth factor receptors*. bioRxiv. doi:[10.1101/259218](https://doi.org/10.1101/259218) (2020). (CI\* = 2)

**Mateus JC<sup>#</sup>**, Weaver S<sup>#</sup>, van Swaay D, Renz A, Hengsteler J, Aguiar P, Vörös J. *Nanoscale patterning of in vitro neuronal circuits*. bioRxiv. doi:[10.1101/2021.12.16.472887](https://doi.org/10.1101/2021.12.16.472887) (2021). (*#equal contribution*)

Girardin S, Clément B, Ihle SJ, Weaver S, Petr JB, **Mateus JC**, Duru J, Forró C, Ruff T, Fruh I, Müller M, Vörös J. Topologically controlled circuits of human iPSC-derived neurons for electrophysiology recordings. bioRxiv. doi:[10.1101/2021.12.10.472063](https://doi.org/10.1101/2021.12.10.472063) (2021).

\* *Google Scholar Citations as of 19<sup>th</sup> of January, 2022*

## Abstract

The axon can be viewed as a neuronal structure capable of concurrently receiving, processing, and transmitting information. This view contrasts with a limiting, but deeply rooted, perspective where the axon functions solely as a polarized transmission cable. Undoubtedly, this perspective has, at least partially, arisen from the technical difficulties in probing axonal function, which bias most neuroscience's approaches to the recording of somatic action potentials alone. Currently, it is experimentally challenging to record from a single axon, let alone multiple axons simultaneously. Still, there is an emerging interest in developing and using new *in vitro* technologies that can drive a new era of experimental opportunities in the study of axon physiology, and consequently, neuronal function. In principle, *in vitro* microelectrode arrays (MEAs) are ideal tools for the study of axon physiology. MEAs allow for high spatiotemporal resolution recordings in long-term experiments, that are compatible with concurrent imaging. However, several technological (e.g., low signal amplitudes) and methodological (e.g., random axonal growth over a fixed electrode grid) limitations have precluded standard MEA technology from attaining its full potential for axonal electrophysiology. This thesis addresses these challenges with two different strategies: 3D-microstructured MEAs and MEA-microfluidic combinations.

Here, we report a new 3D-microstructured MEA design that promotes neuronal topotaxis, particularly axon-electrode guidance and somata-electrode colocalization. Importantly, these non-invasive MEAs enable recordings with higher signal-to-noise (SNR) ratio than standard MEAs. Given the high adaptability, this design may be used in experiments that engineer neuronal networks for a bottom-up study of axon physiology and its impact in neuronal function. For the high-throughput probing of multiple axons' activity simultaneously, we combined MEAs and tailored-made microfluidic chambers. This combination allowed for the following of signal conduction with high spatiotemporal resolution and SNR, which revealed an unforeseen prevalence of antidromic (conduction towards the soma) activity in neuronal cultures. The finding that axonal conduction in neuronal cultures is bidirectional has important implications, completely reshaping our understanding of how information flows *in vitro*.

Overall, this thesis provides the field of neuroengineering with new technologies (and methodologies) for the study of axon physiology, and the field of neurobiology with a new understanding of how information flows in neuronal cultures.

## Resumo

O axónio pode ser visto como uma estrutura neuronal capaz de simultaneamente receber, processar e transmitir informação. Esta visão contrasta com uma perspetiva limitada, mas profundamente enraizada, na qual o axónio funciona apenas como um cabo de transmissão polarizado. Sem dúvida, esta perspetiva surgiu, pelo menos parcialmente, das dificuldades técnicas em registar função axonal, que influenciam a maioria das abordagens em neurociência para o registo de potenciais de ação no corpo celular apenas. Atualmente, o registo da atividade de um único axónio é experimentalmente difícil, quanto mais de vários axónios simultaneamente. Ainda assim, existe um interesse emergente no desenvolvimento e uso de novas tecnologias *in vitro* que podem levar a uma nova era de oportunidades experimentais no estudo da fisiologia axonal e, conseqüentemente, da função neuronal. Em princípio, arranjos de microelétrodos (MEAs) *in vitro* são ferramentas ideais para o estudo da fisiologia dos axónios. MEAs permitem registos de alta resolução espaciotemporal em experiências de longo termo, que são compatíveis com imagiologia simultânea. No entanto, várias limitações tecnológicas (e.g., sinais de baixa amplitude) e metodológicas (e.g., crescimento axonal aleatório num arranjo de elétrodos que é fixo) têm impedido a tecnologia MEA padrão de atingir o seu potencial para eletrofisiologia do axónio. Esta tese aborda estes desafios com duas estratégias diferentes: MEAs microestruturados em 3D e combinações MEA-microfluídica.

Aqui, descrevemos um novo design de MEA microestruturado em 3D que promove a topotaxia neuronal, em particular a orientação axónio-elétrodo e a colocação corpo celular-elétrodo. É importante ressaltar que estes MEAs não invasivos permitem registos com melhor relação sinal-ruído (SNR) do que MEAs padrão. Dada a alta adaptabilidade, este design pode ser usado em experiências que estabelecem redes neuronais para um estudo de baixo para cima (“bottom-up”) da fisiologia dos axónios e do seu impacto na função neuronal. Para o registo em alto rendimento (“high-throughput”) da atividade de múltiplos axónios simultaneamente, combinámos MEAs com câmaras microfluídicas específicas. Esta combinação permitiu o acompanhamento da condução de sinal com alta resolução espaciotemporal e SNR, revelando uma prevalência inesperada de atividade antidrómica (condução em direção ao corpo celular) em culturas neuronais. A descoberta de que a condução axonal em culturas neuronais é bidirecional tem implicações importantes, mudando completamente o nosso entendimento de como a informação flui *in vitro*.

No geral, esta tese fornece o ramo da Neuroengenharia com novas tecnologias (e metodologias) para o estudo da fisiologia dos axónios, e o ramo da neurobiologia com um novo entendimento de como a informação flui em culturas neuronais.



# List of Contents

|  |              |
|--|--------------|
| <b>Acknowledgements</b>                            | <b>XI</b>    |
| <b>Thesis Publications</b>                         | <b>XIII</b>  |
| <b>Abstract</b>                                    | <b>XV</b>    |
| <b>Resumo</b>                                      | <b>XVI</b>   |
| <b>List of Contents</b>                            | <b>XIX</b>   |
| <b>List of Abbreviations</b>                       | <b>XXIII</b> |
| <b>List of Variables</b>                           | <b>XXVI</b>  |
| <b>Thesis Outline</b>                              | <b>XXVII</b> |
| <b>Chapter I – General Introduction</b>            | <b>1</b>     |
| <b>1.1 The Axon – Morphological Aspects</b>        | <b>3</b>     |
| 1.1.1 Overview                                     | 3            |
| 1.1.2 Morphology                                   | 3            |
| 1.1.3 Structure and Function                       | 6            |
| Axon Initial Segment                               | 7            |
| Axon Proper  | 9            |
| Axon Terminals                                     | 10           |
| 1.1.4 Development                                  | 12           |
| 1.1.5 Pathology                                    | 13           |
| Axotomy  | 13           |
| Regeneration                                       | 14           |
| <b>1.2 The Axon – Electrophysiological Aspects</b> | <b>16</b>    |
| 1.2.1 Biophysics of Signal Conduction              | 16           |
| Membrane Potential                                 | 17           |
| Passive Properties                                 | 17           |
| Active Properties                                  | 18           |
| 1.2.2 The Action Potential                         | 23           |
| Initiation   | 23           |
| Conduction   | 24           |
| Conduction Velocity                                | 25           |

|  |           |
|--|-----------|
| Shape  | 26        |
| 1.2.3 The Ectopic Action Potential   | 27        |
| Axo-Axonal Coupling  | 29        |
| Spontaneous Activation   | 32        |
| Ectopic Activity in Dorsal Root Ganglion Neurons                           | 34        |
| <b>1.3 Technologies for the study of axon physiology (<i>in vitro</i>)</b> | <b>35</b> |
| 1.3.1 Axon Guidance  | 35        |
| Engineered Substrates  | 36        |
| Microfluidics  | 37        |
| Chemical Patterning  | 39        |
| 1.3.2 Axon Activity  | 41        |
| Subcellular Patch-clamp  | 43        |
| Microelectrode Arrays (MEAs)   | 44        |
| Functional Imaging   | 49        |
| Technique Combinations   | 51        |
| <b>Chapter II</b>  | <b>57</b> |
| <b>2.1 Abstract</b>  | <b>61</b> |
| <b>2.2 Significance Statement</b>  | <b>62</b> |
| <b>2.3 Introduction</b>  | <b>63</b> |
| <b>2.4 Results and Discussion</b>  | <b>66</b> |
| 2.4.1 Microfabrication of 3D-microstructured MEAs                          | 66        |
| 2.4.2 MEAs Electrochemical Characterization: Impedance and Noise Level     | 67        |
| 2.4.3 Cell Viability   | 68        |
| 2.4.4 Influence on Growth Pattern  | 69        |
| 2.4.5 Influence on Neuron Localization                                     | 73        |
| 2.4.6 Electrophysiological Recordings                                      | 75        |
| <b>2.5 Conclusion</b>  | <b>77</b> |
| <b>2.6 Experimental Section</b>  | <b>79</b> |
| 2.6.1 Fabrication  | 79        |
| 2.6.2 Impedance Measurements   | 80        |
| 2.6.3 Cell Culture   | 80        |
| 2.6.4 Immunofluorescence Staining  | 81        |
| 2.6.5 Cell Viability   | 82        |

|                    |  |            |
|--------------------|--|------------|
| 2.6.6              | Image Processing and Analysis  | 82         |
| 2.6.7              | Electrophysiological Recordings  | 83         |
| 2.6.8              | Statistical Analysis   | 83         |
| <b>2.7</b>         | <b>Supporting Information</b>  | <b>84</b>  |
| <b>Chapter III</b> |  | <b>87</b>  |
| <b>3.1</b>         | <b>Abstract</b>  | <b>91</b>  |
| <b>3.2</b>         | <b>Significance Statement</b>  | <b>92</b>  |
| <b>3.3</b>         | <b>Introduction</b>  | <b>93</b>  |
| <b>3.4</b>         | <b>Results</b>   | <b>96</b>  |
| 3.4.1              | Tracking Signal Propagation Reveals a Bidirectional Flow of Activity                     | 96         |
| 3.4.2              | Backward Propagation is Not Explained by Returning Axons nor $\mu$ EF Electric Artifacts | 99         |
| 3.4.3              | Antidromic Action Potentials Effectively Depolarize the Soma                             | 103        |
| 3.4.4              | Antidromic Action potentials Occur After Distal Axotomy                                  | 105        |
|                    | Hippocampal Neurons  | 105        |
|                    | DRG Explants   | 106        |
| 3.4.5              | Modulation of DRGs' Antidromic Activity with Osteoclast's Conditioned Medium             | 108        |
| 3.4.6              | Conduction Velocity is Asymmetric  | 110        |
| <b>3.5</b>         | <b>Discussion</b>  | <b>113</b> |
| <b>3.6</b>         | <b>Experimental Section</b>  | <b>118</b> |
| 3.6.1              | Microfluidic Design and Fabrication  | 118        |
| 3.6.2              | $\mu$ EF Preparation   | 118        |
| 3.6.3              | Cell Culture   | 119        |
| 3.6.4              | Viral Transductions  | 120        |
| 3.6.5              | Electrophysiological Recording   | 120        |
| 3.6.6              | Axonal Electrical Stimulation and Calcium Imaging  | 121        |
| 3.6.7              | Axonal Activity Modulation   | 121        |
| 3.6.8              | Immunolabeling   | 122        |
| 3.6.9              | Stimulated Emission Depletion (STED) Imaging and Analysis                                | 123        |
| 3.6.10             | Action Potential Detection and Propagation Characterization                              | 123        |
| 3.6.11             | Simulations of Conduction Velocity in Different Axonal Morphologies                      | 124        |
| 3.6.12             | Finite-Element Modeling of the Electrical Potential Inside the Microchannels             | 125        |
| 3.6.13             | Statistical Analysis   | 126        |
| <b>3.7</b>         | <b>Supplementary Materials</b>   | <b>127</b> |

|                            |                       |            |
|----------------------------|-----------------------|------------|
| 3.7.1                      | Supplementary Figures | 127        |
| 3.7.2                      | Supplementary Tables  | 130        |
| 3.7.3                      | Supplementary Movies  | 131        |
| <b>Main Conclusions</b>    |                       | <b>133</b> |
| <b>Future Perspectives</b> |                       | <b>135</b> |
| <b>References</b>          |                       | <b>137</b> |
| <b>Annex</b>               |                       | <b>173</b> |

## List of Abbreviations

|                  |   |
|------------------|---|
| μCP              | Microcontact Printing                         |
| μEF              | MicroElectrode array plus microFluidic device |
| 2D               | Two-dimensional                               |
| 3D               | Three-dimensional                             |
| AAV              | Adeno-Associated Virus                        |
| AC               | Alternating Current                           |
| Ag               | Silver  |
| AIS              | Axon Initial Segment                          |
| AnkG             | Ankyrin G                                     |
| AP               | Action Potential                              |
| ATP              | Adenosine Triphosphate                        |
| ATRA             | All-Trans-Retinoic Acid                       |
| Au               | Gold  |
| BDNF             | Brain-Derived Neurotrophic Factor             |
| BSA              | Bovine Serum Albumin                          |
| Ca <sup>2+</sup> | Calcium ion                                   |
| CAD              | Computer-Aided Design                         |
| Ca <sub>v</sub>  | Voltage-gated calcium channels                |
| ChR              | Channelrhodopsin                              |
| Cl <sup>-</sup>  | Chloride ion                                  |
| CM               | Conditioned Medium                            |
| CMOS             | Complementary Metal-Oxide-Semiconductor       |
| CNS              | Central Nervous System                        |
| Cr               | Chromium                                      |
| DC               | Direct Current                                |
| DIC              | Difference Interference Contrast              |
| DIV              | Days <i>In Vitro</i>                          |
| DMEM             | Dulbecco's Modified Eagle Medium              |
| DRG              | Dorsal Root Ganglia                           |
| EAP              | Ectopic Action Potential                      |
| ECM              | Extracellular Matrix                          |

|                        |                                       |
|------------------------|---------------------------------------|
| EPSP                   | Excitatory Post-Synaptic Potential    |
| FBS                    | Fetal Bovine Serum                    |
| FEM                    | Finite Element Model                  |
| GECI                   | Genetically Encoded Calcium Indicator |
| GEVI                   | Genetically Encoded Voltage Indicator |
| GFP                    | Green Fluorescent Protein             |
| $\text{gM}\mu\text{E}$ | Gold-Mushroom Microelectrode          |
| HBSS                   | Hank's Balanced Salt Solution         |
| HD-MEA                 | High-Density Microelectrode Array     |
| IPSP                   | Inhibitory Post-Synaptic Potential    |
| $\text{K}^+$           | Potassium ion                         |
| KCl                    | Potassium Chloride                    |
| $\text{K}_v$           | Voltage-gated potassium channels      |
| MAP-2                  | Microtubule-Associated Protein 2      |
| MEA                    | Microelectrode Array                  |
| MFR                    | Mean Firing Rate                      |
| MPS                    | Membrane-Periodic Skeleton            |
| mRNA                   | messenger Ribonucleic Acid            |
| $\text{Na}^+$          | Sodium ion                            |
| $\text{Na}_v$          | Voltage-gated sodium channels         |
| NGF                    | Nerve Growth Factor                   |
| NoR                    | Node of Ranvier                       |
| P/S                    | Penicilin/Streptomycin                |
| PBS                    | Phosphate Buffer Saline               |
| PDL                    | Poly-D-Lysine                         |
| PDMS                   | Poly(dimethylsiloxane)                |
| PFA                    | Paraformaldehyde                      |
| PI                     | Propidium Iodide                      |
| PNS                    | Peripheral Nervous System             |
| PSP                    | Post-Synaptic Potential               |
| RT                     | Room Temperature                      |
| SCI                    | Spinal Cord Injury                    |
| SD                     | Standard Deviation                    |
| SEM                    | Scanning Electron Microscopy          |

|                  |  |
|------------------|--|
| SiO <sub>2</sub> | Silica                                   |
| SNR              | Signal-to-Noise Ratio                    |
| STDP             | Spike-Timing Dependent Plasticity        |
| STED             | Stimulated Emission Depletion Microscopy |
| TBI              | Traumatic Brain Injury                   |
| TiN              | Titanium Nitride                         |
| TTL              | Transistor-Transistor Logic              |
| TTX              | Tetrodotoxin                             |
| UV               | Ultraviolet                              |
| VSD              | Voltage Sensitive Dye                    |

## List of Variables

| Variable   | Description                              | Unit             |
|------------|--|------------------|
| $C_e$      | Electrode Capacitance                    | $F$              |
| $C_j$      | Junctional Capacitance                   | $F$              |
| $C_m$      | Specific Membrane Capacitance            | $\mu F\ cm^{-2}$ |
| $C_{nj}$   | Non-junctional Capacitance               | $F$              |
| $D$        | Myelin outer diameter                    | $\mu m$          |
| $d$        | Axon diameter                            | $\mu m$          |
| $E_K$      | Reversal Potential of Potassium channels | $V$              |
| $E_L$      | Reversal Potential of “Leakage” channels | $V$              |
| $E_{Na}$   | Reversal Potential of Sodium channels    | $V$              |
| $f$        | Frequency                                | $Hz$             |
| $g_K$      | Conductance of Potassium channels        | $S$              |
| $g_L$      | Conductance of “leakage” channels        | $S$              |
| $g_{Na}$   | Conductance of Sodium channels           | $S$              |
| $I$        | Current                                  | $A$              |
| $L$        | Internodal length                        | $\mu m$          |
| $R_a$      | Specific Axial Resistance                | $\Omega\ cm$     |
| $R_e$      | Electrode Resistance                     | $\Omega$         |
| $R_j$      | Junctional Resistance                    | $\Omega$         |
| $R_K$      | Resistance of Potassium channels         | $\Omega$         |
| $R_L$      | Resistance of “Leakage” channels         | $\Omega$         |
| $R_m$      | Specific Membrane Resistance             | $\Omega\ cm^2$   |
| $R_{Na}$   | Resistance of Sodium channels            | $\Omega$         |
| $R_{nj}$   | Non-junctional Resistance                | $\Omega$         |
| $R_{seal}$ | Seal Resistance                          | $\Omega$         |
| $V_m$      | Transmembrane Potential                  | $mV$             |
| $z_e$      | Electrode Impedance                      | $\Omega$         |

## Thesis Outline

The main objective of the work presented in this thesis was to devise and combine new technologies and methods of Neuroengineering to better understand axon physiology and signal transmission.

In **Chapter I**, a general introduction to axon physiology and the most relevant techniques for its study is given. The axon can be viewed as a neuronal structure capable of independently receiving, processing, and transmitting information within and across neurons. This view contrasts with a limiting, but deeply embedded, perspective where the axon functions as a simple transmission cable of upstream activity. Undoubtedly, this perspective has, at least partially, arisen from the technical difficulties in probing axonal function, which bias most systems neuroscience's approaches to the recording of somatic action potentials alone. In principle, *in vitro* microelectrode arrays (MEAs) are ideal tools for the study of axonal function with high spatiotemporal resolution in long-term experiments. However, several technological (e.g., low signal amplitudes) and methodological (e.g., random axonal growth over a fixed electrode grid) limitations have precluded standard MEA technology of this study. This thesis addresses these current limitations with two different MEA-based proposals: 3D-structured MEAs (Chapter II) and MEA/microfluidic combinations (Chapter III). These two chapters are structured in the form of two independent papers.

In **Chapter II**, a new 3D-structured MEA, where each electrode incorporates an array of mushroom-shaped microstructures, is presented. These microstructures act as physical cues that promote axon-electrode coupling, promote neuron-electrode colocalization, and allow for high SNR electrophysiological recordings *in vitro*. These results expand our knowledge on the, often overlooked, impact of 3D-structured electrodes on axon guidance, and consequently on network organization.

Still, 3D-structured electrodes *per se* cannot selectively probe axonal activity. For the selective and precise positioning of axons over the electrodes, MEAs and tailored-made microfluidic chambers were combined. We have published a detailed video-protocol and accompanying paper of the methods which enable this MEA/microfluidic combination (Lopes et al., 2018). We have also published a computational tool (*μSpikeHunter*), which allows for the quantification of axonal properties, such as conduction velocity or direction, when using this or similar platforms

(Heiney et al., 2019). These directly-related works were a foundation for the paper presented in Chapter III.

In **Chapter III**, we demonstrate spontaneous bidirectional axonal conduction in both hippocampal and dorsal root ganglia (DRG) cultures. This work was made possible by a combination of several state-of-the-art techniques, such as MEA/microfluidics, fast calcium imaging, or super-resolution microscopy, with advanced data analysis and *in silico* studies. These results reshape our understanding of how information flows *in vitro*.

Finally, it is important to note that this MEA/microfluidic combination was also employed in group collaborations that targeted other aspects of axonal function. We revealed an increase in conduction velocity on hippocampal neurons' axons when non-muscle myosin II was inactivated pharmacologically. As non-muscle myosin-II is involved in axon radial contractility, this could be a regulating mechanism of conduction velocity (Costa et al., 2020). In another work, we revealed a great increase in the firing rate of DRG axons, when their distal terminals were exposed to bone-resorbing osteoclast's conditioned medium. These results shed light on axon electrophysiology within the bone microenvironment (Neto et al., 2020).

**Keywords:** axon physiology; axon electrophysiology; signal conduction; bidirectional axonal conduction; microelectrode array (MEA); 3D-electrodes; microfluidics; neuroengineering

## **Chapter I – General Introduction**



## 1.1 The Axon – Morphological Aspects

### 1.1.1 Overview

The nervous system regulates all aspects of body function. To accomplish this massive task, it communicates fast and efficiently via electrochemical signaling. The crucial role of receiving, processing, and transmitting information (input-output) is carried out by heavily polarized cells - the neurons. Santiago Ramón y Cajal first described the axon as the output structure of the neuron (circa 1894), a key concept that emerged from the neuron doctrine theory – the principle that each neuron is a discrete cell with distinctive processes arising from its cell body, and, ultimately, the structural and functional unit of the nervous system (Kandel et al., 2013).

Most neurons can be morphologically compartmentalized into three canonical structures: cell body, dendrites, and axon (**Fig. 1A**). The cell body, or soma (from the Greek *σῶμα soma*, body), contains the nucleus and the cellular machinery for constituting the metabolic center of the neuron. Typically, two kinds of cytoplasmic tubular-like processes then emerge from the soma: dendrite and axon. The number of processes allows for the classification of neurons as unipolar (e.g., unipolar brush cells in the cerebellum), bipolar (e.g., retina bipolar cells), pseudo-unipolar (e.g., sensory neurons in the dorsal root ganglia (DRG)), or multipolar (e.g., pyramidal cells in the hippocampus). Multipolar neurons with several dendrites and a single axon are the most common type in the mammalian nervous system. Classically, the dendrites (from the Greek *δένδρον déndron*, tree) receive and process incoming information from other neurons, while the axon (from the Greek *ἄξων áxōn*, axis) is defined as the neuronal projection that reliably conducts and transmits information (Kandel et al., 2013).

However, recent technological advances are revealing a much more complex physiology of the axon, thus challenging long-standing dogmas. Importantly, the diversity of neuronal specializations has led axons to evolve intricate geometries, unique structural attributes, and different modes of signal propagation. The next sections aim to elucidate important traits of axonal morphology and physiology that underlie neuronal function.

### 1.1.2 Morphology

Otto Friedrich Karl Deiters first described the basic structure of the neuron and termed what became known as the axon, as “axis cylinder” (circa 1860). Despite axonal morphology being

described as complex and highly variable from very early on (Ramon y Cajal & May, 1928), axons are still commonly described/modeled as far simpler structures than dendrites.

Two distinct types of axons occur in the central and peripheral nervous system (CNS and PNS): unmyelinated and myelinated axons. The latter are wrapped by an insulating myelin sheath that originates from oligodendrocytes or Schwann cells, glial cells of the CNS and PNS, respectively. Typically, myelinated axons (together with the associated cells) make up the white matter, while unmyelinated axons make up the grey matter. The lipidic myelin sheath wraps the axons discontinuously, as it is interrupted for 1-2  $\mu\text{m}$  at regular gaps called nodes of Ranvier (NoR). The internodal length ( $L$ ) ranges from 0.2 to 2 mm,  $\approx 100$  times the myelin outer diameter ( $D$ ) ( $L/D$  ratio). This ratio is consistent in both the CNS and the PNS (Debanne et al., 2011). A  $g$ -ratio (ratio of internodal inner axon diameter ( $d$ ) to  $D$ ,  $d/D$ ) of  $\approx 0.77$  and  $\approx 0.6$  for the CNS (Chomiak & Hu, 2009) and the PNS (Rushton, 1951) follows experimental observations, respectively, and fit reasonably with theoretical analysis of optimal axon myelination.

Generally, axons branch profusely. These axonal branches (or collaterals) can output to multiple target neurons locally and/or distally, or, in the case of afferent neurons (e.g., sensory neurons), receive input from different peripheral sensory endings that innervate non-neuronal targets (e.g., skin). For example, tracing studies of biocytin-filled hippocampal CA3 pyramidal neurons have reported, at least, 100-200 branch points per axon (total axon length of  $\approx 150$ -300 mm), that allow for contact with 30-60k estimated neurons (X. -G Li et al., 1994). Interestingly, a single neuron can have a mix of myelinated and unmyelinated branches. Such branch points, together with other spatial inhomogeneities, such as axonal varicosities (putative *en-passant* synaptic boutons), contribute to a much more complex morphology than the classic “axis cylinder” approximation (Debanne et al., 2011).

Axonal length may range from hundreds of micrometers (e.g., inhibitory interneurons) to meters (e.g., sciatic nerve) *in vivo* (Devor, 1999; Kandel et al., 2013). Despite their great length, axon inner diameter is kept relatively constant, though variable, after a thicker cone-like initial segment (axon hillock). Still, it is a common misconception that myelinated and unmyelinated axons maintain a constant diameter along their length (i.e., perfect cylinder). Recent studies are revealing that myelinated axons are noncylindrical, as they exhibit great variations in diameter due to, at least, obstacles in the local environment (e.g., presence of blood vessels) (Andersson et al., 2020). Unmyelinated axons also present several inhomogeneities (e.g., varicosities, organelles) along their length that can dramatically change their local diameter both temporarily and indeterminately (Greenberg et al., 1990; T. Wang et al., 2020). Moreover,

axonal branches are often thinner than the main axon trunk (Sasaki et al., 2012a). Most individual axons are very thin ( $<1\ \mu\text{m}$ ), but the largest axons in the PNS can reach a diameter of  $\approx 20\ \mu\text{m}$  (Debanne et al., 2011). Even in the CNS alone, axons can differ in diameter by three orders of magnitude ( $\approx 0.1\text{-}10\ \mu\text{m}$ ), hence, in cross-sectional area ( $d^2$ ) by six orders of magnitude. Thicker axons may improve timing precision, increase the information transmission rate (by reducing conduction delays), secure high-frequency transmission rate, or supply more neuronal contacts (i.e., synapses), at the cost of volume and energy usage (Perge et al., 2012). Independently of the neuronal type, axonal volume is orders of magnitude above the volume of the soma, which is typically sphere-like and around  $10\text{-}20\ \mu\text{m}$  in diameter. Consequently, the axoplasm (axonal cytoplasm) can constitute over 99% of the total volume of the neuron (Devor, 1999). A schematic of the realistic size relations of a hippocampal neuron's soma diameter, axon diameter, and total axon length (full arbor) is shown in **Fig. 1B**.

Despite their great morphological complexity, mammalian axons are functionally robust as they conduct electrical signals reliably across their axonal arbors (Radivojevic et al., 2017). Still, the variations in morphology have important functional implications that directly relate to the neuron function. For example, DRG neurons project long axons (up to 1 m) for peripheral innervation, while inhibitory interneurons, that work within and coordinate local circuits, have a short, but highly branched, axonal arbor (Kandel et al., 2013). Axonal diameter influences information transmission, namely the speed of propagation of the electrical impulse (i.e., action potential) (Hodgkin, 1954; Waxman, 1980). These topics will be discussed in detail later in this chapter.

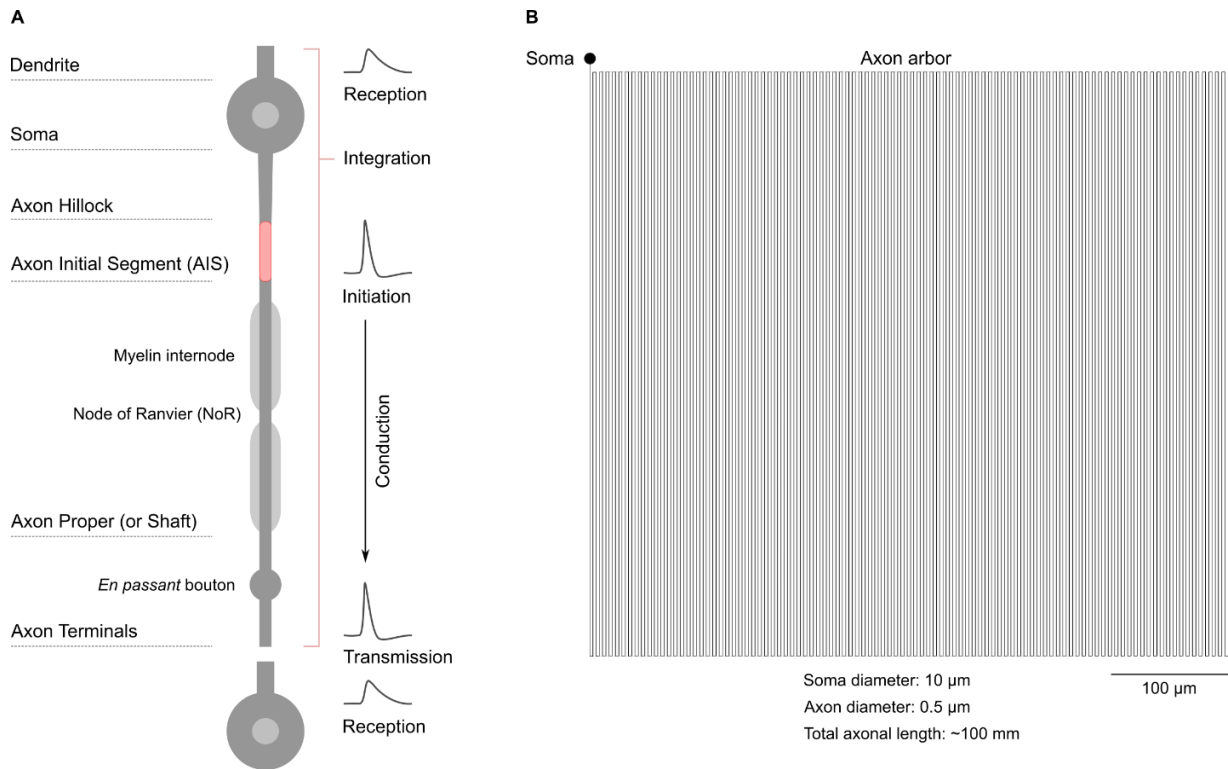


**Figure 1 – The neuron morphological and functional suborganization. (A)** Canonical schematic representation of a neuron with a focus on the different axonal substructures. **(B)** Schematic of the realistic size relations of a hippocampal neuron’s soma diameter, axon diameter, and total axon arbor length. For simplicity, the axon arbor is represented as a single continuous line.

### 1.1.3 Structure and Function

Historically, axons have been viewed as the reliable transmission cables of the nervous system. Their main function being to transmit information from the soma to the pre-synaptic terminals, with high-fidelity, in the form of stereotypical “all-or-none” action potentials (APs). However, an increasing body of knowledge is challenging this traditional view (reviewed in (Alcami & El Hady, 2019; Debanne et al., 2011; Sasaki, 2013)). Axonal signal conduction will be discussed in detail in the following chapter, but first, it is crucial to consider the complex structural organization of the axon. This structural organization is largely influenced by the axonal cytoskeleton, which is mainly composed of microtubules, actin filaments, and neurofilaments (Kevenaar & Hoogenraad, 2015). Different types of actin assemblies (reviewed in (S. Roy, 2016)), in particular, have recently emerged as key components in axonal structure and

function. In turn, this structural organization influences the axonal arbor morphology and the ion channel distribution that equip the axon with special properties for AP initiation, conduction, and transmission. A summary of the main ion channels and proteins involved in AP propagation is represented in **Fig. 2A**.

Generally, main axons can be divided into three distinct sections: an axon initial segment (AIS), an axon proper (or shaft), and axon terminals (**Fig. 1A**). A notable exception is DRG neurons (pseudo-unipolar), where the existence of an AIS-like structure is not clear and whose main axon bifurcates at a T-junction towards both the periphery and the spinal cord (proximal and distal processes) (Devor, 1999; Nascimento et al., 2018).

### ***Axon Initial Segment***

The AIS comprises a specialized unmyelinated region ( $\approx 10\text{-}60\ \mu\text{m}$  in length) of the axon. It is located in or near the axon hillock ( $<120\ \mu\text{m}$  from the soma) and functions as a lower-threshold initiation zone for AP generation (Clark et al., 2005; W. Hu et al., 2009; Kole & Stuart, 2008; Shu et al., 2007). Typically, somatodendritic depolarizations, resulting from the integration of multiple inputs (graded potentials), lead to a suprathreshold activation in the AIS that triggers the AP. Following this canonical view, the AIS can be seen as a nonlinear signal discretizer, where continuous subthreshold signals are subject to a nonlinear operation which may lead to a discrete signal (or event): the AP.

The AIS acts as the preferential site for AP initiation, presumably due to the local high density of specialized voltage-gated sodium ( $\text{Na}^+$ ) channels ( $\text{Na}_v$ ) (Kole & Stuart, 2012), especially the  $\text{Na}_v1.6$  (myelinated axons) and 1.2 (unmyelinated axons) isoforms in the AIS distal region (W. Hu et al., 2009; Kole et al., 2008; Lorincz & Nusser, 2010). Classic theoretical studies estimated that a  $>20$ -fold higher density of  $\text{Na}_v$  channels in the axon, relative to the somatodendritic compartment, was required for the specification of the AP initiation site (Mainen et al., 1995), estimations that were later supported experimentally via immunogold labeling electron microscopy (Lorincz & Nusser, 2010). However, electrophysiological measurements from membrane patches (cell-attached patch-clamp) of the AIS estimated a  $\text{Na}_v$  channel density similar to what is found in the soma ( $3\text{-}4\ \text{channels}/\mu\text{m}^2$ ) (Colbert & Johnston, 1996). A strong anchorage of the AIS  $\text{Na}_v$  channels to the underlying actin cytoskeleton has been reported as the cause for both the local high density of  $\text{Na}_v$  channels and for the inability of drawing  $\text{Na}_v$  channels to the patch pipette, which leads to underestimations of the channel density (Kole et

al., 2008). Findings obtained via high-speed fluorescence  $\text{Na}^+$  imaging of multiple neuronal compartments of rat L5 pyramidal neurons have reported that the AP-associated  $\text{Na}^+$  flux is  $\approx 3$ -fold and  $\approx 8$ -fold higher in the AIS than in the soma and basal dendrites, respectively (suggesting a  $\approx 3:1:0.3$   $\text{Na}_v$  density ratio) (Fleidervish et al., 2010). Although a consensus exists that  $\text{Na}_v$  density is higher in the AIS, the order of magnitude of this difference is yet to be determined (Alcami & El Hady, 2019; Kole & Stuart, 2012). Moreover, the precise and relative  $\text{Na}_v$  densities, are likely to depend on axonal morphology, neuronal cell type, and activity level (Kole & Stuart, 2012).

But is high  $\text{Na}_v$  channel density a requirement for the specification of the AP initiation site? Direct experimental evidence for this hypothesis is still lacking and it is important to note that additional factors contribute to the axon being a low-threshold initiation zone for APs. First, due to the smaller axonal volume (hence smaller capacitance),  $\text{Na}^+$  influx is more efficient in local membrane depolarization than in the soma. Moreover, specialized axonal  $\text{Na}_v$  channels facilitate AP initiation, as their voltage dependence for both activation and inactivation is shifted by  $\approx 10$  mV when compared to the soma counterparts (W. Hu et al., 2009; Kole et al., 2008). Paradoxically, the preferential site for AP initiation – the distal AIS – has four times less  $\text{Na}_v$  density than the middle of the AIS (Baranauskas et al., 2013). Thought-provoking recent experimental and theoretical evidence have shown that high  $\text{Na}_v$  density in the AIS is not required for AP initiation in the axon, but crucial for precise AP timing. In the study, even when axonal  $\text{Na}_v$  density decreased below somatic levels, APs still initiated in the axon (Lazarov et al., 2018).

In addition to being the preferential site for AP initiation, the AIS is increasingly seen as a neuronal compartment capable of processing inputs, which, due to its relative increased electrical isolation (and lower capacitive load), can occur independently of signal processing in the somatodendritic compartments. Several studies have now shown that plastic changes in the expression of voltage-gated ion channels, in soma-AIS distance, or in AIS length can all dynamically regulate neuronal excitability (reviewed in (Debanne et al., 2011; Kole & Stuart, 2012)).

The AIS-associated cytoskeleton is essential for the maintenance of neuronal polarity and acts as a diffusion barrier (“gatekeeper”) for cargo transport between the somatodendritic and axonal compartments (Costa & Sousa, 2021; Winckler et al., 1999). A typical marker of the AIS is a highly-specialized protein – ankyrin G (AnkG) – which is solely expressed in the AIS and NoR. This scaffolding protein is critical for the assembly of the AIS and, together with  $\beta\text{IV}$ -

spectrin, neurofascin, and the binding actin cytoskeleton, cluster voltage-gated  $\text{Na}^+$  and potassium ( $\text{K}^+$ ) channels ( $\text{K}_v$ ) in the AIS (Rasband, 2010) (**Fig. 2B**).  $\beta$ IV-spectrin anchors AnkG and links actin rings at the AIS (Leterrier et al., 2015). Loss of  $\beta$ IV-spectrin results in loss of AnkG, which leads to a marked decrease of  $\text{Na}_v$  density in the AIS, but not in the soma (Lazarov et al., 2018). Deletion of AnkG causes axon dedifferentiation with the emergence of dendritic characteristics, such as spine formation (Hedstrom et al., 2008; Sobotzik et al., 2009). Another indication that the AIS is essential for the maintenance of polarity is that, following axon transection (i.e., axotomy), axonal regeneration starts at the same site if the AIS is intact, but occurs from a dendrite (which becomes the new axon) if the AIS has been removed (Gomis-Rüth et al., 2008). Still, AnkG knock-outs (hence no AIS formed) have shown axon specification and AP generation capabilities, with only gamma oscillations ( $\approx 25\text{-}100$  Hz) being absent (Jenkins et al., 2015). These oscillations are thought to be coordinated by GABAergic interneurons that target the AIS of principal neurons, thus the AIS may also act as a location that allows interneurons to coordinate network oscillations.

Notably, super-resolution microscopy techniques have revealed that  $\text{Na}_v$  channels and associated proteins are organized in a highly periodic ( $\approx 190$  nm) form (Leterrier et al., 2017; K. Xu et al., 2013) (**Fig. 2B**). Such organization was previously unresolved due to the diffraction limit of optical microscopy ( $\approx 200$  nm). The full functional relevance of this periodic organization is still unknown, though an active field of investigation (reviewed in (Costa & Sousa, 2021)), and will be further explored during this chapter.

### ***Axon Proper***

The axon proper constitutes the majority of the axonal length and is responsible for the reliable propagation of the AP. In unmyelinated axons, AP conduction is supported by distributed  $\text{Na}_v 1.2$  channels. In long-projecting myelinated axons, NoR act as hot spots for the clustering of  $\text{Na}_v$  and  $\text{K}_v$  channels that regenerate AP propagation along the axon - a form of conduction often termed as “saltatory” (Debanne et al., 2011).

As previously stated, axons are typically very long, but also very thin. Similarly to the AIS, the axon proper-associated skeleton forms a periodic actin-spectrin organization which is crucial for the needed structural integrity of axons, helping them resist mechanical constraints and shocks (Dubey et al., 2020; K. Xu et al., 2013). Actin rings are present along the entire axon, but different isoforms of spectrin and ankyrin are expressed in the axon proper-only ( $\beta$ II-

spectrin–ankyrin B scaffolds). The functional relevance of this differential expression is still unknown (Leterrier et al., 2017). In contrast, the NoR-associated cytoskeleton and voltage-gated channel composition of the mature NoR is remarkably similar to the AIS (D'Este et al., 2017), reflecting the NoR role in the (re)generation of the AP. For example, AnkG,  $\beta$ IV-spectrin, and Na<sub>v</sub>1.6 channels are highly-expressed in NoR, but not in the remaining axon proper. Concomitantly, the first NoR have also been proposed as preferential sites of AP initiation in, at least, some neuronal types (Clark et al., 2005; Lehnert et al., 2014).

The axonal periodic cytoskeleton is present in every neuron type of the CNS and PNS and it is probably responsible for the relative consistency in inner axon diameter along its length (Costa et al., 2018). Still, recent studies have revealed that this diameter is not immutable, as the axonal cytoskeleton is much more dynamic than previously thought. Axon diameter can be modulated by activity-dependent mechanisms (Chéreau et al., 2017) or for the axonal transport of large cargos (e.g., autophagosomes) (T. Wang et al., 2020), via, at least, actomyosin-II networks (Costa et al., 2020). Importantly, as the axon proper contacts other neurons, it can establish thousands of *en-passant* synapses. *In vitro*, most synapses are formed at *en-passant* synaptic boutons (Leterrier et al., 2017). These synaptic boutons have also been shown to increase in size after periods of increased neuronal activity (Chéreau et al., 2017). These morphological plasticity mechanisms may dynamically fine-tune properties of AP propagation (e.g., conduction velocity), increasing the range of known functions of the axon proper.

### ***Axon Terminals***

The axon terminals comprise the expanded terminal ends of the axonal arbor, where synapses are formed. In a network, their function is to perform excitation-release coupling with high-fidelity. AP arrival at the terminals leads to the opening of pre-synaptic voltage-gated calcium (Ca<sup>2+</sup>) channels (Ca<sub>v</sub>). The consequent Ca<sup>2+</sup> influx triggers the release of neurotransmitter-containing synaptic vesicles to the synaptic cleft near-instantly (within a millisecond after AP arrival, synchronous release), or up to tens of seconds later (asynchronous release). In most neuron types, neurotransmitter release is coordinated by Ca<sub>v</sub>2 channel subtypes (mainly Ca<sub>v</sub>2.1 and/or Ca<sub>v</sub>2.2 channels) (reviewed in (Dolphin & Lee, 2020)). Depending on the released neurotransmitter (e.g., glutamate or glycine), synapses can be excitatory or inhibitory, by depolarizing or hyperpolarizing/shunting the target neuron, respectively (Kandel et al., 2013).

In contrast to the AIS and the NoR, much less is known about the precise composition of ion channels in axon terminals. Still,  $K_v$  channels are thought to exhibit a greater diversity at terminals than in the AIS or axon proper. The slower kinetics of  $K_v$  channels can determine the depolarization duration (modulating AP shape) and regulate the level of neurotransmitter release, by controlling the fraction of time that  $Ca_v$  channels open (I. H. Cho et al., 2020; Gonzalez Sabater et al., 2021; Hoppa et al., 2014; Rowan et al., 2016). Low-threshold repolarizing (or inactivating)  $K_v1$  channels, in particular, are important in the suppression of terminals hyperexcitability following AP invasion (Debanne et al., 2011; Dodson et al., 2003). Such hyperexcitability has been shown to trigger ectopic (distal) AP generation (Dodson et al., 2003; Stasheff et al., 1993).

Actin is considered as the main cytoskeletal element within pre-synaptic terminals, although its function is not well defined. Several structural and dynamic roles of actin have been proposed, such as synaptic vesicles recruitment/positioning; assembly of pre-synaptic scaffolding proteins (e.g., piccolo); or rapid structural remodeling during neuronal plasticity (reviewed in (Kevenaar & Hoogenraad, 2015)).

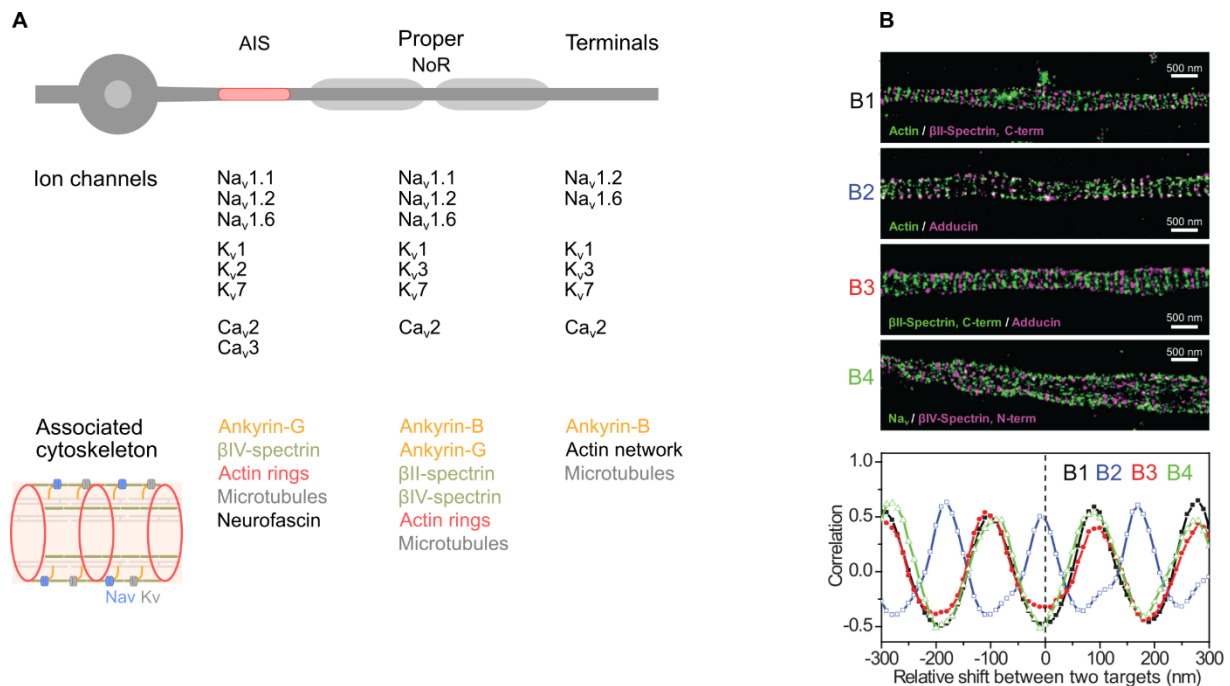


**Figure 2 – The distribution of specialized proteins involved in the structure and function of the axon. (A)** Overview of the main ion channels and associated cytoskeleton involved in the generation, conduction and transmission of action potentials. **(B)** Two-color stochastic optical reconstruction microscopy (STORM) images and spatial correlation demonstrating the

periodic arrangement of actin rings- $\beta$ II-spectrin (*B1*), actin rings-adducin (*B2*),  $\beta$ II-spectrin-adducin (*B3*), and  $\beta$ II-spectrin- $\text{Na}_v$  channels (*B4*) (adapted from (K. Xu et al., 2013)).

#### 1.1.4 Development

The nervous system is precisely connected. While several developmental processes shape the precise patterns of connectivity, none is more important than axonal guidance to the appropriate targets. Remarkably, as it can be already appreciated, axonal arbors need to grow long distances, bypass obstacles, and form high-fidelity connections with appropriate synaptic targets. However, the sheer complexity of the nervous system makes subcellular analysis *in vivo* (i.e., axon-level) a challenging task. Thus, for the last century, *in vitro* neuronal cultures have been widely used in neuroscience (reviewed in ((Millet & Gillette, 2012a)). The most used *in vitro* model consists of dissociated cultures of mammalian neurons randomly plated over a pre-coated glass or plastic substrate.

After plating, CNS neurons acquire their typical morphology through a stereotyped sequence of five developmental stages (Dotti et al., 1988). Dissociated neurons begin to polarize by extending actin-rich processes, that are eventually invaded by microtubules, which lead to neurite formation (stages 1-2, within 2 days *in vitro* (DIV)). Due to a combination of intrinsic and extrinsic (e.g., environmental cues) factors, one of these neurites grows comparatively faster and becomes the axon (stage 3, within 4 DIV). The tip of the growing axon – the growth cone – is highly motile, thus, once the axon is specified, it grows at a sustained speed ( $\approx 1$ -100  $\mu\text{m}$  per hour). This growth is sustained by a retrograde flow of actin and stabilization of microtubule growth. The next stages are marked by the assembly of the AIS (stage 4, within 7 DIV) and the continuous formation of axonal branches, the dendritic arbor, and the first synapses (stage 5, >7 DIV). The formation of axonal branches also relies on actin assembly for initiation and subsequent microtubule invasion for stabilization of the branch. In fact, disruption of actin dynamics leads to a loss of axonal branching, but axon elongation remains unaffected (Dent & Kalil, 2001; Kalil & Dent, 2014).

A key limitation of traditional *in vitro* models is that by providing free open-space for neuronal growth, they are poorly mimicking axonal guidance *in vivo*. *In vivo*, axonal guidance is markedly influenced by environmental biochemical cues that can attract (e.g., ephrins) or repulse (e.g., semaphorins) growth cones. Growth cones are also sensible to topography; thus, axons can grow along other axons, epithelial surfaces and make turning decisions at guidepost cells (e.g.,

glial cells). These extrinsic factors play a key role in directing axon elongation to the appropriate targets, but their implementation *in vitro* requires specialized preparations that will be detailed later (reviewed in (Giger et al., 2010; Hoffman-Kim et al., 2010)).

Typically, cultures of CNS neurons start exhibiting sporadic AP firing around the third stage of development (3-4 DIV). Eventually, a functionally mature neuronal network is formed within 2-3 weeks *in vitro* (Chiappalone et al., 2006). Even in a reductionist model, by then, the extended arborization of a random neuronal network makes following connectivity almost impossible. Besides, as the networks grow freely, they are composed of seemingly random connections, unlike the precisely connected brain (Sporns & Betzel, 2016).

### 1.1.5 Pathology

Axon pathology contributes to neurological symptoms in disorders as diverse as traumatic brain injury (TBI), spinal cord injury (SCI), demyelinating diseases (e.g., multiple sclerosis), epilepsy, or stroke. Such disorders can result from many types of insults, injury, or defects that damage axons and/or affect axonal function. These can range from mechanical trauma (e.g., axotomy) to channelopathies and lead to dysfunction of, for example, axonal conduction (e.g., SCI, multiple sclerosis) or excitability (e.g., epilepsy) (Debanne et al., 2011). Here, I will focus on the effects of axotomy in axonal de/regeneration, even though several of these mechanisms are transversal to different types of insult.

#### **Axotomy**

Axotomy is a transection of the axon that can occur as a result of acute mechanical trauma in TBI or SCI. There are two modes of axotomy: primary and secondary. Primary axotomy occurs immediately and is characterized by complete disconnection of the soma from the distal segments of the lesioned axon. Secondary axotomy evolves over time, ultimately leading to disconnection. In adult neurons, axotomy can induce neuron apoptosis if the lesion site is close to the soma.

Immediately after axotomy, the axonal membrane compromise is accompanied by rapid and transient changes in intracellular ion concentrations. Ubiquitously, a calcium wave has been shown to rapidly backpropagate ( $\approx 1$  mm/min) along the axon (Y. Cho et al., 2013; Ziv & Spira, 1995). This highly-conserved mechanism may serve as a retrograde signal to inform the soma of distant axon injury (Rishal & Fainzilber, 2014). Moreover, a local increase in calcium

concentration is necessary for the resealing of the proximal axon, cytoskeletal reorganization, and the formation of a new growth cone - all within the first hours post-axotomy. After the first ion-based signaling, there is a delayed phase of retrograde signaling that is mediated by the molecular motors (i.e., dyneins) and leads to adaptive neuronal responses (e.g., new transcriptions). Asynchronously, the lesioned distal axonal stump undergoes progressive disassembly via a process called Wallerian degeneration, that can last days. This distal degeneration is characterized by a breakdown of the axonal cytoskeleton, that leads to axonal fragmentation and subsequent phagocytosis by glial cells and macrophages that are recruited to the lesion site. Similar “dying back” degeneration may also occur in the proximal axon, although it is more common in neurological diseases such as peripheral neuropathy. Most often, the injured proximal axon forms a large dystrophic bulb (or retraction bulb) at the tip, which is regeneration-incompetent due to an aberrant cytoskeletal organization (Blanquie & Bradke, 2018). Still, it has been suggested that neuronal activity after axotomy may help promote neuronal survival, axogenesis and axon regeneration in several different cellular models (reviewed in (Corredor & Goldberg, 2009)).

### ***Regeneration***

After axotomy, some neurons can mount a regenerative response. While Santiago Ramon y Cajal’s classic studies (circa 1928) showed that neuroregeneration fails and most injured neurons form dystrophic bulbs that persist indefinitely (Ramon y Cajal & May, 1928), later influential studies by Alberto Aguayo et al. demonstrated that CNS axons are able to regrow in permissive substrates (Aguayo et al., 1981). Still, regeneration in the mature CNS is particularly difficult in relation to other organs (e.g., liver) (Li & Chen, 2016), and most intriguingly, even when compared to the PNS (He & Jin, 2016). In fact, with only sparse interesting exceptions (Hawthorne et al., 2011), severed CNS axons are unable to mount a robust regenerative response.

Aguayo’s reports intuitively steered efforts towards the study of the growth-inhibitory milieu. Consequently, extrinsic factors, such as the glial scar or the inflammatory response, have long been thought to be largely responsible for the CNS inability to repair. However, current knowledge shows that simply counteracting or removing the extracellular inhibitory molecules results in incomplete axon regeneration *in vivo* (Mar et al., 2014). Indeed, the striking contrast in regenerative capacity between CNS and PNS neurons is partially explained by extrinsic determinants, but also due to differences in their intrinsic potential (He & Jin, 2016). In the PNS,

both the extrinsic and intrinsic factors work together to allow regeneration. Schwann cells dedifferentiate, downregulate all myelin proteins, and form new endoneurial tubes that allow axons to grow through, while macrophages clear the debris and produce growth factors and cytokines that stimulate regeneration. Neurons also intrinsically react to the injury by activating regeneration-associated genes expression and producing a new growth cone (Bradke et al., 2012). In contrast, CNS neurons experience both intrinsic and extrinsic mechanisms which negatively influence regeneration. They do not spontaneously activate regeneration-associated genes, cannot synthesize proteins near the lesion, and axons tend to make retraction bulbs rather than growth cones (He & Jin, 2016; Mar et al., 2014). Moreover, the few regeneration-competent axons that form a motile growth cone, often mis-project due to a lack of guidance cues or encounter a highly inhibitory glial scar that further blocks their growth (Cregg et al., 2014). This scar tissue is mainly composed by reactive astrocytes, microglia/macrophages, and extracellular matrix (ECM) molecules, especially chondroitin sulfate proteoglycans. Although these extrinsic factors definitely impact the CNS ability to repair damage, increasing evidence also suggests beneficial roles in regeneration. For example, the delivery of axon-specific growth factors has promoted laminin-dependent axon regrowth, but only when the glial scar was present (Anderson et al., 2016). Recognizably, the glial scar components have key roles in the injury acute phase in sealing the lesion, restoring homeostasis, preserving spared tissue, forming bridges for axonal outgrowth and modulating immunity. Inflammation also appears to be important for spinal cord repair, as M2 macrophages promote a regenerative growth response. Previous research has focused mostly on removing or inhibiting such extrinsic determinants, unfortunately with limited success in clinical practice. Now, events such as glial scar formation and local immune response are being considered as essential healing responses which become detrimental if not resolved on time (Raposo & Schwartz, 2014). Importantly, recent studies are also exploring the effects of enhancing the intrinsic potential for axon regeneration. For example, CNS and PNS axon regeneration has been promoted by enhancing several cytoskeletal dynamics (e.g., microtubules growth speed) via an increase in the levels and activity of profilin 1, a coordinator of actin and microtubules (Pinto-Costa et al., 2020).

## 1.2 The Axon – Electrophysiological Aspects

All axons propagate electrical signals. This propagation results from a combination of specialized passive and active properties of the axon. In general, passive properties are determined by the ion channels and pumps responsible for the resting membrane potential and axonal geometry, whereas active properties are shaped by the voltage-gated ion channels. This chapter begins by detailing the properties behind electrical signal conduction along the axon.

It is important to consider that, due to the inherent difficulties in studying thin mammalian axonal arbors, most of our knowledge about axonal conduction, function, and computation capabilities has been derived from *in silico* studies or experiments on invertebrate neurons (Alcami & El Hady, 2019; Debanne et al., 2011). Only recently, new technological developments are leading to the realization that the computational repertoire of axons is much more complex than originally thought. As detailed in this chapter, this repertoire is not limited to canonical APs, but a variety of electrical signals that can underlie neuronal function. Ectopic action potentials (EAPs), in particular, are an understudied form of activity that initiates in distal parts of the axon.

### 1.2.1 Biophysics of Signal Conduction

Several properties of the axon seem to have been optimized for the conduction of electrical signals. The cell membrane, for example, works as a small capacitor, which maintains an electrical field between the intra- and extracellular milieu. This virtually impermeable membrane contains two kinds of transmembrane proteins, which make it electrogenic: ion pumps and ion channels. Ion pumps actively pump ions in and out (at the cost of energy consumption; this is in fact the core reason for the nervous system being responsible for 20% of the whole-body energy consumption (Niven & Laughlin, 2008)). Ion channels are selectively permeable to different ions. For the understanding of signal conduction, the most important ions are  $\text{Na}^+$  and  $\text{K}^+$ .

Axonal function is not limited to stereotypical digital-like signal conduction. Subthreshold and suprathreshold signals (e.g., APs) have been shown to co-exist and expand the repertoire of computational modalities in the axon. Subthreshold membrane fluctuations, such as synaptic or receptor potentials, in the  $\approx 1$  mV range propagate passively (analog-like) along the axon. As this signaling is not regenerated along the axon, it is more prominent in the proximal axon. Still,

subthreshold signals can reach chemical and electrical synapses, where they can modulate AP efficiency (Mickael Zbili & Debanne, 2019). The combination of these analog and digital modalities leads to a wider range of functions of the axons. Ultimately, the axon is increasingly viewed as a neuronal compartment that performs analog-digital signaling, thus capable of “hybrid computations” (as termed in (Alcami & El Hady, 2019; Bucher & Goaillard, 2011)). While the conduction of subthreshold signals depends only on the passive properties of the axon, suprathreshold signals rely on both passive and active properties for the regeneration of AP propagation.

### ***Membrane Potential***

The different types of signals propagated along the axon are determined in part by the specialized electrical properties of the cell membrane. This membrane is composed of a ~5 nm thick lipid bilayer, which, at rest, maintains a non-zero stable membrane potential. The reference (electrical “ground”) point for measuring the membrane potential difference between inside and outside of the cell is, by convention, the extracellular space. At rest (in the absence of signals being generated/transmitted), the membrane potential ranges from -80 to -40 mV. At the resting state, a fraction of passive  $K^+$  channels and  $Cl^-$  are open (“leaky membrane”), thus the resting membrane potential is approximately close to the reversal potentials of these two ion species. Moreover,  $Na^+$ - $K^+$  exchanger pumps maintain an intracellular low concentration of  $Na^+$  ( $\approx 1/10$  of the extracellular concentration) and a high concentration of  $K^+$  ( $\approx 20$  times the extracellular concentration). These ionic exchangers push two  $K^+$  ions into the cell and pump three  $Na^+$  ions out against their concentration gradients, at the cost of one molecule of adenosine triphosphate (ATP) (**Fig. 3A**) (Kandel et al., 2013).

### ***Passive Properties***

Wilfrid Rall first proposed the “neuronal cable theory” as a method for modelling neuronal compartments for the understanding of signal conduction (reviewed in (Rall, 1977)). Biophysically, the axon can be modelled as a passive cylinder, which can be subdivided in unit lengths (i.e., discretized in space). Each unit length can be approximated by a parallel “RC circuit” with a membrane resistance ( $R_m$ ) and capacitance ( $C_m$ ). In turn, all unit lengths are connected internally and to the extracellular fluid via resistors, which represent the axial resistance ( $R_a$ ) of the axoplasm and the membrane (input) resistance ( $R_m$ ), respectively.

Together, these represent the passive properties of the axon: the lipid bilayer of the axonal membrane (capacitor), together with the passive ion channels and axial resistance (resistors) (**Fig. 3B**).  $R_m$  and  $R_a$  control how far subthreshold signals spread along the axon before being undetected (i.e., becoming undistinguishable from resting membrane potential levels). As shown from cable theory, the signal conduction in such a passive cylinder decays exponentially with distance. The space (or length) constant  $\lambda$  is defined as the distance over which the potential decays to  $1/e$  ( $\approx 37\%$ ) of its initial value, and is expressed as  $\lambda = [(d/4)(R_m/R_a)]$ , where  $d$  is the axon diameter.

Large myelinated axons can have very long space constants (a few mm) due to the large  $d$  and the increase in  $R_m$ , caused by the myelin sheath. Concomitantly, thin unmyelinated axons have small space constants, though greater than theoretically estimated ( $<200 \mu\text{m}$ ). Whole-cell patch-clamp recordings have shown that the space constant in L5 pyramidal neuron axons can be  $\approx 550 \mu\text{m}$  (Kole et al., 2007). Moreover, it is important to note that the space constant is inversely proportional to the signal frequency. Thus, slow varying signals ( $>200 \text{ ms}$  in duration) can reach  $\approx 1 \text{ mm}$  in L5 pyramidal axons. Several studies have now reported facilitation of synaptic transmission via subthreshold depolarization of the pre-synaptic terminals (“analog-digital facilitation”) (reviewed in (Alpizar et al., 2019; Debanne et al., 2013; Mickael Zbili & Debanne, 2019)), highlighting the importance of this type of signaling in axonal function.

### **Active Properties**

Alan Hodgkin and Andrew Huxley were the first to quantitatively describe and model (now known as HH model) the active properties of signal conduction along the axon (Hodgkin & Huxley, 1952). This seminal work was performed using the giant axon of the squid, due to its millimeter-size, hence easier accessibility to direct electrophysiological recording - the insertion of electrodes to perform voltage clamp in a space clamp configuration. The HH model characterized two types of active channels - a  $\text{Na}^+$  channel and a delayed-rectifier  $\text{K}^+$  channel. Even though it is now clear that most mammalian neurons contain far more than these two types of voltage-dependent ion channels described in the squid axon (Bean, 2007) (**Fig. 3C-D**), HH formalism is a popular technique to date. Moreover, the discovered basic mechanism of electrical excitability appears to be universal - the electrogenecity of the axonal membrane relies on  $\text{Na}_v$  and  $\text{K}_v$  channels.

The HH equivalent electrical circuit of the squid axon can be seen as a starting point in the understanding of the HH model (**Fig. 3B**). There are three types of ionic currents in the circuit model:  $I_{Na}$ ,  $I_K$  and  $I_L$  (leak current). The  $Na^+$ ,  $K^+$ , and leaky (mainly  $Cl^-$  ions) reversal potentials are represented by batteries ( $E_{Na}$ ,  $E_K$ , and  $E_L$ , also known as equilibrium potentials). The non-linear (voltage-dependent) and linear (leakage) resistances are represented by variable ( $R_{Na}$  and  $R_K$ ) and constant ( $R_L$ ) resistances. At any moment, the membrane current is the sum of  $Na^+$ ,  $K^+$ , and leak currents, whereas the magnitude of each current type is calculated based on the ion's driving force (i.e., the difference between the membrane potential and the equilibrium potential of the ion) and the membrane conductance for that ion.

Hodgkin and Huxley demonstrated that the difference in ionic concentrations between the intracellular and extracellular milieu was responsible for a ionic flux across the cell membrane through selective “transmembrane aqueous pathways” (now known as ion channels). In turn, the resulting positive increase in membrane potential was responsible for the generation of the AP. When some  $Na_v$  channels are activated (e.g., via electrical stimulation), due to their higher extracellular concentration,  $Na^+$  ions have a tendency to passively enter the cell. As  $Na^+$  ions enter the cell, the membrane is further depolarized and more  $Na_v$  channels are activated. With a large fraction of the  $Na_v$  channels activated, the membrane potential approximates the  $Na^+$  reversal potential, which is when the ionic electrostatic repulsion balances the osmotic force of diffusion of  $Na^+$  ions. Likewise, but slightly later due to the slower kinetic properties, activated  $K_v$  channels allow  $K^+$  ions to exit the cell and the membrane potential returns to a resting level (i.e., repolarizes) (**Fig. 3C**). During the repolarization phase,  $Na_v$  channels close (i.e., deactivate) and then inactivate, which renders them refractory (i.e., unable to activate again for a period of time). Hodgkin and Huxley applied the Nernst equation to calculate this reversal potential (or equilibrium potential) from the known  $Na^+$  and  $K^+$  concentrations and found it to be about 52 mV and -72 mV in relation to the extracellular potential (assuming a temperature of 6.3 °C).

Based on their voltage clamp measurements, Hodgkin and Huxley were able to best-fit parameters to describe the two non-linear  $Na^+/K^+$  currents, a linear leakage current, as well as the time behavior of the intracellular membrane potential, with four ordinary differential equations. The complete HH model of the membrane equation and the three ionic currents that describe how the membrane potential changes over time (under space clamp, i.e., no spatial dependence) is:

$$C_m \frac{dV_m}{dt} = -\bar{g}_L(V_m - E_L) - \bar{g}_{Na}m^3h(V_m - E_{Na}) - \bar{g}_Kn^4(V_m - E_K)$$

$$\frac{dm}{dt} = \alpha_m(1 - m) - \beta_m m$$

$$\frac{dh}{dt} = \alpha_h(1 - h) - \beta_h h$$

$$\frac{dn}{dt} = \alpha_n(1 - n) - \beta_n n$$

where  $\bar{g}_i$  represents the maximal value of conductance;  $n$ ,  $m$  and  $h$  (gating variables) represent potassium conductance activation, sodium conductance activation and sodium conductance inactivation, respectively;  $\alpha_i$  and  $\beta_i$  represent the rate coefficients for the  $i$ -th conductance.

With other sets of parameters, the HH model has since been used to describe many other types of voltage-dependent ion channels and has become a standard technique in compartmental modeling of neurons in *in silico* environments. These compartmental models are often simulated and analyzed in specialized software environments, such as NEURON (Hines & Carnevale, 1997), with tailored numerical engines to solve the systems of differential equations.

As previously mentioned, the mammalian axon displays a much larger variety of ionic currents than those described for the squid axon. The AIS “trigger zone” has the lowest threshold for AP initiation due to the presumed relative high density of specialized  $Na_v$  channels, which are more sensitive to small deviations from the resting membrane potential (due to the lower half activation voltage). Moreover, the different  $Na_v$  channels can generate three different  $Na^+$  currents: the fast transient  $Na^+$  current, the persistent  $Na^+$  current, and the resurgent  $Na^+$  current. The fast-activating and -inactivating transient currents are activated sequentially when membrane potential reaches the firing threshold. The fast-activating drives the AP rise (depolarizing phase), while the fast-inactivating, together with the, then, activated  $K_v$  channels, restores the resting membrane potential (repolarizing phase) (**Fig. 3C**). The persistent and resurgent currents are activated near-threshold and are involved in excitatory post-synaptic potential (EPSP) amplification and re-excitation upon repolarization, respectively. Inactivating  $K_v$  channels function as regulators of neuron excitability. Low-threshold  $K_v$  channels set the AP threshold and repolarize the membrane shortly after activation (delayed rectifiers and A-type) (**Fig. 3D**).

As an AP propagates, it leaves behind inactivated  $Na_v$  channels and hyperpolarizing  $K_v$  channels in a high conductance state (afterhyperpolarization phase) that hyperpolarize the

membrane potential. Consequently, in normal conditions, the previously excited portion of the axonal membrane is not immediately re-excitabile (i.e.,  $\approx 1\text{-}5$  ms absolute refractory period) and the AP conduction is unidirectional. An instantaneous snapshot of the AP plotted spatially along an axon portion is shown in **Fig. 3C**. In several CNS neurons, afterdepolarization (i.e., membrane potential depolarized relative to the resting potential) occurs after a fast afterhyperpolarization. A plethora of ionic currents contribute to afterdepolarization, including persistent and resurgent  $\text{Na}^+$  currents, but also  $\text{Ca}^{2+}$  currents (L-type). If the afterdepolarization reaches the firing threshold, the result is all-or-none burst firing (Bean, 2007; Connors et al., 1982).

Undoubtedly, the firing properties of a neuron depend on the tuning of the active properties of its' axonal membrane. The diversity of ion channel currents, in particular, provides neurons with a vast repertoire of membrane dynamics and, consequently, computations. Remarkably, different invertebrate neurons of the stomatogastric ganglion can have ion channel conductances that vary  $\approx 6$ -fold and yet, display similar burst firing properties (Goldman et al., 2001). Moreover, these properties can be extremely resilient to perturbations (e.g., temperature changes), that drastically change the conductances and kinetics of the ion channels (Alonso & Marder, 2020). These findings put into question how adaptive (or redundant) the active properties of axonal conduction can be in mammalian neurons and which homeostatic mechanisms govern the relative expression of all ion channel types.

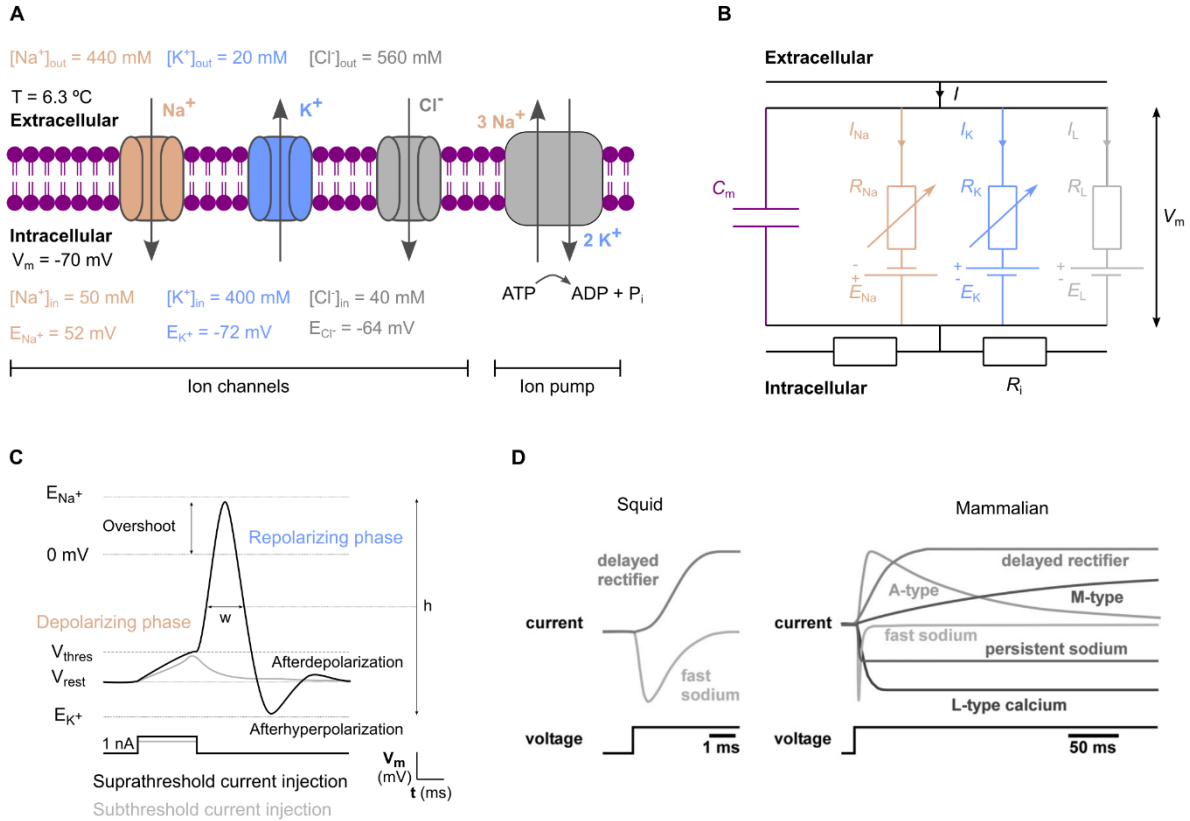


**Figure 3 – The Hodgkin-Huxley model and the action potential. (A)** Schematic of the squid giant axon's cell membrane. The selective to  $Na^+$ ,  $K^+$  and  $Cl^-$  ion channels are represented, as well as the  $Na^+/K^+$  ion pump. The reversal potential values ( $E_{Na}$ ,  $E_K$ , and  $E_{Cl}$ ) were derived using the Nernst equation, assuming a temperature of  $6.3 \text{ }^\circ\text{C}$  **(B)** The Hodgkin-Huxley equivalent electrical circuit of the cell membrane passive and active properties.  $C_m$  represents the lipid bilayer membrane capacitance,  $R_{Na}$  and  $R_K$  represent the variable ion channel resistance influenced,  $R_L$  represents the linear leakage resistance defined by other ions (mainly  $Cl^-$ ). The voltage sources  $E_{Na}$ ,  $E_K$ , and  $E_L$  represent the reversal potentials for  $Na^+$ ,  $K^+$  and other ions (mainly  $Cl^-$ ). **(C)** Schematic of an action potential (AP), elicited by suprathreshold current injection. The response to subthreshold current injection is also shown (in grey). The depolarizing (or upstroke) phase is driven by  $Na^+$  conductance (entry), until the  $E_{Na}$ . Then, the repolarizing phase is characterized by  $Na^+$  deactivation and increase in  $K^+$  conductance, until the  $E_K$ . The AP shape can be characterized by a height ( $h$ ), typically measured from the most negative voltage achieved (afterhyperpolarization), and a width ( $w$ ), typically measured at half-maximal AP height (or amplitude). **(D)** Schematic comparison of two types of ionic current arrangements in axons. First, the simple case of the squid giant axon with only fast sodium and delayed rectifier potassium currents. Then, a more complex (e.g., mammalian axon)

arrangement with several different types of ionic currents, each activating/inactivating with singular time constants (adapted from (Bucher & Goaillard, 2011)).

### 1.2.2 The Action Potential

Most neurons encode and transmit information via the conduction of APs. Thus, AP initiation and its subsequent conduction have been extensively investigated *in vitro* and *in vivo* (Clark et al., 2005; G. Stuart et al., 1997; G. J. Stuart & Sakmann, 1994). In the CNS, after the rapid AP onset, APs propagate orthodromically along the axonal arbor, but also back-propagate towards the somatodendritic compartment. In the PNS, afferent sensory neurons need to carry information from their axon terminals, thus conduction is antidromic. AP propagation controls the reliability and the timing with which neuronal networks communicate, thus the modulation of this process has repercussions for, at least, temporal coding. Importantly, most parameters (if not all) that influence AP propagation (e.g., ion channel density, branching, axon diameter), can be modified by, at least, neuronal activity (reviewed in (Alcami & El Hady, 2019; Bucher & Goaillard, 2011)). Moreover, important AP characteristics, such as AP shape, can be modulated and are known to convey information beyond timing (reviewed in (Rama et al., 2018)). Yet, the relevance of this adapting computational repertoire is far from understood.

#### ***Initiation***

Classically, the somatodendritic compartment is viewed as the main locus for neuronal reception and processing of incoming synaptic inputs. These synaptic inputs can be classified as inhibitory post-synaptic potentials (IPSPs) or EPSPs, as they hyperpolarize or depolarize the target neuron. EPSPs are temporally summated (graded potentials) and, after surpassing a firing threshold, lead to AP initiation in the AIS. An essential feature of the all-or-none property of the AP is the notion of a firing threshold, which is not fixed but rather corresponds to a range. Channel “noise” is thought to account for the high variability of firing thresholds, as the opening of voltage-gated channels is a stochastic process. Alternatively, this variability may be explained by instantaneous differences between subthreshold potentials measured in the soma (where recordings are typically performed) and the AIS (Bean, 2007).

After AP onset, active backpropagation and passive electrotonic spread occur towards the somatodendritic compartment (G. J. Stuart & Sakmann, 1994). This active backpropagation is supported by Na<sub>v</sub>1.2 channels in the proximal AIS and somatodendritic compartment (W. Hu

et al., 2009). This mechanism may provide a retrograde signal of neuronal output, which in well-defined temporal critical windows can potentiate or depress synaptic connections (i.e., spike-timing dependent plasticity (STDP)) (Bi & Poo, 1998; Markram et al., 1997). Still, the extent to which AP backpropagation can invade distal dendrites remains controversial. Additionally, AP backpropagation may fail to depolarize the soma, in which cases, a strongly attenuated version (“spikelet”) of the AP is recorded at the soma (Michalikova et al., 2019).

## **Conduction**

As previously detailed, AP conduction is an active process, dependent on a high density of voltage-gated channels throughout the axon. In unmyelinated axons, AP conduction is supported by  $\text{Na}_v1.2$  channels that are thought to be homogeneously distributed along the axon, though particularly enriched at varicosities and branch points to ensure reliable propagation throughout the axon arbor (H. Hu & Jonas, 2014). In myelinated axons, NoR act as hot spots for  $\text{Na}_v$  (mainly the 1.6 and 1.1 isoforms) and  $\text{K}_v$  channels that regenerate AP propagation (Alpizar et al., 2019).

APs are thought to be conducted with high temporal precision (low jitter) and reliability throughout mammalian axonal arbors (Popovic et al., 2011; Radivojevic et al., 2017; Ritzau-Jost et al., 2021). In fact, axons of the medial superior olive (auditory system) can relay APs at frequencies up to 1 kHz without failures (Scott et al., 2007). Still, conduction failures have been observed in several experimental models, including rat DRGs (X. Wang et al., 2016) and hippocampal neurons (Meeks & Mennerick, 2004). Several factors can determine a conduction failure (e.g., frequency-dependent conduction failures), but geometrical factors, such as axon branch points, are among the most studied (Bucher & Goillard, 2011). Abrupt changes in axon diameter at branching points may cause a conduction failure if the current generated by the main axon fails to load one of the branches. Branching points can also slow down APs in the millisecond range, overcoming the refractory period. In these cases, AP reflection (reverse/antidromic conduction towards the soma) can occur (Goldstein & Rall, 1974; Manor et al., 1991). AP invasion into pre-synaptic terminals is especially critical, as the geometrical perturbation at the terminal arborization can decrease the fidelity of AP propagation. In, at least, hippocampal mossy fibers,  $\text{Na}_v$  channel density is very high at the pre-synaptic terminals ( $\approx 2000$  channels per synaptic bouton), which amplifies the AP to secure propagation and locally increases conduction velocity (Engel & Jonas, 2005). A scaling increase in  $\text{Na}_v$  density at branching points may also secure propagation throughout the arbor in, at least, fast-spiking

hippocampal interneurons (H. Hu & Jonas, 2014). Recently, the  $\beta 2$  subunits of  $\text{Na}_v$  channels were found to be required to prevent conduction failures at branching points in rat hippocampal cultures (I. H. Cho et al., 2017). In cultured Purkinje neurons, APs have been shown to conduct reliably along the axon arbor (including bifurcations) but attenuate strongly close to the terminals, due to a relative sparse and abundant expression of  $\text{Na}_v$  and  $\text{K}_v1$  channels, respectively (Kawaguchi & Sakaba, 2015).

It is important to note that propagation failures induce a mismatch between the number of proximally initiated APs and the ones that reach the pre-synaptic terminals (i.e., successful conduction). Thus, a reliable high-frequency firing at the AIS, for example, may not impact the pre-synaptic terminals uniformly (Alcami & El Hady, 2019).

### **Conduction Velocity**

In clinical practice, a nerve conduction velocity test is important to determine nerve damage in demyelinating diseases, for example. Still, conduction velocity *per se* provides little information about the functional aspects of neuronal communication. Axonal conduction delay (which depends on conduction velocity and axonal length), however, may introduce multiple temporal patterns in the propagation of a neuronal output, with consequences not fully understood (reviewed in (Debanne et al., 2011)). Concisely, a certain temporal pattern in the main axon may transform into multiple patterns along the axonal arbor.

In unmyelinated axons, conduction velocity has been estimated to be  $\approx 0.25\text{--}0.38$  m/s (fastest in CA3 pyramidal neurons), while in large myelinated axons it can achieve  $\approx 100$  m/s. In myelinated fibers, the effective membrane resistance of the axon is increased by several orders of magnitude, and the membrane capacitance is reduced by a similar factor, which enable very fast saltatory conduction in-between NoR. In unmyelinated axons, conduction velocity critically depends on several biophysical factors such as the number of available  $\text{Na}_v$  channels, temperature, membrane capacitance and axial resistance. The larger the  $\text{Na}^+$  current, the faster the rate of AP rise. Consequently, the spatial voltage gradient is faster and conduction velocity is increased. Temperature influences the rate of increase of  $\text{Na}_v$  channels conductance, thus channels open and close more slowly at lower temperature, which in turn decreases conduction velocity. Membrane capacitance determines the amount of charge required to depolarize the membrane, thus an increased capacitance slows conduction (higher time constant). The capacity of unmyelinated membranes is often approximated to  $1 \mu\text{F}/\text{cm}^2$ . Thus, capacitance

measurements of small-to-large axons vary from pico- to nanoFarads. Axial resistance depends on the axoplasm resistance to current flow and the axon diameter. Larger axons present a decreased longitudinal resistance, which allows for a larger current flow, hence a faster conduction. Axon diameter is a key determinant of conduction velocity. Theoretically, in unmyelinated axons, conduction velocity is proportional to the square root of the axon diameter (Hodgkin, 1954), while in myelinated axons, depends linearly on fiber diameter (Waxman, 1980).

Remarkably, even the intrinsic properties of the axon are not immutable (reviewed in (Alcami & El Hady, 2019)). For example, axon diameter (and membrane capacitance consequently) can dynamically change via activity-dependent plasticity mechanisms in CA3 pyramidal neurons, modulating conduction velocity (Chéreau et al., 2017).

### **Shape**

The AP shape differs considerably among various types of neurons. APs are commonly characterized by a width, a height, and an overshoot magnitude (**Fig. 3C**). Although a travelling AP's shape is seen as a stereotyped waveform, it's profile is particularly important in the pre-synaptic terminals, as it modulates  $\text{Ca}_v$  currents and neurotransmitter-containing vesicle release. In fact, pre-synaptic  $\text{Ca}^{2+}$  entry and neurotransmitter release exhibit a non-linear dependence, such that small changes in the level of  $\text{Ca}^{2+}$  can profoundly impact quantal release (i.e., the amount of neurotransmitter-containing vesicles released) (reviewed in (Dolphin & Lee, 2020)).

AP width may vary from  $\approx 180 \mu\text{s}$  (e.g., inhibitory interneurons, Purkinje neurons) to  $\approx 4 \text{ ms}$  (e.g., dopaminergic neurons). AP width can hint at the type of firing behavior. For example, neurons with narrow APs usually exhibit “fast-spiking” behavior, as the fast channel kinetics allow for high-frequency firing, even during prolonged stimulation. AP width may increase during periods of increased frequency firing, due to the cumulative inactivation of  $\text{K}_v$  channels (Bean, 2007).

Unlike subthreshold signals, APs do not decrease in amplitude (height) along the axon, due to the active regeneration. AP height and overshoot magnitude (i.e., the peak relative to 0 mV) are also governed by the different ion channel conductances and kinetics. During bursting activity, APs recorded somatically tend to decrease in amplitude (height), presumably due to  $\text{Na}_v$  channels inactivation, but little attenuation occurs in axonal recordings even at very high firing frequencies (Shu et al., 2007). Several studies have now shown that the AP waveform

can be important in governing vesicle release probability in axon terminals. For example, it has been recently shown that pre-synaptic  $\text{Na}_v$  channels amplify the pre-synaptic AP amplitude (by  $\approx 20\text{--}40\%$ ) when transmitting synchronous somatic inputs to the post-synaptic neuron (Mickaël Zbili et al., 2020).

AP shape can only be determined precisely in intracellular recordings. Still, AP shape is often a criterion for neuronal identification (and differentiation, e.g., pyramidal neurons vs interneurons) in extracellular recordings (since the electrodes typically record APs from several sources). This data-processing step is known as spike-sorting and is an active field of research (reviewed in (Rey et al., 2015)), as state-of-the-art technologies (e.g., neuropixels probes, high-density microelectrode arrays) steadily increase the number and spatial resolution of the recording electrodes (Steinmetz et al., 2021). Consequently, a single neuron activity may be probed by several electrodes, which, in turn, record from several neurons, simultaneously. The different established neuron-electrode interfaces introduce distortions in AP shape that are used for the retrieval of neuronal identity (e.g., via template matching). It is important to note that these spike-sorting methods assume a stereotypical, immutable, AP shape for each source. However, AP shape during axonal conduction can be modulated by several mechanisms, which can put into question the reliability of spike-sorting methods (Sardi et al., 2017). For example, axonal AP broadening has been shown to occur via glutamate-release of periaxonal astrocytes (Sasaki et al., 2011), soma depolarization (Sasaki et al., 2012a), or, as previously mentioned, during periods of increased firing frequency (Lewandowska et al., 2016; Shu et al., 2007). It is also important to note that the recorded shape depends greatly on the probed compartment (e.g., AIS vs axon terminal), axon geometry, and the actual path of signal conduction, all of which can change within and across days of recording (Bestel et al., 2021; Gold et al., 2006). In general, deriving subcellular (or even cellular) classifications from extracellular recordings alone requires caution.

### 1.2.3 The Ectopic Action Potential

In the CNS, AP initiation typically occurs in the AIS, and the generated AP propagates orthodromically along the axon arbor. Thus, generally, APs propagate from the AIS to the axon terminals, with unidirectional propagation being ensured by the refractory period. Still, axon biophysics allow for bidirectional propagation (orthodromic and antidromic) (**Fig. 4A-B**), a fundamental characteristic that has long been used by neuroscientists to characterize axonal conduction (e.g., in collision tests). The distal stimulation of the axon elicits both an orthodromic

AP (towards the terminals), as well as an antidromic AP (towards the soma), which travel oppositely from the excited site.

Intriguingly, several studies have demonstrated that APs can generate spontaneously at distal sites of the axon (reviewed in (Alcami & El Hady, 2019; Bucher & Goaillard, 2011; Sasaki, 2013)). Distally-generated APs, also known as EAPs or antidromic APs, were first described in invertebrate neurons (reviewed in (Pinault, 1995)), but have since been shown conclusively to co-occur in diverse types of CNS mammalian neurons, both *ex vivo* and *in vivo* (Bähner et al., 2011; Bukalo et al., 2013; Chorev & Brecht, 2012; Dugladze et al., 2012). As EAPs travel antidromically, an easily distinguishable shape can be recorded at the soma: the depolarization phase rises sharply from the resting potential, without prior depolarization (Bähner et al., 2011) (**Fig. 4C**).

In invertebrates, some physiological functions for EAPs have been suggested. For example, in the somatogastric ganglion, motor axons can spontaneously generate EAP tonic or bursting activity in the absence of activity from the central pattern generators (Bucher & Goaillard, 2011). In vertebrates, the occurrence of EAPs has been associated with pathological conditions where the axon is hyperexcitable, such as epilepsy (Gutnick & Prince, 1972; Stasheff et al., 1993), nerve injury (Costigan et al., 2009; Pinault, 1995) or demyelination (M. S. Hamada & Kole, 2015), but also with physiological functions, such as fast network oscillations (Bähner et al., 2011; Dugladze et al., 2012; R. D. Traub et al., 2003). As the functional implications of EAPs are very significant, these studies have opened perspectives on neuronal communication beyond the canonical orthodromic signal transmission (Sasaki, 2013; Roger D. Traub et al., 2020).

Still, the physiological relevance of EAPs is very far from being established, as most studies facilitate their occurrence via chemical or electrical stimulation (Bucher & Goaillard, 2011; Roger D. Traub et al., 2020). Even in physiological states (e.g., fast-network oscillations), it is not clear if EAPs appear simply as a by-product (“electrophysiological artifact”) of the underlying network connectivity (e.g., axo-axonal synapses). During kainate-induced gamma oscillations ( $\approx 25\text{-}100\text{Hz}$ ), the firing rate of CA3 pyramidal neurons distal axons ( $>600\text{ }\mu\text{m}$  from the soma) can be  $\approx 4\text{-}5$  times higher than that of the corresponding somata. However, most of these EAPs do not invade the somatodendritic compartment, due to the action of inhibitory axo-axonic cells that target the AIS (Dugladze et al., 2012). Although the mechanisms of EAP generation during gamma oscillations are still unknown, the tonic inhibition of their backpropagation suggests a functional separation of axonal and somatic activity during this network behavior (**Fig. 4D**).

Paradoxically, the facilitation of EAPs has revealed a possible role in synaptic plasticity in CA1 neurons. Eliciting EAPs reduces synaptic strength and leads to an upstream cell-wide synaptic downscaling (Bukalo et al., 2013), which is accompanied by a rapid downregulation of brain-derived neurotrophic factor (BDNF) mRNA transcripts (Bukalo et al., 2016). Subsequent synaptic stimulation can lead to long-lasting synaptic strengthening (Bukalo et al., 2013).

Many uncertainties hold regarding the precise mechanism(s) of initiation of EAPs, although they are not mutually exclusive (reviewed in (Alcami & El Hady, 2019; Michalikova et al., 2019; Roger D. Traub et al., 2020; Trigo, 2019)). Here, I will delve into the most plausible: local depolarization mediated by activity in connected (i.e., electrical or chemical synapses) (Bähner et al., 2011; Schmitz et al., 2001) or adjacent axons (i.e., ephaptic coupling) (Anastassiou & Koch, 2015; Han et al., 2018); and activation (spontaneous or not) of ionic channels in unmyelinated thin segments of the axon (M. S. Hamada & Kole, 2015; Pinault, 1995) (**Fig. 4B**).

Moreover, different mechanisms of EAP initiation may allow for the distinction of different modes of EAP activity (as defined in (Bucher & Goaillard, 2011)). EAPs that initiate spontaneously in the axon (M. S. Hamada & Kole, 2015); that occur after orthodromically propagated activity (e.g., synaptic potentials, distal integration following repetitive activity) (M. E. J. Sheffield et al., 2011; Thome et al., 2018); or that occur in response to input (e.g., axo-axonic synapses, neuromodulators) (Bähner et al., 2011; Schmitz et al., 2001).

### ***Axo-Axonal Coupling***

For a long time, coupling between axons has been known to occur (Katz & Schmitt, 1940). These axo-axonal interactions can occur via three forms: chemical synapses, electrical synapses and ephaptic coupling (**Fig. 4B**). Axo-axonal interactions can give rise to APs that propagate antidromically or bidirectionally (if not initiated in the axon terminals).

Axo-axonal coupling by chemical synapses is typically performed by GABAergic neurons, known as axo-axonic cells (Debanne et al., 2011). For example, the AIS of a single hippocampal neuron can receive up to 30 symmetrical synapses from a single GABAergic interneuron (chandelier cell). These GABAergic terminals onto principal cells' axons can control AP initiation, or even, shunt EAP invasion of the soma in the CA3 region (Dugladze et al., 2012). It is important to note that even though GABAergic currents in the proximal axon are normally associated with inhibition (Debanne et al., 2011), there is conflicting evidence that this is always the case (Szabadics et al., 2006). The conflicting evidence may be explained by a

known developmental switch in GABA polarity (Ben-Ari et al., 2007), in which chandelier GABAergic axo-axonic synapses are initially excitatory (at least until 2-3 weeks post-natal, in mice) but become inhibitory in mature networks, as recently shown (Pan-Vazquez et al., 2020).

Direct axo-axonal coupling via electrical synapses is mediated by gap junctions (Schmitz et al., 2001). Electrical synapses are most prevalent during early development, preceding the development of persisting chemical synapses. Still, an uncertain degree of electrical coupling persists into adulthood in the CNS (Roger D. Traub et al., 2020). Recent findings have suggested that mature glutamatergic CNS networks (e.g., CA3 neurons) maintain a high number of electrical synapses, which are normally silent but can be readily recruited (e.g., via pH changes) (Ixmatlahua et al., 2020). At least some classes of central neurons, such as GABAergic interneurons (Hestrin & Galarreta, 2005) or inferior olivary cells (Lefler et al., 2020), are known to establish and maintain electrically coupled networks throughout adulthood (reviewed in (Alcamí & Pereda, 2019)). In electrical synapses, an AP in the pre-junctional axon induces a “spikelet” (or fast prepotential) in the post-junctional axon ( $\approx 2$ -30 mV), which corresponds to a strongly attenuated version (“low-pass filtered”) of the AP. The spikelet reaches a detectable level  $\approx 1$  ms after transmission, a delay which is introduced by the capacitive loading of the post-junctional membrane. These spikelets can propagate bidirectionally along the axon and unraveling their exact origin and function is an active field of investigation (reviewed in (Michalikova et al., 2019; Trigo, 2019)). For example, spikelets have been shown to represent  $\approx 1/3$  of the activity of CA1 neurons *in vivo* and spikelet frequency is thought to play a role in spatial exploration (Epsztein et al., 2010). If the spikelets depolarize the distal axon sufficiently (i.e., crossing threshold), an EAP initiates (Chorev & Brecht, 2012; Y. Wang et al., 2010). This electrical coupling allows for the synchronization of axons and is thought to mediate, at least partially, high-frequency oscillations (100-200 Hz) in the hippocampus, known as sharp-wave “ripple” complexes (reviewed in (Roger D. Traub et al., 2020)). These complexes can quickly propagate bidirectionally along the hippocampus (Imbrosci et al., 2021), and have been implied in memory consolidation (Bukalo et al., 2013; Buzsáki, 2015). Critically, these  $>100$  Hz oscillations are thought to be too fast for originating from chemical synapses alone. Such “ripples” persist during pharmacological blockade of chemical synapses, but are sensitive to gap junction blockers (e.g., carbenoxolone), proving their reliance on electrical coupling (Draguhn et al., 1998; R. D. Traub et al., 2003). Concomitantly, this activity is facilitated by increasing gap junction electrotonic coupling (e.g., alkalization by  $\text{NH}_4\text{Cl}$ ) or via  $\text{GABA}_A$ -mediated axon depolarization (e.g., via  $\text{GABA}_A$  agonists)

(Bukalo et al., 2013). *In silico* models have suggested that these oscillations originate from connected thin branches, where EAPs invade the main axon with a low safety factor (Böhner et al., 2011; Roger D. Traub et al., 2012). It is important to note, however, that the precise mechanism (e.g., which gap-junction protein is involved, and where exactly) is hard to decipher, as there is a lack for specific gap junction blockers and decisive anatomical data (e.g., via electron microscopy). Researchers usually resort to a cocktail of different blockers (each with non-specific actions) to achieve a gap junction blockade. Other approaches, such as the use of knock-out animal models, can also have issues, such as compensating expression of other gap junction proteins (Roger D. Traub et al., 2020). Concerning anatomical data, although there is immunohistological evidence that principal neurons express several gap junction proteins (e.g., mainly connexin36), most studies have only (indirectly) shown axo-axonal coupling via dye coupling (i.e., intracellular dye loading of one neuron “diffuses” to another) (Schmitz et al., 2001).

Axo-axonal direct coupling (i.e., chemical and electrical synapses) enables neuron-to-neuron communication in a few milliseconds, however, a few studies have reported neuronal synchronization in the sub-millisecond scale (Han et al., 2018). This ability to ultra-fast synchronize activity is thought to be mediated by ephaptic coupling. In ephaptic coupling, the AP conduction along an active axon depolarizes a neighbor/adjacent ( $<20\ \mu\text{m}$ ) resting axon via a locally generated extracellular potential ( $\approx 0.5\text{--}0.1\ \text{mV}$  at a  $\approx 0\text{--}40\ \mu\text{m}$  distance) (Han et al., 2018). This type of coupling is “capacitive” since there is no transmembrane current flow (unlike “resistive” electrical synapses). Thus, the resulting AP (or spikelet) waveforms are typically narrower than the originating APs (“high-pass filtered”). Together with membrane fluctuations or endogenous electrical fields ( $\approx 5\ \text{mV/mm}$  *in vivo*), this slight depolarization can be sufficient to entrain AP timing (Anastassiou et al., 2011). Thus, beyond recruitment of neighboring inactive axons, ephaptic coupling may accelerate AP conduction of near-concurrently active axons (within a  $\approx 1\text{--}2\ \text{ms}$  delay), promoting ultra-fast synchronization (Debanne et al., 2011). This effect is expected to occur in bundles of unmyelinated axons, where the periaxonal distance is reduced. Also, due to the stronger extracellular potentials formed (Bakkum et al., 2018), this effect is more likely to occur between nearby AISs (Han et al., 2018).

Finally, it is important to note that neuron-glia interactions may also synchronize activity across bundles of myelinated axons in an ultra-fast manner. Interestingly, a single oligodendrocyte can myelinate several axons and depolarize in response to axonal activity with unknown consequences in the network behavior (Micu et al., 2018).

### ***Spontaneous Activation***

There are a few instances where spontaneous activation of the distal axon seems to occur, that is, cases where EAP initiation may occur independently of AP propagation on another neuron. These cases are dependent on axonal excitability, which can change pathologically and physiologically.

In the CNS, EAP initiation has been described in *in vitro* models of epilepsy where the axon is hyperexcitable, such as the penicillin-induced (Gutnick & Prince, 1972), the 4-aminopyridine-induced (Avoli et al., 1998; Roger D. Traub et al., 2001), or the tetanic stimulation epilepsy models (Stasheff et al., 1993). In these studies, distal GABA<sub>A</sub> receptors seem to exert excitatory actions on the axon (Papatheodoropoulos, 2008; R. D. Traub et al., 2003). Demyelination has also been associated with EAP initiation. In a cuprizone-induced myelin loss model, demyelinated axons of L5 neurons were intrinsically more excitable and had an increased sensitivity for spontaneously generating EAPs ( $\approx 0.1/\text{min}$ ) (M. S. Hamada & Kole, 2015).

Physiologically, several neurotransmitters and neuromodulators can affect axon excitability, such as glutamate, adenosine (Sasaki et al., 2011), or GABA (Papatheodoropoulos, 2008). GABA<sub>A</sub> receptors are present throughout the axon of principal cells and the main modulators of axon excitability (Debanne et al., 2011). While in the soma and the proximal axon of mature neurons, their function seems to be mainly inhibitory (hence the AIS being the main site for axo-axonic GABAergic synapses) (Dugladze et al., 2012; Pan-Vazquez et al., 2020), several studies have found an excitatory effect in the axon proper and terminals (Zorrilla de San Martin et al., 2017). This is presumed to be driven by a GABA<sub>A</sub> current reversal potential (i.e., Cl<sup>-</sup> reversal potential) that is transiently depolarizing in the distal axon, due to the relatively high axoplasmic Cl<sup>-</sup> concentration. This dual GABAergic effect of depolarization and hyperpolarization of the axonal and somatodendritic compartments, respectively, has been used for the facilitation of EAP initiation in several studies by the use of GABA<sub>A</sub> receptor agonists (e.g., muscimol) (Böhner et al., 2011; Bukalo et al., 2013; Papatheodoropoulos, 2008).

Theoretically, stochastic activation of Na<sub>v</sub> channels may be sufficient for EAP initiation in very thin segments of the axonal arbor (e.g., axon collaterals, axon terminals) (Pinault, 1995). In such a small-capacitance portion of the axon, membrane fluctuations due to, for example, channel noise may cause EAP generation (Chow & White, 1996; O'Donnell & van Rossum, 2014).

The previous mechanisms portray distal axon initiation as being independent of somatic activity. However, a few studies have challenged this view. Interestingly, EAP initiation may be modulated by incoming PSPs (i.e., subthreshold signals that propagate passively). Recently, it was shown that EPSPs paired with sub-threshold distal axon stimulation facilitate EAP initiation (up to  $\approx 350$   $\mu\text{m}$  down the axon), while IPSPs inhibit EAP initiation (Thome et al., 2018). Lastly, it has been shown that hippocampal and neocortical interneurons produce a form of persistent EAP firing that can last for minutes (also known as “retroaxonal barrage”), following realistic or repeated patterns of somatic electrical stimulation (M. E. J. Sheffield et al., 2011). This indicates a form of slow integration of activity by the distal axon, that, interestingly, can propagate to non-stimulated cells and is inhibited by gap junction blockers and  $\text{Ca}_v1$  blockers. Though, most probably, population synchronization is mediated by electrical coupling, connexin36 knock-outs still exhibit population-level retroaxonal barrages (M. E. J. J. Sheffield et al., 2013).

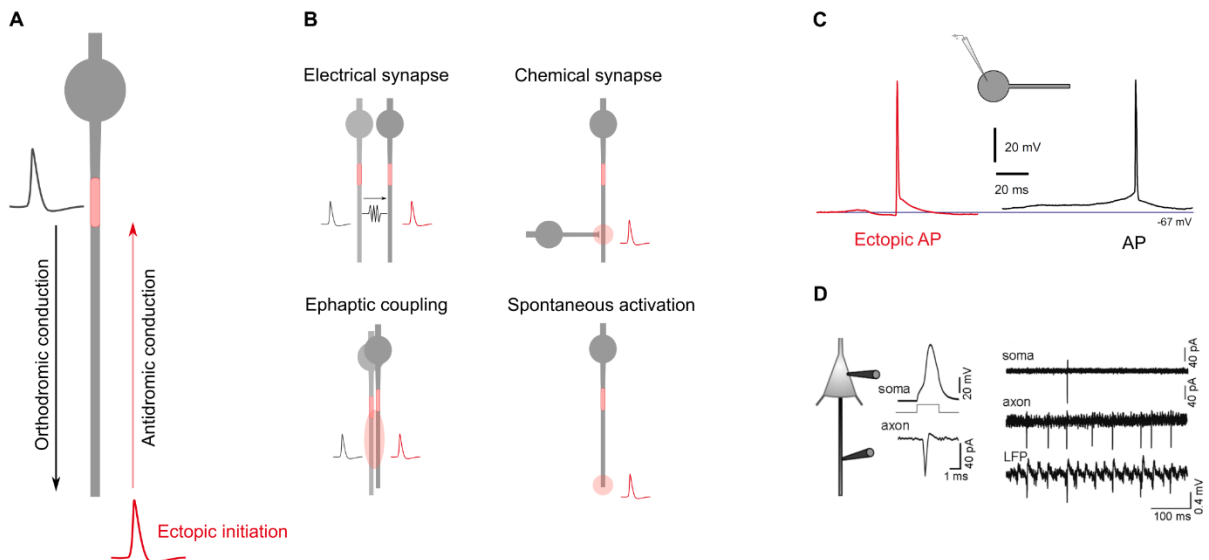


**Figure 4 – Mechanisms of ectopic action potential initiation and identification. (A)** Schematic representation of orthodromic conduction following action potential (AP) initiation, and antidromic conduction following ectopic AP (EAP) initiation. **(B)** Schematic representations of different modes of EAP initiation. **(C)** Distinct EAP and AP shapes as recorded intracellularly in the soma via whole-cell patch-clamp. Note that the EAP upstroke rises from the resting membrane potential without previous soma depolarization (adapted from (Bähner et al., 2011)). **(D)** Dual somatic and axon-attached recordings of a CA3 pyramidal neuron demonstrate that axons can fire independently of the corresponding somata during gamma oscillations. Most of

the EAPs do not invade the somatodendritic compartment, due to the inhibitory action of chandelier cells on the AIS (adapted from (Dugladze et al., 2012)).

### ***Ectopic Activity in Dorsal Root Ganglion Neurons***

In many aspects, DRG neurons are a special case in the nervous system's structural and functional organization (Devor, 1999; Nascimento et al., 2018). Likewise, ectopic activity (sometimes termed as “ectopia” in the DRG literature) terminology acquires a different meaning than what has been previously discussed for the CNS.

The axons of DRG neurons are afferent. Thus, under physiological conditions, APs are initiated in the peripheral terminals of DRG neurons and conducted antidromically towards the CNS. Clearly, and in contrast with the CNS case, the definition of ectopic activity in DRG neurons cannot be described by distal initiation and antidromic conduction of the AP.

In the case of DRGs, EAP terminology is associated with abnormal activity following injury, which can be caused by axotomy, inflammation, or compression of DRG axons (reviewed in (Nascimento et al., 2018)). Despite the prevalence of EAPs under pathological conditions, many uncertainties remain regarding the location and mechanism of EAP initiation in the DRG. EAPs may arise in the soma, in the stem axon, or the injured axon end (i.e., neuroma) (Amir et al., 2005). EAP activity is thought to be caused by exacerbated subthreshold oscillations and hyperexcitability following lesion, due to a structural reorganization of  $\text{Na}_v$  densities (C. N. Liu et al., 2000). Since EAP activity is thought to be a major driver of neuropathic pain (Costigan et al., 2009), its study and pharmacological modulation are of great interest.

It is important to emphasize again that, while EAPs in the CNS are initiated in the distal axon in physiological or pathological conditions; in DRG neurons, EAP activity refers to abnormal initiation that results from an axon insult, and may not necessarily initiate in the distal axon end.

### 1.3 Technologies for the study of axon physiology (*in vitro*)

As it can be already appreciated, the history of neuroscience has been largely shaped by the history of its' technological developments. Likewise, as postulated by Edgar Adrian in 1932, “*The history of electrophysiology has been decided by the history of electrical recording instruments*”. Almost a century later, it is still experimentally challenging to record from axons. Thus, in systems neuroscience, most studies are based on data derived from extracellular recordings or functional imaging of, mainly, somatic APs. Beyond technical specificities, this emphasis on somatic APs introduces several biases, as it assumes that supra-threshold activity initiated in the soma/AIS is the only type of neuronal output capable of influencing up/downstream neurons. However, from the previous sub-chapters, it should be apparent that axon function is not limited to orthodromic conduction of APs. In fact, in certain network behaviors (e.g., sharp-wave ripple complexes, gamma oscillations), distal axons can generate APs at much higher rates than the corresponding somata (Dugladze et al., 2012). Another interesting case is that of substantia nigra dopaminergic neurons, in which dopamine release is often defined by dopamine receptors in the axon terminals and independent from somatic APs (Berke, 2018). Ultimately, in some cases, somatic APs may represent only a fraction of a given neuron output. Thus, it is now clear that neuronal function cannot be fully understood based on somatic recordings alone.

Typically, axons are both extremely long and very thin (often below the  $\approx 200$  nm diffraction limit). This huge length-to-diameter ratio complicates immensely their study with traditional techniques. Additionally, axonal arbors can adopt very complex morphologies that are hard to track, even in 2D *in vitro* cultures. Consequently, the study of axonal function is full of technical challenges. Still, there is an emerging interest in developing technologies that will allow to structurally and electrophysiologically study axons in unprecedented detail. This chapter details on the most recent advances on this front.

#### 1.3.1 Axon Guidance

The first step in dissecting axonal function is to identify and/or control the axon trajectory. Given the growth cone highly motile and cue-sensitive capacity, neuroengineers have long attempted to engineer substrates that can control axon guidance *in vitro* (reviewed in (J. Roy et al., 2013)). The advantage of controlling axon guidance *in vitro* is, at least, two-fold: it simplifies the study of axonal function, as it allows for the following/probing of the whole axon-length (from the soma

to the terminals); and techniques that promote guidance (and correct pathfinding) may be used in, for example, regenerative therapies (e.g., after SCI). A wide range of techniques have been employed to control axon guidance, which can be grossly divided in physical (e.g., substrate structuring) and chemical (e.g., protein patterning) methods of patterning.

The most important methods for *in vitro* patterning are 3D-substrate structuring, microfluidics, and chemical patterning. Still, it is important to note that most of the guidance strategies (e.g., 3D-substrate structuring) do not distinguish between axon, soma, and dendrites *per se* (**Fig. 5A**). For this reason, different methods are often combined to enhance the degree of control over the desired axon path (Amin et al., 2018; Santoro et al., 2014). For example, the establishment of chemical gradients along microfluidic channels, or the biofunctionalization of 3D-structures can help specify axon growth to target regions (**Fig. 5C**).

It is important to note that most of the here mentioned techniques define static patterns for posterior axon growth. However, recent developments have employed photo-reactive (e.g., two-photon patterning) (Broguiere et al., 2020), or thermosensitive (Hong & Nam, 2020) coating materials that allow for the manipulation of axon growth by creating and/or modifying patterns in an *in situ* manner. The maturation of these techniques will certainly allow for more controllable axon guidance in the future, leading to new insights into axon function.

### ***Engineered Substrates***

During development *in vivo*, axon outgrowth and pathfinding partially depend on the physical features of the environment. Taking advantage of the recapitulation of this contact-mediated guidance *in vitro* (“topotaxis”) and the advances in micro- and nanofabrication, researchers have engineered 3D-substrates that greatly impact axon morphology. The outcome of these neuron-substrate interactions can vary across neuron origin or age, but also across the topographical feature dimension, geometry, material, and chemical properties (reviewed in (Leclech & Villard, 2020; Marcus et al., 2017; Raj et al., 2021; Simitzi et al., 2017)).

Different guiding 3D features can be broadly separated into unidirectional and multidirectional, which in turn can be continuous (e.g., grooves, gratings) or discontinuous (e.g., an array of pillars) (**Fig. 5A-C**). While unidirectional structures provide a (most often continuous) topographical cue along a single axis, multidirectional structures promote outgrowth along multiple axis. Most of the structured substrates presented in the literature can also be considered anisotropic, since they impose two (unidirectional) or more (multidirectional)

symmetrical orientations (Leclech & Villard, 2020). Pure isotropic structures (e.g., “random forest” of pillars, nanowires) do not impose a direction on axon outgrowth, but can influence aspects such as axon branching (Gautam et al., 2017; Seo et al., 2018).

Numerous studies have demonstrated that axons from different cell types elongate along discontinuous or continuous anisotropic topographical features in the direction of the pattern (parallel contact guidance) (**Fig. 5A**). The most pronounced effects are usually achieved in linear continuous structures, such as grooves with sub-micron depth and  $\approx$ micron width (Chua et al., 2014). Still, discontinuous topographies, such as arrays of micropillars, can also promote axon guidance (Amin et al., 2018; Leclech et al., 2019; Micholt et al., 2013; Milos et al., 2021). In this case, the critical parameter for strong guidance is the spacing (or pitch) between features, with  $\approx 0.5$ -3  $\mu\text{m}$  being optimal (Simitzi et al., 2017). These discontinuous features are of particular interest, as they can be adapted for the fabrication of 3D devices capable of probing neuronal activity (e.g., MEAs). This will be detailed later on the chapter.

Li et al. (2015) performed a large-scale screening of 71 different continuous and discontinuous micro and nanopatterns to extensively cover different combinations of shape, size, and pitch. In general, continuous features (e.g., gratings) promoted longer axon outgrowth (up to 60%) than discontinuous features (e.g., pillars), or flat substrates (W. Li et al., 2015). Still, it is important to note that continuous unidirectional features tend to decrease the complexity of the branching pattern of the axon (Chua et al., 2014; W. Li et al., 2015), while discontinuous multidirectional features tend to increase the number of branches, and the branches themselves can be guided by the topography (Gautam et al., 2017; Milos et al., 2021; Seo et al., 2018).

Interestingly, perpendicular contact guidance can also rarely occur, but is highly dependent on the cell type and/or the age of the embryo, suggesting a developmental regulation of this phenomena (Leclech & Villard, 2020; Simitzi et al., 2017).

### **Microfluidics**

Microfluidic devices follow a different rationale, which was pioneered in the 70s with the Campenot compartmented chambers (Campenot, 1977). Then, and now, the objective was to guide the axon to a separate culture compartment than the soma. Campenot’s concept together with advances in microfabrication (e.g., photolithography, soft lithography) allowed for a key breakthrough almost 20 years ago (Taylor et al., 2003, 2005). This first microfluidic device

allowed, for the first time, for the spatial and fluidic compartmentalization of the somatodendritic and axonal neuronal compartments. The device comprised two-compartments where neurons could be plated, interconnected by high aspect ratio microchannels (straight lines) into which only neurites could grow. If the microchannels were longer than 450  $\mu\text{m}$ , only axons were able to cross the entire microchannel (Taylor et al., 2005). This simple, yet effective, design is widely used to date (reviewed in (Holloway et al., 2021; Neto et al., 2016)). Concurrently, several asymmetric microchannel geometries (e.g., diodes) that promote unidirectional axonal outgrowth have also been proposed in the literature (Forró et al., 2018; Gladkov et al., 2017; Holloway et al., 2019; Peyrin et al., 2011) (**Fig. 5B**).

Microfluidic devices take advantage of soft lithography for fabricating the desired pattern using biocompatible silicones, typically polydimethylsiloxane (PDMS) (Duffy et al., 1998). Besides neuronal compartmentalization, microfluidic devices' advantages include the usage of less reagent and sample amounts, low cost, and high-throughput potential. These devices allow for targeted chemical or mechanical manipulations of the axon, thus have been used as tools for studying neuroregeneration (J. W. Park et al., 2006), neurodegeneration (reviewed in (H. J. Kim et al., 2012)), neurodevelopment (reviewed in (Fantuzzo et al., 2019; Millet & Gillette, 2012b)), among others. Due to their versatility, microfluidic devices are currently the main tool for the structuring of a "brain-on-a-chip" (Bang et al., 2019; Holloway et al., 2021).

In most neuroscience applications, microfluidic devices are passive, but flow can be driven by capillarity, hydrostatic pressure differences, or external pumps. Hydrostatic pressure differences (e.g., via unbalanced liquid quantities between compartments) are routinely used to establish chemical gradients along the microchannels (via diffusion), or to treat target compartments (J. W. Park et al., 2006). Moreover, a recent study has shown that the precise control of the flow rate and angle can be used to induce mechanical stress on the axon, leading to axonal injury (W. Li et al., 2021).

Importantly, in combination with functional readouts, such as MEAs or calcium imaging, these microfluidic devices have also been used to study fundamental characteristics of neuronal networks. This microfluidic/MEA combination is very relevant for the work presented in this thesis, thus will be thoroughly explored later.

## **Chemical Patterning**

Chemical patterning takes advantage of the growth cone sensitivity (“chemotaxis”) to substrate-bound (e.g., protein coatings) and/or soluble chemical cues (e.g., nerve growth factor (NGF)) for controlling axon guidance (**Fig. 5C**). Microcontact printing ( $\mu$ CP) is the classical technique for substrate patterning, while soluble cues are often used to establish chemical gradients within microfluidic devices (reviewed in (Aebbersold et al., 2016; Raj et al., 2021)).

Most often, in  $\mu$ CP, PDMS stamps with microscale features are initially inked in a coating solution (e.g., poly-D-lysine (PDL), laminin). Then, the stamps are used to imprint the desired patterns in a cell culture substrate. Upon plating, neurons tend to adhere or migrate towards the areas that promote cell adhesion and then extend within the patterned surface (Kleinfeld et al., 1988). This technique can be used to micropattern neurons at single-cell resolution (H. Yamamoto et al., 2016). Still, the simplest application of  $\mu$ CP in neuroscience has been to create isolated networks (neuronal modules) of various sizes to study relationships between network size and connectivity. As an example,  $\mu$ CP has been used to study the great impact of varying the degrees of coupling between neuronal modules on their intra- and inter-activity dynamics (M. U. Park et al., 2021; Hideaki Yamamoto et al., 2018) (**Fig. 5C6**). Yamamoto et al. (2018) created a small-world topology where up to 4 neuronal modules ( $200 \times 200 \mu\text{m}$  squares, where less than 100 neurons adhered) were connected by varying numbers of  $200 \mu\text{m}$ -long lines (defining the degrees of coupling), along which the neurites extended (Hideaki Yamamoto et al., 2018).

$\mu$ CP can be used to more precisely control axon guidance, via the use of both promoting and repelling cues (Oliva et al., 2003; Weydert et al., 2019) or by the application of geometrical constraints on neurite outgrowth (Roth et al., 2012). Interestingly, curved, but not straight, lines exert a strong inhibitory effect on axon specification. After axon specification in a straight line, axons outgrow seamlessly along both straight and curved paths (Roth et al., 2012). These results suggest that, during development, physical cues may precede biochemical cues in axon specification.

Still,  $\mu$ CP is not compatible with long-term control of axonal guidance. Neurons produce their growth factors (e.g., ECM components) and, typically, start extending beyond the micropatterned surface after a few weeks in culture (Aebbersold et al., 2016). For more reproducible and long-term control, physical barriers (e.g., microfluidics) need to be considered (Forró et al., 2018).

Physical Patterning

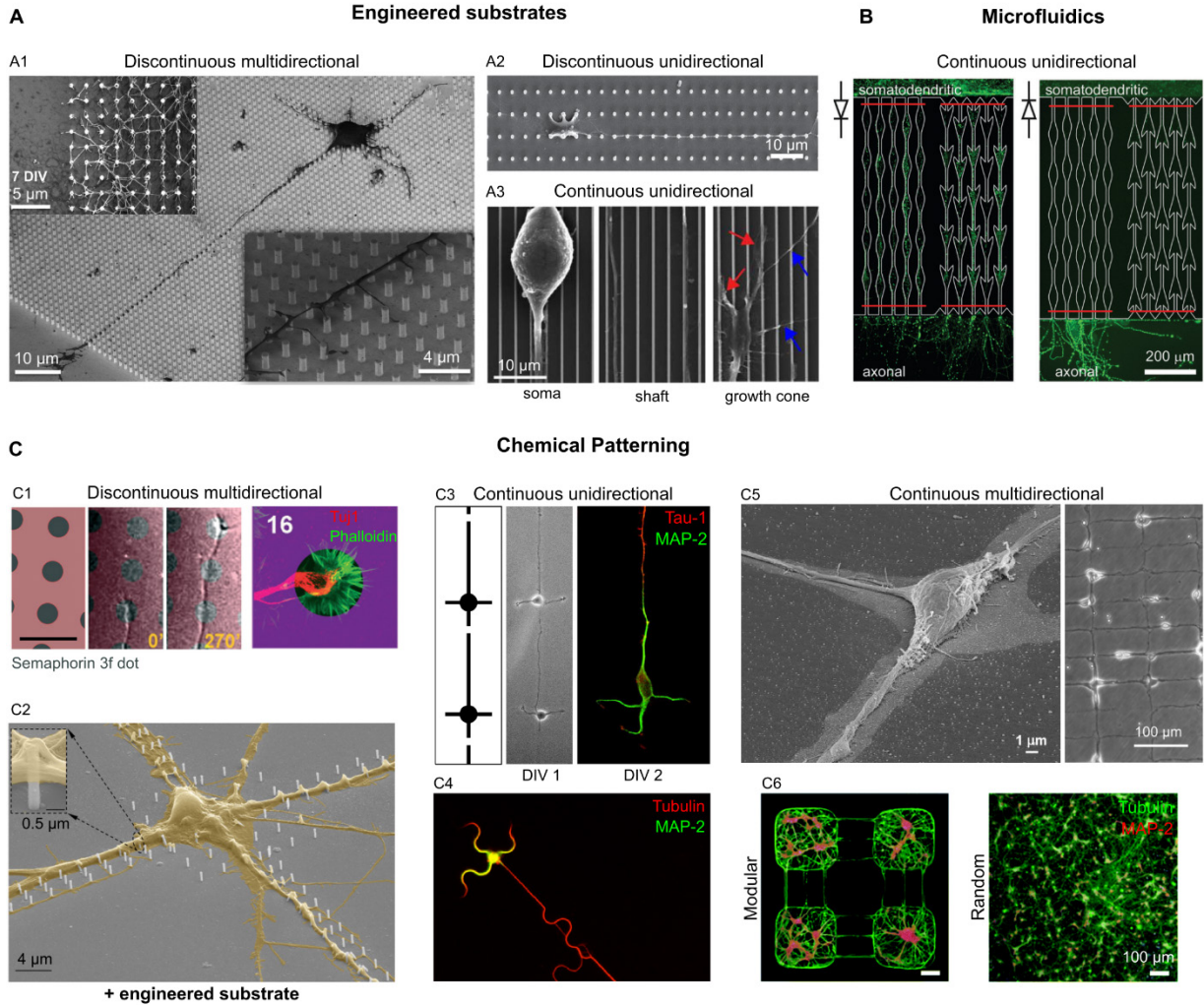


**Figure 5 – Patterning methods for axon guidance.** **(A)** Scanning electron microscopy (SEM) images of neurons growing aligned to discontinuous (vertical nanopillars) (A1 and A2, adapted from (Gautam et al., 2017; M. Park et al., 2016)) and continuous topography (ridges/grooves) (A3, adapted from (K.-J. Jang et al., 2010)) – parallel contact guidance. **(B)** Fluorescent imaging of neurons growing within microfluidic chambers with asymmetric microchannels for unidirectional axonal outgrowth (adapted from (Holloway et al., 2019)). **(C)** Examples of chemical patterning (via microcontact patterning, except for C2) for multidirectional (C1, C2, C5 and C6 adapted from (Amin et al., 2018; M. U. Park et al., 2021; Ryu et al., 2019; A. K. Vogt et al., 2005)) and unidirectional (C3 and C4, adapted from (Roth et al., 2012; H. Yamamoto et al., 2016)) axonal outgrowth. In C2, arrays of nanopillars (engineered substrate) were

biofunctionalized with an adhesion-promoting molecule - poly-DL-ornithine (adapted from (Amin et al., 2018)).

### 1.3.2 Axon Activity

The study of axon function is intimately related to neurophysiology – the study of the activity of the nervous system. Classically, this study relied heavily on electrophysiological techniques (e.g., patch-clamp) which were not adapted to the study of the thin and complex arborizations of mammalian neurons. However, recent technological developments are driving a new era of experimental opportunities. Here I will delve into the most relevant: subcellular patch-clamp, MEAs, and functional imaging techniques (**Fig. 6**).

These approaches enable the probing of axonal activity on a variety of scales. Subcellular patch-clamp allows for stimulation and extracellular-like (axon-attached configuration) or intracellular recordings (whole-cell configuration) from a single point of a single axon. Standard MEAs can be adapted for the extracellular recording and stimulation of multiple axons, while high-density MEAs can be used for the electrical mapping of axonal arbors. Functional imaging techniques (e.g., voltage imaging) can theoretically probe networks with high-spatial resolution. A comparison of the key characteristics, advantages and limitations of these different techniques for the study of axon activity is summarized in **Table 1**.

## Chapter I

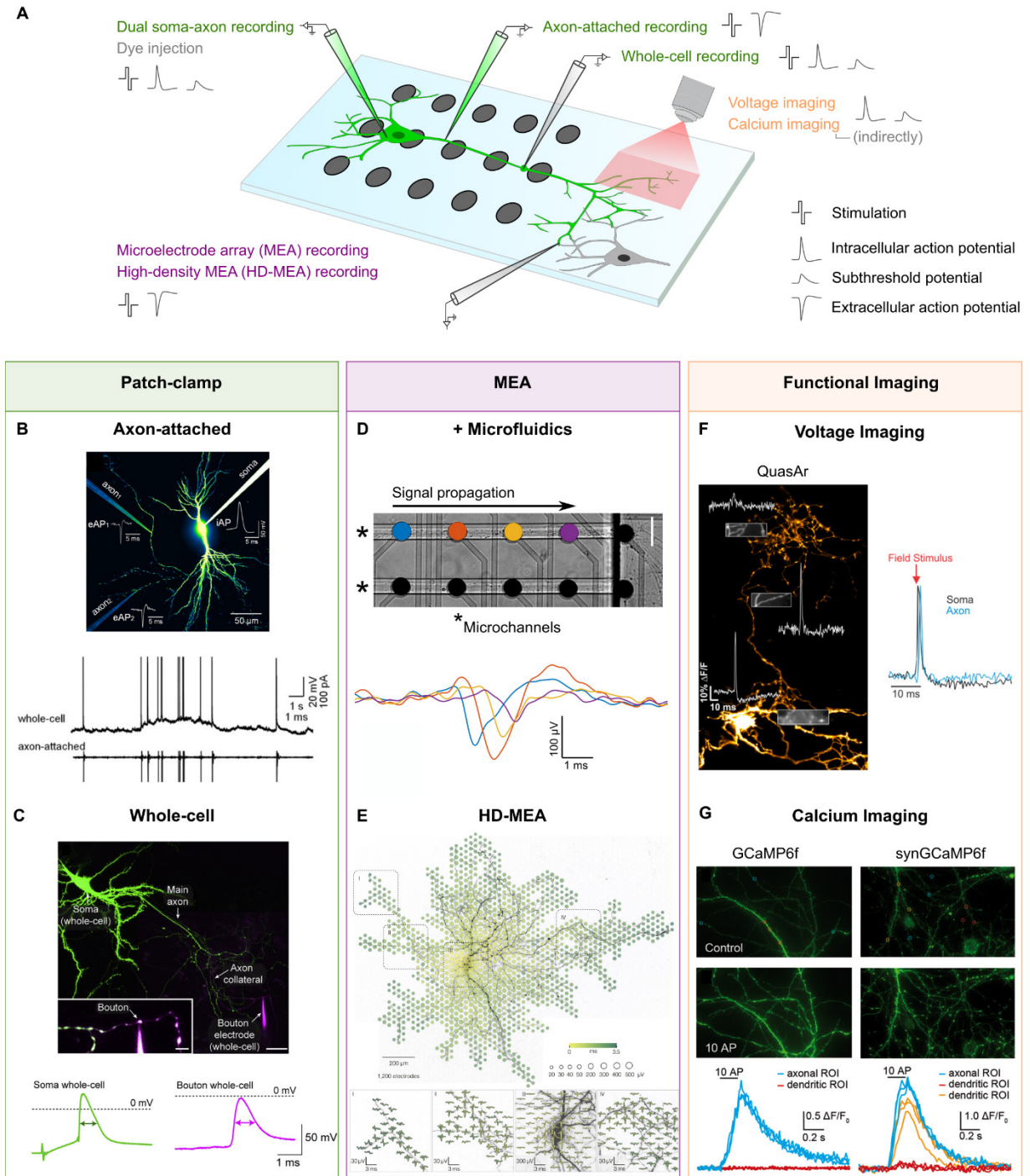


**Figure 6 – Methods for probing axon activity.** (A) Schematic representation of the main experimental approaches to probe axonal activity and the respective readout capabilities. (B) Dual somatic (whole-cell) and axon-attached recording (adapted from (Sasaki et al., 2012a)). (C) Whole-cell bouton recording (adapted from (Ritzau-Jost et al., 2021)). (D) Microelectrode array (MEA) recording in combination with microfluidics (adapted from (Costa et al., 2020)). (E)

High-density MEA (HD-MEA) recording (adapted from (Radivojevic et al., 2017)). **(F)** Voltage imaging (adapted from (I. H. Cho et al., 2017)). **(G)** Calcium imaging (adapted from (Brockhaus et al., 2019)).

### ***Subcellular Patch-clamp***

For a long time, patch-clamp has been the gold-standard for studying neurophysiology at single-cell resolution (Hamill et al., 1981). Typically, a recording micropipette is pressed against a patch of the membrane to form a strong seal resistance (gigaohm seal), which allows for high-fidelity recordings in the cell-attached or whole-cell (if the patch is ruptured via suction, gaining intracellular access) configurations. However, most studies are limited to large compartments of the neuron (usually the soma) due to their easier accessibility.

Until recently, patch-clamp recordings from intact mammalian axons were limited to specific giant axonal structures (3-5  $\mu\text{m}$ ) (e.g., Calyx of Held, mossy fiber boutons) (Engel & Jonas, 2005). Most often, recordings from thin structures could only be obtained upon severing the axon, since the resulting swollen ends (i.e., blebs) were much larger (3-6  $\mu\text{m}$ ) than the intact axon (H. Hu & Jonas, 2014; Kole et al., 2008; Sasaki et al., 2011; Shu et al., 2007; Mickaël Zbili et al., 2020). For the study of axon physiology this is problematic, as axonal lesioning leads to an aberrant reorganization of the cytoskeleton and ion channel distribution. Still, dual soma-axonal bleb recordings in the whole-cell configuration were the basis for the determination of the AP initiation zone (Debanne et al., 2011), for example.

Axon-attached recordings from intact unmyelinated axons ( $\approx 1 \mu\text{m}$  diameter) have been made feasible by fluorescence-guided subcellular patch-clamp (Rowan et al., 2016; Sasaki et al., 2012b) **(Fig. 6B)**. The key advantage of this technique is that both the axon and the recording glass pipette are fluorescently labeled, which greatly facilitates live optical control. Dual somatic and axon-attached recordings have revealed that CA3 pyramidal axons can fire at much higher rates than the corresponding somata during gamma oscillations (Dugladze et al., 2012). Still, this technique is limited to single-site short-term recordings ( $< 1\text{h}$ ) of extracellular-like AP waveforms ( $\mu\text{V}$  range), which are around three orders of magnitude lower than those recorded intracellularly (mV range), and as with other extracellular-based techniques (e.g., MEAs), subthreshold events are not detected (Sasaki et al., 2012a, 2012b). Moreover, the axons' shaft can be as thin as  $\approx 100 \text{ nm}$ , which poses several challenges for obtaining axon-attached recordings.

Whole-cell recordings from varicosities (putative *en passant* boutons) (Ritzau-Jost et al., 2021; Vandael et al., 2021; Vivekananda et al., 2017) or pre-synaptic terminals (Kawaguchi & Sakaba, 2015; Zorrilla de San Martin et al., 2017) (**Fig. 6C**), as well as outside-out patch from the axon shaft (H. Hu & Jonas, 2014) have also been demonstrated, but obtaining the precise AP waveform (one of the main advantages of conventional intracellular recordings) is compromised by technical difficulties. The necessary amplifier configurations and small pipette tip sizes (with increased resistance), adapted for very thin structures, inevitably distort axonal APs (Oláh et al., 2021). Still, direct recordings from varicosities have allowed for the characterization of the pre-synaptic AP duration and amplitude. Ritzau-Jost et al. (2021) demonstrated that pre-synaptic APs broaden during high-frequency firing in excitatory L5 pyramidal neurons, but not in inhibitory fast-spiking interneurons. In both cellular models, APs propagated reliably and at constant large amplitude (larger than at the soma) into axon collaterals, even during high-frequency firing (Ritzau-Jost et al., 2021).

Overall, subcellular patch-clamp techniques, in particular the intracellular configurations, allow for the highest possible fidelity in axonal recordings. However, while axon-attached recordings allow for minimally-invasive (i.e., extracellular-like) recordings from the axon shaft, current intracellular methods are limited to relatively large structures of the axon (e.g., varicosities). Moreover, their technical complexity and invasiveness limit the throughput and compatibility with long-term experiments, respectively. Critically, the inability to record from multiple sites along the axon simultaneously, precludes subcellular patch-clamp from tracking AP propagation throughout the axon arbor.

### ***Microelectrode Arrays (MEAs)***

MEA technology is at the forefront of recording electrical activity from large neuronal ensembles (reviewed in (Forro et al., 2021; Obien et al., 2015; L. Xu et al., 2021)). Typically, standard MEAs are composed by a fixed grid of multiple planar microelectrodes (most often 60-256 electrodes, interspaced by  $\approx 30$ -500  $\mu\text{m}$ ), which are embedded in a transparent substrate (e.g., glass wafer) that functions as a cell culture vessel. After cell plating on MEAs, the activity of self-organized neuronal ensembles can be monitored and modulated (e.g., via stimulation) for over a year (Potter & DeMarse, 2001). Currently, MEAs provide a reliable, versatile, non-invasive, and high-throughput functional assay at the network level.

However, these planar microelectrodes only allow for the recording of strongly-attenuated extracellular signals ( $\mu\text{V}$  range) and are limited to the detection of suprathreshold activity (**Fig. 7A-B**). Moreover, the recorded potentials are highly dependent on the relative positioning of the electrogenic compartment (e.g., soma) to the electrode (neuron-electrode interface) (**Fig. 7C-D**), and, typically, the microelectrodes only probe a very small fraction of the whole substrate (Spira & Hai, 2013). These limitations make apparent the main reasons why standard MEA technology, together with conventional culture procedures, are not adapted to the study of axonal function: 1) axons navigate the substrate freely, most frequently not crossing probing areas (i.e., the electrodes' vicinity); 2) the network complexity difficults source-target identification (optically or electrophysiologically); 3) the signal-to-noise ratio (SNR) of axonal signals is so low that propagating extracellular APs can only be identified after averaging noise several times (Abbott et al., 2020; Bakkum et al., 2008, 2013; Tovar et al., 2018).

Several research groups, including ours, have circumvented these disadvantages by merging the benefits of MEAs and microfluidics (Gladkov et al., 2017; Gribi et al., 2018; Rouhollah Habibey et al., 2017; Hong et al., 2017; J. M. Jang et al., 2016; Lewandowska et al., 2015; Lopes et al., 2018; Moutaux et al., 2018; Pan et al., 2011; Shimba et al., 2021) (**Fig. 6D** and **Fig. 7E**). Aligned microchannels can be used to guide axons over the microelectrodes, allowing for the study of signal propagation with high temporal and spatial resolution. To this end, we have developed specialized algorithms that enable, for example, the characterization of conduction direction and velocity, when using MEA-microfluidic platforms (Heiney et al., 2019). This combination creates more advantages beyond axon guidance over the microelectrodes. Conveniently, the microchannels' small cross-section creates an electrophysiological environment with increased resistance that greatly amplifies (by 1-2 orders of magnitude) the axonal signals (Dworak & Wheeler, 2009; FitzGerald et al., 2008; L. Wang et al., 2012). It has been speculated that the resulting recorded amplitudes of axonal APs (up to units of mV) may be large enough to modulate adjacent axons activity via ephaptic coupling (Narula et al., 2017; Pan et al., 2014), though no study has observed this phenomenon conclusively (Lewandowska et al., 2015). Moreover, the axon-specific compartmentalization allows for selective treatments (e.g., chemical blockers) and/or manipulations (e.g., axotomy), while directly probing the axonal responses (Gribi et al., 2018; R Habibey et al., 2015; Moutaux et al., 2018; Shimba et al., 2021). Probably due to the distinctive advantage of allowing for non-invasive (hence multiple and long-term) recordings with very high temporal resolution (up to 20  $\mu\text{s}$  at 50 kHz), until now, the most relevant insights obtained from this combination have been related to conduction velocity.

These platforms have helped characterize the increase in conduction velocity after pharmacologically-induced axon enlargement (Costa et al., 2020), the increase along network maturation (Rouhollah Habibey et al., 2017; Hong et al., 2017), or the decrease upon  $\text{Na}_v1.2$  blockade (Shimba et al., 2021). Still, most studies have not moved beyond the proof-of-concept stage. Thus, new insights into axonal function remain to be obtained from this promising combination of micro technologies.

A different type of MEA technology has also gained momentum in the study of axons (reviewed in (Emmenegger et al., 2019)). Complementary metal oxide semiconductor (CMOS)-based, planar MEAs with higher spatial resolution than conventional MEAs have been used to probe axonal arbors at single-cell resolution in low-density (Bakkum et al., 2013, 2018; Radivojevic et al., 2017; Yuan et al., 2020) (**Fig. 6E**) and high-density (Abbott et al., 2020) random cultures. These high-density MEAs (HD-MEAs) can pack up  $\approx 5000$  electrodes/ $\text{mm}^2$  (up to 60.000 total) that can be read-out simultaneously with high-noise levels, or in subsets with low-noise (Yuan et al., 2020). Until recently, due to the high-noise amplifiers and low axonal SNR constraints, mapping axonal arbors was only possible following electrical stimulation of the axon and noise averaging of several stimulation trials (“stimulus-triggered averaging”) (Bakkum et al., 2013). New generation HD-MEAs, with improved SNR, now enable the mapping of axonal arbors based on their spontaneous activity (“spike-triggered averaging”) (Abbott et al., 2020; Yuan et al., 2020). This technology has allowed for the discovery that mammalian cortical axons conduct with high temporal precision (low jitter) and reliability (no conduction or branch-point failures) (Radivojevic et al., 2017), or that the AIS is the main contributor to the extracellular potential (Bakkum et al., 2018). A key disadvantage of HD-MEAs is their substrate opacity, which difficults simultaneous probing with optical methods. Still, the relatively high spatial resolution ( $\approx 10\text{-}20\ \mu\text{m}$ ) of HD-MEAs allows for a pure electrical mapping (“electrical imaging”) of the axon morphology (Abbott et al., 2020; Yuan et al., 2020; Zeck et al., 2017). Moreover, their temporal resolution is, typically, lower than conventional MEA setups ( $\approx 2\text{-}5$  times less in low-high noise modes) (Yuan et al., 2020), thus prone to less precise measures of conduction velocity. These exciting new technological developments should accelerate the study of the conduction properties of single-cell axonal arbors.

Finally, in recent years, many research groups have made efforts to improve the SNR of MEA recordings by fabricating 3D electrodes at the micro or nanoscale (reviewed in (Abbott et al., 2018; Acarón Ledesma et al., 2019; Y. H. Cho et al., 2021; Spira & Hai, 2013; D. Xu et al., 2021)). In general, 3D-structured electrodes increase the effective surface area between the

electrode and the electrogenic compartment, which leads to an increase in the seal resistance at the electrode-membrane interface (**Fig. 7C**). The field was fueled by the discovery that large invertebrate *Aplysia* neurons spontaneously engulfed mushroom-like microelectrodes (Hai et al., 2010), which enabled the intracellular-like recording of APs and synaptic potentials (reviewed in (Spira et al., 2018; Teixeira et al., 2020)). Since then, intracellular-like recordings (units of mV) from the somata of mammalian neurons after spontaneous partial membrane engulfment (Shmoel et al., 2016), or after poration (Abbott et al., 2019; Dipalo et al., 2017; R. Liu et al., 2017; Robinson et al., 2012) have been achieved. However, due to their relatively small size, intracellular-like recordings from axons are yet to be demonstrated. Even the smallest reported nanoelectrodes are in the same size order of mammalian axons (Y. H. Cho et al., 2021) (**Fig. 7F**), thus it is unlikely that this approach may allow for stable poration and probing of axonal structures. Still, even though the effects of topography on axon guidance are well characterized (as previously detailed), surprisingly, the effect of 3D-electrodes on network organization and axonal recordings has been largely neglected. A few studies have demonstrated the potential of incorporating discontinuous 3D features (e.g., nanopillars or micro-mushrooms arrays) on axonal guidance (Amin et al., 2018; Santoro et al., 2014), but ultimately, these were not integrated into MEAs.

Interestingly, CMOS-based MEAs that integrate 4096 3D-nanostructured electrodes have shown short-term intracellular-like recording capabilities from thousands of somata simultaneously (in “pseudocurrent-clamp” mode), allowing for a partial connectome mapping (Abbott et al., 2019, 2020). In the future, the combination of higher spatial resolution HD-MEAs with 3D-electrodes should allow for the extracellular probing of full axonal arbors, while recording somata intracellularly, hence gaining access to the subthreshold fluctuations (e.g., synaptic potentials) that precede and follow axonal conduction.

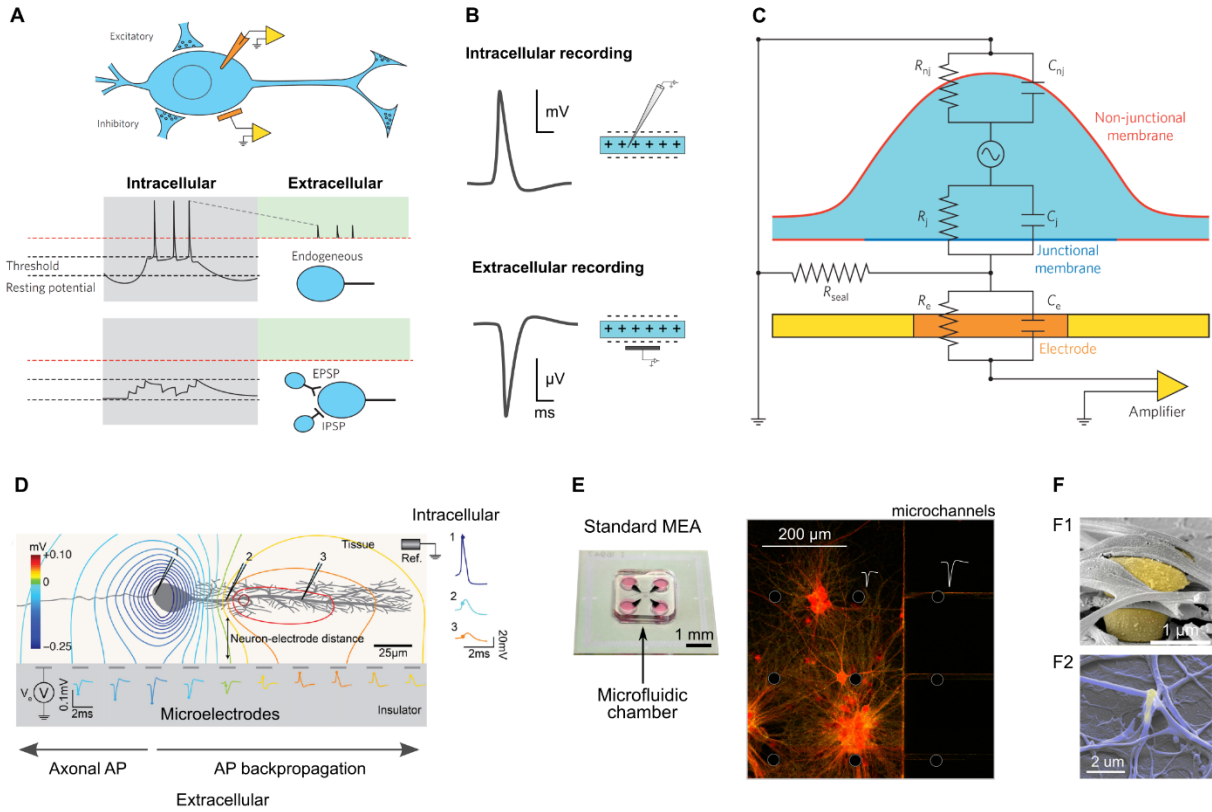


**Figure 7 – The extracellular recording concept.** **(A)** Subthreshold and suprathreshold activity as detected by an intracellular (grey box) and extracellular (green box) electrode. Note that the extracellular electrode cannot detect subthreshold activity (adapted from (Spira & Hai, 2013)). **(B)** Representation of an action potential (AP) shape and amplitude as recorded intra- and extracellularly. **(C)** Schematic of the passive electrical circuit equivalent for the neuronal membrane/electrode interface (in the case of a standard planar electrode).  $R_{nj}$  and  $C_{nj}$  represent the non-junctional resistance and capacitance, respectively, of the non-junctional part of the membrane (red).  $R_j$  and  $C_j$  represent the junctional resistance and conductance, respectively, of the junctional part of the membrane (blue).  $R_e$  and  $C_e$  represent the electrode resistance and capacitance, which together represent the electrode impedance. In-between the junctional membrane and the electrode,  $R_{seal}$  represents the seal resistance to ground of the junctional cleft (adapted from (Spira & Hai, 2013)). **(D)** Schematic of the neuron/electrode interface and typical signals recorded extracellularly (in high-density recordings) and intracellularly in different subcompartments (adapted from (Obien et al., 2015)). **(E)** Photograph of a microelectrode array (MEA) and microfluidic chamber combination plus a confocal microscopy image of hippocampal neurons (expressing mRuby3 and preSynTagMA) in the MEA/microfluidic platform. **(F)** Examples of interactions of neurites with 3D-structured

electrodes at the microscale (F1, adapted from (Ojovan et al., 2015)) and nanoscale (F2, adapted from (Dipalo et al., 2017)).

### ***Functional Imaging***

Optical imaging methods offer the advantage of probing axonal activity at the highest possible spatial resolution (essentially limited by the field of view/acquisition rate relationship), albeit at the cost of temporal resolution (reviewed in (W. Wang et al., 2019)). The main functional imaging methods are calcium imaging and voltage imaging.

APs reliably lead to calcium influx ( $\approx$ ten-fold rise in intracellular concentration which reverts within  $\approx$ 100 ms) (Koester & Sakmann, 2000), thus calcium imaging has long been used as an indirect proxy for neuronal activity (reviewed in (Grienberger & Konnerth, 2012)). Classical studies loaded neurons with calcium indicators (e.g., BAPTA-1 dye) to image the calcium dynamics at pre-synaptic terminals (Koester & Sakmann, 2000), however the rapid progress in viral vector tools (particularly adeno-associated viruses (AAVs)) (Haggerty et al., 2020) has established genetically encoded calcium indicators (GECIs) as the most prominent tool for imaging calcium in neurons (Gerard J. Broussard et al., 2014). Currently, GECIs are routinely used to assess neuronal activity at the network, cellular and subcellular scales with high SNR (Dana et al., 2019). For the detection of fast calcium transients, the sensors with faster responses are XCaMP-Gf (Inoue et al., 2019), jGCaMP7f (Dana et al., 2019), and the newest jGCaMP8 family (unpublished). The fastest sensor to date (jGCaMP8f) has reported on/off kinetics of around 100 ms, which has greatly reduced the mismatch between calcium sensor kinetics and actual calcium transients in the axon. Still, it is important to note that untargeted GECIs preferentially label the somatodendritic compartment and diffuse poorly along the axonal arbor, thus are biased towards the detection of somatic APs (Gerard Joey Broussard & Petreanu, 2021; Knöpfel & Song, 2019). To circumvent this limitation, several variants of GCaMP have been fused to pre-synaptic scaffolding proteins (e.g., synaptophysin) to enable pre-synaptic calcium imaging (Dreosti et al., 2009; Zhang et al., 2018). These probes are known collectively as syGCaMPs and have allowed for studies relating pre-synaptic calcium entry and vesicular release (Brockhaus et al., 2019; Jackson & Burrone, 2016) (**Fig. 6G**). For high SNR calcium imaging of axonal arbors, an axon-targeted GECI (axon-GCaMP6) has been developed by fusing GCaMP6 to the growth-associated protein 43 (GAP43) (Gerard Joey Broussard et al., 2018). State-of-the-art GECIs allow for the detection of single axonal APs without averaging, if imaged with sufficiently high spatiotemporal resolution (Gerard Joey

Broussard & Petreanu, 2021; Huang et al., 2021). Thus, the applications of calcium imaging range from monitoring the activity of multiple axons simultaneously to that of single pre-synaptic terminals (or boutons) (reviewed in (Gerard Joey Broussard & Petreanu, 2021)). Since  $\text{Ca}_v$  channels are particularly concentrated at pre-synaptic structures, these regions display higher SNR measurements than the axon shaft (**Fig. 6G**). Still, it is important to note that calcium activity in pre-synaptic terminals can be modulated by AP propagation (and firing frequency), but also by other pre-synaptic mechanisms (e.g., excitatory actions of neuromodulators). Recent advances in multicolor calcium imaging, in particular, allow for simultaneous imaging of pre- and post-synaptic activity from differentially labeled neurons (Inoue et al., 2019). Still, calcium sensors are (inherently) not sensible to hyperpolarizing activity, limiting the readout repertoire of this technique. Moreover, even in optimal imaging conditions (i.e., minimal field of view, high SNR, high acquisition rate), debate continues if calcium imaging can faithfully report the whole extent of suprathreshold activity (especially in high firing rate conditions) (Huang et al., 2021).

Voltage-sensitive dyes (VSDs) and genetically encoded voltage indicators (GEVIs) have the potential to overcome calcium imaging limitations since the changes in fluorescence are a direct proxy for changes in voltage (reviewed in (Peterka et al., 2011)). These indicators' responses to voltage change can be linear (e.g., opsin-based) or non-linear (e.g., ASAP-based), with linear indicators having generally faster on/off kinetics ( $\tau < 1$  ms), but less sensitivity (low %/mV). Consequently, linear and non-linear indicators are more suitable for the recording of AP (fast kinetics, but large voltage change) and subthreshold (slow kinetics, but small voltage change) activity, respectively. Early studies using VSDs revealed multiple AP initiation zones in invertebrate neurons (Zečević, 1996). Later studies with higher-sensitivity dyes (e.g., JPW3028) allowed for the determination of the AP trigger zone location (20-40  $\mu\text{m}$  from the soma) and length ( $\approx 20$   $\mu\text{m}$ ) in L5 pyramidal neurons, as well as the reliability of propagation along the axonal arbor, even at very high firing frequencies ( $\approx 400$  Hz) (Popovic et al., 2011). However, concerns regarding the VSDs effects on the physiological properties of the cellular membrane (Peterka et al., 2011), as well as their lack of neuronal-specificity, have stalled their use. GEVIs circumvent the need of intracellular-loading to achieve neuronal specificity, via targeted expression (e.g., synapsin I promoter), thus are currently the preferred tool for probing voltage changes in the axon. Still, due to their comparatively lower brightness, most studies need to average several stimulation trials to distinguish axonal APs (I. H. Cho et al., 2017, 2020; Hoppa et al., 2014; Ma et al., 2017) and subthreshold activity (Rowan & Christie, 2017)

from noise levels. As an application example, Cho et al. (2017) used QuasAr (opsin-based) to reveal a novel role for the Nav $\beta$ 2 subunits in the prevention of conduction failures at branching points (I. H. Cho et al., 2017) (**Fig. 6F**). Recently, new-generation GEVIs (e.g., opsin-based Archon1 and 2, FRET-opsin Ace-mNeon) have shown the necessary kinetics and brightness to resolve the axonal AP in single trials (reviewed in (Panzera & Hoppa, 2019)). Voltage imaging with Ace-mNeon at  $\approx 3$  kHz has been used to assess the direction and velocity of AP conduction, as well as to compare the AP waveform between different axonal segments (proximal vs distal) (Gonzalez Sabater et al., 2021). Due to the very high spatial resolution, voltage imaging is particularly useful for the study of voltage changes in structures difficult to probe with electrophysiological techniques, such as the axon shaft or the pre-synaptic terminals (I. H. Cho et al., 2020; Hoppa et al., 2014; Rowan et al., 2016). These studies have helped unveil the contribution of  $K_v$  channels to the pre-synaptic AP width and amplitude (I. H. Cho et al., 2020; Gonzalez Sabater et al., 2021; Hoppa et al., 2014). Still, the widespread adoption of GEVIs for the study of axon function has been undoubtedly limited by low SNR. It is particularly difficult to resolve the axonal AP due to the limited surface area (hence few emitted photons). Moreover, the rapid kinetics of APs force very high acquisition rates (hence few contributing photons), which require ever more sensitive (i.e., larger dynamic range), bright and photostable fluorophores.

One general limitation of functional imaging techniques is that the activity measured in each pixel may result from the superposition of multiple neurites, or other electrogenic compartments. In the future, the combination of brighter and more photostable fluorophores with super-resolution techniques may help circumvent this problem.

### ***Technique Combinations***

Virtually all of the previously described techniques can be combined to extract more information from a single experiment (**Fig. 6A**). The combination of electrophysiological and optical techniques, in particular, allows for the probing of axon subcompartments' morphological and functional traits with superior spatiotemporal resolution. All-electric (e.g., MEA and patch-clamp) and all-optical (e.g., voltage and calcium imaging) approaches can also be used complementarily, even though they are less common.

Probably the most used combination of techniques in the study of axonal activity is that of patch-clamp and functional imaging dyes. Typically, patch pipettes are first used for neuron

filling with the sensor of interest. Then, intracellular recording and stimulation of the soma are used as a “ground truth” for neuron activity, while spatiotemporal information (e.g., varicosities depolarization duration) is extracted from functional imaging. Rowan et al. (2016), using a whole-cell patch-clamp and VSD (di-2-AN-(F)EPTEA) combination, revealed the heterogeneity of the AP waveform at different varicosities, even within the same axonal branch (Rowan et al., 2016). Sasaki et al. (2012) used a calcium dye (BAPTA-1) to measure the dependence of AP-evoked calcium elevations, in varicosities, on the axonal length and number of crossed branch points (Sasaki et al., 2012a). Recently, Zbili et al. (2020) used the same principle - imaging calcium transients in varicosities in response to evoked APs - with another synthetic dye (Fluo-4). The amplitude of the calcium transients was increased when APs were evoked by a synchronous-like input (a depolarizing pulse directly from the resting membrane potential), which suggests that synaptic transmission may be facilitated when the pre-synaptic AP originates from synchronous inputs (Mickaël Zbili et al., 2020). MEA electrophysiology has the benefit of allowing for concurrent recording/stimulation and imaging of the axon non-invasively. Even though MEA electrophysiology and calcium imaging of the axon dynamics have been shown feasible (Moutaux et al., 2018), new insights from this combination remain to be obtained. The recent development of fully transparent MEAs, compatible with high-resolution microscopy (Middya et al., 2021; Susloparova et al., 2021), should expedite the adoption of this technique combination. Future studies may take advantage of the distinctive characteristics of MEAs and functional imaging for tracking AP depolarization with unprecedented spatiotemporal resolution in long-term experiments.

All-optical approaches have the potential to monitor and modulate axonal subcompartments at will with minimal invasiveness, but so far, their use has been limited. Remarkably, Cho et al. (2020) co-expressed (bicistronically) GCaMP6f and QuasAr to measure the pre-synaptic calcium transients and shaft depolarizations in single APs, within the same axonal arbor. Theoretically, non-linear and linear voltage indicators may be combined to assess sub- and suprathreshold activity (Panzera & Hoppe, 2019), although no study has so far reported such a combination. VSDs and calcium dyes can also be combined (K. E. Vogt et al., 2011), though these require intracellular loading for cell specificity. Finally, even though optogenetic tools are gaining huge momentum in the all-optical study of neuronal function (Hochbaum et al., 2014), attempts of subcellular targeting channelrhodopsins (ChRs) to the axon have been mostly unsuccessful (reviewed in (Rost et al., 2017)). For example, targeting ChR2 to the AIS, via an ankyring G-binding domain, disrupts the local endogenous  $Na_v$  clusters (Grubb & Burrone,

2010). Still, the advent of new engineered ChRs that target the pre-synaptic terminals (S. Hamada et al., 2021) may enable new strategies where electrode-free setups can stimulate/inhibit (via optogenetics) and measure activity (via functional imaging) of targeted regions of the axon.

All-electric combinations may allow for the precise control of membrane potential (via whole-cell patch-clamp) and mapping of axonal arbor conduction (via HD-MEAs) concurrently. However, HD-MEAs are considerably harder to combine with other techniques due to their substrate opacity, which precludes experimental setups comprising inverted microscopes, and difficult optical microscopy with upright microscopes. Still, HD-MEA recordings have been combined with somatic whole-cell patch-clamp recordings (Jäckel et al., 2017). In the study, somata could be patched by imaging the cultures with an upright microscope equipped with difference interference contrast (DIC). By taking advantage of the concurrent recording capabilities, this all-electric approach allowed for the mapping of the PSPs triggered by the patched neuron. Standard MEAs (transparent substrate) have also been combined with whole-cell patch-clamp in a study that showed that the somatic AP waveform may vary depending on the dendritic tree input (Sardi et al., 2017). As this combination allows for the highest temporal resolution in axonal recordings, while spatial clamping, it can be used to study propagation jitter, and how it influences efficient information transmission. It is important to note that the introduction of propagation jitter may impact the coincidence detection of multiple PSPs in the post-synaptic neuron, impacting synaptic transmission strength.



**Table 1** – Comparison of key characteristics, advantages and limitations of different techniques for the study of axon activity.

|                            | <b>Subcellular Patch-clamp</b>   |  | <b>MEA</b>  |  | <b>Functional Imaging</b>  |   |
|----------------------------|--|--|---|--|--|---|
|                            | <b>Axon-attached</b>   | <b>Whole-cell</b>  | <b>+ Microfluidics</b>  | <b>HD-MEA</b>  | <b>GECI</b>  | <b>GEVI</b>   |
| <b>Signal</b>              | Extracellular ( $\mu\text{V}$ )  | Intracellular (mV/pA)  | Extracellular ( $\mu\text{V}$ -mV)  | Extracellular ( $\mu\text{V}$ )                                    | Fluorescence ( $\Delta\text{F}/\text{F}$ )                                       | Fluorescence ( $\Delta\text{F}/\text{F}$ )                                  |
| <b>Stimulation</b>         | Yes  | Yes  | Yes   | Yes  | No   | No  |
| <b>SNR</b>                 | ++   | +++  | ++  | ++   | +  | +   |
| <b>Spatial information</b> | +  | +  | ++  | +++  | +++  | +++   |
| <b>Temporal resolution</b> | +++  | +++  | +++   | ++   | +  | +   |
| <b>Throughput</b>          | +  | +  | ++  | +++  | ++   | ++  |
| <b>Recordings duration</b> | +  | +  | +++   | +++  | +  | +   |
| <b>Key Advantages</b>      | - Minimally invasive<br>- Spatial precision                              | - High-fidelity<br>- Subthreshold detection                                | - Non-invasive<br>- Optical compatible<br>- Axon compartmentalization                 | - Non-invasive<br>- Single-cell axon arbors                        | - Minimally invasive<br>- Cell-type targeted labelling<br>- Spatial resolution   | - Cell-type targeted labelling<br>- Spatial resolution<br>- Direct proxy    |
| <b>Key Limitations</b>     | - Single-site extracellular-like recordings only<br>- Difficult          | - Invasive<br>- Large axonal structures only<br>- Difficult                | - APs only<br>- Imposed axonal geometry<br>- Fixed electrodes                         | - APs only<br>- Opaque substrate<br>- Fixed electrodes             | - Temporal resolution<br>- Indirect proxy  | - Low SNR<br>- Photobleaching<br>- Phototoxicity                            |
| <b>References</b>          | (Dugladze et al., 2012; Rowan et al., 2016; Sasaki et al., 2012a, 2012b) | (Kawaguchi & Sakaba, 2015; Ritzau-Jost et al., 2021; Vandaal et al., 2021) | (Costa et al., 2020; Habibey et al., 2017; Moutaux et al., 2018; Shimba et al., 2021) | (Abbott et al., 2020; Radivojevic et al., 2017; Yuan et al., 2020) | (Brockhaus et al., 2019; Gerard Joey Broussard et al., 2018; Zhang et al., 2018) | (I. H. Cho et al., 2020; Gonzalez Sabater et al., 2021; Hoppe et al., 2014) |

**Abbreviations by order of appearance** – MEA: Microelectrode array; HD-MEA: high-density microelectrode array; GECI: genetically-encoded calcium indicator; GEVI – genetically-encoded voltage indicator; SNR: signal-to-noise ratio; AP: action potential



## **Chapter II**

### **Paper I**

*Improved in vitro electrophysiology using 3D-structured microelectrode arrays with a micro-mushrooms islets architecture capable of promoting topotaxis.*



**Improved in vitro electrophysiology using 3D-structured microelectrode arrays with a micro-mushrooms islets architecture capable of promoting topotaxis**

*The content of this chapter is published in the following original research paper:*

**Mateus JC**, Lopes CD, Cerquido M, Leitão L, Leitão DC, Cardoso S, Ventura J, Aguiar P. *Improved in vitro electrophysiology using 3D-structured microelectrode arrays with a micro-mushrooms islets architecture capable of promoting topotaxis. Journal of Neural Engineering* (16), 036012, doi:10.1088/1741-2552/ab0b86 (2019).

*This is an original research paper and it is presented for the first time in a thesis.*

*Full paper and Copyright License in Annex.*



## 2.1 Abstract

Planar microelectrode arrays are widely used in neuroscience but have relatively low electrical coupling and signal-to-noise ratio (SNR) in electrophysiology recordings. Strong efforts are therefore being made in improving microelectrode arrays (MEAs) performance, exploring both the microelectrode's shape and the array's architecture. Topographical features can be used in MEAs for promoting neuron-microelectrode contact, making 3D-microstructured MEAs an interesting design strategy for better electrophysiology measurements. Here, we present a novel MEA architecture, where planar microelectrodes are replaced by localized 3×3 arrays of mushroom-shaped microstructures. Contrarily to previous studies, the purpose for the micro-mushrooms in this islets configuration is not membrane engulfment but rather entrapment, for somata, and embracement, for neurites. We show that these islet-like agglomerates of micro-mushrooms act as strong physical cues, causing topotaxis and increasing the probability by two-fold for somata to localize in the islets, and neurites to curl on the microelectrodes. Importantly, we carry this topotaxis study not only with rat cortical neurons but also with human-derived SH-SY5Y cells. With recent evidence that extracellular signals have a significant contribution from axons initial segment it becomes clear that MEA designs should also address the electrode-neurites coupling. We detail the fabrication process of these chips, designed to be compatible with a standard MEA recording system, and make the computer-aided design (CAD) publically available. We also demonstrate the electrophysiological capabilities of this new MEA by electrochemical impedance spectroscopy and recordings of cortical and hippocampal neurons, showing excellent SNR. Overall, this new MEA islets configuration has a significant impact in the array efficiency and contributes towards improved high yield and high fidelity/quality extracellular recordings from mammalian neurons.

**Keywords:** topotaxis and neuronal guidance, neuron-electrode interface and neurite-electrode interface, human-derived SH-SY5Y cells, mushroom-shaped microelectrodes, microelectrode array

## **2.2 Significance Statement**

A novel MEA architecture with excellent electrophysiological recordings is presented, where planar microelectrodes are replaced by localized  $3\times 3$  arrays of mushroom-shaped microstructures. The micro-mushrooms in this islets configuration are not for membrane engulfment but rather for somata entrapment and neurites embracement. As extracellular signals have a significant contribution from axons initial segment, this MEA design also addresses the electrode-neurites electrical coupling. These islets act as strong physical cues, causing topotaxis and increasing by 2-fold the probability for somata to localize in the islets. We carry this topotaxis study not only with rat cortical neurons but also with human-derived SH-SY5Y cells.

## 2.3 Introduction

Understanding neuronal dynamics in normal and pathological conditions requires precise electrophysiological measurements and detailed information about neuronal activity, as this is the proxy for neuronal function. Electrophysiology “on-a-chip” in the form of microelectrode arrays (MEAs) allows for simultaneous, multi-site, noninvasive, long-term extracellular stimulation and recording of neuronal networks (Nam & Wheeler, 2011; Obien et al., 2015). Over the last decades, in vitro MEA recordings have helped describe fundamental properties of network activity patterns (Wagenaar et al., 2005), plasticity (Massobrio et al., 2015) and have also shown promise from a clinical perspective in neurotoxicity research (Johnstone et al., 2010), pharmacological testing (Accardi et al., 2016) or disease modelling (Chong et al., 2011). Still, conventional MEA technology is impaired by relatively low signal-to-noise ratio (SNR) and yield of active/populated microelectrodes, which limits its potential applications (Seymour et al., 2017). Although the noise level of commercial MEAs is in the range of a few tens of  $\mu V$ , source signals are greatly attenuated (2-3 orders of magnitude) due to a very low neuron-microelectrode electrical coupling coefficient. Weak membrane potential fluctuations (e.g. subthreshold activity, slow frequency modulations, synaptic signals) are therefore not detected with planar MEAs (Spira et al., 2018; Spira & Hai, 2013).

Recently, some groups have focused on improving the quality of the recorded signal by modifying the microelectrode’s topography. Of particular importance are the promising *ad hoc* tri-dimensional (3D)-structured microelectrodes that merge some of the advantages of both intracellular and extracellular recordings (Spira & Hai, 2013). These include MEA structured with vertical micro- or nanoprotusions, e.g. nanopillars (Xie et al., 2012), nanotubes (Duan et al., 2012), nanowires (R. Liu et al., 2017; Robinson et al., 2012), nanostraws (VanDersarl et al., 2012) and nanocylinders (Dipalo et al., 2017) (for reviews see (Abbott et al., 2018; Angle et al., 2015; Spira & Hai, 2013)). In general, nanoprotusions function as cell-penetrating nanoprobe that either need spontaneous poration (Duan et al., 2012; Tian et al., 2010), electroporation (Robinson et al., 2012; Xie et al., 2012) or plasmonic optoporation (Dipalo et al., 2017) to measure intracellular-like activity. The interface established between the cell and the microelectrode 3D structure has been a topic of great interest in recent reviews (Kwak et al., 2015; McGuire et al., 2018). Despite the promising nanotechnologies proof-of-concept results (Abbott et al., 2018), until now only a few studies have shown their capability to perform

intracellular-like recordings from single mammalian neurons, following electroporation (Robinson et al., 2012) or plasmonic optoporation (Dipalo et al., 2017).

The design of the 3D-structured microelectrodes has often taken inspiration from naturally occurring morphological structures dedicated to cell coupling, such as the synaptic cleft (Wijdenes et al., 2016) or the shape (mushroom-like) and dimension of dendritic spines (Hai et al., 2010; Panaitov et al., 2011). In particular, work pioneered by Spira and collaborators have enabled intracellular-like recordings using mushroom-shaped extracellular microelectrodes (gM $\mu$ Es), due to the formation of a neuron-gM $\mu$ E high seal resistance ( $R_{\text{seal}}$ ) and an increase in the junctional membrane conductance (Spira & Hai, 2013). First reported to record subthreshold synaptic signals in large invertebrate (*Aplysia californica*) neurons (Hai et al., 2010), these gM $\mu$ Es have more recently been used in “loose-patch-like” configurations with rat hippocampal neurons failing to unequivocally record synaptic potentials (Shmoel et al., 2016). While large *Aplysia californica* neurons (80  $\mu$ m diameter) tightly engulf gM $\mu$ Es through the formation of actin rings around the gM $\mu$ E stem (Hai et al., 2009), larger than 2-2.5  $\mu$ m mushroom-shaped caps preclude engulfment by the relatively small mammalian neurons (10-20  $\mu$ m diameter). However, producing smaller caps limits the junctional membrane conductance and significantly increases the impedance and noise level (Ojovan et al., 2015). Other laboratories' attempts to mimic the mushroom-shaped protusion at the nanoscale (~500 nm) (Sileo et al., 2013) have not yet succeeded in exhibiting the intracellular-like recordings, characterized by positive peaks in the mV range. Therefore, the translation of extracellular electrodes' stable, multi-site and long-term intracellular-like recording capabilities to mammalian neurons remains challenging (Spira et al., 2018).

Low yield of active/populated microelectrodes is also a common problem in MEA experiments. Typically, conventional MEA cultures with standard cell densities register activity in less than half of the available microelectrodes (Gertz et al., 2017). As high  $R_{\text{seal}}$  is crucial for appropriate signal detection, somata and/or large neurites need to be in close vicinity with the sensing microelectrodes. Research groups tend to use high-densities (> 1000 cells/mm<sup>2</sup>) in cell plating to increase the probability of effective electrodes (Nam & Wheeler, 2011; Shmoel et al., 2016), though such solution may bias the viability of the mature neuronal population. Besides, neuron-microelectrode proximity may change over time due to neuronal migration and/or death, which may impair long-term studies. An alternative approach consists in constraining neurons' localization to the electrodes recording sites through parylene small cages (Erickson et al., 2008), nanopillars (Xie et al., 2010), 3D-wells made of carbon nanotubes (Cools et al., 2017),

or micro-/nano-patterning techniques (Aebersold et al., 2016; Samhaber et al., 2016). Biochemical substrate functionalization has also been used to constrain localization, and used in both planar (James et al., 2004; Ryu et al., 2016; Samhaber et al., 2016; Suzuki et al., 2013) and 3D-structured microelectrodes (Santoro et al., 2014). None of these solutions are ideal though, as some lead to MEAs that i) have very limited reusability, ii) are costly, and iii) require advanced microfabrication techniques. Biochemical substrate functionalization typically only works during the neuronal culture's initial stage, losing the ability to constrain neuron localization after some days in vitro (as neurons cover the remaining surface with ECM proteins).

The fact that topographical features can be used to manipulate neuron placement, growth and connectivity is supported by a growing body of knowledge demonstrating that neurons are affected by physical cues (Aebersold et al., 2016; Hoffman-Kim et al., 2010; Marcus et al., 2017; Simitzi et al., 2017). Despite the interesting early findings that a single *Aplysia californica* neuron growth pattern is markedly altered in a highly dense (inter-interval  $< 8 \mu\text{m}$ ) multi-gM $\mu$ Es substrate, without loss of functionality (Hai et al., 2009), no further studies have attempted to quantitatively assess how the topography of 3D-microstructured MEAs affects the localization of somata, the placement of neurites and the spatial organization of mammalian neuronal networks.

Here, we present our recent work involving the design, fabrication and performance assessment of a new MEA architecture alternative to the conventional planar MEAs. In our design, individual planar microelectrodes are replaced by islets of (3×3) mushroom-shaped 3D microelectrodes (micro-mushrooms), in a configuration that can be seen as arrays of microelectrode arrays. These chips are made compatible with standard MEA commercial amplifier systems and can be adapted depending on the fabrication design and experimental needs. We describe the microfabrication procedure involved and assess the biocompatibility of the chip with mammalian neurons. We also demonstrate the topography effect on the spatial organization of individual primary embryonic rat cortical neurons and human-derived SH-SY5Y cells. The 3D microstructures influence the growth pattern, neurite guidance and somata localization in a way that enhances the coupling between cell structures and microelectrodes, with relevant improvements in the yield and quality of electrophysiological recordings. The electrophysiological properties of this chip configuration are analyzed here in terms of background noise, signal-to-noise ratio (SNR) and amplitude of the recorded signals.

## 2.4 Results and Discussion

### 2.4.1 Microfabrication of 3D-microstructured MEAs

Two different configurations of 3D-microstructured arrays were developed and used in the experiments. The key new configuration consists of a MEA where each microelectrode is composed of an islet of  $3 \times 3$  micro-mushrooms. These islets are in turn arranged in an array of roughly  $8 \times 8$  units (including ground electrodes). The optimization of the fabrication procedure which permitted fabricating well-ordered hemispherical mushroom caps has been recently reported by our teams (Cerquido et al., 2018). A second, simpler, configuration was also fabricated and used in supporting experiments. In this configuration, the chip consists of a continuous large array of micro-mushrooms ( $2 \text{ mm} \times 2 \text{ mm}$ ) in a gold substrate area (**Fig. S1, Supporting Information**). These simpler chips have been recently shown by our teams to be able to record the synchronized and cooperative dynamics of astrocyte populations (Mestre et al., 2017). The inter-distance between adjacent micro-mushrooms in both configurations was kept at  $10 \mu\text{m}$ . The choice for a  $3 \times 3$  layout in the islets configuration was made to satisfy the following constraints: a) spacing between the microelectrodes similar to mammalian neurons' cell body diameter ( $\sim 10 \mu\text{m}$ ); b) base area of the islet in the same scale as conventional planar microelectrodes; and c) potentiate that each islet would hold, on average, a single neuron.

The new developed 3D-microstructured MEA with the micro-mushroom islets was designed to be compatible with commercial MEA systems (Multi Channel Systems, Reutlingen, Germany), with contact pads in the same position as those of commercial 60-MEAS. **Figure S2** in the Supporting Information shows the different levels of the computer aided design (CAD) diagram used for the fabrication of the MEA.

The microfabrication of the 3D-microstructured MEAs was analyzed through SEM, and **Fig. 1** shows SEM images at two different magnifications. **Figure 1A** shows four different 3D-microstructured microelectrodes islets with the  $3 \times 3$  array of micro-mushrooms present in the final portion of each lead (**Fig. 1B**). SEM analysis revealed that the grown micro-mushrooms have an inter-distance of  $10 \mu\text{m}$ , a cap diameter of  $3.1 \mu\text{m}$ , a base of  $1.9 \mu\text{m}$  and a stalk height of  $1.4 \mu\text{m}$ , with an intrinsic variability on the dimensions below  $0.2 \mu\text{m}$ . **Figure 1C** shows a schematic drawing of a representative 3D-microstructured microelectrode.

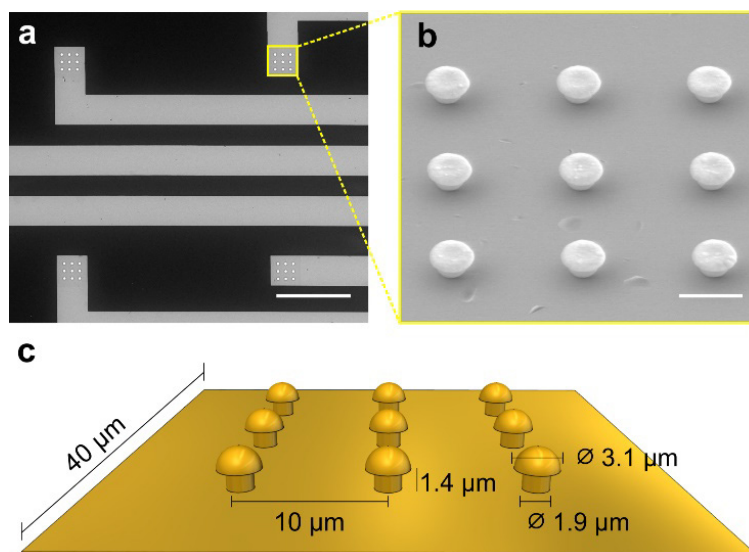


**Figure 1 – Scanning electron microscopy (SEM) images of 3D-microstructured microelectrodes. (A)** Top view of the reading tracks and the islets where the micro-mushrooms are deposited (scale bar = 100 μm). **(B)** Tilted image of a fabricated 3 × 3 islet of micro-mushrooms (scale bar = 5 μm). **(C)** Schematic diagram of one 3D-microstructured microelectrode with associated measurements.

#### 2.4.2 MEAs Electrochemical Characterization: Impedance and Noise Level

Measurements of the planar and 3D-structured microelectrode's capacitance, impedance and electrical noise levels were performed to assess the advantages of using a microstructured surface in comparison to a flat microelectrode (**Fig. 2**). The planar version used for comparison had the same specifications as the 3D-structured version except for the presence of the micro-mushrooms. **Figure 2A** shows the frequency dependence of the capacitance and loss components for planar and 3D-microstructured microelectrodes. The 3D-microstructured surface increases the capacitance of the electrode/electrolyte interface. Microelectrode impedance is an important characteristic for in vitro recordings, as low impedance values decrease the thermal noise and increase the SNR of the recorded signals. Standard commercial MEAs with 30 μm of diameter have impedance values in the order of hundreds of kΩ. **Figure 2B** shows the total impedance spectrum measured in the frequency range from  $10^2$  to  $2 \times 10^5$  Hz for planar and 3D-microstructured microelectrodes. As expected, the impedance magnitude decreased with frequency and with the microelectrode surface area. The 3D-microstructured microelectrodes offer therefore lower impedances.

We also analyzed the power spectral density of the voltage noise (Sv), as a function of frequency for the 3D-microstructured microelectrodes. As expected, the magnitude of the noise decreases with the increase of the frequency. For frequencies above 1 kHz, the noise follows a  $1/f$ . This frequency dependence confirms that the thermal noise of the resistive elements dominates the electrical noise of the system. The voltage noise is 0.15  $\mu\text{V}$  and determines the detection limit of the measuring system for signals in the frequency range of 1 kHz.

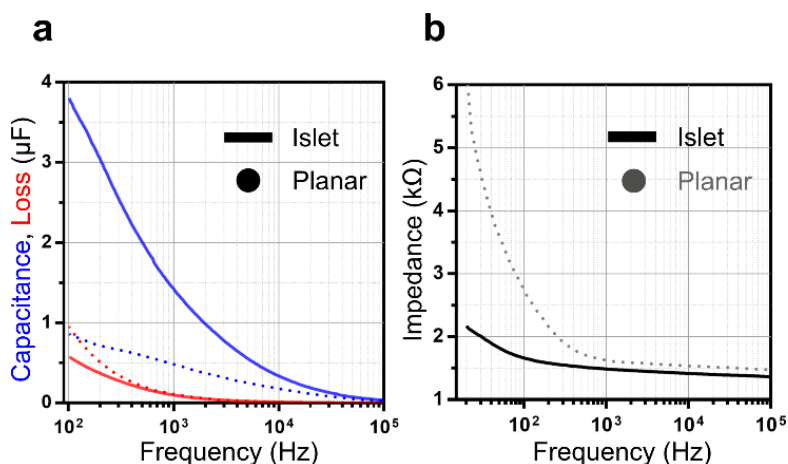


**Figure 2 – Electrical properties of the fabricated microelectrodes. (A)** Capacitance and loss as a function of frequency for planar and for 3D-microstructured microelectrodes (islets), showing that the capacitance of the micro-mushrooms islets is higher in comparison to the planar microelectrodes. **(B)** Total impedance ( $|Z|$ ) as a function of frequency, showing that planar microelectrodes are more resistive than the 3D-microstructured microelectrodes.

### 2.4.3 Cell Viability

Biocompatibility was expected as the chip is composed by materials that have been previously reported as safe in the literature (Brüggemann et al., 2011). The viability of rat cortical neurons cultured on 3D-microstructured arrays was assessed at 3 and 13 DIV (days in vitro). The fluorescence microscopy images of live/dead stained cells revealed vital neurons with multiple neurites distributed over the flat and 3D-microstructured areas of the 3D-microstructured arrays (**Fig. 3A**). At 3 DIV the percentage of live cells in the 3D-microstructured area was of  $32.3 \pm 6.1$  SD, which is in the range of what has been previously reported in the literature (Panaitov et al., 2011). The differences between the flat and 3D-microstructured areas were not significant, suggesting that the micro-mushrooms do not affect cell viability (**Fig. 3B**). The

cultures remained viable at 13 DIV, but the extensive network formation did not allow for precise cell counting of the live cells.

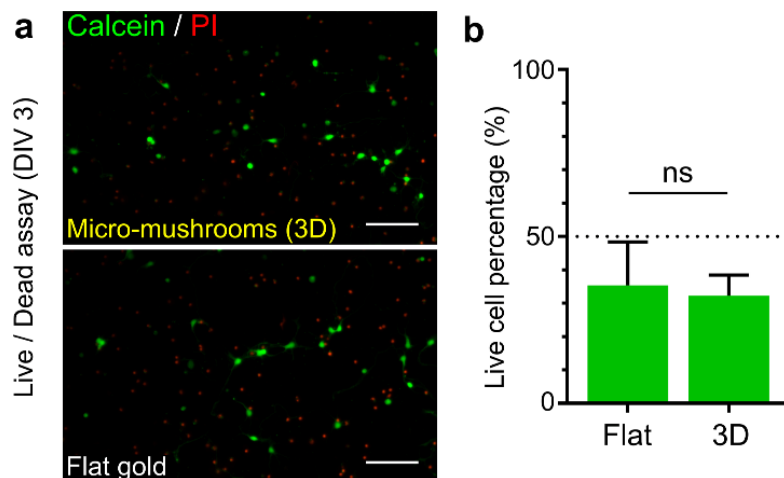


**Figure 3 – Rat cortical neurons live/dead assay at 3 days in vitro (DIV).** (A) The number of live and dead cells was determined by a live/dead assay using the calcein-AM (live) and propidium iodide (dead) double staining (scale bars = 100  $\mu$ m). (B) Bar graph showing the percentage of live cells. Results are expressed as mean percentage  $\pm$  SD ( $n = 15$ ). No significant differences (ns) were observed between the flat and 3D areas of the 3D-microstructured array. Mann-Whitney U test;  $p = 0.65$ .

#### 2.4.4 Influence on Growth Pattern

The ability to guide neurite extension in the desired directions is an objective constantly sought in neuronal networks engineering. Although neurite directionality is mostly achieved by anisotropic substrate topography (e.g. grooves, ridges) (Marcus et al., 2017), interspaced vertical structures have previously been shown to be able to guide neurite extensions (Hanson et al., 2009; Micholt et al., 2013).

Our initial cell culturing experiments suggested that the discontinuous topographical feature of the 3D-microstructured arrays could, *per se*, influence neuronal growth pattern. To evaluate the influence of 3D-microstructured arrays in neurite guidance and growth pattern, primary rat cortical neurons as well as SH-SY5Y cells, a human neuroblastoma cell line that acquires many of the morphologic characteristics of primary neuronal cultures upon a sequential treatment with ATRA and BDNF (Encinas et al., 2000), were cultured on top of the 3D-microstructured arrays.

Neurite orientation was isotropic on the flat gold substrate regions (without micro-mushrooms; data not shown), whereas in the continuous large arrays of micro-mushrooms neurites tended to align preferentially at  $0^\circ$ ,  $45^\circ$ , and  $90^\circ$  (**Fig. 4A-C**). These are the angles established by near-neighbor/adjacent micro-mushrooms, which indicates a preference for neurite elongation along the array topography. This effect was particularly robust in the SH-SY5Y cells; to the best of our knowledge, this is the first report of orientation preference of human-derived cells in mushroom-shaped microelectrodes. Interestingly, in the SH-SY5Y culture, a peak around  $63^\circ$  is also noticeable in the orientation distributions (**Fig. 4C**), which could be due to a second order of proximity between micro-mushrooms, since  $\tan(2) \approx 63^\circ$ . The obtained orientation distribution for both cortical neurons and SH-SY5Y cells could not be described by a uniform distribution (two-sample Kolmogorov-Smirnov test;  $p = 0.001$ ), thus we can state that the observed preferences are not random.

It was observed that frequently neurites visibly altered their path to contact with the micro-mushrooms and extended along sequential microstructures. Furthermore, neurite wrapping around the micro-mushrooms was also often observed (**Fig. 4D**). Interestingly, this occurred both in neurites extending from the soma and in secondary branches. An increase in the network complexity was also observed at the transition from flat substrate (without micro-mushrooms) to the 3D-microstructured array, but a detailed quantification was not performed. Multiple studies have now demonstrated that topographical features which guide neurites in multiple directions, also enhance the rate and degree of neurite branching development and network interconnection (Gautam et al., 2017; Seo et al., 2018). Thus, beyond influencing neurite directionality, topographical features could have an outgrowth-promoting effect. However, further studies are needed to explore this situation in 3D MEA chip settings.

It is important to emphasize that all these changes in growth pattern were observed in both rat cortical neurons and human-derived SH-SY5Y cells, despite their morphological differences and maturation status. Together, these results indicate that whereas the growth pattern on flat gold substrate is random, it considerably changes into a micro-mushrooms-seeking pattern in the 3D-microstructured area.

This anisotropic behavior of mammalian neurons has been shown before in other similar discontinuous isotropic topographies of PDMS protrusions (Hanson et al., 2009) and semiconductor nanowires (Gautam et al., 2017) but a pitch of  $\sim 0.5\text{-}3\ \mu\text{m}$  was indicated as critical for optimal alignment of neurite extension (Simitzi et al., 2017). Moreover, in Hai et al. experiments with larger *Aplysia californica* neurons, no change in growth pattern was observed

when using gMuEs arrays with spacing ranges above 8  $\mu\text{m}$  (Hai et al., 2009). In alignment with the results presented here, Panaitov et al. reported that neurites of rat cortical neurons tended to follow the micro-mushrooms (spacing ranges of 3-5  $\mu\text{m}$ ) and wrapped around the mushroom-like caps, albeit no quantifications were shown (Panaitov et al., 2011). More recently, the same group reported guiding rat cortical neurons in a grid-like pattern selectively functionalized with self-assembled monolayers (Santoro et al., 2014). However, this combination of chemical and physical cues impairs the analysis of to which extent the topography, *per se*, influenced the neuronal network organization, as 85% of the neurons grew on the predefined pattern. Interestingly, somata tended to agglomerate in the larger grid nodes (25  $\mu\text{m} \times 25 \mu\text{m}$ ), whereas neurites grew along the grid lines (10  $\mu\text{m}$  width). These nodes were of similar dimensions to the islets used in our 3D-MEA configuration, which influence somata localization even in the absence of a restricting biochemical pattern, as shown in the next section.

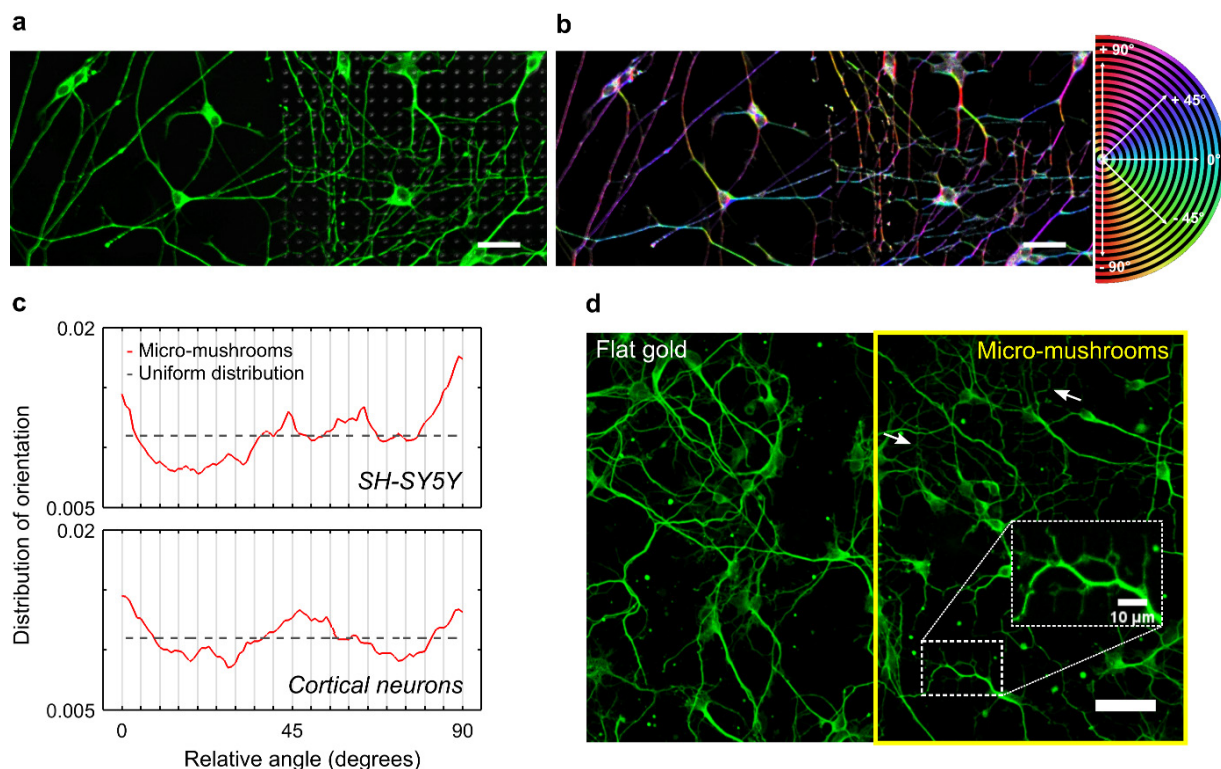


**Figure 4 – Influence of 3D-microstructured arrays in neurite guidance and growth pattern.** **(A)** Differentiated SH-SY5Y cells reveal different growth pattern on flat gold substrate and on the large contiguous array of micro-mushrooms at 8 DIV. Note the increased neurite branching complexity in the micro-mushrooms array region. **(B)** Color coded image of the neurite orientation. The color-orientation association is shown in the color-wheel (right side). In the micro-mushrooms array neurites tend to project in straight lines along the array main axis and diagonals, and are thus mainly colored in light blue (0°), purple/green (45°) and red (90°). It is relevant to note that neurites frequently appear as dashed lines as they extend immediately under the mushroom-like caps (scale bars = 30  $\mu$ m). **(C)** Orientation distribution shows that neurites of SH-SY5Y cells extend preferentially at angles around 0°, 45°, 63° and 90° (n = 59) and that neurites of rat cortical neurons extend preferentially at angles around 0°, 45°, and 90° in the 3D-microstructured area (n = 47). Dashed line is the reference uniform (isotropic) distribution. **(D)** Rat cortical neurons exhibit a different growth pattern on flat gold substrate and on the contiguous array of micro-mushrooms at 3 DIV (scale bar = 40  $\mu$ m). The white arrows indicate extensive secondary branching along the contiguous array of micro-mushrooms. Inset shows neurites wrapping around the micro-mushrooms. SH-SY5Y cells and neurons were immunolabelled for  $\beta$ III-tubulin (green).

### 2.4.5 Influence on Neuron Localization

One of the key motives behind the use of micro-mushrooms is the increase in area for cell-electrode contact. But beyond increasing the area per microelectrode, the islet configuration with localized agglomerates of micro-mushrooms influenced neuronal localization and increased the propensity for neuron-microelectrode co-localization and effective contact. To quantify the effect of the islets on neuronal localization, the density of neuronal cell bodies (somata) located in the 3D-microstructured area (islet) was calculated and compared with the planar substrate area (SiO<sub>2</sub>). To avoid repetition of the planar substrate area to be analyzed (due to microelectrodes proximity), each image was restricted to a region of interest (gray ROI in **Fig. 5A**) of  $200 \times 200 \mu\text{m}$  surrounding the  $30 \times 30 \mu\text{m}$  3D-microstructured area (yellow ROI in **Fig. 5A**). Somata located in the planar area of each microelectrode (red ROI of  $50 \times 50 \mu\text{m}$  in **Fig. 5A**) were excluded from the analysis to separate the effects of the micro-mushrooms from the effects of the surface material transition (SiO<sub>2</sub>-Au).

From the total number of microelectrodes analyzed ( $n = 22$ , from two independent experiments), the majority of the islets contained somata (18/22;  $\approx 82\%$ ), whereas neurites crossed and caught micro-mushrooms in the 3D-microstructured area (islet) in all of them (**Fig. 5B**). **Figure 5C** shows that the number of somata located in the area varied between 0 (minimum) and 5 (maximum), with one somata per islet being the most common occurrence (10/22 ;  $\approx 45\%$ ). The probability for somata to localize in the islets increased near 2-fold ( $1.9 \pm 1.5$  SD) when compared to the planar substrate ( $*p = 0.0195$ , two tailed unpaired  $t$ -test with Welch's correction) (**Fig. 5D**). It was found that neuronal density in the 3D-microstructured and planar areas was of  $2.0 \times 10^{-3}$  neurons/ $\mu\text{m}^2$  and  $1.1 \times 10^{-3}$  neurons/ $\mu\text{m}^2$ , respectively. Moreover, the presence of a microstructured substrate influenced neurite navigation, and every islet was covered with cellular components as early as 3 DIV.

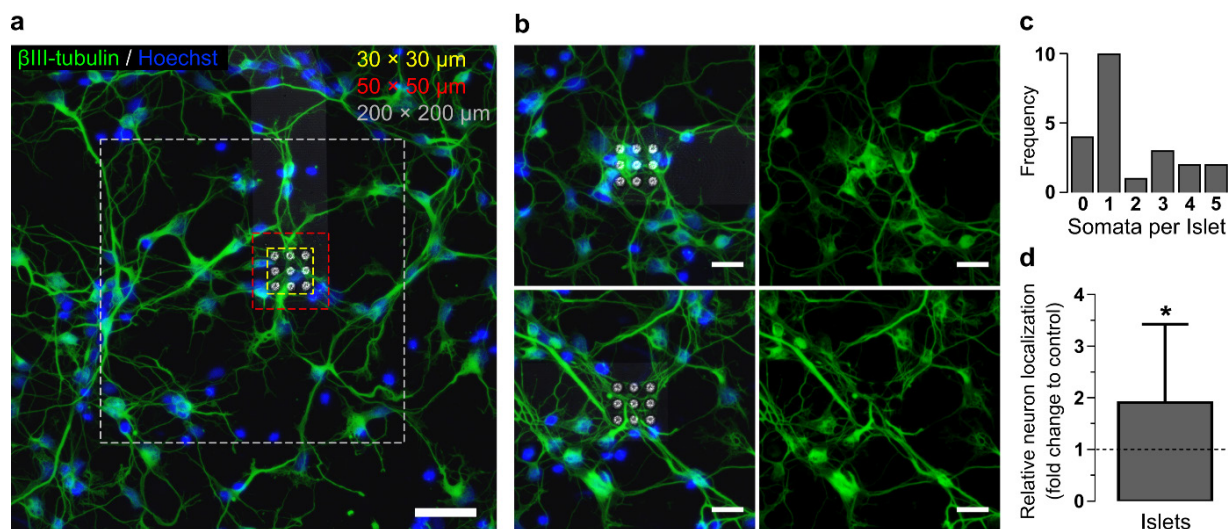


**Figure 5 – Islets of micro-mushrooms promote neuron-microelectrode co-localization and effective contact. (A)** Composite fluorescence image of rat cortical neurons, at 3 days in vitro, cultured on an islet of micro-mushrooms. The nuclei were stained with Hoechst (blue) and the cytoskeleton with  $\beta$ III-tubulin (green). This staining allowed for quantification of the number of neurons (somata) located inside (yellow ROI) and outside (between red and gray borders) the islets. Somata located in the peripheral planar area of each microelectrode (between red and yellow borders) were excluded from the analysis (scale bar = 40  $\mu$ m). **(B)** Composite fluorescence images (left side) showing islets of micro-mushrooms with the most frequent situation of having at least one somata (top), and one of the few situations without somata (bottom).  $\beta$ III-tubulin single-channel (right side) show neurites and somata spatial organization in planar and 3D-microstructured substrates. Note that neurites still cross and embrace the micro-mushrooms in the bottom example where no cells co-localize (scale bars = 20  $\mu$ m). **(C)** Frequency plot of the number of somata co-localized with the 3D-microstructured area (islet). **(D)** Bar graph shows the relative increase in somata co-localization with the 3D-microstructured area to the remaining planar SiO<sub>2</sub> substrate (control). Representative data of two independent experiments was normalized and expressed as mean  $\pm$ SD (n = 22). Results are shown as fold change to control (indicated by the dashed line). Two tailed unpaired t-test with Welch's correction; \*p < 0.05.

### 2.4.6 Electrophysiological Recordings

The novel islets 3D-microstructured MEAs were used for long-term recordings of rat cortical and hippocampal neurons. Spontaneous neuronal activity from 10 to 24 DIV cultures were recorded in multiple islets from three different chips. The noise level was about  $2.1\text{--}4.3\ \mu\text{V}_{\text{SD}}$  (and never exceeded  $40\ \mu\text{V}_{\text{pp}}$ ) so spikes were easily distinguishable over the baseline (SD: standard deviation noise scale; pp: peak-to-peak noise scale).

It is important to note that recordings by conventional planar MEAs are predominantly characterized by negative monophasic signals with low amplitude ( $\leq 100\ \mu\text{V}$ ). In the recordings with the islets configuration, mainly positive monophasic or biphasic signals with amplitudes bigger than  $100\ \mu\text{V}$  were obtained. Smaller extracellular positive biphasic signals were also observed. It is well established that the spike's shape is influenced by cell geometry, size and maturation status (Nam & Wheeler, 2011), as well as by the source electrogenic cell compartment. Importantly, these small positive spikes may be axonal signals originating from axons that establish a close contact with the micro-mushrooms (embracing or curling round the 3D micro-structures).

Most interestingly, spontaneous intracellular-like activity (positive spikes in the mV range) with very high SNR were also recorded in the islet chip configuration (**Fig. 6**). **Figure 6A** shows a single-channel signal trace with both extracellular and intracellular-like recorded activity from cortical neurons.

The recorded SNR was consistently high across all islet electrodes. **Figure 6B** shows representative concurrent recording traces from three microelectrodes of the same chip, all with high amplitude positive spikes. Pooling the recorded activity of all islet electrodes, the average noise level was  $2.4\ \mu\text{V}_{\text{SD}}$  and the average SNR was 52. On the other, all recordings from the equivalent planar electrodes (same electrode base, but without micro-mushrooms) showed an average noise level of  $1.9\ \mu\text{V}_{\text{SD}}$  but a significantly lower average SNR of 28. Comparing the distribution of the amplitudes of the recorded spikes (using a threshold detection method at  $10\times\ \text{SD}$ ), there is a clear advantage towards the micro-mushrooms islets configuration (**Fig. 6C**). It is important to note that the flat gold at the base of the islet electrodes is not passivated, thus the recorded signals result from a combination of the 3D and planar components of the microelectrode.

Altogether, these results show the potential of the proposed micro-mushrooms islets configuration for attaining *in vitro* MEA recordings with higher fidelity than conventional planar MEA.

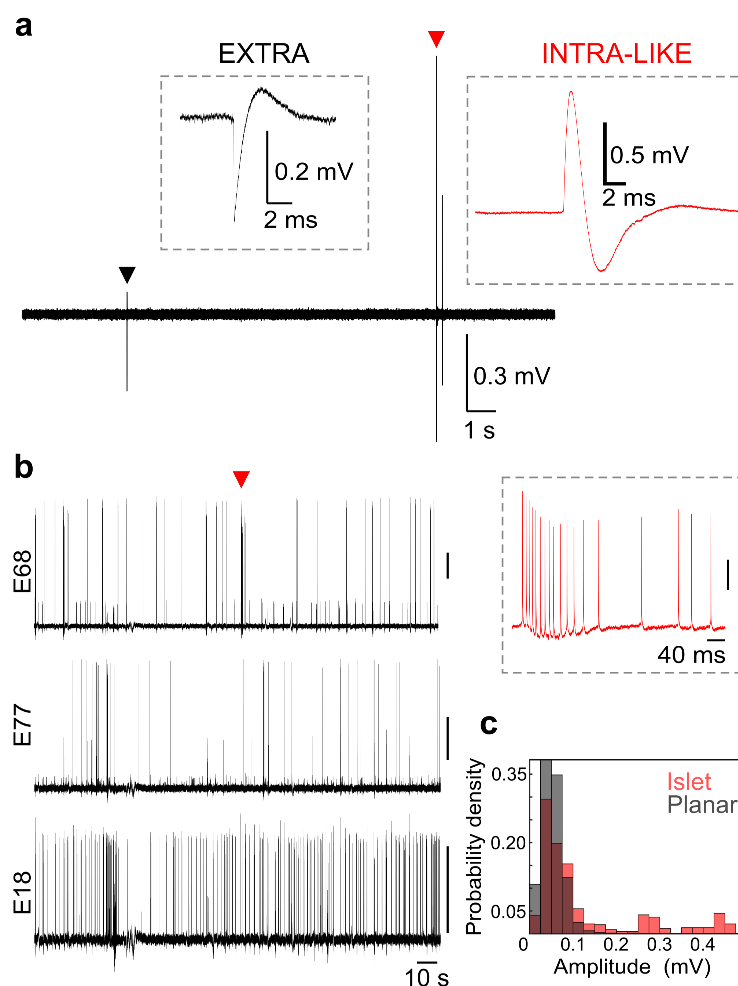


**Figure 6 – Islets of micro-mushrooms enable high-fidelity electrophysiological recordings from neurons. (A)** Single-channel electrophysiological recording of spontaneous extracellular and intracellular-like firing activity of rat cortical neurons at 24 DIV. A large extracellular spike (384  $\mu$ Vpp, SNR=104) and two intracellular-like spikes are easily distinguishable from the baseline. The biggest intracellular-like spike (red inset) had the positive phase clipped (at +1 mV) by the recording software range, therefore it had an amplitude of at least 1.49 mVpp (SNR=272). **(B)** Raw data traces of spontaneous activity as recorded by three different microelectrodes from rat hippocampal neurons at 10 DIV. The inset shows an enlargement of a burst recorded in electrode E68. Note the relative decrease in amplitude in

consecutive spikes (all amplitude scale bars = 0.1 mV). **(C)** Probability distribution of spike amplitudes recorded by 3D-microstructured (islets) and planar microelectrodes at 10 DIV.

## 2.5 Conclusion

The importance of incorporating physical cues in *in vitro* electrophysiology research is becoming more and more evident. From a biological perspective, it is clear that topography influences neuronal development and potentially helps recapitulating an *in vivo* environment. However, with rare exceptions (Cools et al., 2017), many of the recent efforts in this front have not integrated such findings into MEA devices that have been tested/validated in actual electrophysiological recordings. A novel 3D-microstructured MEA architecture was presented here, which holds promise for multisite *in vitro* electrophysiological recordings with high-yield and high-fidelity. The configuration is a hybrid between the canonical planar microelectrodes and the continuous array of 3D micro-mushrooms (Mestre et al., 2017), where the planar microelectrodes are replaced by islets of 3×3 micro-mushrooms, leading to improvements in the recordings by: i) promoting the co-localization (topotaxis) of neuron active structures with the electrodes (somata and neurites); ii) decreasing the impedance and increasing the SNR; iii) enhancing membrane-electrode coupling allowing measurement of signals with intracellular characteristics; and iv) raising the number of useful (recording) microelectrodes in cultures with normal cell densities. Importantly, this new MEA architecture is easy to fabricate and structurally robust, allowing conventional cleaning protocols and multiple uses of the same chip.

When compared to the most recent mushroom-shaped microelectrodes reported by Spira and collaborators (Shmoel et al., 2016), one of the most distinctive features of our design is the size and the organization of the micro-mushrooms in islets instead of using a single micro-mushroom per sensing microelectrode. But more importantly, the approach taken here is different from the original effort for producing patch-clamp intracellular-like recordings from the engulfment of mushroom-shaped microelectrodes (caps larger than 2.5  $\mu\text{m}$  preclude engulfment by the small mammalian neurons (Ojovan et al., 2015)). In the islets configuration proposed here, the objective of engulfment is replaced by entrapment, for somata, and by embracement, for neurites (axons/dendrites). The islets 3D topography greatly increases the cell-electrode contact surface and enables the acquisition of spontaneous activity with intracellular characteristics in the mV range. The high-quality recordings with cortical and hippocampal neurons presented here confirm the potential of the proposed configuration.

In MEAs, in addition to excellent SNR, it is also important to promote useful microelectrodes (i.e. electrodes with active neuronal structures in their vicinity), at adequate cell densities. With recent evidence that a large contribution of the extracellular signals comes, not from the somas, but from axons initial segment (Bakkum et al., 2018; Radivojevic et al., 2017), it becomes clear that clever MEA designs should also address the electrode-neurites coupling. This is achieved with our micro-mushrooms islets configuration, with localized neurites embracement. In the configurations presented here, a spacing range of 10  $\mu\text{m}$  in-between micro-mushrooms already produces effects on neurite guidance. Not only could we find neurites wrapped in all the islets analyzed but also the probability for somata to co-localize with the islets increased near 2-fold. We show that topographical features of the islets 3D-MEAs cause directional topotaxis not only in rat cortical neurons but also in human derived SH-SY5Y cells. A plausible mechanism is that the micro-mushrooms may function as anchors, serving as focal adhesion points for the neurons, providing long-term stable interfaces.

To the best of our knowledge, this is the first study employing cultures of human-derived cells on top of mushroom-shaped microelectrodes. The here proven advantages of the islets configuration holds promise for the translation of this technology to *in vitro* drug screening applications with, for example, induced human pluripotent stem cells. Naturally, future efforts will benefit from the combination of the gold microstructures with conductive polymers (e.g PEDOT-PSS) (Abidian et al., 2010; Aqrave et al., 2018) or carbon nanotubes (G. H. Kim et al., 2017), as previously suggested in the literature. This combination should help to reduce further the impedance of the islets 3D-microstructured microelectrodes.

## 2.6 Experimental Section

### 2.6.1 Fabrication

The fabrication process of the MEAs starts with the magnetron sputtering deposition of an electrically conductive Cr (5nm)/Au (40 nm) layer on top of  $49 \times 49 \text{ mm}^2$  glass substrates. The dimensions of the glass substrate were chosen for compatibility with the commercial MEA2100 system (**Fig S2A**). A three-level lithography process (corresponding to the three layers of the CAD design represented in different colors in **Fig. S2B** in the Supporting Information) was then used to fabricate the micro-mushrooms. The first step begins with spin-coating of PFR7790G27cP photoresist (1.5  $\mu\text{m}$  nominal thickness) followed by a soft bake (1 min at 86 °C). The first level (schematized in white in **Fig. S2B**, Supporting Information) of the lithography mask was then exposed using a Heidelberg DWLii direct laser writing system with a 405 nm diode laser, defining sixty electrical leads and  $2.2 \times 2.2 \text{ mm}^2$  pads for independent reading points. After post-bake for 1 min at 110 °C and development in TMA238WA for 1 min, the pattern was transferred to the Cr/ Au layer by ion-milling etching. This was performed in a Nordiko 3600 system with base pressure  $1 \times 10^{-7}$  Torr, an RF forward power of 203 W, first grid voltage 724 V and current 103 mA, a second grid voltage of -345 V and current 2.4 mA, and an Ar flow of 10.2 sccm corresponding to a working pressure of  $3 \times 10^{-5}$  Torr. The second level consists on the passivation of the electrical leads with 800 Å of  $\text{Al}_2\text{O}_3$ . The oxide is deposited by RF sputtering with a base pressure of  $3 \times 10^{-7}$  Torr, an RF power of 200 W, Ar flow of 45 sccm leading to a working pressure of  $3 \times 10^{-3}$  Torr. Using optical lithography, the outside reading pads and  $40 \mu\text{m} \times 40 \mu\text{m}$  areas (the islets where mushroom-shaped protrusions are grown) were previously protected. Oxide lift-off was then performed by immersing the sample in Microstrip 3001 at 60 °C for 30 min in ultrasonic bath, leaving the leads insulated while vias to the pads and islets were opened in a planar MEA design. The final level defined the micrometric holes in 1.5  $\mu\text{m}$  photoresist where the micro-mushrooms were to be fabricated (red layer in **Fig. S2B**, Supporting Information). In each of the islets, a square array of  $3 \times 3$  holes with nominal diameters of 2  $\mu\text{m}$  and center-to-center distance of 10  $\mu\text{m}$  was opened. To create the mushroom shape, gold was potentiostatically electrodeposited inside the opened holes using an Orosene bath, with an applied potential of -1.0 V during 39 min, at room temperature (RT, 23.5 °C) (Cerquido et al., 2018). Finally, at the end of the electrodeposition process the photoresist was removed using acetone and the 3D-microstructured MEA obtained. The morphology of the fabricated micro-structures was analyzed by scanning electron microscopy

(SEM) using a FEI Quanta 400FEG ESEM. In some comparison experiments, planar versions of 3D-structured microelectrodes were used, where the only difference in the specifications was the absence of the micro-mushrooms on top of the  $40\text{ }\mu\text{m} \times 40\text{ }\mu\text{m}$  islets areas.

### 2.6.2 Impedance Measurements

The electrical impedance of the  $40\text{ }\mu\text{m} \times 40\text{ }\mu\text{m}$  areas both with and without  $3 \times 3$  3D-microstructured microelectrodes was measured using a Precision Component Analyzer 6440B from Wayne Kerr Electronics in the  $10^2$  to  $2 \times 10^6$  Hz frequency range. This equipment uses four-terminal connections to measure with more accuracy the impedance and reduce the effect of contact resistance. To perform the measurements, the microelectrodes were emerged in a PBS (phosphate buffered saline) solution at RT.

### 2.6.3 Cell Culture

Before cell culture, chips were rinsed in distilled water to remove residues from fabrication. Afterwards, chips were sterilized by a brief immersion in 70% ethanol followed by UV light exposure. A sterilized silicon or PDMS ring was attached to the chip to hold the cells and culture medium. To assure a good cell attachment to the surface, chips were coated with 0.01 mg/ml poly(D-lysine) (PDL, 500 kDa, Corning) diluted in sterile distilled water for 1 h at RT. After three washes with sterile distilled water, they were let to air-dry before cell seeding.

Experimental procedures involving animals were carried out in accordance with current Portuguese laws on Animal Care (DL 113/2013) and with the European Union Directive (2010/63/EU) on the protection of animals used for experimental and other scientific purposes. The experimental protocol (reference 0421/000/000/2017) was approved by the ethics committee of the Portuguese official authority on animal welfare and experimentation (Direção-Geral de Alimentação e Veterinária). All efforts were made to minimize as possible the number of animals and their suffering.

Primary embryonic rat cortical and hippocampal neurons were isolated from Wistar embryo rats (E15-18). Embryos cortices were dissected in Hanks' Balanced Salt Solution (HBSS) and enzymatically digested in 0.05% (w/v) trypsin (1:250, Gibco®, Thermo Fisher Scientific) in HBSS for 15 min at 37°C. Subsequently, tissue fragments were washed once with 10% (v/v) heat-inactivated fetal bovine serum (hiFBS, Biowest) in HBSS, to inactivate trypsin, and twice with HBSS to remove hiFBS residues from solution. Tissue fragments were then mechanically

dissociated with a 5 ml serological pipette followed by a 1 ml pipette tip. Viable cells were counted using the trypan blue (0.4% (w/v), Sigma-Aldrich Co.) exclusion assay and seeded in PDL-coated 3D-microstructured arrays at a density around 1000 viable cells/mm<sup>2</sup>. Cells were cultured in Neurobasal medium supplemented with 0.5 mM glutamine, 2 % (v/v) B27 supplement and 1% (v/v) penicillin/streptomycin (P/S, 10,000 units ml<sup>-1</sup> penicillin and 10,000 µg.ml<sup>-1</sup> streptomycin) (all from Gibco®, Thermo Fisher Scientific), and kept in a humidified incubator at 37°C supplied with 5% CO<sub>2</sub> until use.

SH-SY5Y cells (a human neuroblastoma cell line), obtained from DSMZ (Germany) were routinely cultured in Dulbecco's Modified Eagle Medium/ Hams F-12 (DMEM/F-12, 50/50 Mix, Corning), supplemented with 10% (v/v) hiFBS and 1% (v/v) P/S (Biowest). SH-SY5Y cells were subcultured in PDL-coated 3D-microstructured arrays at a density of 100 viable cells/mm<sup>2</sup>, and incubated with differentiation medium I (DMEM/F-12 supplemented with 10% (v/v) hiFBS, 10 µM all-trans-retinoic acid (ATRA) and 1% (v/v) P/S) for 5 days, followed by incubation with differentiation medium II (DMEM/F-12 supplemented with 50 ng/ml brain-derived neurotrophic factor (BDNF, PeproTech) and 1% (v/v) P/S) for an additional 2 days, as reported by Encinas et al (2000) (Encinas et al., 2000).

After the experiments, cells were detached from the chip surface by a brief treatment with 0.25% (w/v) trypsin/ 0.05% (w/v) EDTA solution (Sigma-Aldrich, Co) at 37°C, followed by an overnight incubation with a commercial alkaline detergent solution containing proteases (Terg-A-Zyme®, Sigma-Aldrich, Co) at RT. This procedure allowed the reuse of chips.

### **2.6.4 Immunofluorescence Staining**

Primary cortical neurons and SH-SY5Y cells were fixed at 3 or 8 days in vitro (DIV), respectively, with 4% (w/v) paraformaldehyde (PFA) in 0.1 M phosphate buffer (pH 7.4) for 15 min, at RT. After washing in PBS, cells were blocked and permeabilized with 0.1% (w/v) bovine serum albumin (BSA, Sigma-Aldrich Co) containing 0.3% (v/v) Triton X-100 (Sigma-Aldrich Co) for 1 h, at RT. Afterwards, cells were incubated with primary antibody solution (rabbit anti-βIII tubulin, 1:500, Abcam) overnight, at 4°C. After washing in PBS, cells were incubated with fluorescently-labeled secondary antibody solution (anti-rabbit Alexa Fluor® 488 conjugate, 1:1000, Molecular Probes®, Thermo Fisher Scientific) for 1 h, at RT. Nuclei were stained with 0.5 µg/ml Hoechst (Molecular Probes®, Thermo Fisher Scientific).

Cells were imaged using a laser scanning confocal microscope Leica TCS SP5 II (Leica Microsystems, Germany) with the HCX PL APO CS 40x/1.3 oil objective. Laser lines at 405 or 488 nm were used for Hoechst or Alexa 488 excitation, respectively. For each condition (primary neuron or SH-SY5Y cell cultures), a total of 47 and 59 images (3D-microstructured areas) were acquired from 5 and 6 independent 3D-microstructured arrays, respectively.

### **2.6.5 Cell Viability**

The cell viability after seeding in 3D-microstructured arrays was assessed by the live/dead assay using calcein-AM/ propidium iodide (PI). Primary cortical neurons were isolated and seeded as previously described. At 3 and 13 DIV, cells were incubated with 1 mM calcein-AM (Molecular Probes®, Thermo Fisher Scientific) for 10 min at 37°C, followed by incubation with 2  $\mu$ M PI (Sigma-Aldrich Co) for 5 min, at RT. After incubation, cells were imaged in an inverted fluorescence microscope (Axiovert 200M, Zeiss) with a Plan NeoFluar 20x/0.4 Ph2 Korr objective. Laser lines at 488 and 543 nm were used for calcein-AM or PI excitation, respectively. For each 3D-microstructured array, a total of 5 fields from 3D-microstructured or flat areas were randomly selected for representative imaging and analysis. Images were acquired from 3 independent 3D-microstructured arrays, for each time point.

### **2.6.6 Image Processing and Analysis**

Image processing and quantitative analysis were performed using ImageJ software (Rueden et al., 2017). Experiments involving manual cell counting procedures were assisted by an ImageJ cell counter plug-in. For the quantitative analysis of the neurite directionality of both cortical neurons and SH-SY5Y cells, maximum intensity projection images from z stacked images were evaluated using the OrientationJ Distribution plug-in (Rezakhaniha et al., 2012). This plug-in computes the local orientation properties of structures in the image at the pixel level. The algorithm assesses local directionality in terms of two measures: coherency and energy. Distributions of orientations (directionality analysis) were built taking into account the pixels that had a coherency larger than 90% (min-coherency) and an energy larger than 10% (min-energy). The final orientation distributions were calculated and visualized using custom-made MATLAB (The MathWorks Inc., USA) scripts. The obtained distributions of orientations were tested for uniformity using the two-sample Kolmogorov-Smirnov test.

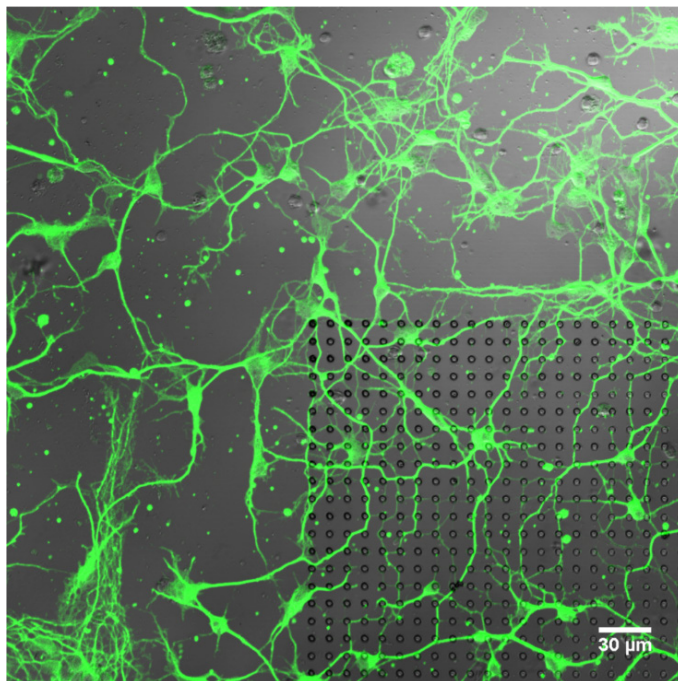
### 2.6.7 Electrophysiological Recordings

AC voltage electrophysiological recordings of rat cortical neuron cultures started at 13 DIV. Single-channel extracellular acquisitions were performed inside a Faraday cage at RT (22°C). All data was analog-filtered (0.3-20 kHz) and amplified ( $\times 100$ ) with a 4-channel amplifier (Model 1700, A-M Systems). The amplifier was connected to the contact pads of the chips via pogo pins held in place by manipulators. One Ag/AgCl electrode was submerged in the medium to be used as ground. Signals were digitized via an oscilloscope with 16-bit resolution at a sampling rate of 1 gigasamples/sec. The recording setup capability was successfully tested with planar 256-microelectrodes MEA cultures that also exhibited spontaneous activity in a commercial MEA system (MEA2100-256-System, MultiChannel Systems, Germany). The fabricated chips' compatibility with a commercial system was confirmed by performing recordings from hippocampal neurons at 10 DIV with a 60-channel MEA2100-Mini-System (MultiChannel Systems, Germany). These recordings were performed inside a humidified incubator (37°C, 5% CO<sub>2</sub>) at a sampling rate of 20 kHz. The estimated SNR was calculated by dividing the peak-to-peak (pp) amplitude of the recorded spikes by the standard deviation (SD) of the noise level. Presented figures for measured electrical potential are scaled to pre-amplification values.

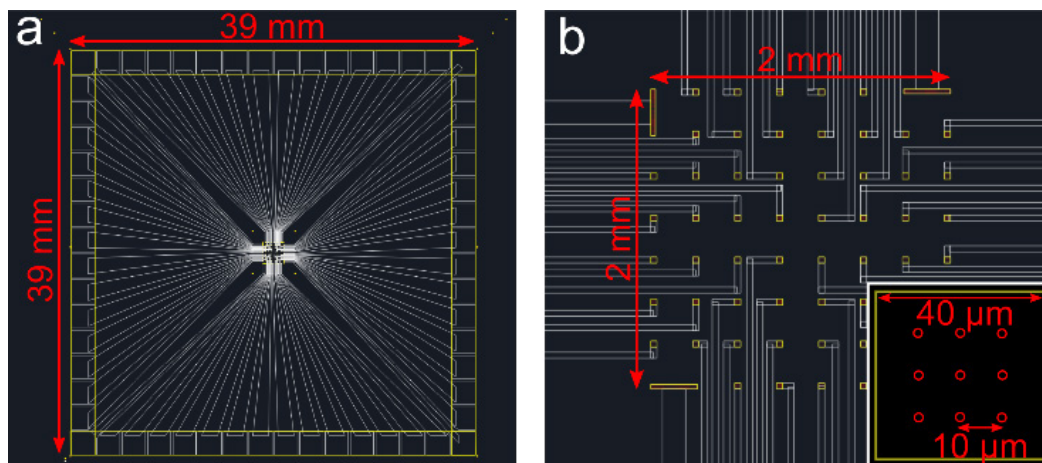
### 2.6.8 Statistical Analysis

Statistical analysis was performed using GraphPad Prism version 7.0 (GraphPad Software Inc., CA, USA). The ROUT method did not identify any outlier in all datasets. The method of D'Agostino & Pearson was used as a normality test and parametric or non-parametric tests were chosen as appropriate. Statistical significance was considered for  $p < 0.05$ . All statistical data was presented as mean and SD.

## 2.7 Supporting Information



**Supporting Figure S1** – Confocal microscopy image of cortical neurons at 3 DIV cultured on a simpler chip configuration (used only in supporting experiments) where the micro-mushrooms were limited to a continuous large array of 2 mm × 2 mm (lower right corner). The micro-mushrooms spacing was the same as in the islets configuration, i.e., 10 μm. Neurons were immunolabelled for  $\beta$ III-tubulin (green).



**Supporting Figure S2 – Computer aided design (CAD) diagram used for the fabrication of the arrays of micro-mushroom islets. (A)** The chip layout was made compatible with the 60 electrodes MEA2100 system by MultiChannel Systems. **(B)** Detail of the electrodes area in the center, showing the array of islets, where each islet was in turn an array of  $3 \times 3$  micro-mushrooms (lower right corner inset).

### **Acknowledgements**

This work was partly financed by FEDER - Fundo Europeu de Desenvolvimento Regional funds through the COMPETE 2020 - Operational Programme for Competitiveness and Internationalisation (POCI), Portugal 2020, and by Portuguese funds through FCT - Fundação para a Ciência e a Tecnologia/ Ministério da Ciência, Tecnologia e Inovação in the framework of the project "Institute for Research and Innovation in Health Sciences" (POCI-01-0145-FEDER-007274) and in the framework of the financed project PTDC/CTM-NAN/3146/2014. José Mateus was supported by FCT (PD/BD/135491/2018). Paulo Aguiar was supported by Programa Ciência – Programa Operacional Potencial Humano (POPH) – Promotion of Scientific Employment, ESF and MCTES and program Investigador FCT, POPH and Fundo Social Europeu. The SH-SY5Y cells (DSMZ, Germany), were kindly provided by the UniGENe group at i3S.

## **Chapter III**

### **Paper II**

*Neuronal cultures show bidirectional axonal conduction with antidromic action potentials depolarizing the soma*



**Neuronal cultures show bidirectional axonal conduction with antidromic action potentials depolarizing the soma**

*The content of this chapter is based in the following original research paper:*

**Mateus JC**, Lopes CD, Aroso M, Costa A, Gerós A, Meneses J, Faria P, Neto E, Lamghari M, Sousa MM, Aguiar P. *Neuronal cultures show bidirectional axonal conduction with antidromic action potentials depolarizing the soma*. bioRxiv. doi: 10.1101/2021.03.07.434278 (2021).

*This is an original research paper and it is presented for the first time in a thesis.*



### 3.1 Abstract

Recent technological advances are revealing the complex physiology of the axon and challenging long-standing assumptions. Namely, while most action potential (AP) initiation occurs at the axon initial segment in central nervous system neurons, initiation in distal parts of the axon has been shown to occur in both physiological and pathological conditions. However, such ectopic action potential (EAP) activity has not been reported yet in studies using *in vitro* neuronal networks and its functional role, if exists, is still not clear. Here, we report the spontaneous occurrence of EAPs and effective antidromic conduction in hippocampal neuronal cultures. We also observe a significant fraction of bidirectional axonal conduction in dorsal root ganglia neuronal cultures. We investigate and characterize this antidromic propagation via a combination of microelectrode arrays, microfluidics, advanced data analysis and *in silico* studies. We show that EAPs and antidromic conduction can occur spontaneously, and also after distal axotomy or physiological changes in the axon biochemical environment. Importantly, EAPs may carry information (as orthodromic action potentials do) and can have a functional impact on the neuron, as they consistently depolarize the soma. Plasticity or gene transduction mechanisms triggered by soma depolarization can, therefore, be also affected by these antidromic action potentials/EAPs. Finally, we show that this bidirectional axonal conduction is asymmetrical, with antidromic conduction being slower than orthodromic. Via computational modeling and super-resolution microscopy, we show that the experimental difference can be explained by axonal morphology. Altogether, these findings have important implications for the study of neuronal function *in vitro*, reshaping completely our understanding on how information flows in neuronal cultures.

**Keywords:** ectopic action potential, antidromic propagation, brain-on-a-chip, hippocampal neurons, dorsal root ganglia, microelectrode array, microfluidics

### 3.2 Significance Statement

Embedded in the canonical perspective on how neurons communicate is the idea of unidirectional axonal conduction: orthodromic in central nervous system, and antidromic in the peripheral nervous system. Taking advantage of state-of-the-art microelectrode arrays technology, we demonstrate bidirectional conduction in hippocampal and dorsal root ganglion cultures, reshaping our understanding on how information flows *in vitro*. Antidromic action potentials, even in hippocampal cultures, effectively depolarize the soma (potentially triggering plasticity/protein translation mechanisms, as dendritic-driven depolarization do). It remains to be shown if these dynamics hold for *in vivo* conditions, but with *in vitro* models being used extensively in conditions where network dynamics play an important role (e.g., plasticity, neuronal circuits), acknowledging this prevalence of bidirectional axonal conduction is of fundamental importance.

### 3.3 Introduction

A neuron is a highly specialized cell, well-compartmentalized into dendrites, soma, and the axon. In a reductionist view, the axon is often seen as a mere transmission cable in which action potential (AP) orthodromic propagation occurs after generation at the axon initial segment (AIS). This is, however, a very limiting view which partially arises from the technical challenges in recording action potentials activity from the thin axonal branches of vertebrate neurons (Alcami & El Hady, 2019; Debanne et al., 2011). Recent breakthroughs, made possible by *in vitro* technological developments such as super-resolution microscopy (Chéreau et al., 2017), voltage imaging (Peterka et al., 2011), fluorescence-guided subcellular patch-clamp (Sasaki et al., 2011), microfluidic tools (Holloway et al., 2021; Neto et al., 2016), or microelectrode arrays (MEAs) (Emmenegger et al., 2019) have opened new insights into axonal signal conduction and generated a renewed interest in axon physiology. Accordingly, accumulating evidence shows that the computational repertoire of the axon is much more complex than traditionally thought (for reviews see (Alcami & El Hady, 2019; Bucher & Goaillard, 2011; Debanne et al., 2011; Sasaki, 2013; Roger D. Traub et al., 2020)).

After the seminal work by Hodgkin and Huxley on axonal propagation (Hodgkin & Huxley, 1952), the AP initiation and its subsequent propagation have been extensively investigated (Bucher & Goaillard, 2011). These studies have placed the AIS as the main site capable of AP generation in central nervous system (CNS) neurons. Intriguingly, several studies have demonstrated that APs generated at distal sites of the axon, also known as ectopic APs (EAPs), co-occur in diverse types of neurons both *ex vivo* and *in vivo* (Bähner et al., 2011; Bukalo et al., 2013; Chorev & Brecht, 2012; Dugladze et al., 2012; Pinault, 1995; M. E. J. Sheffield et al., 2011; Thome et al., 2018). Such studies opened perspectives on neuronal communication beyond the canonical orthodromic signal transmission (Sasaki, 2013; Roger D. Traub et al., 2020). In vertebrates, the occurrence of EAPs has been associated with pathological conditions where the axon is hyperexcitable (e.g., epilepsy, nerve injury, demyelination) (Gutnick & Prince, 1972; M. S. Hamada & Kole, 2015; Pinault, 1995; Stasheff et al., 1993), but also with physiological functions, such as synaptic plasticity (Bukalo et al., 2013, 2016), or fast network oscillations (Bähner et al., 2011; Dugladze et al., 2012; M. E. J. Sheffield et al., 2011). Still, as these studies relied on patch-clamp paired recordings, or paired field recordings from brain slices, the fine detection and characterization of the antidromic conduction properties (e.g., conduction velocity) could not be attained. Moreover, many uncertainties still hold regarding

the precise mechanism(s) of EAPs' initiation (Alcami & El Hady, 2019; Roger D. Traub et al., 2020). Hypotheses such as local depolarization mediated by activity in connected (e.g., axo-axonal coupling) (Bähner et al., 2011; Schmitz et al., 2001) or adjacent axons (ephaptic coupling) (Anastassiou et al., 2011), as well as stochastic activation of sodium channels in unmyelinated distal thin segments of the axon (M. S. Hamada & Kole, 2015; Pinault, 1995) have been proposed, but the characterization and function of EAPs remain elusive. Importantly, it remains to be shown if EAPs/antidromic APs carry usable information to the cell body or if they are simply an electrophysiological glitch. From a functional perspective, a bidirectional flow of activity would certainly increase the complexity, but also the computational power of the axon (Alcami & El Hady, 2019). Learning and plasticity studies in theoretical neuroscience have demonstrated the vast functional relevance of hypothetical mechanisms that could propagate signals (namely error signals) back to presynaptic neurons (for review see (Whittington & Bogacz, 2019). This is tightly related to the ideas behind the backpropagation algorithm (Rumelhart et al., 1986), a central element in state-of-the-art artificial neuronal networks, such as deep neuronal networks.

Axonal conduction in the peripheral nervous system has, however, different specificities. *In vivo*, the peripheral process of sensory neurons generates APs distally, which propagate antidromically towards the dorsal root ganglia (DRG). Still, the majority of *in vitro* studies have focused on molecular processes (e.g. antero/retrograde axonal transport), with no electrophysiological characterizations of axon physiology (Black et al., 2019; Nascimento et al., 2018). Thus, it remains to be shown if cultured DRGs recapitulate the ability to generate APs at their distal terminals in both physiological and pathological contexts (e.g., EAPs after axotomy).

Emerging technologies that allow probing axonal function with high temporal and spatial resolution can help characterize and understand EAPs/antidromic APs. We and others have combined microElectrode arrays and microFluidics ( $\mu$ EFs) to compartmentalize neuronal cultures in well-defined topologies that allow functional readouts (Rouhollah Habibey et al., 2017; Heiney et al., 2019; Lewandowska et al., 2016; Lopes et al., 2018), as well as selective manipulations of the different neuronal compartments (Moutaux et al., 2018; Neto et al., 2016, 2020). In particular,  $\mu$ EFs allow the isolation of axons within microchannels, which are aligned over a set of microelectrodes. Thus,  $\mu$ EFs allow for the detection of propagating axonal signals with very high fidelity and temporal resolution in long-term experiments, which are not possible with any other technique (Lopes et al., 2018; Moutaux et al., 2018).

Here, using  $\mu$ EFs and detailed temporal analysis, we report the consistent occurrence of bidirectional axonal conduction in two different *in vitro* models: dissociated hippocampal neurons and DRG organotypic cultures. Critically, the antidromic signals depend on the activation of axonal  $\text{Na}^+$  current, as the selective application of tetrodotoxin (TTX) to the axonal compartment completely ceases antidromic activity. Via a combination of extracellular electrophysiological recording/stimulation and fast calcium imaging, we show that evoked antidromic events effectively depolarize the soma – anticipating functional roles of antidromic activity. Addressing this frequent occurrence of antidromic APs in both hippocampal and DRG cultures, we explore possible functional roles of these signals under two different conditions: in the pathological context of axonal lesions, we show that EAPs occur after distal axotomy; additionally, we show that physiological changes in the biochemical environment of the distal axon can promote antidromic activity. Finally, we report differences in the velocity of signal propagation, as antidromic conduction is slower than orthodromic. These differences can be explained by different axon morphologies.

The demonstration of the occurrence of antidromic APs, which can effectively depolarize the soma (and potentially trigger plasticity/protein translation mechanisms, as dendritic-driven depolarizations), reshapes our understanding on how information flows in neuronal networks.

### 3.4 Results

#### 3.4.1 Tracking Signal Propagation Reveals a Bidirectional Flow of Activity

In this study, we improved on our previous microfluidic chamber design (Heiney et al., 2019; Lopes et al., 2018), by optimizing it for the study of axonal function (details in the Methods section). Importantly, we set the number of microchannels to match the number of microelectrode columns, so that every microchannel would be probed electrophysiologically. The alignment of this microfluidic chamber with 252-electrode MEAs allowed for the probing of 16 microchannels, encompassing 7 microelectrodes each, per experiment (**Fig. 1A**). This configuration enabled the separation of somal and axonal activity within the same experiment (**Fig. 1B-D**). A schematized  $\mu$ EF is shown in **Fig. 1B**. The higher impedance within the microchannels greatly amplifies the otherwise difficult-to-detect axonal signals (Lopes et al., 2018; Pan et al., 2014). Due to the increase in SNR and the controlled placement of electrogenic compartments (i.e., axon proper) on top of the microelectrodes, the mean firing rate (MFR) (**Fig. 1C-E**) and the percentage of active microelectrodes (**Fig. 1F**) were consistently higher within the microchannels. A representative raster plot of activity and signal traces from a single microchannel are shown as insets in **Fig. 1C**.

In the used configuration, single-compartment neuronal cultures (mono-cultures), somata were maintained in a somal compartment and extended their axons along the microchannels to a pure axonal compartment (**Fig. 1A-B**). We investigated axonal function in two different *in vitro* models: dissociated hippocampal neurons and organotypic cultures of DRG. These different models exhibited marked differences in axonal outgrowth and electrophysiological maturation. Hippocampal neurons' axons grew through the microchannel within 5 to 7 days (**Fig. 1A**), while DRG axons took 3 to 5 days. Unlike mature hippocampal neurons, DRG neurons did not fire in bursts but rather exhibited sporadic spontaneous activity. In physiological conditions, this relatively low level of activity also occurs *in vivo* (Black et al., 2019). As DRG explants were placed outside the MEA active area, activity was only recorded in the microchannels (**Fig. 1D**). This further highlights the importance of microchannels to record axonal activity extracellularly.

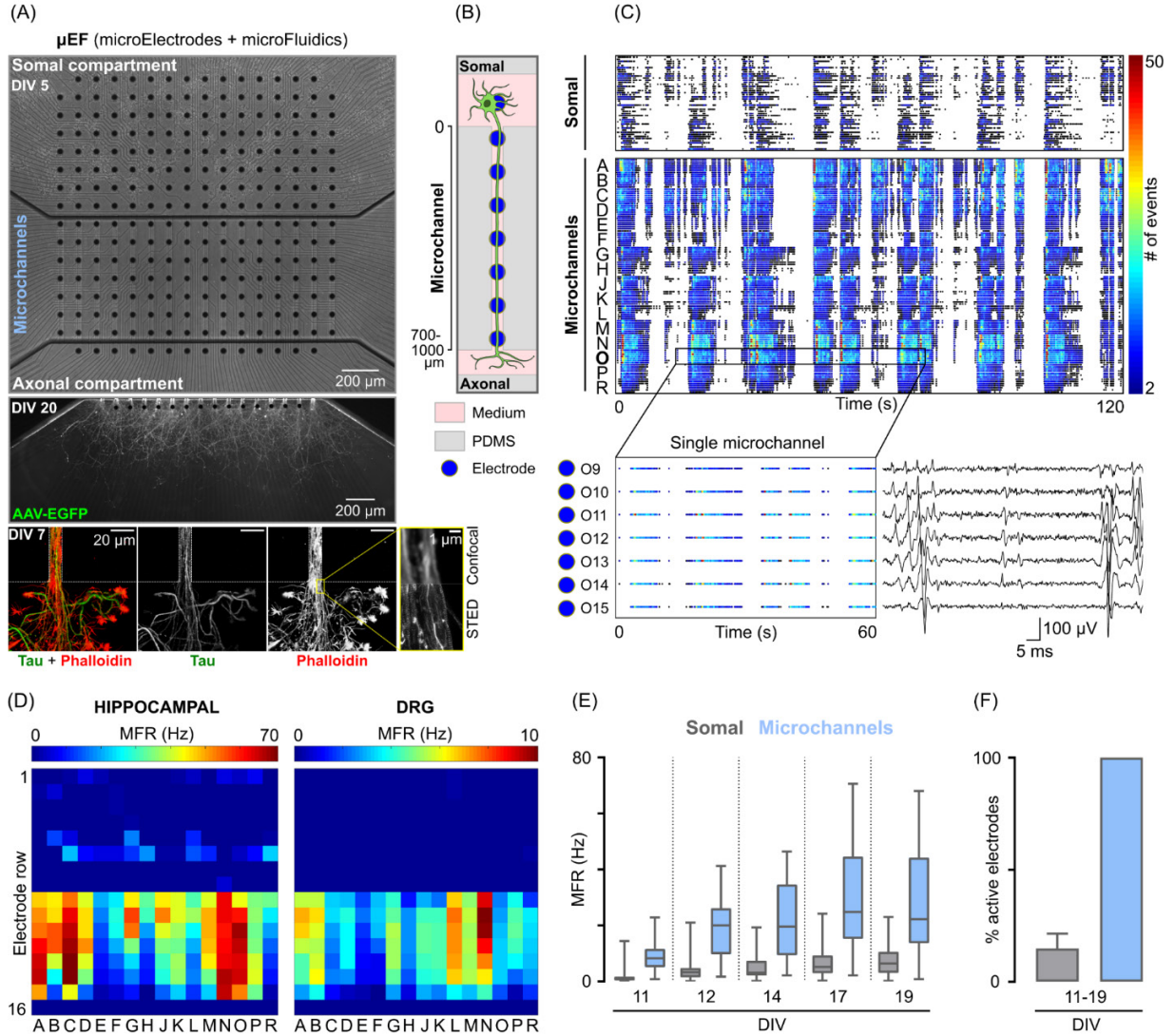


**Figure 1 – The combination of microElectrode arrays and microFluidics ( $\mu$ EFs) allows tracking of axonal signal propagation *in vitro* with high fidelity. (A)** Phase-contrast microscopy image mosaic of a hippocampal mono-culture at 5 days in vitro (DIV). The whole microelectrode array (MEA) active area ( $1.5 \times 1.5$  mm) is shown by a combination of images (10 $\times$  objective mosaic) from different parts of the culture. A microfluidic device composed of 16 microchannels (10  $\mu$ m width; 700  $\mu$ m minimum length) is aligned to encompass 7 microelectrodes. Details of axonal morphology can be seen in the somal compartment, microchannels, and axonal compartment. Below, an axonal compartment of a hippocampal culture (expressing EGFP) at DIV 20 (scale bars = 200  $\mu$ m) and the exit of a single microchannel at DIV 7 are shown. **(B)** Schematized  $\mu$ EF concept. **(C)** Color-coded raster plots of 2 minutes of activity of all the active microelectrodes of a hippocampal culture at DIV19. In

total, the activity of 45 microelectrodes from the somal compartment and 112 microelectrodes within the 16 microchannels (A-R) is represented. The inset shows a segment of a single microchannel (O9-15) and an example signal trace. **(D)** Activity maps of a hippocampal and a DRG culture at 19 (same as in (C)) and 7 DIV, respectively. Each pixel corresponds to one recording microelectrode. The mean firing rate (MFR) is color-coded for each microelectrode. Notice that while somal activity can be recorded in the somal compartment of the hippocampal culture, only axonal activity within the microchannels can be recorded in the DRG explant culture. **(E)** Tukey plots of the MFR of all consistently active microelectrodes, during hippocampal maturation, within the somal compartment and microchannels ( $n = 57$  somal microelectrodes,  $n = 48$  microchannels; from 3 independent  $\mu$ EFs). **(F)** Percentage of consistently active microelectrodes, during hippocampal maturation, within the somal compartment and the microchannels ( $n = 3$  independent  $\mu$ EFs).

We unbiasedly analyzed the direction of propagation of spontaneous APs within the microchannels. We found that in experiments using either dissociated hippocampal neurons or DRG explants' mono-cultures, a significant number of events propagated from the axonal to the somal compartment - backward propagation (**Fig. 2A**). Examples of isolated forward and backward propagating events occurring in the same microchannel can be seen in the inset of **Fig. 2A**. This backward propagation completely ceased after selectively adding TTX to the axonal compartment ( $n = 6$  independent  $\mu$ EFs) (**Supplementary Fig. S2**), supporting the hypothesis that the observed activity initiates in the axonal compartment.

Different causes can support the observed backward propagation (**Fig. 2B**). First, the simple case of an axon growing back to the somal compartment after having extended to the axonal compartment ("U"-turn). Additionally, although axons do not find dendritic targets in the axonal compartment, they may establish axo-axonal synapses and/or couple via gap junctions (Schmitz et al., 2001), so that one axon conducts APs orthodromically and the other antidromically along the microchannels. Alternatively, very close proximity between axons in the axonal compartment, combined with high electrical coupling conditions, can originate ephaptic coupling (Anastassiou et al., 2011) where, as with gap junctions or axo-axonic connections, an axon conducts APs antidromically. Finally, this activity may consist of EAPs initiation caused by activation of sodium channels (stochastic, or not) at the axon distal end followed by antidromic propagation (M. S. Hamada & Kole, 2015; Pinault, 1995). The possible origin of the backward propagation was dissected through a set of experiments that selectively manipulated the axonal compartment.

### 3.4.2 Backward Propagation is Not Explained by Returning Axons nor $\mu$ EF Electric Artifacts

The  $\mu$ EF design did not prevent axons from growing back to the somal compartment after reaching the axonal compartment (“U”-turns), though these axons would have to elongate for, at least,  $\sim 1.5$  mm. Thus, we hypothesized that the detected backward propagation could simply be caused by axon grow back (**Fig. 2B**). As the AP activity in returning axons would be temporally correlated with AP activity in another microchannel, we performed time-delay analysis of the backward propagation events against the preceding AP activity in all microchannels (**Fig. 2C**).

For hippocampal neurons at 11 and 19 DIV ( $n = 5$  independent  $\mu$ EFs), only a minority ( $<10\%$ ) of the microchannels where backward propagating events were detected showed temporal correlations (within 10 ms) with AP activity in other microchannels. An example of neighboring microchannels with a strong temporal correlation is shown in **Fig. 2D**. In DRG experiments at 6 DIV ( $n = 5$  independent  $\mu$ EFs), we found a single pair of temporally correlated microchannels. Moreover, we could not detect a correlation within the same microchannel in any experiment. Thus, the great majority of the detected backward propagation does not emerge from axon grow back to the somal compartment after a “U”-turn. Similarly, the obtained time-delay distributions do not favor the hypotheses of strong axo-axonal coupling as a major cause for the detected backward propagating activity.

Ephaptic coupling has been suggested as a mechanism of fast neuronal synchronization ( $<1$  ms) via axonal extracellular signaling (Anastassiou et al., 2011; Han et al., 2018). As axons grow in close-proximity within the microchannels, even in the absence of synapses (chemical or electrical), the ephaptic coupling could lead to distal initiation of EAPs, as hypothesized in (Pan et al., 2014). Whereas we cannot exclude ephaptic coupling inside a microchannel, it should be noted that the detected backward propagation events always transverse the whole microchannel, meaning that the coupling locus would need to be, consistently, at or after the last microelectrode (in the axonal compartment). In our method for detecting APs propagation, the exclusion window is 4 ms, meaning that the observed backward propagation never follows a forward propagation in the same microchannel. The only option would be ephaptic coupling taking place in the axonal compartment between axons from different microchannels, and in that case we would capture this situation in the time-delay histograms. Therefore, we also

exclude ephaptic coupling as a possible cause for the majority of the detected backward propagating events.

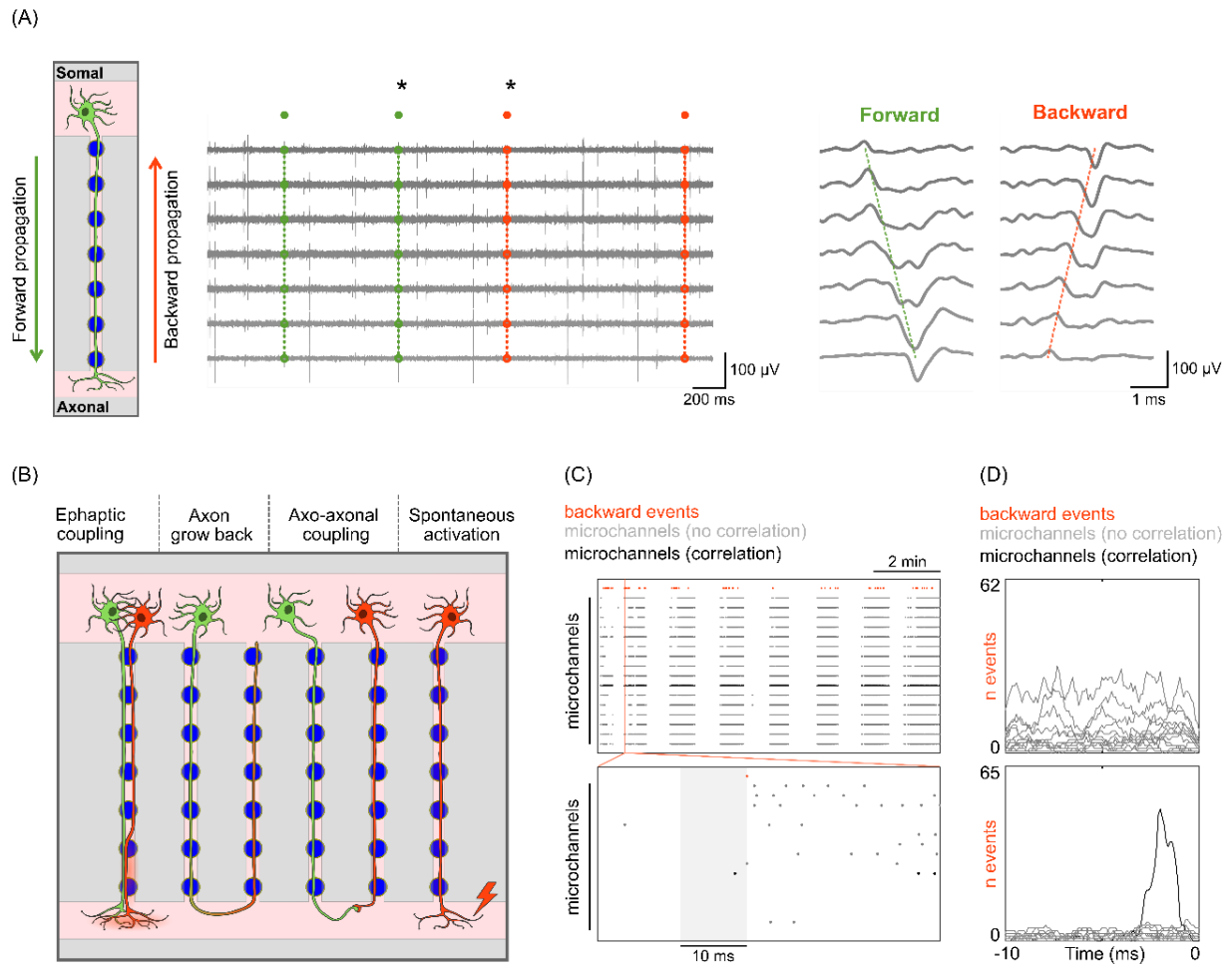


**Figure 2 – Tracking signal propagation reveals a bidirectional flow of activity which is not explained by axon grow back. (A)** Schematic representation of the two possible direction flows of signal propagation (forward and backward). Example traces of 3 seconds of activity within a microchannel of a DRG culture at 11 DIV. Detected forward and backward propagating events are marked as green and orange, respectively. The asterisks (\*) highlight the two traces expanded in the inset. **(B)** Schematic of the possible causes for backward propagation. Neurons are colored by their propagating direction (forward or backward). Leftmost: nonsynaptic electrical coupling (ephaptic coupling). Center-left: axon grow back to the somal compartment after having extended to the axonal compartment (“U”-turn). Center-right: Axo-axonal coupling via electrical synapse and/or gap junction. Rightmost: Spontaneous activation of the axon distal portion. **(C)** Raster plot of 10 minutes of activity in all microchannels (one

electrode per microchannel) from a hippocampal culture at 19 DIV. The first line (in orange) represents all detected backward propagating events ( $n = 65$ ) from a single microchannel. The zoom-in shows 50 ms of activity in all microchannels. A time-window of 10 ms before each backpropagating event was used for isolating possible microchannel correlations (e.g., “U”-turns). **(D)** Pre-backpropagating event time histograms. Examples of no correlation (top) and correlation (bottom; same microchannel as in (C)) are shown.

A last, but not less relevant alternative hypothesis for the observed backward propagation signals is the presence of electric artifacts in the  $\mu$ EF microchannels. Detailed simulations using FEM, recreating the core geometrical elements of the microchannels (**Fig. 3A**), were carried out to assess two situations that could be incorrectly interpreted as a backward propagation signal: i) complex electrical behaviors driven by the extracellular currents of forward APs, and ii) influence of axonal activity at the exit of the microchannels on the readout of the microelectrodes. The microchannels' small cross-section leads to higher impedances and increased recorded signal amplitudes, in accordance with the experimental data (**Fig 3B-C**). However, the forward propagation of APs inside the microchannels does not generate any unexpected potential readings at the microchannel extremities that could trigger another AP (**Supp. Mat. Movie 1**). The increased impedance inside the microchannels is also responsible for the fact that axonal electrical activity just outside the microchannel does not generate relevant electrical potential/currents that could trigger an AP in an axon inside the microchannel (i.e., the microchannels do not “channel in” outside currents) (**Fig 3D**). Finally, the FEM model also excludes the possibility of axonal activity at the exit point of the microchannel being picked up by the microelectrodes inside and incorrectly interpreted as a backward propagation signal. In such case, not only the signal amplitudes in the microelectrodes further away would be extremely low, the signal deflection in all electrodes would be virtually synchronous (as we would be recording the electric disturbance in the medium and not a traveling wave in an axon) (**Fig 3E**).

Concluding, since the vast majority of the detected backward propagating activity does not come from axons growing back, nor electrical artifacts at microchannel entrance, the origin is necessarily the distal parts of the axons. As such, the terminology backward propagation will be replaced by antidromic conduction for the remainder of the manuscript.

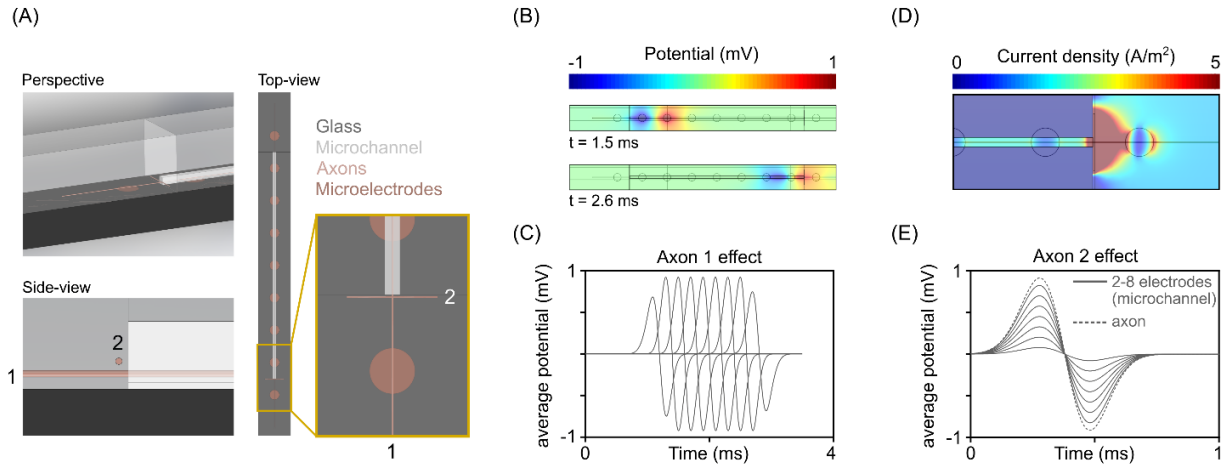


**Figure 3 – Backward propagation is not explained by electric artifacts. (A)** Representation of the finite element model (FEM) geometry replicating the  $\mu$ EF microchannels, microelectrodes and axons. Two axons in different positions (axon 1 and 2) were considered: axon inside the microchannel, and axon outside the microchannel and perpendicular to the exit. Three views are presented: perspective, side view and top view with detail on microchannel exit point. **(B)** Simulation of an action potential (AP) propagation along axon position 1. **(C)** Impedance levels inside the microchannel contribute significantly to the ability to record signals from axons. In the model, as well as in experimental data, the amplitudes of the recorded signals are higher in the microelectrodes inside the microchannels. **(D)** Given the higher impedance inside the microchannels, axonal activity at the exit point does not produce current densities that could stimulate axons inside the microchannel. **(E)** The FEM simulations show that (in low noise conditions) electric activity outside the microchannel (axon position 2) can be detected by the microelectrodes inside. However, the signal deflection recorded at each microelectrode would be “simultaneous” (propagation of the electric field in the medium), and would not be confused with an AP.

### 3.4.3 Antidromic Action Potentials Effectively Depolarize the Soma

For EAPs/antidromic APs to carry usable information to the cell body (as orthodromic APs carry information to post-synaptic neurons) and have a functional role there, they should reach and effectively depolarize the soma. Thus, we tested if eliciting antidromic activity could lead to soma depolarization. For that, we retrogradely transduced hippocampal mono-cultures with ssAAV-retro/2-hSyn1-chI-jGCaMP7f-WPRE-SV40p(A) at 9-10 DIV, which allowed us to perform calcium imaging of neurons extending to the axonal compartment (**Fig. 4A**). This AAV2-retro variant (Tervo et al., 2016) allows for the robust retrograde expression of the protein of interest. Here, we used it to selectively induce the expression of jGCaMP7f ('fast'), a genetically encoded calcium indicator (GECI) with fast kinetics and single-AP sensitivity (Dana et al., 2019). As relatively few neurons project axons to the axonal compartment, labeling was sparse even weeks post-transduction (**Fig. 4B**).

A standard electrical stimulation protocol was used to elicit antidromic activity on transduced neurons (18-21 DIV), while performing fast calcium imaging and electrophysiological recording (**Fig. 4A**). For that, 5 electrical pulses were delivered to the last microelectrode within the microchannel of interest (at least 600  $\mu\text{m}$  away from the soma) per trial. The microchannel of interest (i.e., containing the axon of the transduced neuron) could be readily identified via labeling (mRuby3 and/or jGCaMP7f) (**Fig. 4B**). Antidromic APs were elicited reliably for the range of tested stimulation amplitudes (-0.5/0.5 to -1.0/1.0 V) and frequencies (0.5-1 Hz) (**Fig. 4C** and **Supplementary Fig. S3**). The resulting stimulation artifact precluded the electrophysiological recording of the immediate responses (within ~5 ms post-stimuli) along the microchannel, even when stimulation artifact blanking was used. However, somal depolarizations could be recorded when neurons were near a somal microelectrode (**Fig. 4D**).

Somatodendritic depolarizations were consistently obtained in response to evoked antidromic APs, as can be seen in the calcium imaging traces (**Fig. 4E-F** and **Fig. S3**) (**Supplementary Movies 2-3**). These results were reproduced in several neurons from 6 independent  $\mu\text{EFs}$  at 18-21 DIV. With antidromic APs being able to carry information and effectively depolarizing the soma (potentially triggering, for example, protein translation or plasticity mechanisms), the following sections address different physiological contexts capable of triggering/modulating antidromic activity.

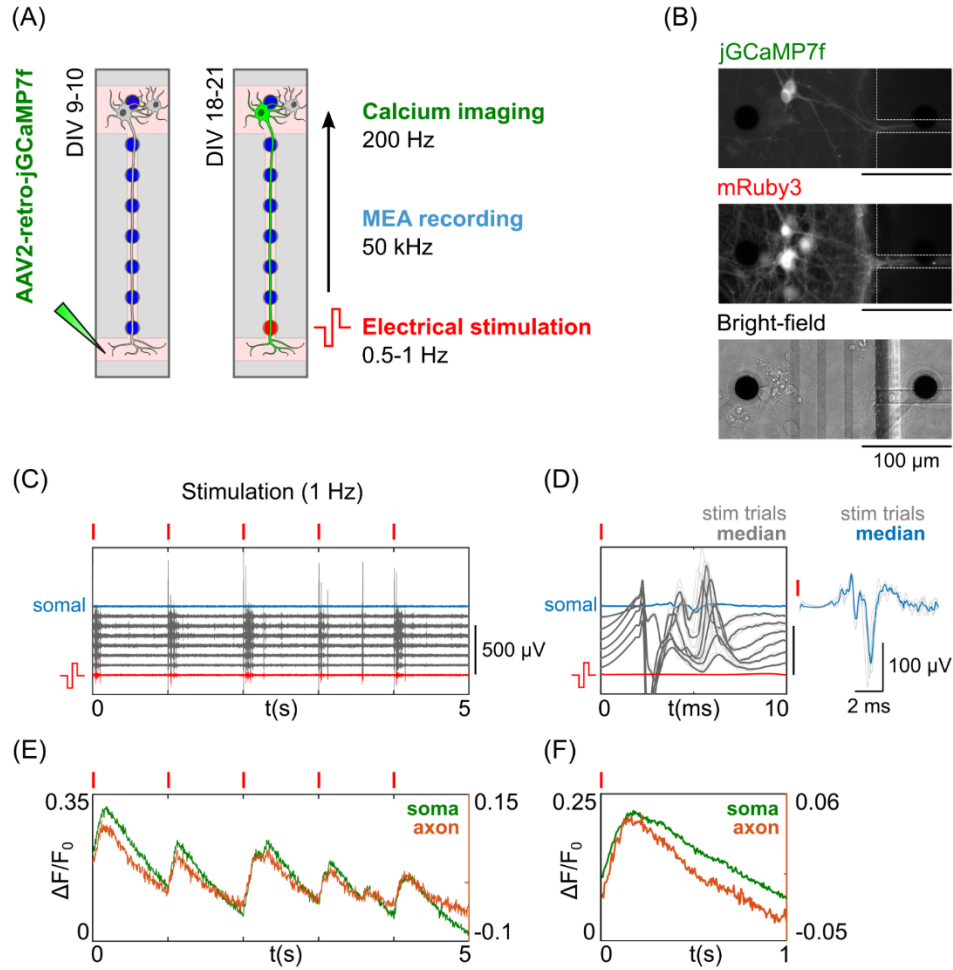


**Figure 4 – Evoked antidromic activity effectively depolarizes the somatodendritic compartment** **(A)** Schematic of the experimental protocol. Hippocampal neurons extending axons to the axonal compartment were retrogradely transduced at 9-10 DIV with the AAV2-retro-jGCaMP7f. This allowed for distal electrical stimulation of the axon, electrophysiological recording, and calcium imaging of the soma at 18-21 DIV. The last electrode within the microchannel was used for evoking antidromic activity (>600  $\mu\text{m}$  away from the soma). **(B)** Fluorescence (jGCaMP7f and mRuby3) and bright-field imaging of transduced neurons at 21 DIV (40 $\times$  objective) (scale bars = 100  $\mu\text{m}$ ). **(C)** Electrophysiological traces of 5s of stimulated activity of the microelectrodes of interest – within the microchannel containing the axon (red and gray) and below the soma (blue). For stimulation, 5 biphasic pulses were delivered at 1Hz (-500/500 mV). Red ticks represent the timing of electrical stimulation. **(D)** Overlay of the 10 ms post-stimulation for the 5 trials (peri-stimulus response). **(E)** Calcium imaging traces of the

soma and proximal axon's responses to the distal axon electrical stimulation in (C-D). **(F)** Average calcium response to the 5 stimulation trials.

### 3.4.4 Antidromic Action potentials Occur After Distal Axotomy

Spontaneous EAP generation has been shown to occur following axonal injury (Pinault, 1995; Stasheff et al., 1993). Here, we studied the effect of axon lesions on the generation of antidromic signaling. Taking advantage of the high fluidic resistance between compartments, we could subject neurons to distal axotomy >700  $\mu\text{m}$  away from their undisturbed somata. This procedure effectively disrupted axonal projections in the axonal compartment, while sparing the axon proper within the microchannel (**Fig. 5A-B**), mimicking the conditions of severe axonal lesions (Shrirao et al., 2018). Both before and following axotomy we recorded the spontaneous axonal activity of hippocampal and DRG cultures (**Fig. 5C**). From now on, we will refer to microchannels in which propagating events were detected as “active microchannels”.

#### *Hippocampal Neurons*

Distal axotomy in hippocampal cultures has been explored in different contexts, including in *in vitro* models for post-traumatic epilepsy (Shrirao et al., 2018), an established complication from traumatic brain injury. Here we studied the electrophysiological effects of distal axotomy in different hippocampal cultures at two stages of maturation: 11 DIV and 19 DIV. Cultures that were subjected to axotomy at 11 DIV ( $n = 2$  independent  $\mu\text{EFs}$ ), exhibited a significant fraction of antidromic activity immediately after axotomy ( $28.3 \pm 1.7\%$ ) (**Fig. 5D**). We observed, nevertheless, a decrease in the number of active microchannels immediately after axotomy (24 to 19), as well as a decrease in the average number of detected propagating events per minute (from 149 to 61). After axotomy the antidromic events are expected to be triggered at the injury site (**Fig. 5B**). Immediately after axotomy, ~37% of the microchannels (7 out of 19) exhibited antidromic activity. This ratio was very similar at 12 DIV (8 out of 19), although the fraction of antidromic events varied greatly (**Fig. 5E**). Hippocampal cultures that were subject to axotomy at DIV 19 ( $n = 3$  independent  $\mu\text{EFs}$ ) showed a tendency to increase the fraction of antidromic activity during maturation. Immediately after axotomy, ~32% of the active microchannels (13 out of 41) exhibited a bidirectional flow and a significant fraction of antidromic activity ( $35.8 \pm 24\%$ ) (**Fig. 5E**). The average number of detected propagating events per minute decreased from 104 to 59, immediately after axotomy.

**DRG Explants**

In sensory neurons *in vivo*, spontaneous EAP generation at the site of axonal injury is an important generator of pathological conditions, such as neuropathic pain (Costigan et al., 2009). However, in acute *ex vivo* whole DRG preparations (after lesion), EAPs are rarely encountered, as activity originates primarily in the soma. Typically, ectopic activity needs to be facilitated by applying K<sup>+</sup> blockers to the recording bath (Amir et al., 2005). Here we studied the effects of distal axotomy on the antidromic initiation of organotypic DRG cultures at 7-8 DIV.

Since most spontaneous axonal activity in DRGs *in vitro* is orthodromic, we analyzed here if ectopic/antidromic activity would emerge after lesion in DRG axon's distal end (**Fig. 5A**). At 7 DIV, DRG cultures exhibited a relevant percentage of antidromic events ( $24.2 \pm 13.7\%$ ,  $n = 5$  independent  $\mu$ EFs) at baseline (pre-axotomy) (**Fig. 5D**). We detected antidromic activity in ~70% (41 out of 59) of the active microchannels. Immediately after axotomy, we observed a great decrease in the average number of detected propagating events per minute (from 460 to 30). We detected a much smaller fraction of antidromic events after axotomy ( $6.7 \pm 5.7\%$ ), which originated from ~28% (10 out of 36) of the active microchannels. Together, these results suggest that, while intact, *in vitro* DRG axons generate and conduct antidromic activity; however, immediately after axotomy, although many injured axons are silent, some antidromic activity occurs. Most probably, this activity is the result of AP initiation at the compromised axonal membrane (**Fig. 5A**). After axotomy, axons may degenerate or, instead, undergo a cytoskeletal reorganization (e.g., axon blebs, neuromas), which affects sodium channel dynamics. This may explain the variability of responses that we observed at DIV 8, when the fraction of antidromic events in the axotomized cultures varied greatly between 0 and ~57% (**Fig. 5D**).

Overall, these results show that EAPs/antidromic activity occur after distal axotomy in both hippocampal and DRG cultures. Interestingly, the two models behaved in opposite ways: DRG explants showed a significant portion of antidromic activity at baseline that decreased after injury, while hippocampal cultures tended to increase the fraction of antidromic activity after injury.

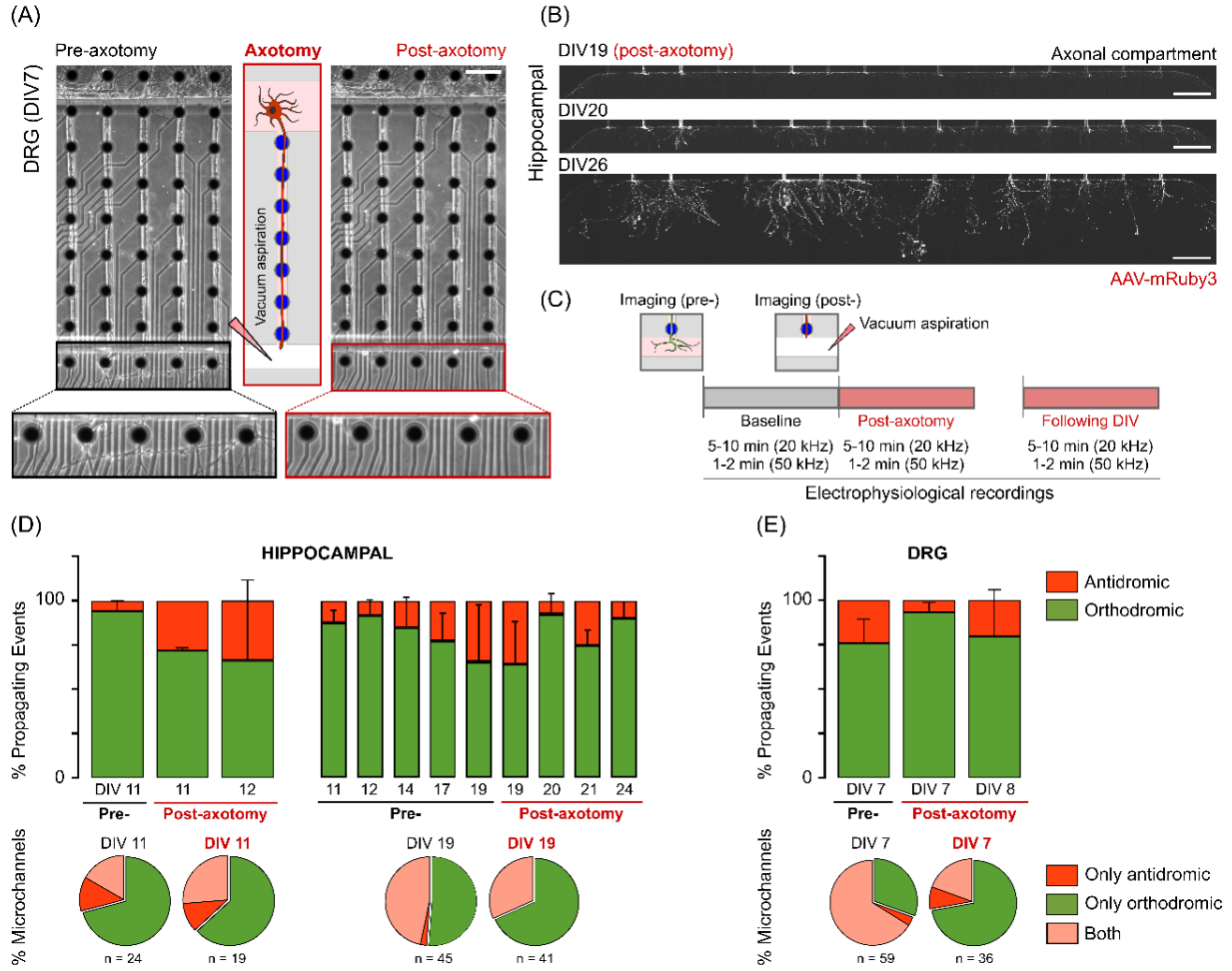


**Figure 5 – Antidromic activity occurs after distal axotomy in hippocampal and dorsal root ganglia (DRG) cultures.** (A) Phase-contrast images (10 $\times$ ) of a DRG culture at 7 DIV immediately before and after distal axotomy. Axotomy via vacuum aspiration (schematized) effectively disrupted the axonal projections in the axonal compartment, while sparing the axon proper within the microchannel and the somal compartment (scale bar = 100  $\mu$ m). (B) Mosaic of fluorescence images (neurons expressing mRuby3) of a hippocampal culture at 19 DIV immediately after axotomy (10 $\times$ ), one day after axotomy (10 $\times$ ), and one week after axotomy (20 $\times$ ) (scale bars = 200  $\mu$ m). (C) Diagram of the experimental protocol. (D) Bar plots show the percentage of orthodromic and antidromic events in hippocampal cultures (n = 2-3 independent  $\mu$ EF) before and after axotomy (11 or 19 DIV). (E) Bar plots show the percentage of orthodromic and antidromic events in DRG cultures (7 DIV) (n = 5 independent  $\mu$ EF) immediately before and after axotomy, as well as in the following day. (D-E) Pie charts show the percentage of active microchannels exhibiting only antidromic, only orthodromic, or in both directions'

propagating events immediately before and after axotomy for hippocampal (11 and 19 DIV) and DRG (7 DIV) cultures.

### 3.4.5 Modulation of DRGs' Antidromic Activity with Osteoclast's Conditioned Medium

Compartmentalized microfluidic chambers are fluidically isolated, thus can be selectively treated with different compounds (Moutaux et al., 2018; Neto et al., 2016). The high fluidic resistance between the somal and axonal compartment help maintain chemical treatments in a defined compartment, especially if a hydrostatic pressure difference is maintained (J. W. Park et al., 2006). Previous studies have shown that osteoclastic activity produces changes in the biochemical microenvironment that activate the nociceptors of the innervating DRG nerve terminals (Hiasa et al., 2017). We took advantage of the  $\mu$ EF's fluidic compartmentalization to selectively stimulate DRG axons with the secretome of osteoclasts cultured in mineralized substrates (active-resorbing osteoclasts) (**Fig. 6A**). We have previously reported that axonal stimulation with osteoclast's CM greatly increases the overall levels of axonal activity of DRG explants at 6-7 DIV (Neto et al., 2020), without assessing conduction direction. Here, we tested if this increase in the level of axonal activity was accompanied by an increase in the fraction of antidromic activity.

At 6 DIV, DRG cultures exhibited a relatively low fraction of antidromic events ( $28.4 \pm 5.9\%$ ,  $n = 3$  independent  $\mu$ EFs). Immediately after distal axonal stimulation with osteoclast's CM, this fraction increased to  $52.8 \pm 13.4\%$ . The following recording time points (3h and 24h post-CM) showed a tendency for this fraction to return to baseline levels, which may be the result of CM's metabolization. At 7 DIV (24h post-CM), the fraction of antidromic events was  $41.1 \pm 13.6\%$  (**Fig. 6B**).

These results indicate that distal axon stimulation with osteoclast's CM can boost the initiation of antidromic activity. Importantly, by modulating antidromic initiation in a more physiologically-relevant model than commonly-used chemical stimulants (e.g., KCl), these results also show that  $\mu$ EFs may be used to study the physiological generation and function of antidromic activity in DRG cultures.

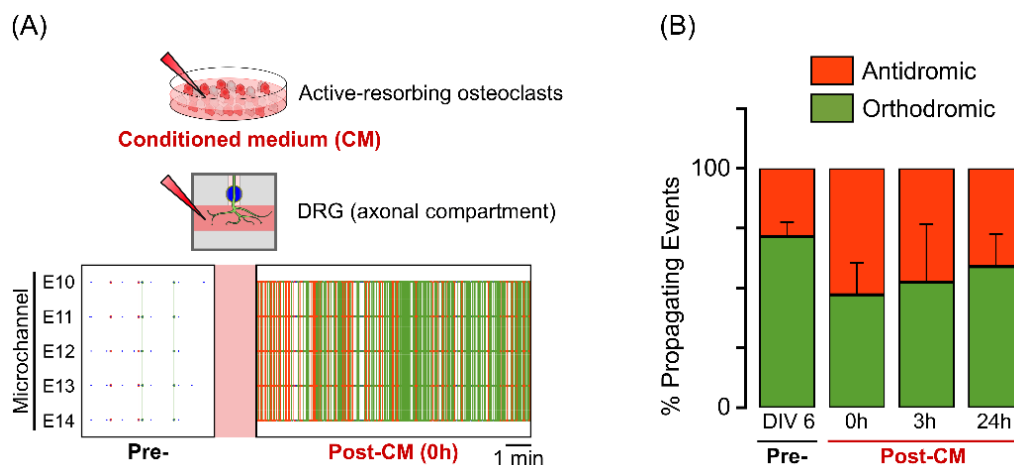


**Figure 6 – Biochemical stimulation of the dorsal root ganglia (DRG) distal axon modulates antidromic activity.** **(A)** Schematic of the experiment of DRG stimulation with osteoclast's conditioned medium (CM). A representative example of the activity of a microchannel pre- and post-exposure to the active-resorbing osteoclasts' CM is shown. **(B)** Bar plot of the percentage of antidromic and orthodromic events in DRG cultures pre- and post-exposure to the CM ( $n = 3$  independent  $\mu$ EFs) at different timepoints (post-0h, post-3h and post-24h).

### 3.4.6 Conduction Velocity is Asymmetric

AP conduction along the axon is a tightly regulated and modulated process (Bucher & Goillard, 2011). Biophysical parameters of the membrane (Waxman, 1980), variations in axon diameter (Chéreau et al., 2017; Goldstein & Rall, 1974), or ion channel densities and kinetics (W. Hu et al., 2009) greatly influence axonal conduction velocity. Here, the high-temporal resolution (20  $\mu$ s) of the  $\mu$ EF recordings allowed for the precise calculation of propagation velocity of each propagating event along the microchannels (details in the Methods section). Thus, propagation velocities along axons were compared between orthodromic and antidromic events.

In hippocampal cultures ( $n = 3$  independent  $\mu$ EFs) we observed a moderate increase in propagation velocity along maturation in both orthodromic and antidromic events (**Fig. 7A-B**). At 11 DIV the average propagation velocity per microchannel was of  $\sim 0.40 \pm 0.06$  m/s (orthodromic) and  $\sim 0.37 \pm 0.03$  m/s (antidromic), while at 24 DIV (after axotomy at 19 DIV) it had increased to  $\sim 0.45 \pm 0.08$  m/s (orthodromic) and  $\sim 0.43 \pm 0.09$  m/s (antidromic). The orthodromic propagating velocity values were very consistent with previous results obtained from unmyelinated hippocampal neurons (Bakkum et al., 2013; Rouhollah Habibey et al., 2017; Yuan et al., 2020). However, antidromic events were generally slower than orthodromic events (**Fig. 7A-B**). This can be observed in the trend of the microchannels' average propagation velocity (**Fig. 7A**) and in the shift in the velocities distributions (**Fig. 7B**). Although, the difference was as large as 21.3% at 19 DIV (immediately after axotomy), in physiological conditions the difference was below 10%. Propagation velocity for both orthodromic and antidromic events was not correlated with the microchannel's MFR (Pearson's correlation,  $p = 0.49$ ,  $p = 0.31$ , respectively), thus was independent of spontaneous firing frequency within the microchannel.

We used the NEURON simulation environment to test the hypothesis if asymmetry in the axon's morphology could explain the observed difference. We implemented models to test two different axon morphologies capable of generating asymmetric electrotonic lengths: continuous axon tapering, and step-decreases in axon diameter at branching points (**Fig. 7C**). We observed that both axon morphologies introduced differences in antidromic and orthodromic conduction velocity, even for mild values of axon diameter reduction after branching or axonal tapering (**Fig. 7D-E**). The velocity difference was as high as 4%, at 50%/mm reduction.

Beyond the well-described tapering in the soma-to-axon proper transition, little is known on how axon diameter changes along its length (Costa et al., 2018). We performed stimulated

emission depletion (STED) microscopy of axons growing along microchannel patterns to understand if the average hippocampal axon diameter could vary along the microchannel length (up to 1 mm). For the unequivocal identification of axons, we relied on specific stainings (Tau antibody) and the presence of periodic (~190 nm) actin rings (**Fig. 7F**), a characteristic cytoskeleton organization (Costa et al., 2020; K. Xu et al., 2013).

Analysis of different axonal segments at 6-7 DIV ( $n = 42$ ) revealed that axon diameter correlated negatively with distance from the entry of the microchannel pattern (Pearson's correlation,  $p = 0.002$ ,  $r = -0.46$ ,  $R^2 = 0.21$ ) (**Fig. 7G**). The linear regression slope represented a 28-43%/mm (95% confidence interval) decrease in diameter. In some cases, we could measure the diameter of both the main axon and its thinner branch (**Fig. 7H**). The reduction in diameter at these branching points ranged from 15% to 53% ( $n = 5$  main axon/branch pairs). In summary, STED analysis confirmed the possibility of tapering levels and/or diameter reduction after branching in the order of 40-50%/mm. Thus, the difference in antidromic and orthodromic conduction velocity may originate, at least partially, from these morphological conditions.

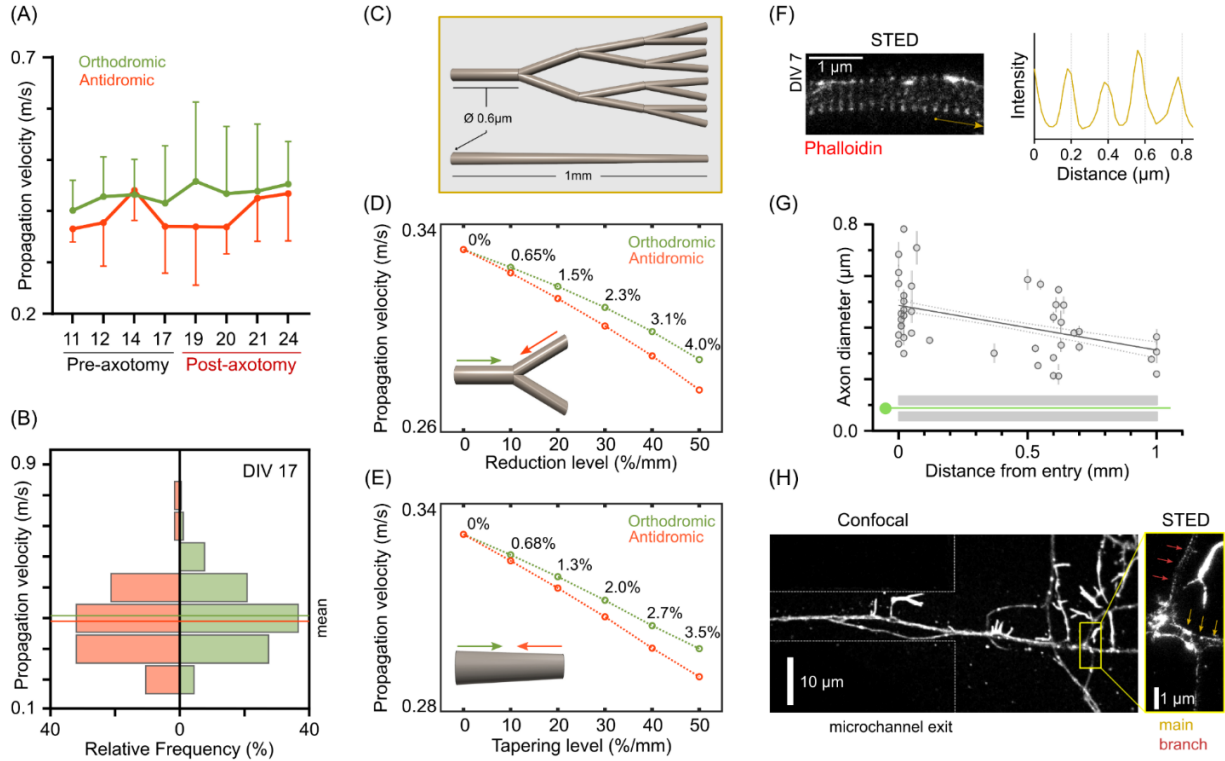


**Figure 7 – Antidromic conduction is slower than orthodromic conduction due to axon morphology.** (A) Mean  $\pm$ SD of the microchannels' median propagation velocity (orthodromic and antidromic). Distal axotomy was performed at 19 DIV ( $n = 3$  independent  $\mu$ EF). Unpaired t-test or Mann-Whitney test,  $*p < 0.05$ . (B) Frequency distribution of the propagation velocity for all orthodromic and antidromic events at 17 DIV (0.1 m/s binning). (C) Asymmetric axon morphologies in the *in silico* models: step-decrease in axon caliber at branching points and continuous axon tapering. (D) Effect of the reduction level (%/mm) in axon caliber at branching points in orthodromic and antidromic propagation velocity. (E) Effect of axon tapering (%/mm) in orthodromic and antidromic propagation velocity. (F) Representative stimulated emission depletion (STED) microscopy image of an axonal segment (labeled with phalloidin 635) and analysis of actin ring periodicity. The intensity profile was plotted after image processing with a 1-pixel radius median filter. (G) Axon diameter in function of distance from the entry of the microchannel ( $n = 42$  axonal segments; from 4 independent experiments) and linear regression. (H) Confocal microscopy image of a microchannel exit with a single axon. Inset shows the corresponding STED image of the main axon and its branch.

### 3.5 Discussion

The characterization and understanding of EAPs/antidromic activity have been hampered by the technical difficulties of performing classic electrophysiology in the very thin mammalian axonal branches. Recently, high-density complementary metal-oxide-semiconductor (CMOS)-based MEAs have been used to follow AP propagation along the axonal arbors of random neuronal cultures (Bakkum et al., 2013; Yuan et al., 2020). However, due to the very low amplitude of the axonal signals, these studies relied on repetitive electrical stimulation of an axonal segment (usually the AIS) to average out noise (event-triggered averaging) and track signal propagation. In this study, we made use of a powerful combination of micro-technologies (MEAs and microfluidics -  $\mu$ EF) to study axonal electrophysiology. This setup allowed us to compartmentalize neuronal cultures and perform spontaneous axonal signal conduction recordings with very high SNR and temporal resolution.

Remarkably,  $\mu$ EF recordings of different mono-culture *in vitro* models revealed the unforeseen presence of antidromic APs. These events could not be explained by returning axons (“U”-turns), nor  $\mu$ EF electric artifacts, and were completely abolished after selectively adding TTX to the axonal compartment. These results support the hypothesis of distal initiation of APs, consistent with EAP/antidromic initiation, in *in vitro* neuronal networks. Importantly, distal electrical stimulation of hippocampal neurons’ axons consistently led to somatodendritic depolarization, which suggests that antidromic activity may affect neuronal function. We observed similar results with DRG explants which, *in vitro*, show very different axonal conduction characteristics than what is expected from afferent sensory neurons *in vivo*. We explored the possible functional roles of this antidromic activity in the pathological context of axonal lesions and physiological changes of the axonal biochemical environment. We showed that antidromic activity occurs after distal axotomy in dissociated hippocampal neurons as well as in DRG explants. Moreover, the antidromic activity could be biochemically stimulated in physiological conditions by modulating the biochemical environment of the DRG neurons’ axon terminals with osteoclasts’ CM. Finally, we showed that antidromic conduction is consistently slower than orthodromic and that this difference may be explained by axonal morphologies that lead to slight electrotonic length asymmetries.

To date, most studies using  $\mu$ EFs that addressed axonal function have employed dual-compartment (or co-culture) neuronal cultures of CNS neurons, where signal transmission was assumed to travel orthodromically from the supposed compartment of origin (Gladkov et al.,

2017; Moutaux et al., 2018; Pan et al., 2014). Moreover, in the few studies where neurons were seeded only in one compartment, the propagating event detection methods presumed orthodromic propagation from the somal to the axonal compartment (forward propagation) (Rouhollah Habibey et al., 2017; Lewandowska et al., 2016). It is important to note that no study has previously attempted to characterize the signal conduction of DRG cultures (Black et al., 2019). Still, preliminary *in vitro* experiments using DRGs had suggested that most APs propagate orthodromically (Heiney et al., 2019). Our data shows clearly that bidirectional axonal conduction (EAP initiation/antidromic conduction in particular) must be considered when analyzing functional data from both hippocampal and DRG cultures.

Regarding potential functional roles in physiological states, EAP generation at the distal portions of hippocampal neurons' axons has been reported in studies using *ex vivo* and *in vivo* models, particularly during sharp-wave ripple complexes (Bähner et al., 2011; Bukalo et al., 2013; Chorev & Brecht, 2012; Dugladze et al., 2012; M. E. J. Sheffield et al., 2011). Interestingly, EAP generation is susceptible to conventional synaptic modulation, as somatic excitatory or inhibitory input can facilitate or suppress EAP generation, respectively (Thome et al., 2018). Still, it is not understood in which conditions can EAPs depolarize the soma and have physiological functions. *Ex vivo* studies have shown that backpropagation of EAPs during gamma oscillations can be inhibited by axo-axonic interneurons that target the AIS of CA3 hippocampal neurons (Dugladze et al., 2012). Yet, antidromic activity of CA1 hippocampal axons has been shown to reduce synaptic strength and lead to a widespread downscaling of upstream synaptic weights. Conversely, subsequent synaptic stimulation led to long-lasting synaptic potentiation (Bukalo et al., 2013). More recently, the same authors associated antidromic activity with a rapid downregulation of brain-derived neurotrophic factor (BDNF) mRNA levels (Bukalo et al., 2016), a protein critically involved in canonical forms of synaptic plasticity. Ultimately, these studies suggest that orthodromic and antidromic activity may differentially regulate synaptic plasticity and gene expression. Here, we have shown that EAP generation/antidromic conduction spontaneously occurs in hippocampal cultures. Moreover, we confirmed that evoked antidromic APs consistently lead to somatodendritic depolarization. Given the non-invasive nature of our setup, future studies may assess what is the short- and long-term impact of antidromic APs (spontaneous or elicited) at single-cell and/or network level.

We have also explored the effects of distal axotomy in hippocampal neurons, as in a model for post-traumatic epilepsy (Shrirao et al., 2018), and found that EAP/antidromic activity occurs after axonal lesion. This is in line with previous studies that have shown that, in pathological

conditions, EAPs occur during epileptic seizures (Bucher & Goaillard, 2011; Gutnick & Prince, 1972; Stasheff et al., 1993). An important follow-up to our study is the confirmation of the source of the observed antidromic activity in both physiological and pathological conditions. Possibly, in the context of a neuronal network, not all antidromic activity can be traced back to a single cause but results of a combination of mechanisms. Further analysis are required to unveil the mechanisms behind AP triggering at the distal axons.

It is not clear if EAPs are as prevalent in CNS neurons *in vivo* as in our *in vitro* conditions, especially in the case of myelinated axons. For instance, myelinated fibers may have evolved mechanistic responses at the nodes of Ranvier that prevent EAP initiation and propagation, as recently suggested (Brohawn et al., 2019). Beyond increasing conduction velocity, myelin may also limit hyper-excitability. In brain slices of mice with cuprizone-induced myelin loss, demyelinated L5 pyramidal neurons were intrinsically more excitable and around 15% exhibited EAP generation. In the study, local application of TTX or K<sup>+</sup> was sufficient to eliminate or evoke EAPs, respectively, providing compelling evidence for the hypothesis that EAPs may arise from the integration of local environment signals by unmyelinated segments of the axon (M. S. Hamada & Kole, 2015). Furthermore, due to the embryonic tissue of origin, our *in vitro* models lack the high prevalence of glial cells observed *in vivo*. Glial cells are known to be key players in the regulation of neuronal excitability, including AP initiation and propagation (Cserép et al., 2021; Micu et al., 2018; Sasaki et al., 2011). We cannot exclude, therefore, the possibility for an increased prevalence of EAPs when a reduced number of glial cells is present, and the unmyelinated axons extend in a pure axonal compartment.

Most DRG neurons (particularly nociceptive C-fibers) are unmyelinated, however, so far, the study of their axonal physiology has been very limited, as most of our knowledge comes from experiments with myelinated fibers due to their easier accessibility (Black et al., 2019; Nascimento et al., 2018). Here, to the best of our knowledge, DRGs were employed in compartmentalized cultures over MEAs, and selectively manipulated (mechanically and chemically), for the first time. Related studies have obtained functional readouts via calcium imaging or patch-clamp (Huval et al., 2015; Tsantoulas et al., 2013), though these techniques do not have the desirable temporal or spatial resolution, respectively, for assessing axonal conduction dynamics. Tsantoulas and co-workers, in particular, had previously demonstrated somal depolarization in compartmentalized cultures of dissociated DRG neurons after chemical (capsaicin and KCl) or electrical stimulation of the axonal compartment (Tsantoulas et al.,

2013). Here, we show that organotypic DRG cultures spontaneously generate APs distally and propagate antidromically both before and after injury, hence recapitulating *in vivo* mechanisms.

Injured sensory neurons exacerbate ectopic activity *in vivo*, a mechanism thought to be an originator of neuropathic pain (Costigan et al., 2009). Here, DRGs' spontaneous electrical activity and fraction of ectopic activity were diminished immediately after axotomy. It is important to note that silencing following peripheral injury also occurs *in vivo* and it has been proposed as a necessary trigger for axon regeneration (Enes et al., 2010). Likewise, in acute *ex vivo* preparations, EAPs are rarely encountered after lesion, as APs originate primarily in the soma (Amir et al., 2005). Still, the short- and long-term effects of axotomy in DRG axonal function should be the subject of further research, and future *in vitro* studies should explore ways of better mimicking the post-lesion axon environment. Importantly, the antidromic activity could be modulated via distal axon stimulation with osteoclasts' CM, a physiologically-relevant model of the innervated bone microenvironment (Hiasa et al., 2017; Neto et al., 2020). The results using DRG explants reinforce the potential of using  $\mu$ EFs as a powerful tool for preclinical testing. Due to their versatility,  $\mu$ EFs could help elucidate conduction dynamics in physiological and pathological conditions.

Further characterization of the bidirectional signal conduction with high-temporal resolution recordings revealed an asymmetry in conduction velocity. This difference could be replicated in computational models of two different morphologies that introduce an asymmetry in axon diameter: axon tapering and diameter reduction at branching points (mimicking propagation into/from higher-order small-diameter collaterals). STED imaging analysis confirmed the occurrence of ~36%/mm reductions in average axon diameter, or up to ~50% at branching points. Due to the inherent difficulties in assuring axonal identity along the full microchannel length (up to 1 mm), we cannot currently ascertain if this decrease in average diameter is due to axon tapering or branching alone. Moreover, it is not clear if the asymmetry in conduction velocity - which is only dependent on the direction of propagation - has functional implications *per se*.

Importantly, axonal branching has been shown to introduce axonal delays with functional implications, since the main axon temporal activity pattern transforms into multiple patterns in its varying -length and -diameter branches (reviewed in (Debanne et al., 2011)). Concomitantly, related *in vitro* studies have found marked differences (as high as 5-fold) in orthodromic conduction velocity along the length of unmyelinated axon arbors, presumably due to diameter inhomogeneities (Bakkum et al., 2013; Rouhollah Habibey et al., 2017; Yuan et al., 2020).

Here, we reconcile these studies with experimental evidence for axon diameter reduction along the length of microchannel patterns.

Taken together, our results show that EAPs/antidromic conduction occur in *in vitro* models of hippocampal and DRG neurons. Several studies have now tried to impose unidirectional outgrowth of axons via complex physical/chemical patterning (reviewed in (Aebbersold et al., 2016; Holloway et al., 2021)). Our study suggests that unidirectional axonal outgrowth may not necessarily lead to unidirectional information flow, a finding with important implications for the “brain-on-chip” field. It remains to be shown if these reported mechanisms hold for *in vivo* conditions, but with *in vitro* models being used extensively in conditions where network dynamics play an important role (e.g., plasticity, neuronal circuits), acknowledging the prevalence of these antidromic APs is of fundamental importance.

### 3.6 Experimental Section

#### 3.6.1 Microfluidic Design and Fabrication

The polydimethylsiloxane (PDMS) microfluidic chambers used in this study followed a design reported on our previous publications (Heiney et al., 2019; Lopes et al., 2018), with minor optimizations regarding the number of microchannels, as well as their length and width. The number of microchannels was reduced to match exactly the number of microelectrode columns (16 microchannels in total). The microchannel width was reduced to 10  $\mu\text{m}$  to isolate fewer axons per microchannel, thus decreasing the complexity of the recorded signals. Moreover, the microchannel length was set to 700  $\mu\text{m}$  to selectively probe axonal function, as microchannels must be 450  $\mu\text{m}$  or greater in length to restrict the axonal compartment neurite access to axons only (Neto et al., 2016; J. W. Park et al., 2006). Concisely, the microfluidic chambers were composed of two separate compartments (somal and axonal) interconnected by 16 microchannels with 700  $\mu\text{m}$  length  $\times$  10  $\mu\text{m}$  height  $\times$  10  $\mu\text{m}$  width dimensions and interspaced by 100  $\mu\text{m}$ . In specific imaging experiments, chambers with longer microchannels (1000  $\mu\text{m}$  length) and 200  $\mu\text{m}$  spacing were also used.

From the microfabricated SU-8 mold, the PDMS microfluidic chambers were produced by replica molding. PDMS was prepared using a 10:1 mix of silicone elastomer and its curing agent (Sylgard 184, Dow Corning) and degassed using a vacuum desiccator. Polymerization was achieved at 70  $^{\circ}\text{C}$  for 3 h, after which the PDMS microfluidic chambers were unmolded and cut. The medium reservoirs were manually punched with a steel biopsy punch ( $\varnothing$  6 mm). Microfluidic chambers used for cultures with DRG explants were adapted by adding an extra smaller reservoir ( $\varnothing$  3 mm), which allowed the seeding of the DRG in a central position, closer to the microchannels (as in (Neto et al., 2014, 2020)).

#### 3.6.2 $\mu\text{EF}$ Preparation

$\mu\text{EFs}$  were prepared as previously detailed (Lopes et al., 2018). Briefly, planar MEAs (Multi Channel Systems (MCS), Germany) of 252 titanium nitride recording microelectrodes (30  $\mu\text{m}$  in diameter) and 4 internal reference electrodes (organized in a 16 by 16 square grid) were air plasma-cleaned for 2 min. Then, both the MEAs and the microfluidic chambers were briefly submerged in 70% ethanol, allowed to air-dry inside a laminar flow hood, and sterilized by ultraviolet (UV) light exposure.  $\mu\text{EF}$  assembly was guided by a stereomicroscope, to correctly

align the microchannels with the microelectrode grid. The  $\mu$ EFs were then sequentially coated with poly-D-lysine (PDL) (20  $\mu$ g/ml) and laminin (5  $\mu$ g/ml) to promote cell adhesion. Each microchannel encompassed 7 microelectrodes, as these were interspaced by 100  $\mu$ m (the first and last microelectrodes were at 50  $\mu$ m of the microchannel entry and exit point, respectively). Thin MEAs (tMEAs) with 200  $\mu$ m interspacing were used in calcium imaging experiments, due to their compatibility with high-magnification objectives. When using tMEAs, longer microchannels (1000  $\mu$ m length) with appropriate spacing were used to encompass 5 microelectrodes.

### 3.6.3 Cell Culture

Experimental procedures involving animals were carried out following current Portuguese laws on Animal Care (DL 113/2013) and the European Union Directive (2010/63/EU) on the protection of animals used for experimental and other scientific purposes. The experimental protocol (reference 0421/000/000/2017) was approved by the ethics committee of the Portuguese official authority on animal welfare and experimentation (Direção-Geral de Alimentação e Veterinária). All possible efforts were made to minimize the number of animals and their suffering.

Primary embryonic rat hippocampal neurons were isolated from Wistar rat embryos (E18). Tissues were dissected in Hank's Balanced Salt Solution (HBSS) and enzymatically digested in 0.6% (w/v) trypsin (1:250) in HBSS for 15 min at 37 °C. Then, trypsin was inactivated with culture medium containing 10% fetal bovine serum and washed away. Tissue fragments were mechanically dissociated with a plastic pipette and the cells' suspension was filtered with a 40  $\mu$ m strainer (Falcon) to exclude remaining tissue clumps. After cell counting, 150k viable cells suspended in 5  $\mu$ l were seeded in the somal compartment of the  $\mu$ EF. Cells were cultured in Neurobasal Plus medium supplemented with 0.5 mM glutamine, 2% (v/v) B27 Plus, and 1% (v/v) penicillin/streptomycin (P/S). For stimulated emission depletion (STED) experiments, 75k viable cells were seeded on microfluidic chambers (with 700 or 1000  $\mu$ m-long microchannels) assembled on 22  $\times$  22 mm glass coverslips (#1.5 thickness, Corning). These microfluidic chambers were peeled-off at 1 DIV and neurons were allowed to grow along the coated patterns (i.e., microchannels patterns).

Primary embryonic mouse DRG explants were isolated from wild-type C57BL/6 mice embryos (E16.5). Lumbar DRG explants were removed and placed in HBSS until use. A single DRG

explant was seeded in the somal compartment of each prepared  $\mu$ EF. Cells were cultured in Neurobasal medium supplemented with 0.5 mM glutamine, 2% (v/v) B27, 50 ng/ml of NGF 7S (Calbiochem), and 1% (v/v) (P/S).

For the experiments which involved modulation of the DRG's distal axon biochemical environment, conditioned medium was obtained from bone resorbing osteoclasts. Bone resorbing osteoclasts were obtained via mouse bone marrow cells flushing. Pre-osteoclasts were obtained after 3 days of stimulation with macrophage colony-stimulating factor (M-CSF 30 ng/mL, PeproTech). Adherent cells were then detached and seeded on top of bone slices (boneslices.com, Denmark) in the presence of 30 ng/mL M-CSF and 100 ng/mL receptor activator of nuclear factor kappa-B ligand (RANKL, PeproTech) (Sousa et al., 2016). After 4 DIV, resorbing osteoclasts' secretome was collected, centrifuged at 140 g, 4°C, 5 min, and stored at -80°C before use.

All cultures were kept in a humidified incubator at 37 °C supplied with 5% CO<sub>2</sub>.

### 3.6.4 Viral Transductions

Transductions with adeno-associated viruses (AAVs) were performed to live-image neuronal morphology, axonal outgrowth and calcium imaging. For neuronal morphology, ssAAV-1/2-hCMV-chl-EGFP-WPRE-SV40p(A) ( $8.3 \times 10^{12}$  vg/ml titer) or scAAV-DJ/2-hSyn1-chl-loxP-mRuby3-loxPSV40p(A) ( $7.2 \times 10^{12}$  vg/ml titer) were added to the somal compartment (0.3  $\mu$ l per  $\mu$ EF at DIV 1-5). For performing calcium imaging of neurons extending to the axonal compartment, ssAAV-retro/2-hSyn1-chl-jGCaMP7f-WPRESV40p(A) ( $5.2 \times 10^{12}$  vg/ml titer) was selectively added to the axonal compartment (0.5  $\mu$ l per  $\mu$ EF at 9-10 DIV).

All viral vectors were produced by the Viral Vector Facility of the Neuroscience Center Zurich (Zentrum für Neurowissenschaften Zürich, ZNZ, Switzerland).

### 3.6.5 Electrophysiological Recording

DRG explants at 6-11 DIV and hippocampal neurons at 11-25 DIV were used in the electrophysiology experiments. Recording sessions started after 5 minutes of adjustment to recording conditions. Electrophysiological recordings of spontaneous electrical activity were obtained at a sampling rate of 20 or 50 kHz for 5-10 or 1-2 minutes, respectively, unless otherwise specified. All recordings were obtained using a commercial MEA2100-256 system

(Multichannel Systems MCS, Germany). Temperature was maintained at 37 °C by an external temperature controller. For long-term experiments (e.g., axonal activity modulation experiments), and whenever imaging was performed concurrently, recordings were performed with the system mounted on an incubated (37 °C) inverted widefield microscope (Axiovert 200M, Zeiss or Eclipse Ti2-E, Nikon) stage supplied with 5% CO<sub>2</sub>.

### 3.6.6 Axonal Electrical Stimulation and Calcium Imaging

Calcium imaging experiments were performed with hippocampal neurons at 18-21 DIV (at least one week post-transduction with AAV2-retro-jGCaMP7f). Images were acquired by a sCMOS camera Prime 95B, 22mm (Teledyne Photometrics, UK), mounted on a Nikon Eclipse Ti2-E (Nikon, Japan) inverted microscope with a Nikon PI Apo 10X/0.4NA, a Nikon PI Apo 20X/0.75NA, or a Nikon PI Apo 40X/1.15NA objective. Image acquisition was performed using Micromanager (Version 1.4) at 200 Hz (5 ms exposure), which allowed for the temporal discrimination of soma depolarizations in response to single electrical pulse stimulations. Electrical stimulations were performed using the MEA2100-256 system's (MCS, Germany) internal stimulator. Per trial, 5 biphasic voltage pulses (-500/500 to -1000/1000 mV, 100  $\mu$ s per phase) were delivered to the last microelectrode within a microchannel at 0.5 or 1 Hz. To synchronize electrical stimulation, recording, and fast image acquisition, the whole setup was triggered via a transistor-transistor logic (TTL) signal sent at the start of the MEA recording/stimulation protocol.

The resulting videos were median-filtered, regions of interest (i.e., somas, axons) were delineated manually and  $\Delta F/F_0$  traces were calculated in ImageJ using custom macros.  $\Delta F/F$  traces were exported for analysis in MATLAB 2018a (The Mathworks, Inc., USA).

### 3.6.7 Axonal Activity Modulation

Distal axotomy was performed as previously described (J. W. Park et al., 2006). After a baseline recording, the medium from the axonal compartment was removed and stored for future use. Then, a pipette tip was placed at the entrance of the main channel and vacuum suction was applied. Axons were severed by the resulting air bubble that passed through the main channel. Then, the stored culture medium was returned to the axonal compartment. Axotomy was confirmed by imaging the whole culture pre- and post-axotomy.

For the selective blocking of activity, a medium pre-mixed with 1  $\mu$ M TTX, a potent fast voltage-gated sodium channels blocker, was added to the desired  $\mu$ EF compartment after removing and storing the original medium. A hydrostatic pressure difference was used to impair the flow of TTX between compartments. In the same recording session, we performed recordings before adding TTX (baseline), after adding to the axonal compartment, and after adding to the somal compartment. At the end of the recording session, the exposed compartments were washed-out with three rounds of fresh medium replenishment and then allowed to equilibrate in the stored medium. A final recovery recording was performed on the following day.

Axonal stimulation through changes in the biochemical environment was tested in DRG cultures. For the modulation of the axon terminals' biochemical environment, osteoclast's conditioned medium (CM) was selectively applied to the axonal compartment as in (Neto et al., 2020). First, a baseline recording of DRG cultures at DIV6 was obtained. Afterward, the medium from the axonal compartment was gently aspirated and replaced by 100  $\mu$ l of osteoclast's CM. Post-treatment (0h) recordings (20-30 minutes) were started as soon as the baseline stabilized following liquid flow perturbation (less than 1 minute). Two post-treatment recordings (3h and 24h post-treatment) were performed additionally.

In all experiments, cultures were not moved out of the MEA2100-256 system during the experimental protocol of the day.

### 3.6.8 Immunolabeling

Hippocampal neurons were fixed at 6-7 DIV for STED imaging. Half the media was carefully aspirated and replaced by 4% PFA (2% final concentration) for 20 min at room temperature (RT). Then, the fixative was washed-out with three rounds of PBS 1 $\times$  and the fixed cells were permeabilized with 0.1% (v/v) triton X-100 (in PBS) for 5 min and autofluorescence was quenched with 0.2M ammonium chloride (NH<sub>4</sub>Cl, Merck, cat# 1.01145.0500). Non-specific labeling was blocked by incubation with blocking buffer (5% FBS in PBS 1 $\times$ ) for 1 h. Rabbit anti-Tau (GeneTex, cat# GTX130462, 1:1000) primary antibody diluted in blocking buffer was incubated for 1h at RT. After three washes with PBS 1 $\times$ , incubation with secondary antibody (anti-rabbit Alexa Fluor® 488, Molecular Probes®, Thermo Fisher Scientific, 1:500) and 0.3  $\mu$ M phalloidin 635P (cat# 2-0205-002-5, Abberior GmbH) for actin staining, was performed for 1 h at RT. After three washes with PBS 1 $\times$ , coverslips were mounted in 80% glycerol and sealed.

### 3.6.9 Stimulated Emission Depletion (STED) Imaging and Analysis

STED imaging was performed in an Abberior Instrument 'Expert Line' gated-STED coupled to a Nikon Ti microscope with an oil-immersion 60x 1.4NA Plan-Apo objective (Nikon, Lambda Series) and a pinhole size set at 0.8 Airy units. The system features 40 MHz modulated excitation (405, 488, 560 and 640nm) and depletion (775nm) lasers. The microscope's detectors are avalanche photodiode detectors (APDs) which were used to gate the detection between ~700ps and 8ns. Typically, STED images were obtained near the entrance and exit of the microchannel patterns. After STED imaging, microchannel regions were fully imaged in a widefield microscope (20× objective) for mapping of the culture topology. This allowed for the precise measure of the STED image localization, in relation to the microchannel length. Axons were identified based on the Tau specific staining and the presence of periodic actin rings within the membrane periodic skeleton (MPS). The diameter of axons focused on the maximum wide plan was measured manually. Per axon, at least 5 measures were acquired perpendicularly to the longitudinal axon axis by connecting the brighter outer pixels (most often actin rings).

### 3.6.10 Action Potential Detection and Propagation Characterization

Raw signals were band-pass filtered (200-3000 Hz) and analyzed offline using custom MATLAB scripts. APs were detected by a threshold method set to 4.5-6× (DRG experiments) or 6× (hippocampal experiments) the standard deviation (SD) of the peak-to-peak electrode noise. An AP time was extracted at this surpassing point and no detection was considered for the next 2 ms ("dead time"). Events propagating along a microchannel were identified based on the extracted AP times. Propagation sequence identification and propagation velocity calculation were performed as previously reported (Costa et al., 2020) and the scripts are available in GitHub at:

[https://github.com/paulodecastroaguiar/Calculate\\_AP\\_velocities\\_in\\_MEAs](https://github.com/paulodecastroaguiar/Calculate_AP_velocities_in_MEAs).

For the hippocampal culture experiments, a propagating event had to fulfill the following requirements: event detected over the entire microchannel (7 microelectrodes); time delay between electrode pairs lower than or equal to 1 ms (minimum propagation velocity of 0.1 m/s); each AP time isolated, with no neighboring APs in a 4 ms time window. For the DRG culture experiments, due to the decrease in signal-to-noise ratio (SNR) at the extremities of the microchannels, we only considered the 5 inner electrodes of the microchannels for the forward/backward events ratios. The remaining requirements were kept the same. This

stringent detection method profoundly reduced the number of possible propagating events, as it eliminated any ambiguity during bursts and excluded sequences with missing AP times on at least one microelectrode (**Supplementary Fig. S1**). Due to the very high firing frequency observed during bursts, we consider interpretations from such instances as unclear: during bursts, it is very challenging to track specific APs (identity is lost); given the short inter-spike intervals in a burst, the conduction direction can be easily misperceived as being antidromic if the signal delay between electrodes is in the same order of magnitude as the inter-spike intervals (in an electrophysiology equivalent of the stroboscopic effect).

For the propagation velocity calculations, the extracted AP times were further corrected based on the voltage waveforms. Each AP time, originally identified by the threshold method, was subject to a post-detection time correction (within a limited 1 ms window), allowing the AP time to assume the instant of the maximum absolute voltage of the signal trace. The corrected AP times ensured that the propagation velocity was calculated based on the reference APs' maximum absolute voltage (instead of the instant that the voltage profile crossed the threshold line). Propagation velocities per event were then calculated by dividing the first-to-last electrode distance (600  $\mu\text{m}$  span) by the delay between AP times of the two electrodes (the first and last electrodes in the detected sequence).

Analysis of possible temporal correlations between AP times in different microchannels was carried out using a method very similar to the calculation of peristimulus time histograms. To assess the time dependence between antidromic APs in a particular microchannel (here called "events") with the APs in all other microchannels, histograms of the time delays between each event and all APs times were calculated. The AP times were all obtained from a predefined reference electrode (the middle microelectrode) in each microchannel, and each histogram (one per microchannel) was calculated in a limited causal time window of 10 ms. Presumed antidromic APs consistently preceded by an AP in another microchannel would lead, using this method, to a pronounced peak in the histogram centered at the typical time delay between both.

### **3.6.11 Simulations of Conduction Velocity in Different Axonal Morphologies**

Analysis of potential causes for asymmetric AP conduction was carried out in NEURON simulation environment (Hines & Carnevale, 1997) using a detailed biophysical model of an axon. The Hodgkin-Huxley formalism was used to describe ion conductances in the axon.

Three currents were modeled: fast sodium and rectifying potassium currents responsible for action potentials in hippocampal neurons (Roger D Traub & Miles, 1991), and a leakage current supporting the resting potential. Default (original) parameters were used with the exception of: axial resistance  $R_a = 150 \, \Omega \cdot \text{cm}$ , leakage conductance  $g_L = 0.1 \, \text{mS}/\text{cm}^2$ , sodium conductance  $g_{\text{Na}} = 0.1 \, \text{S}/\text{cm}^2$ , and potassium conductance  $g_K = 0.1 \, \text{S}/\text{cm}^2$ . Simulations were carried out assuming a temperature of  $37 \, ^\circ\text{C}$ . Two distinct overall morphologies were considered. In the first, the axon was modeled as a cylindrical structure with a length of 1 mm and a diameter of  $0.6 \, \mu\text{m}$ , with a spatial grid of  $10 \, \mu\text{m}$  (100 segments). Different diameter tapering levels were studied by keeping the somal end at  $0.6 \, \mu\text{m}$  and varying the diameter at the axonal terminal side. Tapering was quantified as the percentage of reduction in diameter in 1 mm distance. In the second morphology, branching was considered. The axon was still modeled as a cylindrical structure but now branching every  $250 \, \mu\text{m}$  for a full total length of 1 mm on each of the 8 branches. After each branch node the axon diameter was allowed to be reduced. As with tapering, this reduction quantified as the percentage of reduction in diameter in 1 mm distance (%/mm). In both morphologies, conduction velocity was calculated for both propagation directions by providing stimulation (at rheobase level, for 1 ms) at either axonal end.

### 3.6.12 Finite-Element Modeling of the Electrical Potential Inside the Microchannels

The tridimensional (3D) finite element model (FEM) geometry replicating the  $\mu\text{EF}$  microchannels, was constructed with SOLIDWORKS software (v. 2018, Dassault Systemes SolidWorks Corporation, France). The dimensions' details for all components of the model are available in **Supplementary Table 1**. Finite element analysis was performed with the AC/DC module of the COMSOL Multiphysics software (v. 5.2a, Stockholm, Sweden). The Electric Current (ec) physics interface was selected, considering a transient time-dependent study. A 3D model physics-controlled mesh was also generated in COMSOL for the constructed MEA 3D geometry model, with the extremely fine mesh option. This model is composed of thirteen different domains, whose description, number and electrical properties are available in **Supplementary Table 2**. Electrical boundary conditions were added to the model: two ground conditions at each of the culture medium domain extremities, and an electric potential boundary condition added to each of the axons' surfaces. The axon's boundary condition served the purpose of recreating, in global terms, the biphasic profile observed in extracellular recordings. The derivative of a Gaussian function was used here as the biphasic profile. Instead of

stationary, the center of the Gaussian function in the axon's boundary condition was made to depend on time, introducing a wave motion that propagates the entire axon length.

Two different studies were carried, each corresponding to the AP traveling across one of the two axons. Domain probes were added to all of the electrodes to gather the predicted average electric potential in each time-step for each study solution. The direct solver NUMPS was used for both studies.

### 3.6.13 Statistical Analysis

Electrodes with a mean firing rate (MFR) of at least 0.1 Hz were considered as “active electrodes”. We defined as “active microchannels” those that had at least one detected propagating event per recording. In the stringent conditions of our conduction detection algorithm, propagating events require consistent readouts in all microelectrodes in the microchannel. Consequently, it is important to note that the number of detected propagating events per microchannel did not necessarily correlate with the firing rate. Moreover, the propagating event detection method excluded most APs within bursts (**Supplementary Fig. S1**), as these could lead to ambiguous detections of propagation direction. As the total number of detected propagating events could vary greatly across days within the same microchannel/ $\mu$ EF (although their direction flow was generally maintained), we opted for characterizing the ratio of antidromic/orthodromic activity in relative fractions for the analyses of the axotomy and chemical blocking/stimulation experiments. Statistical significance was considered for  $p < 0.05$ . All statistical data is presented as mean  $\pm$  SD, unless otherwise specified.

### 3.7 Supplementary Materials

#### 3.7.1 Supplementary Figures

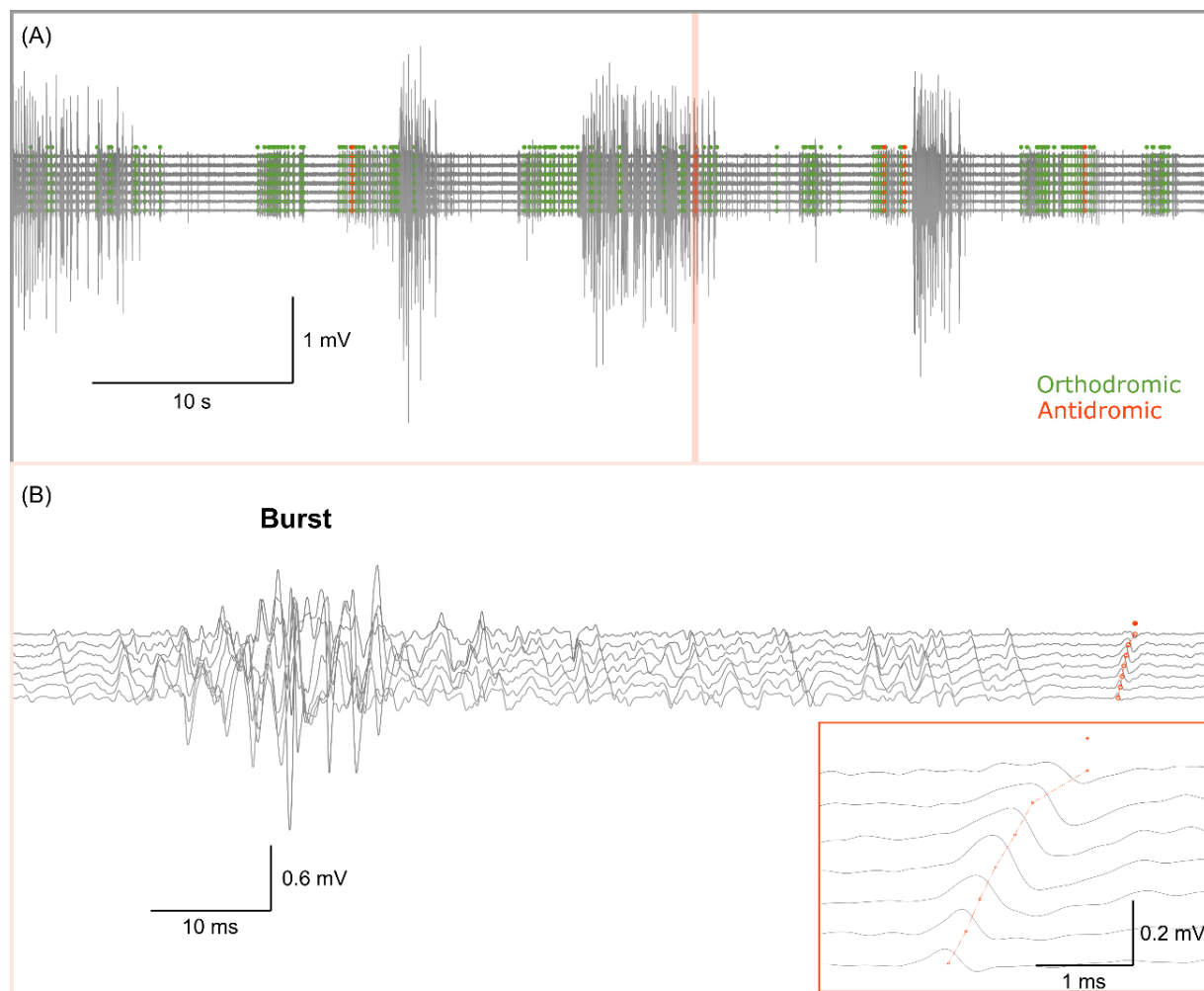


**Figure S1 – (A)** Traces of 60 seconds of activity within a microchannel of a hippocampal culture at 19 DIV. Note the extracellular activity in the mV range. **(B)** Zoom-in of 100 ms of activity. Due to the stringent detection methods, propagating events are detected outside bursting activity. Inset shows the single detected propagating event (antidromic).

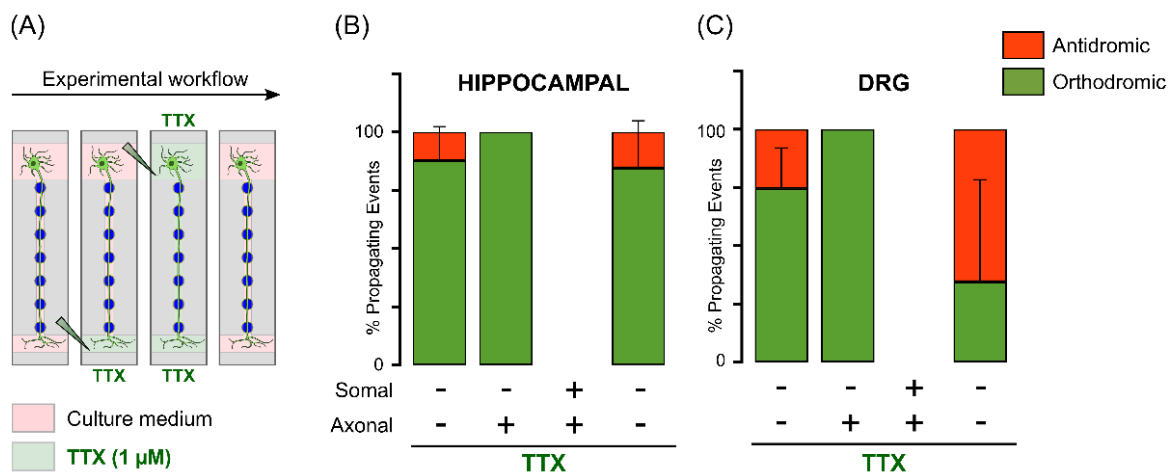


**Figure S2 – Antidromic activity completely ceases after selective application of tetrodotoxin (TTX).** (A) Schematic of the experimental workflow for TTX experiments. After a baseline recording, TTX-containing medium is sequentially added to the axonal and somal compartments. After wash-out, a recovery recording is performed on the next day. (B-C) Bar plots of the percentage of antidromic and orthodromic propagating events in dorsal root ganglia (DRG) ( $n = 2$  independent  $\mu$ EFs at 7 DIV) and hippocampal cultures ( $n = 4$  independent  $\mu$ EFs at 11 or 17 DIV).

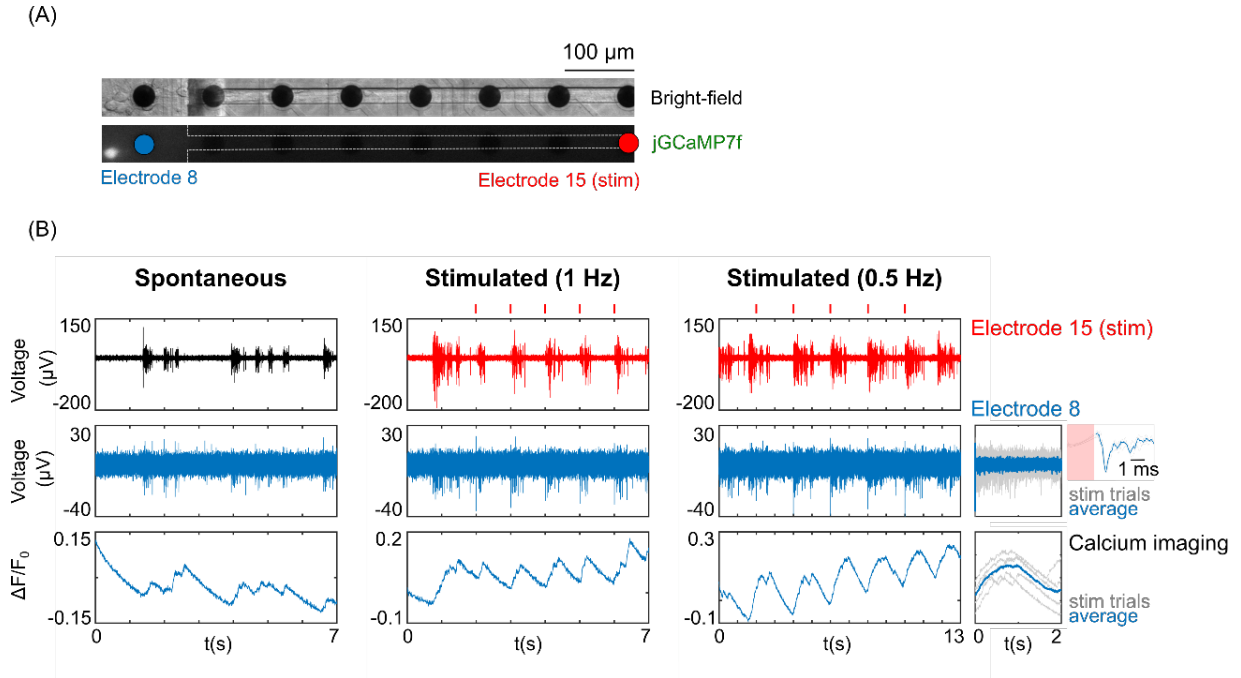


**Figure S3 – (A)** Bright-field and fluorescence imaging (jGCaMP7f) of a transduced neuron (10 $\times$  objective). The last electrode within the microchannel (electrode 15) was used for eliciting antidromic activity via electrical stimulation (>700  $\mu\text{m}$  away from the soma). **(B)** Electrophysiological and jGCaMP7f traces of spontaneous and elicited activity. For stimulation, 5 biphasic pulses were delivered at 1 Hz (-1000/1000 mV, 100  $\mu\text{s}$  each phase) or 0.5 Hz (-800/800 mV, 100  $\mu\text{s}$  each phase). Red ticks represent the timing of electrical stimulation. Insets show the peri-stimulus response on electrode 8 (closest to soma) and calcium imaging (soma) to 0.5 Hz stimulation.

### 3.7.2 Supplementary Tables

**Supplementary Table 1** – Geometrical details of the 3D finite element model (FEM) model replicating the  $\mu$ EF microchannel used in the finite element analysis.

| MODEL<br>ELEMENTS             | WIDTH ( $\mu$ M)<br>(DIAMETER FOR<br>AXONS/ELECTRODES) | HEIGHT<br>( $\mu$ M) | LENGTH<br>( $\mu$ M) | #<br>(units) |
|-------------------------------|--|----------------------|----------------------|--------------|
| Microchannel                  | 10   | 10                   | 700                  | 1            |
| PDMS chamber                  | 100  | 80                   | 700                  | 1            |
| Glass substrate               | 100  | 50                   | 2000                 | 1            |
| TiNi electrode                | 30   | 10                   | N.A.                 | 9            |
| Coating layer                 | 10   | 1                    | 700                  | 1            |
| Longitudinal axon<br>(axon 1) | 1  | N.A.                 | 1000                 | 1            |
| Transversal axon<br>(axon 2)  | 1  | N.A.                 | 60                   | 1            |

Abbreviations: PDMS: polydimethylsiloxane; TiNi: titanium nitride

**Supplementary Table 2** – Description of the electrical properties of the different domains of the 3D finite element model.

| MATERIAL        | DOMAIN  | ELECTRICAL<br>CONDUCTIVITY (S/m) | ELECTRICAL RELATIVE<br>PERMITTIVITY (E <sub>R</sub> ) |
|-----------------|---------|----------------------------------|---|
| Glass substrate | 1       | 1.00E-15                         | 10  |
| Culture medium  | 2       | 1.5                              | 80.1  |
| Axon            | 3       | 2                                | 1   |
| Coating layer   | 4       | 0.1                              | 5   |
| PDMS chamber    | 6       | 2.50E-14                         | 2.8   |
| TiNi electrode  | 6 to 14 | 1.20E+04                         | 1   |

Abbreviations: PDMS: polydimethylsiloxane; TiNi: titanium nitride

### 3.7.3 Supplementary Movies

**Supplementary Movie 1** – Finite element model of a propagating action potential inside a microchannel. Available at:

<https://www.biorxiv.org/content/biorxiv/early/2021/06/22/2021.03.07.434278/DC1/embed/media-1.gif?download=true>

**Supplementary Movie 2** – Fast calcium imaging (200Hz; 5s raw movie) of somatodendritic depolarizations in response to distal electrical stimulation (1 Hz; -500/500 mV) (same neuron as in **Fig. 3C-F**). Movie was obtained with the 20× objective. Available at:

<https://www.biorxiv.org/content/biorxiv/early/2021/06/22/2021.03.07.434278/DC2/embed/media-2.avi?download=true>

**Supplementary Movie 3** – Fast calcium imaging (200Hz; 13s raw movie) of soma depolarizations in response to distal electrical stimulation (0.5 Hz; -800/800 mV) (same neuron as in **Fig. S2**). Movie was obtained with the 20× objective. Available at:

<https://www.biorxiv.org/content/biorxiv/early/2021/06/22/2021.03.07.434278/DC3/embed/media-3.avi?download=true>

### **Acknowledgments**

This work was partially financed by FEDER - Fundo Europeu de Desenvolvimento Regional funds through the COMPETE 2020 - Operacional Programme for Competitiveness and Internationalisation (POCI), Portugal 2020, and by Portuguese funds through FCT - Fundação para a Ciência e a Tecnologia/Ministério da Ciência, Tecnologia e Ensino Superior in the framework of the project PTDC/EMD-EMD/31540/2017 (POCI-01-0145-FEDER-031540). We thank Alla Karpova from the Janelia Virus Service Facility (HHMI Janelia Research Campus) for providing the AAV-retro vector. All the members of the Neuroengineering and Computational Neuroscience (NCN) group for help and critical discussions. NCN alumni, especially Kristine Heiney, for help and critical discussions. Sean Weaver (ETH Zurich) for critical discussions. Hélder Maiato and António Pereira (Chromosome Instability and Dynamics, IBMC/i3S) for support in STED microscopy. We acknowledge the support of the i3S Scientific Platform Bioimaging, member of the national infrastructure PPBI – Portuguese Platform of Bioimaging (PPBI-POCI-01-0145-FEDER-022122). JCM was supported by FCT (PD/BD/135491/2018) in the scope of the BiotechHealth PhD Program (Doctoral Program on Cellular and Molecular Biotechnology Applied to Health Sciences).

## Main Conclusions

It is becoming increasingly clear that axons are much more than unidirectional highways for communication and have in fact a complex physiology that contributes actively to information processing (Alcami & El Hady, 2019). The axon is, by far, the longest subcellular structure known, but also extremely thin to save energy and space (Costa et al., 2018; Perge et al., 2012). These key morphological characteristics, together with an often-intricate growth path and complex/compact networks, difficult immensely the study of axon physiology *in vivo*. Understandably, this has led to an emerging interest in developing technologies that allow for this study *in vitro* (Emmenegger et al., 2019). Aiming at better understanding axonal electrophysiology and signal transmission, this thesis combines work on specific questions in basic neurobiology with the development of the technological tools enabling these questions to be addressed experimentally. From a technological and methodological perspective, the work presented proposes different MEA-based approaches to probe and analyze axonal activity in a controlled manner *in vitro*. From a basic neurobiology perspective, this work provides novel insights into axonal signal conduction in neuronal cultures.

Since standard MEAs are planar substrates, axons grow freely and, most often, far from the electrodes' vicinity. In **Chapter II**, we present a new MEA design, where each electrode is structured with a 3×3 array of mushroom-shaped microstructures. We showed that these biocompatible microstructures promote neuronal topotaxis, specifically axon-electrode coupling and neuron-electrode colocalization. Most studies that have previously reported axon contact guidance have used densely-packed 3D structures (0.5-3  $\mu\text{m}$  pitch), that can hardly be implemented in recording electrodes ("bed of nails" electrodes) (Leclech & Villard, 2020). With this work, we showed for the first time that a 10  $\mu\text{m}$  pitch between anisotropic 3D-structures still influences axon guidance and can be incorporated in MEAs. Crucially, these 3D-structured electrodes allowed for high SNR electrophysiological recordings, paving the way for high-fidelity recordings from engineered neuronal networks.

Although this MEA design promotes axon-electrode contact, *per se* it is not selective for the recording of axons alone. For the systematic study of axon activity, one should be able of isolating axonal signals consistently and, preferably, in high-throughput. Currently, it is experimentally difficult to probe single axons, let alone multiple axons simultaneously. The combination of MEAs with tailored-made microfluidics (Lopes et al., 2018), and advanced

analysis algorithms (Heiney et al., 2019), used in **Chapter III** enabled the probing of multiple axons in long-term experiments. This allowed for the observation, for the first time, that spontaneous axonal conduction in neuronal cultures of hippocampal and DRG neurons is bidirectional. We observed a high prevalence of EAP/antidromic activity in basal conditions, that could be modulated by lesioning or chemical stimulation of the distal axon portions. Importantly, evoked antidromic APs consistently depolarized the soma, anticipating functional roles for EAPs in plasticity or gene transduction mechanisms. Further characterization of this bidirectional conduction revealed an asymmetry in conduction velocity, with antidromic conduction being slightly slower than orthodromic. Via computational modeling and super-resolution microscopy, we showed that the difference can be explained by different axon morphologies that introduce an asymmetry in axon diameter. Altogether these results completely reshape our understanding of how information flows *in vitro*, since axonal conduction has been typically presumed to be unidirectional. Furthermore, these results have great implications for the design, analysis and interpretation of several types of *in vitro* experiments (e.g., neuronal plasticity studies), which have assumed canonical pre- to post-synaptic (i.e., axon to dendrite) connectivity alone.

Overall, this thesis provides the fields of Neuroengineering and Neurobiology with novel insights into axonal function, made possible by the development and use of new technologies and methodologies for the study of axon physiology *in vitro*. Hopefully, these insights and approaches can help accelerate the understanding of neuronal function.

## Future Perspectives

As the Neuroengineering field moves towards higher spatiotemporal control of neuronal networks, new technologies and methodologies need to be combined to allow finer control in the recording and modulation of axonal activity.

To characterize the new 3D-MEA design capabilities, the biological experiments employed conventional cell culture techniques, hence the neuronal networks formed were randomly connected. However, the morphological and functional complexity (even *in vitro*) of these seemingly random neuronal networks makes the systematic study of their organization and connectivity hugely challenging.

Future studies may merge the advantages of this MEA design with techniques that control axon guidance (e.g., chemical patterning) for the dissection of the axonal contribution in neuronal networks' function. Given their higher SNR, these 3D-structured electrodes should allow for the reliable recording of axonal signals from such networks. Theoretically, these MEAs can also be combined with microfluidic chambers, though the assembly procedure would need to be automated in a way that prevents damage to the fragile microstructures. Furthermore, these patterning techniques may also be used to engineer modular or node-like networks (Amin et al., 2018; M. U. Park et al., 2021; Santoro et al., 2014), where the 3D-structured electrodes co-promote neuron localization and improve the recordings SNR. This could allow for the study of small-scale connectomes, which is nearly impossible in *in vivo* vertebrate models and conventional *in vitro* models (Schröter et al., 2017). Importantly, several studies link findings in engineered modular networks (Barral et al., 2019; Schroeter et al., 2015; Hideaki Yamamoto et al., 2018) to properties found at a larger scale and *in silico* (Bassett & Sporns, 2017; Schröter et al., 2017), which validates these tools for the study of fundamental mechanisms of neuronal circuits.

The finding that spontaneous signal conduction in neuronal cultures is bidirectional opens several new perspectives. Still, crucial questions remain to be addressed in future studies: What is the mechanism of EAP/antidromic initiation in hippocampal and DRG cultures? Given their high prevalence, what is the impact of EAP/antidromic activity in neuronal cultures' function? Can these findings be translated to neuronal function *in vivo*?

Future technologies and methodologies capable of isolating (or separating the activity of) single neurons and axons may help decipher how EAPs/antidromic APs arise and what is their

function at different scales (from single-cell to network level). Still, we anticipate that, in the context of a neuronal network, all antidromic activity may not be traced back to a single cause (e.g., axo-axonal synapses or spontaneous initiation). Moreover, other mechanisms beyond those herein described/considered may influence EAP initiation. For example, subthreshold potentials can propagate along the axon over long distances and have been shown to exert excitatory actions that co-promote EAP initiation (when synchronous subthreshold stimulation is applied to the distal axon) (Thome et al., 2018). Still, it remains to be shown whether this mechanism of EAP initiation can happen spontaneously, and in which circumstances. We could not investigate a relationship between subthreshold propagation and EAP initiation since the extracellular recording of subthreshold potentials is currently not feasible. Future technologies that allow access to the full repertoire of axon electrophysiology in non-invasive, long-term, high-throughput experiments will certainly help to test this hypothesis.

Ultimately, the relevance and translation of these findings to what happens *in vivo* is hard to decipher, but indications that EAPs occur *in vivo* in both physiological and pathological conditions encourage further research (Chorev & Brecht, 2012; Roger D. Traub et al., 2020).

## References

- Abbott, J., Ye, T., Ham, D., & Park, H. (2018). Optimizing Nanoelectrode Arrays for Scalable Intracellular Electrophysiology. *Accounts of Chemical Research*, acs.accounts.7b00519. <https://doi.org/10.1021/acs.accounts.7b00519>
- Abbott, J., Ye, T., Krenek, K., Gertner, R. S., Ban, S., Kim, Y., Qin, L., Wu, W., Park, H., & Ham, D. (2019). A nanoelectrode array for obtaining intracellular recordings from thousands of connected neurons. *Nature Biomedical Engineering*, 1–10. <https://doi.org/10.1038/s41551-019-0455-7>
- Abbott, J., Ye, T., Krenek, K., Gertner, R. S., Wu, W., Jung, H. S., Ham, D., & Park, H. (2020). Extracellular recording of direct synaptic signals with a CMOS-nanoelectrode array. *Lab on a Chip*, 17(17), 3239–3248. <https://doi.org/10.1039/D0LC00553C>
- Abidian, M. R., Corey, J. M., Kipke, D. R., & Martin, D. C. (2010). Conducting-Polymer Nanotubes Improve Electrical Properties, Mechanical Adhesion, Neural Attachment, and Neurite Outgrowth of Neural Electrodes. *Small*, 6(3), 421–429. <https://doi.org/10.1002/smll.200901868>
- Acarón Ledesma, H., Li, X., Carvalho-de-Souza, J. L., Wei, W., Bezanilla, F., & Tian, B. (2019). An atlas of nano-enabled neural interfaces. *Nature Nanotechnology*, 14(7), 645–657. <https://doi.org/10.1038/s41565-019-0487-x>
- Accardi, M. V., Pugsley, M. K., Forster, R., Troncy, E., Huang, H., & Authier, S. (2016). The emerging role of in vitro electrophysiological methods in CNS safety pharmacology. *Journal of Pharmacological and Toxicological Methods*, 81, 47–59. <https://doi.org/10.1016/J.VASCN.2016.03.008>
- Aebersold, M. J., Dermutz, H., Forró, C., Weydert, S., Thompson-Steckel, G., Voros, J., & Demkó, L. (2016). “Brains on a chip”: Towards engineered neural networks. *TrAC - Trends in Analytical Chemistry*, 78, 60–69. <https://doi.org/10.1016/j.trac.2016.01.025>
- Aguayo, A. J., David, S., & Bray, G. M. (1981). Influences of the glial environment on the elongation of axons after injury: transplantation studies in adult rodents. *J Exp Biol*, 95, 231–240. <https://www.ncbi.nlm.nih.gov/pubmed/7334319>
- Alcami, P., & El Hady, A. (2019). Axonal Computations. *Frontiers in Cellular Neuroscience*, 13, 413. <https://doi.org/10.3389/fncel.2019.00413>

- Alcamí, P., & Pereda, A. E. (2019). Beyond plasticity: the dynamic impact of electrical synapses on neural circuits. *Nature Reviews Neuroscience*, 20(5), 253–271. <https://doi.org/10.1038/s41583-019-0133-5>
- Alonso, L. M., & Marder, E. (2020). Temperature compensation in a small rhythmic circuit. *eLife*, 9, 1–24. <https://doi.org/10.7554/eLife.55470>
- Alpizar, S. A., Cho, I. H., & Hoppe, M. B. (2019). Subcellular control of membrane excitability in the axon. In *Current Opinion in Neurobiology* (Vol. 57, pp. 117–125). Elsevier Ltd. <https://doi.org/10.1016/j.conb.2019.01.020>
- Amin, H., Dipalo, M., De Angelis, F., & Berdondini, L. (2018). Biofunctionalized 3D nanopillar arrays fostering cell-guidance and promoting synapse stability and neuronal activity in networks. *ACS Applied Materials & Interfaces*, acsami.8b00387. <https://doi.org/10.1021/acsami.8b00387>
- Amir, R., Kocsis, J. D., & Devor, M. (2005). Multiple interacting sites of ectopic spike electrogenesis in primary sensory neurons. *Journal of Neuroscience*, 25(10), 2576–2585. <https://doi.org/10.1523/JNEUROSCI.4118-04.2005>
- Anastassiou, C. A., & Koch, C. (2015). Ephaptic coupling to endogenous electric field activity: why bother? *Current Opinion in Neurobiology*, 31, 95–103. <https://doi.org/10.1016/j.conb.2014.09.002>
- Anastassiou, C. A., Perin, R., Markram, H., & Koch, C. (2011). Ephaptic coupling of cortical neurons. *Nature Neuroscience*, 14(2), 217–223. <https://doi.org/10.1038/nn.2727>
- Anderson, M. A., Burda, J. E., Ren, Y., Ao, Y., O'Shea, T. M., Kawaguchi, R., Coppola, G., Khakh, B. S., Deming, T. J., & Sofroniew, M. V. (2016). Astrocyte scar formation aids central nervous system axon regeneration. *Nature*, 532(7598), 195–200. <https://doi.org/10.1038/nature17623>
- Andersson, M., Kjer, H. M., Rafael-Patino, J., Pacureanu, A., Pakkenberg, B., Thiran, J. P., Ptito, M., Bech, M., Bjorholm Dahl, A., Andersen Dahl, V., & Dyrby, T. B. (2020). Axon morphology is modulated by the local environment and impacts the noninvasive investigation of its structure-function relationship. *Proceedings of the National Academy of Sciences of the United States of America*, 117(52), 33649–33659. <https://doi.org/10.1073/pnas.2012533117>
- Angle, M. R., Cui, B., & Melosh, N. A. (2015). Nanotechnology and neurophysiology. *Curr Opin*

- Neurobiol*, 32, 132–140. <https://doi.org/10.1016/j.conb.2015.03.014>
- Aqrawe, Z., Montgomery, J., Travas-Sejdic, J., & Svirskis, D. (2018). Conducting polymers for neuronal microelectrode array recording and stimulation. *Sensors and Actuators B: Chemical*, 257, 753–765. <https://doi.org/10.1016/J.SNB.2017.11.023>
- Avoli, M., Methot, M., & Kawasaki, H. (1998). GABA-dependent generation of ectopic action potentials in the rat hippocampus. *European Journal of Neuroscience*, 10(8), 2714–2722. <https://doi.org/10.1046/j.1460-9568.1998.00275.x>
- Bähner, F., Weiss, E. K., Birke, G., Maier, N., Schmitz, D., Rudolph, U., Frotscher, M., Traub, R. D., Both, M., & Draguhn, A. (2011). Cellular correlate of assembly formation in oscillating hippocampal networks in vitro. *Proc Natl Acad Sci U S A*, 108(35). <https://doi.org/10.1073/pnas.1103546108>
- Bakkum, D. J., Chao, Z. C., & Potter, S. M. (2008). Long-Term Activity-Dependent Plasticity of Action Potential Propagation Delay and Amplitude in Cortical Networks. *PLoS ONE*, 3(5), e2088. <https://doi.org/10.1371/journal.pone.0002088>
- Bakkum, D. J., Frey, U., Radivojevic, M., Russell, T. L., Müller, J., Fiscella, M., Takahashi, H., & Hierlemann, A. (2013). Tracking axonal action potential propagation on a high-density microelectrode array across hundreds of sites. *Nature Communications*, 4(1), 2181. <https://doi.org/10.1038/ncomms3181>
- Bakkum, D. J., Obien, M. E. J., Radivojevic, M., Jäckel, D., Frey, U., Takahashi, H., & Hierlemann, A. (2018). The Axon Initial Segment is the Dominant Contributor to the Neuron's Extracellular Electrical Potential Landscape. *Advanced Biosystems*, 1800308, 1800308. <https://doi.org/10.1002/adbi.201800308>
- Bang, S., Jeong, S., Choi, N., & Kim, H. N. (2019). Brain-on-a-chip: A history of development and future perspective. In *Biomicrofluidics* (Vol. 13, Issue 5). American Institute of Physics Inc. <https://doi.org/10.1063/1.5120555>
- Baranauskas, G., David, Y., & Fleidervish, I. A. (2013). Spatial mismatch between the Na<sup>+</sup> flux and spike initiation in axon initial segment. *Proceedings of the National Academy of Sciences of the United States of America*, 110(10), 4051–4056. <https://doi.org/10.1073/pnas.1215125110>
- Barral, J., Wang, X.-J., & Reyes, A. D. (2019). Propagation of temporal and rate signals in cultured multilayer networks. *Nature Communications*, 10(1), 3969.

<https://doi.org/10.1038/s41467-019-11851-0>

- Bassett, D. S., & Sporns, O. (2017). Network neuroscience. *Nat Neurosci*, 20(3), 353–364. <https://doi.org/10.1038/nn.4502>
- Bean, B. P. (2007). The action potential in mammalian central neurons. In *Nature Reviews Neuroscience* (Vol. 8, Issue 6, pp. 451–465). Nature Publishing Group. <https://doi.org/10.1038/nrn2148>
- Ben-Ari, Y., Gaiarsa, J. L., Tyzio, R., & Khazipov, R. (2007). GABA: A pioneer transmitter that excites immature neurons and generates primitive oscillations. In *Physiological Reviews* (Vol. 87, Issue 4, pp. 1215–1284). American Physiological Society. <https://doi.org/10.1152/physrev.00017.2006>
- Berke, J. D. (2018). What does dopamine mean? In *Nature Neuroscience* (Vol. 21, Issue 6, pp. 787–793). Nature Publishing Group. <https://doi.org/10.1038/s41593-018-0152-y>
- Bestel, R., Van Rienen, U., Thielemann, C., & Appali, R. (2021). Influence of Neuronal Morphology on the Shape of Extracellular Recordings with Microelectrode Arrays: A Finite Element Analysis. *IEEE Transactions on Biomedical Engineering*, 68(4), 1317–1329. <https://doi.org/10.1109/TBME.2020.3026635>
- Bi, G. Q., & Poo, M. M. (1998). Synaptic modifications in cultured hippocampal neurons: dependence on spike timing, synaptic strength, and postsynaptic cell type. *The Journal of Neuroscience: The Official Journal of the Society for Neuroscience*, 18(24), 10464–10472. <https://doi.org/10.1523/JNEUROSCI.18-24-10464.1998>
- Black, B. J., Atmaramani, R., Plagens, S., Campbell, Z. T., Dussor, G., Price, T. J., & Pancrazio, J. J. (2019). Emerging neurotechnology for antinociceptive mechanisms and therapeutics discovery. *Biosensors and Bioelectronics*, 126, 679–689. <https://doi.org/10.1016/J.BIOS.2018.11.015>
- Blanquie, O., & Bradke, F. (2018). Cytoskeleton dynamics in axon regeneration. *Current Opinion in Neurobiology*, 51, 60–69. <https://doi.org/10.1016/J.CONB.2018.02.024>
- Bradke, F., Fawcett, J. W., & Spira, M. E. (2012). Assembly of a new growth cone after axotomy: the precursor to axon regeneration. *Nature Reviews Neuroscience*, 13(3), 183–193. <https://doi.org/10.1038/nrn3176>
- Brockhaus, J., Brüggemann, B., & Missler, M. (2019). Imaging and analysis of presynaptic calcium

- influx in cultured neurons using syngcamp6f. *Frontiers in Synaptic Neuroscience*, 11. <https://doi.org/10.3389/fnsyn.2019.00012>
- Broguiere, N., Lüchtfeld, I., Trachsel, L., Mazunin, D., Rizzo, R., Bode, J. W., Lutolf, M. P., Zenobi-Wong, M., & Zenobi-Wong, M. (2020). Morphogenesis Guided by 3D Patterning of Growth Factors in Biological Matrices. *Advanced Materials*, 32(25), 1908299. <https://doi.org/10.1002/adma.201908299>
- Brohawn, S. G., Wang, W., Handler, A., Campbell, E. B., Schwarz, J. R., & MacKinnon, R. (2019). The mechanosensitive ion channel TRAAK is localized to the mammalian node of Ranvier. *ELife*, 8. <https://doi.org/10.7554/eLife.50403>
- Broussard, Gerard J., Liang, R., & Tian, L. (2014). Monitoring activity in neural circuits with genetically encoded indicators. In *Frontiers in Molecular Neuroscience* (Vol. 7, Issue DEC, p. 97). Frontiers Media S.A. <https://doi.org/10.3389/fnmol.2014.00097>
- Broussard, Gerard Joey, Liang, Y., Fridman, M., Unger, E. K., Meng, G., Xiao, X., Ji, N., Petreanu, L., & Tian, L. (2018). In vivo measurement of afferent activity with axon-specific calcium imaging. *Nature Neuroscience*, 21(9), 1272–1280. <https://doi.org/10.1038/s41593-018-0211-4>
- Broussard, Gerard Joey, & Petreanu, L. (2021). Eavesdropping wires: Recording activity in axons using genetically encoded calcium indicators. *Journal of Neuroscience Methods*, 360, 109251. <https://doi.org/10.1016/j.jneumeth.2021.109251>
- Brüggemann, D., Wolfrum, B., Maybeck, V., Mourzina, Y., Jansen, M., & Offenhäusser, A. (2011). Nanostructured gold microelectrodes for extracellular recording from electrogenic cells. *Nanotechnology*, 22(26), 265104. <https://doi.org/10.1088/0957-4484/22/26/265104>
- Bucher, D., & Goillard, J.-M. (2011). Beyond faithful conduction: Short-term dynamics, neuromodulation, and long-term regulation of spike propagation in the axon. *Progress in Neurobiology*, 94(4), 307–346. <https://doi.org/10.1016/J.PNEUROBIO.2011.06.001>
- Bukalo, O., Campanac, E., Hoffman, D. A., & Fields, R. D. (2013). Synaptic plasticity by antidromic firing during hippocampal network oscillations. *Proc Natl Acad Sci U S A*, 110(13). <https://doi.org/10.1073/pnas.1210735110>
- Bukalo, O., Lee, P. R., & Fields, R. D. (2016). BDNF mRNA abundance regulated by antidromic action potentials and AP-LTD in hippocampus. *Neuroscience Letters*, 635, 97–102. <https://doi.org/10.1016/j.neulet.2016.10.023>

- Buzsáki, G. (2015). Hippocampal sharp wave-ripple: A cognitive biomarker for episodic memory and planning. *Hippocampus*, 25(10), 1073–1188. <https://doi.org/10.1002/hipo.22488>
- Campenot, R. B. (1977). Local control of neurite development by nerve growth factor. *Proceedings of the National Academy of Sciences of the United States of America*, 74(10), 4516–4519. <https://doi.org/10.1073/pnas.74.10.4516>
- Cerquido, M., Proenca, M. P., Dias, C., Leitao, D. C., Cardoso, S., Freitas, P. P., Aguiar, P., & Ventura, J. (2018). Tailoring the cap's morphology of electrodeposited gold micro-mushrooms. *Applied Surface Science*, 445, 512–518. <https://doi.org/10.1016/j.apsusc.2018.03.158>
- Chéreau, R., Saraceno, G. E., Angibaud, J., Cattaert, D., & Nägerl, U. V. (2017). Superresolution imaging reveals activity-dependent plasticity of axon morphology linked to changes in action potential conduction velocity. *Proceedings of the National Academy of Sciences of the United States of America*, 114(6), 1401–1406. <https://doi.org/10.1073/pnas.1607541114>
- Chiappalone, M., Bove, M., Vato, A., Tedesco, M., & Martinoia, S. (2006). Dissociated cortical networks show spontaneously correlated activity patterns during in vitro development. *Brain Research*, 93. <https://doi.org/10.1016/j.brainres.2006.03.049>
- Cho, I. H., Panzera, L. C., Chin, M., Alpizar, S. A., Olveda, G. E., Hill, R. A., & Hoppa, M. B. (2020). The potassium channel subunit Kv $\beta$ 1 serves as a major control point for synaptic facilitation. *Proceedings of the National Academy of Sciences of the United States of America*, 117(47), 29937–29947. <https://doi.org/10.1073/pnas.2000790117>
- Cho, I. H., Panzera, L. C., Chin, M., & Hoppa, M. B. (2017). Sodium channel  $\beta$ 2 subunits prevent action potential propagation failures at axonal branch points. *Journal of Neuroscience*, 37(39), 9419–9533. <https://doi.org/10.1523/JNEUROSCI.0891-17.2017>
- Cho, Y. H., Park, Y., Kim, S., & Park, J. (2021). 3D Electrodes for Bioelectronics. *Advanced Materials*, 2005805. <https://doi.org/10.1002/adma.202005805>
- Cho, Y., Sloutsky, R., Naegle, K. M., & Cavalli, V. (2013). Injury-Induced HDAC5 Nuclear Export Is Essential for Axon Regeneration. *Cell*, 155(4), 894–908. <https://doi.org/10.1016/J.CELL.2013.10.004>
- Chomiak, T., & Hu, B. (2009). What is the optimal value of the g-ratio for myelinated fibers in

- the rat CNS? A theoretical approach. *PLoS ONE*, 4(11). <https://doi.org/10.1371/journal.pone.0007754>
- Chong, S.-A., Benilova, I., Shaban, H., De Strooper, B., Devijver, H., Moechars, D., Eberle, W., Bartic, C., Van Leuven, F., & Callewaert, G. (2011). Synaptic dysfunction in hippocampus of transgenic mouse models of Alzheimer's disease: A multi-electrode array study. *Neurobiology of Disease*, 44(3), 284–291. <https://doi.org/10.1016/j.nbd.2011.07.006>
- Chorev, E., & Brecht, M. (2012). In vivo dual intra- and extracellular recordings suggest bidirectional coupling between CA1 pyramidal neurons. *Journal of Neurophysiology*, 108(6), 1584–1593. <https://doi.org/10.1152/jn.01115.2011>
- Chow, C. C., & White, J. A. (1996). Spontaneous action potentials due to channel fluctuations. *Biophysical Journal*, 71(6), 3013–3021. [https://doi.org/10.1016/S0006-3495\(96\)79494-8](https://doi.org/10.1016/S0006-3495(96)79494-8)
- Chua, J. S., Chng, C. P., Moe, A. A. K., Tann, J. Y., Goh, E. L. K., Chiam, K. H., & Yim, E. K. F. (2014). Extending neurites sense the depth of the underlying topography during neuronal differentiation and contact guidance. *Biomaterials*, 35(27), 7750–7761. <https://doi.org/10.1016/j.biomaterials.2014.06.008>
- Clark, B. A., Monsivais, P., Branco, T., London, M., & Häusser, M. (2005). The site of action potential initiation in cerebellar Purkinje neurons. *Nature Neuroscience*, 8(2), 137–139. <https://doi.org/10.1038/nn1390>
- Colbert, C. M., & Johnston, D. (1996). Axonal action-potential initiation and Na<sup>+</sup> channel densities in the soma and axon initial segment of subicular pyramidal neurons. *Journal of Neuroscience*, 16(21), 6676–6686. <https://doi.org/10.1523/jneurosci.16-21-06676.1996>
- Connors, B. W., Gutnick, M. J., & Prince, D. A. (1982). Electrophysiological properties of neocortical neurons in vitro. *Journal of Neurophysiology*, 48(6), 1302–1320. <https://doi.org/10.1152/jn.1982.48.6.1302>
- Cools, J., Copic, D., Luo, Z., Callewaert, G., Braeken, D., & De Volder, M. (2017). 3D Microstructured Carbon Nanotube Electrodes for Trapping and Recording Electrogenic Cells. *Advanced Functional Materials*, 27(36), 1–9. <https://doi.org/10.1002/adfm.201701083>
- Corredor, R. G., & Goldberg, J. L. (2009). Electrical activity enhances neuronal survival and regeneration. *Journal of Neural Engineering*, 6(5). <https://doi.org/10.1088/1741-2560/6/5/055001>

- Costa, A. R., Pinto-Costa, R., Sousa, S. C., & Sousa, M. M. (2018). The Regulation of Axon Diameter: From Axonal Circumferential Contractility to Activity-Dependent Axon Swelling. *Frontiers in Molecular Neuroscience*, 11, 319. <https://doi.org/10.3389/fnmol.2018.00319>
- Costa, A. R., & Sousa, M. M. (2021). The role of the membrane-associated periodic skeleton in axons. *Cellular and Molecular Life Sciences*, 1, 3. <https://doi.org/10.1007/s00018-021-03867-x>
- Costa, A. R., Sousa, S. C., Pinto-Costa, R., Mateus, J. C., Lopes, C. D., Costa, A. C., Rosa, D., Machado, D., Pajuelo, L., Wang, X., Zhou, F., Pereira, A. J., Sampaio, P., Rubinstein, B. Y., Mendes Pinto, I., Lampe, M., Aguiar, P., & Sousa, M. M. (2020). The membrane periodic skeleton is an actomyosin network that regulates axonal diameter and conduction. *ELife*, 9. <https://doi.org/10.7554/eLife.55471>
- Costigan, M., Scholz, J., & Woolf, C. J. (2009). Neuropathic Pain: A Maladaptive Response of the Nervous System to Damage. *Annual Review of Neuroscience*, 32(1), 1–32. <https://doi.org/10.1146/annurev.neuro.051508.135531>
- Cregg, J. M., DePaul, M. A., Filous, A. R., Lang, B. T., Tran, A., & Silver, J. (2014). Functional regeneration beyond the glial scar. *Exp Neurol*, 253, 197–207. <https://doi.org/10.1016/j.expneurol.2013.12.024>
- Cserép, C., Pósfai, B., & Dénes, Á. (2021). Shaping Neuronal Fate: Functional Heterogeneity of Direct Microglia-Neuron Interactions. In *Neuron* (Vol. 109, Issue 2, pp. 222–240). Cell Press. <https://doi.org/10.1016/j.neuron.2020.11.007>
- D'Este, E., Kamin, D., Balzarotti, F., & Hell, S. W. (2017). Ultrastructural anatomy of nodes of Ranvier in the peripheral nervous system as revealed by STED microscopy. *Proceedings of the National Academy of Sciences of the United States of America*, 114(2), E191–E199. <https://doi.org/10.1073/pnas.1619553114>
- Dana, H., Sun, Y., Mohar, B., Hulse, B. K., Kerlin, A. M., Hasseman, J. P., Tsegaye, G., Tsang, A., Wong, A., Patel, R., Macklin, J. J., Chen, Y., Konnerth, A., Jayaraman, V., Looger, L. L., Schreier, E. R., Svoboda, K., & Kim, D. S. (2019). High-performance calcium sensors for imaging activity in neuronal populations and microcompartments. *Nature Methods*, 16(7), 649–657. <https://doi.org/10.1038/s41592-019-0435-6>
- Debanne, D., Bialowas, A., & Rama, S. (2013). What are the mechanisms for analogue and digital signalling in the brain? In *Nature Reviews Neuroscience* (Vol. 14, Issue 1, pp. 63–

- 69). Nature Publishing Group. <https://doi.org/10.1038/nrn3361>
- Debanne, D., Campanac, E., Bialowas, A., Carlier, E., & Alcaraz, G. (2011). Axon Physiology. *Physiological Reviews*, 91(2), 555–602. <https://doi.org/10.1152/physrev.00048.2009>.- Axons
- Dent, E. W., & Kalil, K. (2001). Axon branching requires interactions between dynamic microtubules and actin filaments. *Journal of Neuroscience*, 21(24), 9757–9769. <https://doi.org/10.1523/jneurosci.21-24-09757.2001>
- Devor, M. (1999). Unexplained peculiarities of the dorsal root ganglion. *Pain*, 82, S27–S35. [https://doi.org/10.1016/S0304-3959\(99\)00135-9](https://doi.org/10.1016/S0304-3959(99)00135-9)
- Dipalo, M., Amin, H., Lovato, L., Moia, F., Caprettini, V., Messina, G. C., Tantussi, F., Berdondini, L., & De Angelis, F. (2017). Intracellular and Extracellular Recording of Spontaneous Action Potentials in Mammalian Neurons and Cardiac Cells with 3D Plasmonic Nanoelectrodes. *Nano Letters*, 17(6), 3932–3939. <https://doi.org/10.1021/acs.nanolett.7b01523>
- Dodson, P. D., Billups, B., Rusznák, Z., Szucs, G., Barker, M. C., & Forsythe, I. D. (2003). Presynaptic Rat Kv1.2 Channels Suppress Synaptic Terminal Hyperexcitability Following Action Potential Invasion. *The Journal of Physiology*, 550(1), 27–33. <https://doi.org/10.1113/jphysiol.2003.046250>
- Dolphin, A. C., & Lee, A. (2020). Presynaptic calcium channels: specialized control of synaptic neurotransmitter release. In *Nature Reviews Neuroscience* (Vol. 21, Issue 4, pp. 213–229). Nature Research. <https://doi.org/10.1038/s41583-020-0278-2>
- Dotti, C. G., Sullivan, C. A., & Banker, G. A. (1988). The establishment of polarity by hippocampal neurons in culture. *Journal of Neuroscience*, 8(4), 1454–1468. <https://doi.org/10.1523/jneurosci.08-04-01454.1988>
- Draguhn, A., Traub, R. D., Schmitz, D., & Jefferys, J. G. R. (1998). Electrical coupling underlies high-frequency oscillations in the hippocampus in vitro. *Nature*, 394(6689), 189–192. <https://doi.org/10.1038/28184>
- Dreosti, E., Odermatt, B., Dorostkar, M. M., & Lagnado, L. (2009). A genetically encoded reporter of synaptic activity in vivo. *Nature Methods*, 6(12), 883–889. <https://doi.org/10.1038/nmeth.1399>

- Duan, X., Gao, R., Xie, P., Cohen-Karni, T., Qing, Q., Choe, H. S., Tian, B., Jiang, X., & Lieber, C. M. (2012). Intracellular recordings of action potentials by an extracellular nanoscale field-effect transistor. *Nature Nanotechnology*, 7(3), 174–179. <https://doi.org/10.1038/nnano.2011.223>
- Dubey, S., Bhembre, N., Bodas, S., Veer, S., Ghose, A., Callan-Jones, A., Pullarkat, P., & Sens, P. (2020). The axonal actin-spectrin lattice acts as a tension buffering shock absorber. *ELife*, 9. <https://doi.org/10.7554/eLife.51772>
- Duffy, D. C., McDonald, J. C., Schueller, O. J. A., & Whitesides, G. M. (1998). Rapid prototyping of microfluidic systems in poly(dimethylsiloxane). *Analytical Chemistry*, 70(23), 4974–4984. <https://doi.org/10.1021/ac980656z>
- Dugladze, T., Schmitz, D., Whittington, M. A., Vida, I., & Gloveli, T. (2012). Segregation of Axonal and Somatic Activity During Fast Network Oscillations. *Science*, 336(6087), 1458–1461. <https://doi.org/10.1126/science.1222017>
- Dworak, B. J., & Wheeler, B. C. (2009). Novel MEA platform with PDMS microtunnels enables the detection of action potential propagation from isolated axons in culture. *Lab on a Chip*, 9(3), 404–410. <https://doi.org/10.1039/b806689b>
- Emmenegger, V., Obien, M. E. J., Franke, F., & Hierlemann, A. (2019). Technologies to Study Action Potential Propagation With a Focus on HD-MEAs. *Frontiers in Cellular Neuroscience*, 13, 159. <https://doi.org/10.3389/fncel.2019.00159>
- Encinas, M., Iglesias, M., Liu, Y., Wang, H., Muhaisen, A., Ceña, V., Gallego, C., & Comella, J. X. (2000). Sequential treatment of SH-SY5Y cells with retinoic acid and brain-derived neurotrophic factor gives rise to fully differentiated, neurotrophic factor-dependent, human neuron-like cells. *Journal of Neurochemistry*, 75(3), 991–1003. <http://www.ncbi.nlm.nih.gov/pubmed/10936180>
- Enes, J., Langwieser, N., Ruschel, J., Carballosa-Gonzalez, M. M., Klug, A., Traut, M. H., Ylera, B., Tahirovic, S., Hofmann, F., Stein, V., Moosmang, S., Hentall, I. D., & Bradke, F. (2010). Electrical Activity Suppresses Axon Growth through Cav1.2 Channels in Adult Primary Sensory Neurons. *Current Biology*, 20(13), 1154–1164. <https://doi.org/10.1016/j.cub.2010.05.055>
- Engel, D., & Jonas, P. (2005). Presynaptic action potential amplification by voltage-gated Na<sup>+</sup> channels in hippocampal mossy fiber boutons. *Neuron*, 45(3), 405–417.

<https://doi.org/10.1016/j.neuron.2004.12.048>

- Epsztein, J., Lee, A. K., Chorev, E., & Brecht, M. (2010). Impact of spikelets on hippocampal CA1 pyramidal cell activity during spatial exploration. *Science*, 327(5964), 474–477. <https://doi.org/10.1126/science.1182773>
- Erickson, J., Tooker, A., Tai, Y.-C., & Pine, J. (2008). Caged neuron MEA: A system for long-term investigation of cultured neural network connectivity. *Journal of Neuroscience Methods*, 175(1), 1–16. <https://doi.org/10.1016/j.jneumeth.2008.07.023>
- Fantuzzo, J. A., Hart, R. P., Zahn, J. D., & Pang, Z. P. (2019). Compartmentalized Devices as Tools for Investigation of Human Brain Network Dynamics. *Developmental Dynamics*, 248(1), 65–77. <https://doi.org/10.1002/dvdy.24665>
- FitzGerald, J. J., Lacour, S. P., McMahon, S. B., & Fawcett, J. W. (2008). Microchannels as Axonal Amplifiers. *IEEE Transactions on Biomedical Engineering*, 55(3), 1136–1146. <https://doi.org/10.1109/TBME.2007.909533>
- Fleidervish, I. A., Lasser-Ross, N., Gutnick, M. J., & Ross, W. N. (2010). Na<sup>+</sup> imaging reveals little difference in action potential-evoked Na<sup>+</sup> influx between axon and soma. *Nature Neuroscience*, 13(7), 852–860. <https://doi.org/10.1038/nn.2574>
- Forro, C., Caron, D., Angotzi, G. N., Gallo, V., Berdondini, L., Santoro, F., Palazzolo, G., & Panuccio, G. (2021). Electrophysiology Read-Out Tools for Brain-on-Chip Biotechnology. *Micromachines* 2021, Vol. 12, Page 124, 12(2), 124. <https://doi.org/10.3390/mi12020124>
- Forró, C., Thompson-Steckel, G., Weaver, S., Weydert, S., Ihle, S., Dermutz, H., Aebbersold, M. J., Pilz, R., Demkó, L., & Vörös, J. (2018). Modular microstruture design to build neuronal networks of defined functional connectivity. *Biosensors and Bioelectronics*, 122(September), 75–87. <https://doi.org/10.1016/j.bios.2018.08.075>
- Gautam, V., Naureen, S., Shahid, N., Gao, Q., Wang, Y., Nisbet, D., Jagadish, C., & Daria, V. R. (2017). Engineering Highly Interconnected Neuronal Networks on Nanowire Scaffolds. *Nano Letters*, 17(6), 3369–3375. <https://doi.org/10.1021/acs.nanolett.6b05288>
- Gertz, M. L., Baker, Z., Jose, S., & Peixoto, N. (2017). Time-dependent Increase in the Network Response to the Stimulation of Neuronal Cell Cultures on Micro-electrode Arrays. *Journal of Visualized Experiments*, 123, e55726–e55726. <https://doi.org/10.3791/55726>
- Giger, R. J., Hollis 2nd, E. R., & Tuszynski, M. H. (2010). Guidance molecules in axon

- regeneration. *Cold Spring Harbor Perspectives in Biology*, 2(7).  
<https://doi.org/10.1101/cshperspect.a001867>
- Gladkov, A., Pigareva, Y., Kutyina, D., Kolpakov, V., Bukatin, A., Mukhina, I., Kazantsev, V., & Pimashkin, A. (2017). Design of Cultured Neuron Networks in vitro with Predefined Connectivity Using Asymmetric Microfluidic Channels. *Scientific Reports*, 7(1), 15625.  
<https://doi.org/10.1038/s41598-017-15506-2>
- Gold, C., Henze, D. A., Koch, C., & Buzsáki, G. (2006). On the origin of the extracellular action potential waveform: A modeling study. *Journal of Neurophysiology*, 95(5), 3113–3128.  
<https://doi.org/10.1152/jn.00979.2005>
- Goldman, M. S., Golowasch, J., Marder, E., & Abbott, L. F. (2001). Global structure, robustness, and modulation of neuronal models. *Journal of Neuroscience*, 21(14), 5229–5238. <https://doi.org/10.1523/jneurosci.21-14-05229.2001>
- Goldstein, S. S., & Rall, W. (1974). Changes of action potential shape and velocity for changing core conductor geometry. *Biophysical Journal*, 14(10), 731–757.  
[https://doi.org/10.1016/S0006-3495\(74\)85947-3](https://doi.org/10.1016/S0006-3495(74)85947-3)
- Gomis-Rüth, S., Wierenga, C. J., & Bradke, F. (2008). Plasticity of Polarization: Changing Dendrites into Axons in Neurons Integrated in Neuronal Circuits. *Current Biology*, 18(13), 992–1000. <https://doi.org/10.1016/j.cub.2008.06.026>
- Gonzalez Sabater, V., Rigby, M., & Burrone, J. (2021). Voltage-gated potassium channels ensure action potential shape fidelity in distal axons. *BioRxiv*, 2020.09.15.297895.  
<https://doi.org/10.1101/2020.09.15.297895>
- Greenberg, M. M., Leitao, C., Trogadis, J., & Stevens, J. K. (1990). Irregular geometries in normal unmyelinated axons: A 3D serial EM analysis. *Journal of Neurocytology*, 19(6), 978–988. <https://doi.org/10.1007/BF01186825>
- Gribi, S., du Bois de Dunilac, S., Ghezzi, D., & Lacour, S. P. (2018). A microfabricated nerve-on-a-chip platform for rapid assessment of neural conduction in explanted peripheral nerve fibers. *Nature Communications*, 9(1), 4403. <https://doi.org/10.1038/s41467-018-06895-7>
- Grienberger, C., & Konnerth, A. (2012). Imaging Calcium in Neurons. *Neuron*, 73(5), 862–885.  
<https://doi.org/10.1016/j.neuron.2012.02.011>

- Grubb, M. S., & Burrone, J. (2010). Channelrhodopsin-2 localised to the axon initial segment. *PLoS ONE*, 5(10), 13761. <https://doi.org/10.1371/journal.pone.0013761>
- Gutnick, M. J., & Prince, D. A. (1972). Thalamocortical relay neurons: Antidromic invasion of spikes from a cortical epileptogenic focus. *Science*, 176(4030), 424–426. <https://doi.org/10.1126/science.176.4033.424>
- Habibey, R, Golabchi, A., Latifi, S., Difato, F., & Blau, A. (2015). A microchannel device tailored to laser axotomy and long-term microelectrode array electrophysiology of functional regeneration. *Lab on a Chip*, 15(24), 4578–4590. <https://doi.org/10.1039/c5lc01027f>
- Habibey, Rouhollah, Latifi, S., Mousavi, H., Pesce, M., Arab-Tehrany, E., & Blau, A. (2017). A multielectrode array microchannel platform reveals both transient and slow changes in axonal conduction velocity. *Scientific Reports*, 7(1), 8558. <https://doi.org/10.1038/s41598-017-09033-3>
- Haggerty, D. L., Grecco, G. G., Reeves, K. C., & Atwood, B. (2020). Adeno-Associated Viral Vectors in Neuroscience Research. In *Molecular Therapy - Methods and Clinical Development* (Vol. 17, pp. 69–82). Cell Press. <https://doi.org/10.1016/j.omtm.2019.11.012>
- Hai, A., Kamber, D., Malkinson, G., Erez, H., Mazurski, N., Shappir, J., & Spira, M. E. (2009). Changing gears from chemical adhesion of cells to flat substrata toward engulfment of micro-protrusions by active mechanisms. *Journal of Neural Engineering*, 6(6), 066009. <https://doi.org/10.1088/1741-2560/6/6/066009>
- Hai, A., Shappir, J., & Spira, M. E. (2010). In-cell recordings by extracellular microelectrodes. *Nature Methods*, 7(3), 200–202. <https://doi.org/10.1038/nmeth.1420>
- Hamada, M. S., & Kole, M. H. P. (2015). Myelin Loss and Axonal Ion Channel Adaptations Associated with Gray Matter Neuronal Hyperexcitability. *The Journal of Neuroscience*, 35(18). <https://doi.org/10.1523/JNEUROSCI.4747-14.2015>
- Hamada, S., Nagase, M., Yoshizawa, T., Hagiwara, A., Isomura, Y., Watabe, A. M., & Ohtsuka, T. (2021). An engineered channelrhodopsin optimized for axon terminal activation and circuit mapping. *Communications Biology*, 4(1), 1–11. <https://doi.org/10.1038/s42003-021-01977-7>
- Hamill, O. P., Marty, A., Neher, E., Sakmann, B., & Sigworth, F. J. (1981). Improved patch-clamp techniques for high-resolution current recording from cells and cell-free membrane patches. *Pflügers Archiv European Journal of Physiology*, 391(2), 85–100.

<https://doi.org/10.1007/BF00656997>

- Han, K.-S., Guo, C., Chen, C. H., Witter, L., Osorno, T., & Regehr, W. G. (2018). Ephaptic Coupling Promotes Synchronous Firing of Cerebellar Purkinje Cells. *Neuron*, 100(3), 564–578.e3. <https://doi.org/10.1016/j.neuron.2018.09.018>
- Hanson, J. N., Motala, M. J., Heien, M. L., Gillette, M., Sweedler, J., & Nuzzo, R. G. (2009). Textural guidance cues for controlling process outgrowth of mammalian neurons. *Lab on a Chip*, 9(1), 122–131. <https://doi.org/10.1039/B803595D>
- Hawthorne, A. L., Hu, H., Kundu, B., Steinmetz, M. P., Wylie, C. J., Deneris, E. S., & Silver, J. (2011). The unusual response of serotonergic neurons after CNS Injury: lack of axonal dieback and enhanced sprouting within the inhibitory environment of the glial scar. *J Neurosci*, 31(15), 5605–5616. <https://doi.org/10.1523/jneurosci.6663-10.2011>
- He, Z., & Jin, Y. (2016). Intrinsic Control of Axon Regeneration. *Neuron*, 90(3), 437–451. <https://doi.org/10.1016/j.neuron.2016.04.022>
- Hedstrom, K. L., Ogawa, Y., & Rasband, M. N. (2008). AnkyrinG is required for maintenance of the axon initial segment and neuronal polarity. *Journal of Cell Biology*, 183(4), 635–640. <https://doi.org/10.1083/jcb.200806112>
- Heiney, K., Mateus, J. C., Lopes, C. D. F., Neto, E., Lamghari, M., & Aguiar, P. (2019).  $\mu$ SpikeHunter: An advanced computational tool for the analysis of neuronal communication and action potential propagation in microfluidic platforms. *Scientific Reports*, 9(1), 5777. <https://doi.org/10.1038/s41598-019-42148-3>
- Hestrin, S., & Galarreta, M. (2005). Electrical synapses define networks of neocortical GABAergic neurons. In *Trends in Neurosciences* (Vol. 28, Issue 6 SPEC. ISS., pp. 304–309). Elsevier Ltd. <https://doi.org/10.1016/j.tins.2005.04.001>
- Hiasa, M., Okui, T., Allette, Y. M., Ripsch, M. S., Sun-Wada, G. H., Wakabayashi, H., Roodman, G. D., White, F. A., & Yoneda, T. (2017). Bone pain induced by multiple myeloma is reduced by targeting V-ATPase and ASIC3. *Cancer Research*, 77(6), 1283–1295. <https://doi.org/10.1158/0008-5472.CAN-15-3545>
- Hines, M. L., & Carnevale, N. T. (1997). The NEURON Simulation Environment. In *Neural Computation* (Vol. 9, Issue 6, pp. 1179–1209). MIT Press Journals. <https://doi.org/10.1162/neco.1997.9.6.1179>

- Hochbaum, D. R., Zhao, Y., Farhi, S. L., Klapoetke, N., Werley, C. A., Kapoor, V., Zou, P., Kralj, J. M., MacLaurin, D., Smedemark-Margulies, N., Saulnier, J. L., Boulting, G. L., Straub, C., Cho, Y. K., Melkonian, M., Wong, G. K. S., Harrison, D. J., Murthy, V. N., Sabatini, B. L., ... Cohen, A. E. (2014). All-optical electrophysiology in mammalian neurons using engineered microbial rhodopsins. *Nature Methods*, 11(8), 825–833. <https://doi.org/10.1038/NMETH.3000>
- Hodgkin, A. L. (1954). A note on conduction velocity. *The Journal of Physiology*, 125(1), 221–224. <https://doi.org/10.1113/jphysiol.1954.sp005152>
- Hodgkin, A. L., & Huxley, A. F. (1952). A quantitative description of membrane current and its application to conduction and excitation in nerve. *The Journal of Physiology*, 117(4), 500–544. <https://doi.org/10.1113/jphysiol.1952.sp004764>
- Hoffman-Kim, D., Mitchel, J. A., & Bellamkonda, R. V. (2010). Topography, Cell Response, and Nerve Regeneration. *Annual Review of Biomedical Engineering*, 12(1), 203–231. <https://doi.org/10.1146/annurev-bioeng-070909-105351>
- Holloway, P. M., Hallinan, G. I., Hegde, M., Lane, S. I. R., Deinhardt, K., & West, J. (2019). Asymmetric confinement for defining outgrowth directionality. *Lab on a Chip*, 19(8), 1484–1489. <https://doi.org/10.1039/C9LC00078J>
- Holloway, P. M., Willaime-Morawek, S., Siow, R., Barber, M., Owens, R. M., Sharma, A. D., Rowan, W., Hill, E., & Zagnoni, M. (2021). Advances in microfluidic in vitro systems for neurological disease modeling. *Journal of Neuroscience Research*, 00, 1–32. <https://doi.org/10.1002/jnr.24794>
- Hong, N., Joo, S., & Nam, Y. (2017). Characterization of axonal spikes in cultured neuronal networks using microelectrode arrays and microchannel devices. *IEEE Transactions on Biomedical Engineering*, 64(2), 492–498. <https://doi.org/10.1109/TBME.2016.2567424>
- Hong, N., & Nam, Y. (2020). Thermoplasmonic neural chip platform for in situ manipulation of neuronal connections in vitro. *Nature Communications*, 11(1), 1–12. <https://doi.org/10.1038/s41467-020-20060-z>
- Hoppa, M. B., Gouzer, G., Armbruster, M., & Ryan, T. A. (2014). Control and plasticity of the presynaptic action potential waveform at small CNS nerve terminals. *Neuron*, 84(4), 778–789. <https://doi.org/10.1016/j.neuron.2014.09.038>
- Hu, H., & Jonas, P. (2014). A supercritical density of Na<sup>+</sup> channels ensures fast signaling in

- GABAergic interneuron axons. *Nature Neuroscience*, 17(5), 686–693. <https://doi.org/10.1038/nn.3678>
- Hu, W., Tian, C., Li, T., Yang, M., Hou, H., & Shu, Y. (2009). Distinct contributions of Nav1.6 and Nav1.2 in action potential initiation and backpropagation. *Nature Neuroscience*, 12(8), 996–1002. <https://doi.org/10.1038/nn.2359>
- Huang, L., Ledochowitsch, P., Knoblich, U., Lecoq, J., Murphy, G. J., Reid, R. C., de Vries, S. E. J., Koch, C., Zeng, H., Buice, M. A., Waters, J., & Li, L. (2021). Relationship between simultaneously recorded spiking activity and fluorescence signal in gcamp6 transgenic mice. *ELife*, 10. <https://doi.org/10.7554/eLife.51675>
- Huval, R. M., Miller, O. H., Curley, J. L., Fan, Y., Hall, B. J., & Moore, M. J. (2015). Microengineered peripheral nerve-on-a-chip for preclinical physiological testing. *Lab on a Chip*, 15(10), 2221–2232. <https://doi.org/10.1039/C4LC01513D>
- Imbrosci, B., Nitzan, N., McKenzie, S., Donoso, J. R., Swaminathan, A., Böhm, C., Maier, N., & Schmitz, D. (2021). Subiculum as a generator of sharp wave-ripples in the rodent hippocampus. *Cell Reports*, 35(3), 109021. <https://doi.org/10.1016/j.celrep.2021.109021>
- Inoue, M., Takeuchi, A., Manita, S., Horigane, S. ichiro, Sakamoto, M., Kawakami, R., Yamaguchi, K., Otomo, K., Yokoyama, H., Kim, R., Yokoyama, T., Takemoto-Kimura, S., Abe, M., Okamura, M., Kondo, Y., Quirin, S., Ramakrishnan, C., Imamura, T., Sakimura, K., ... Bito, H. (2019). Rational Engineering of XCaMPs, a Multicolor GECI Suite for In Vivo Imaging of Complex Brain Circuit Dynamics. *Cell*, 177(5), 1346-1360.e24. <https://doi.org/10.1016/j.cell.2019.04.007>
- Ixmattlahua, D. J., Vizcarra, B., Gómez-Lira, G., Romero-Maldonado, I., Ortiz, F., Rojas-Piloni, G., & Gutiérrez, R. (2020). Neuronal Glutamatergic Network Electrically Wired with Silent but Activatable Gap Junctions. *Journal of Neuroscience*, 40(24), 4661–4672. <https://doi.org/10.1523/JNEUROSCI.2590-19.2020>
- Jäckel, D., Bakkum, D. J., Russell, T. L., Müller, J., Radivojevic, M., Frey, U., Franke, F., & Hierlemann, A. (2017). Combination of High-density Microelectrode Array and Patch Clamp Recordings to Enable Studies of Multisynaptic Integration. *Scientific Reports*, 7(1), 978. <https://doi.org/10.1038/s41598-017-00981-4>
- Jackson, R. E., & Burrone, J. (2016). Visualizing presynaptic calcium dynamics and vesicle fusion with a single genetically encoded reporter at individual synapses. *Frontiers in*

*Synaptic Neuroscience*, 8(JUL). <https://doi.org/10.3389/fnsyn.2016.00021>

- James, C. D., Spence, A. J. H., Dowell-Mesfin, N. M., Hussain, R. J., Smith, K. L., Craighead, H. G., Isaacson, M. S., Shain, W., & Turner, J. N. (2004). Extracellular Recordings From Patterned Neuronal Networks Using Planar Microelectrode Arrays. *IEEE Transactions on Biomedical Engineering*, 51(9), 1640–1648. <https://doi.org/10.1109/TBME.2004.827252>
- Jang, J. M., Lee, J., Kim, H., Jeon, N. L., & Jung, W. (2016). One-photon and two-photon stimulation of neurons in a microfluidic culture system. *Lab on a Chip*, 16(9), 1684–1690. <https://doi.org/10.1039/C6LC00065G>
- Jang, K.-J., Kim, M. S., Feltrin, D., Jeon, N. L., Suh, K.-Y., & Pertz, O. (2010). Two Distinct Filopodia Populations at the Growth Cone Allow to Sense Nanotopographical Extracellular Matrix Cues to Guide Neurite Outgrowth. *PLOS ONE*, 5(12), e15966. <https://doi.org/10.1371/JOURNAL.PONE.0015966>
- Jenkins, P. M., Kim, N., Jones, S. L., Tseng, W. C., Svitkina, T. M., Yin, H. H., & Bennett, V. (2015). Giant ankyrin-G: A critical innovation in vertebrate evolution of fast and integrated neuronal signaling. *Proceedings of the National Academy of Sciences of the United States of America*, 112(4), 957–964. <https://doi.org/10.1073/pnas.1416544112>
- Johnstone, A. F. M. M., Gross, G. W., Weiss, D. G., Schroeder, O. H.-U. U., Gramowski, A., & Shafer, T. J. (2010). Microelectrode arrays: A physiologically based neurotoxicity testing platform for the 21st century. *NeuroToxicology*, 31(4), 331–350. <https://doi.org/10.1016/j.neuro.2010.04.001>
- Kalil, K., & Dent, E. W. (2014). Branch management: Mechanisms of axon branching in the developing vertebrate CNS. In *Nature Reviews Neuroscience* (Vol. 15, Issue 1, pp. 7–18). <https://doi.org/10.1038/nrn3650>
- Kandel, E., Schwartz, J., & Jessel, T. (2013). *Principles of Neural Science* (5th ed.). The McGraw-Hill Companies.
- Katz, B., & Schmitt, O. H. (1940). Electric interaction between two adjacent nerve fibres. *The Journal of Physiology*, 97(4), 471–488. <https://doi.org/10.1113/jphysiol.1940.sp003823>
- Kawaguchi, S. ya, & Sakaba, T. (2015). Control of inhibitory synaptic outputs by low excitability of axon terminals revealed by direct recording. *Neuron*, 85(6), 1273–1288. <https://doi.org/10.1016/j.neuron.2015.02.013>

- Kevenaar, J. T., & Hoogenraad, C. C. (2015). The axonal cytoskeleton: From organization to function. In *Frontiers in Molecular Neuroscience* (Vol. 8, Issue AUGUST, p. 44). Frontiers Media S.A. <https://doi.org/10.3389/fnmol.2015.00044>
- Kim, G. H., Kim, K., Nam, H., Shin, K., Choi, W., Shin, J. H., & Lim, G. (2017). CNT-Au nanocomposite deposition on gold microelectrodes for improved neural recordings. *Sensors and Actuators B: Chemical*, 252, 152–158. <https://doi.org/10.1016/J.SNB.2017.04.142>
- Kim, H. J., Park, J. W. J. W., Byun, J. H., Vahidi, B., Rhee, S. W., Jeon, N. L., Park, J. W. J. W., Byun, J. H., Vahidi, B., Rhee, S. W., & Jeon, N. L. (2012). Integrated microfluidics platforms for investigating injury and regeneration of CNS axons. *Ann Biomed Eng*, 40(6), 1268–1276. <https://doi.org/10.1007/s10439-012-0515-6>
- Kleinfeld, D., Kahler, K. H., & Hockberger, P. E. (1988). Controlled outgrowth of dissociated neurons on patterned substrates. *Journal of Neuroscience*, 8(11), 4098–4120. <https://doi.org/10.1523/jneurosci.08-11-04098.1988>
- Knöpfel, T., & Song, C. (2019). Optical voltage imaging in neurons: moving from technology development to practical tool. In *Nature Reviews Neuroscience* (Vol. 20, Issue 12, pp. 719–727). Nature Research. <https://doi.org/10.1038/s41583-019-0231-4>
- Koester, H. J., & Sakmann, B. (2000). Calcium dynamics associated with action potentials in single nerve terminals of pyramidal cells in layer 2/3 of the young rat neocortex. *Journal of Physiology*, 529(3), 625–646. <https://doi.org/10.1111/j.1469-7793.2000.00625.x>
- Kole, M. H. P., Ilshner, S. U., Kampa, B. M., Williams, S. R., Ruben, P. C., & Stuart, G. J. (2008). Action potential generation requires a high sodium channel density in the axon initial segment. *Nature Neuroscience*, 11(2), 178–186. <https://doi.org/10.1038/nn2040>
- Kole, M. H. P., Letzkus, J. J., & Stuart, G. J. (2007). Axon Initial Segment Kv1 Channels Control Axonal Action Potential Waveform and Synaptic Efficacy. *Neuron*, 55(4), 633–647. <https://doi.org/10.1016/j.neuron.2007.07.031>
- Kole, M. H. P., & Stuart, G. J. (2008). Is action potential threshold lowest in the axon? *Nature Neuroscience*, 11(11), 1253–1255. <https://doi.org/10.1038/nn.2203>
- Kole, M. H. P., & Stuart, G. J. (2012). Signal Processing in the Axon Initial Segment. In *Neuron* (Vol. 73, Issue 2, pp. 235–247). Neuron. <https://doi.org/10.1016/j.neuron.2012.01.007>

- Kwak, M., Han, L., Chen, J. J., & Fan, R. (2015). Interfacing Inorganic Nanowire Arrays and Living Cells for Cellular Function Analysis. *Small*, 11(42), 5600–5610. <https://doi.org/10.1002/sml.201501236>
- Lazarov, E., Dannemeyer, M., Feulner, B., Enderlein, J., Gutnick, M. J., Wolf, F., & Neef, A. (2018). An axon initial segment is required for temporal precision in action potential encoding by neuronal populations. *Science Advances*, 4(11), eaau8621. <https://doi.org/10.1126/sciadv.aau8621>
- Leclech, C., Renner, M., Villard, C., & Métin, C. (2019). Topographical cues control the morphology and dynamics of migrating cortical interneurons. *Biomaterials*, 214. <https://doi.org/10.1016/j.biomaterials.2019.05.005>
- Leclech, C., & Villard, C. (2020). Cellular and Subcellular Contact Guidance on Microfabricated Substrates. In *Frontiers in Bioengineering and Biotechnology* (Vol. 8, p. 1198). Frontiers Media S.A. <https://doi.org/10.3389/fbioe.2020.551505>
- Lefler, Y., Amsalem, O., Vrieler, N., Segev, I., & Yarom, Y. (2020). Using subthreshold events to characterize the functional architecture of the electrically coupled inferior olive network. *ELife*, 9. <https://doi.org/10.7554/eLife.43560>
- Lehnert, S., Ford, M. C., Alexandrova, O., Hellmundt, F., Felmy, F., Grothe, B., & Leibold, C. (2014). Action Potential Generation in an Anatomically Constrained Model of Medial Superior Olive Axons. *Journal of Neuroscience*, 34(15), 5370–5384. <https://doi.org/10.1523/JNEUROSCI.4038-13.2014>
- Leterrier, C., Dubey, P., & Roy, S. (2017). The nano-architecture of the axonal cytoskeleton. *Nature Reviews Neuroscience*. <https://doi.org/10.1038/nrn.2017.129>
- Leterrier, C., Potier, J., Caillol, G., Debarnot, C., Rueda Boroni, F., & Dargent, B. (2015). Nanoscale Architecture of the Axon Initial Segment Reveals an Organized and Robust Scaffold. *Cell Reports*, 13(12), 2781–2793. <https://doi.org/10.1016/j.celrep.2015.11.051>
- Lewandowska, M. K., Bakkum, D. J., Rompani, S. B., & Hierlemann, A. (2015). Recording Large Extracellular Spikes in Microchannels along Many Axonal Sites from Individual Neurons. *PLOS ONE*, 10(3), e0118514. <https://doi.org/10.1371/journal.pone.0118514>
- Lewandowska, M. K., Radivojević, M., Jäckel, D., Müller, J., & Hierlemann, A. R. (2016). Cortical Axons, Isolated in Channels, Display Activity-Dependent Signal Modulation as a Result of Targeted Stimulation. *Frontiers in Neuroscience*, 10, 83.

<https://doi.org/10.3389/fnins.2016.00083>

- Li, W., Tang, Q. Y., Jadhav, A. D., Narang, A., Qian, W. X., Shi, P., & Pang, S. W. (2015). Large-scale topographical screen for investigation of physical neural-guidance cues. *Scientific Reports*, 5(1), 1–8. <https://doi.org/10.1038/srep08644>
- Li, W., Wang, H., Pan, X., Gagoski, D., Durisic, N., Li, Z., Zhao, C.-X., & Wang, T. (2021). Axons-on-a-Chip for Mimicking Non-Disruptive Diffuse Axonal Injury underlying Traumatic Brain Injury. *BioRxiv*, 2021.05.06.442958. <https://doi.org/10.1101/2021.05.06.442958>
- Li, X. -G, Somogyi, P., Ylinen, A., & Buzsáki, G. (1994). The hippocampal CA3 network: An in vivo intracellular labeling study. *Journal of Comparative Neurology*, 339(2), 181–208. <https://doi.org/10.1002/cne.903390204>
- Liu, C. N., Michaelis, M., Amir, R., & Devor, M. (2000). Spinal nerve injury enhances subthreshold membrane potential oscillations in DRG neurons: Relation to neuropathic pain. *Journal of Neurophysiology*, 84(1), 205–215. <https://doi.org/10.1152/jn.2000.84.1.205>
- Liu, R., Chen, R., Elthakeb, A. T., Lee, S. H., Hinckley, S., Khraiche, M. L., Scott, J., Pre, D., Hwang, Y., Tanaka, A., Ro, Y. G., Matsushita, A. K., Dai, X., Soci, C., Biesmans, S., James, A., Nogan, J., Jungjohann, K. L., Pete, D. V., ... Dayeh, S. A. (2017). High Density Individually Addressable Nanowire Arrays Record Intracellular Activity from Primary Rodent and Human Stem Cell Derived Neurons. *Nano Letters*, 17(5), 2757–2764. <https://doi.org/10.1021/acs.nanolett.6b04752>
- Lopes, C. D. F., Mateus, J. C., & Aguiar, P. (2018). Interfacing Microfluidics with Microelectrode Arrays for Studying Neuronal Communication and Axonal Signal Propagation. *Journal of Visualized Experiments*, 142, 1–8. <https://doi.org/10.3791/58878>
- Lorincz, A., & Nusser, Z. (2010). Molecular identity of dendritic voltage-gated sodium channels. *Science*, 328(5980), 906–909. <https://doi.org/10.1126/science.1187958>
- Ma, Y., Bayguinov, P. O., & Jackson, M. B. (2017). Action Potential Dynamics in Fine Axons Probed with an Axonally Targeted Optical Voltage Sensor. *ENeuro*, 4(4), ENEURO.0146-17.2017. <https://doi.org/10.1523/ENeuro.0146-17.2017>
- Mainen, Z. F., Joerges, J., Huguenard, J. R., & Sejnowski, T. J. (1995). A Model of Spike Initiation in Neocortical Pyramidal Neurons. In *Neuron* (Vol. 15). [https://doi.org/10.1016/0896-6273\(95\)90020-9](https://doi.org/10.1016/0896-6273(95)90020-9)

- Manor, Y., Koch, C., & Segev, I. (1991). Effect of geometrical irregularities on propagation delay in axonal trees. *Biophysical Journal*, 60(6), 1424–1437. [https://doi.org/10.1016/S0006-3495\(91\)82179-8](https://doi.org/10.1016/S0006-3495(91)82179-8)
- Mar, F. M., Bonni, A., & Sousa, M. M. (2014). Cell intrinsic control of axon regeneration. *EMBO Rep*, 15(3), 254–263. <https://doi.org/10.1002/embr.201337723>
- Marcus, M., Baranes, K., Park, M., Choi, I. S., Kang, K., & Shefi, O. (2017). Interactions of Neurons with Physical Environments. *Advanced Healthcare Materials*, 6(15). <https://doi.org/10.1002/adhm.201700267>
- Markram, H., Lübke, J., Frotscher, M., & Sakmann, B. (1997). Regulation of synaptic efficacy by coincidence of postsynaptic APs and EPSPs. *Science (New York, N.Y.)*, 275(5297), 213–215. <https://doi.org/10.1126/science.275.5297.213>
- Massobrio, P., Tessadori, J., Chiappalone, M., & Ghirardi, M. (2015). In Vitro Studies of Neuronal Networks and Synaptic Plasticity in Invertebrates and in Mammals Using Multielectrode Arrays. *Neural Plasticity*, 2015, 196195. <https://doi.org/10.1155/2015/196195>
- Mcguire, A. F., Santoro, F., & Cui, B. (2018). Interfacing Cells with Vertical Nanoscale Devices : Applications and Characterization. *Annual Review of Analytical Chemistry*, March, 1–26.
- Meeks, J. P., & Mennerick, S. (2004). Selective Effects of Potassium Elevations on Glutamate Signaling and Action Potential Conduction in Hippocampus. *Journal of Neuroscience*, 24(1), 197–206. <https://doi.org/10.1523/JNEUROSCI.4845-03.2004>
- Mestre, A. L. G., Cerquido, M., Inácio, P. M. C., Asgarifar, S., Lourenço, A. S., Cristiano, M. L. S., Aguiar, P., Medeiros, M. C. R., Araújo, I. M., Ventura, J., & Gomes, H. L. (2017). Ultrasensitive gold micro- structured electrodes enabling the detection of extra-cellular long- lasting potentials in astrocytes populations. *Scientific Reports*, May, 1–11. <https://doi.org/10.1038/s41598-017-14697-y>
- Michalikova, M., Remme, M. W. H., Schmitz, D., Schreiber, S., & Kempster, R. (2019). Spikelets in pyramidal neurons: Generating mechanisms, distinguishing properties, and functional implications. *Reviews in the Neurosciences*, 31(1), 101–119. <https://doi.org/10.1515/revneuro-2019-0044>
- Micholt, L., Gärtner, A., Prodanov, D., Braeken, D., Dotti, C. G., & Bartic, C. (2013). Substrate Topography Determines Neuronal Polarization and Growth In Vitro. *PLoS ONE*, 8(6),

e66170. <https://doi.org/10.1371/journal.pone.0066170>

- Micu, I., Plemel, J. R., Caprariello, A. V., Nave, K.-A., & Stys, P. K. (2018). Axo-myelinic neurotransmission: a novel mode of cell signalling in the central nervous system. *Nature Reviews Neuroscience*, 19(1), 49–58. <https://doi.org/10.1038/nrn.2017.128>
- Middya, S., Curto, V. F., Fernández-Villegas, A., Robbins, M., Gurke, J., Moonen, E. J. M., Kaminski Schierle, G. S., & Malliaras, G. G. (2021). Microelectrode Arrays for Simultaneous Electrophysiology and Advanced Optical Microscopy. *Advanced Science*, 2004434. <https://doi.org/10.1002/advs.202004434>
- Millet, L. J., & Gillette, M. U. (2012a). Over a century of neuron culture: From the hanging drop to microfluidic devices. *Yale Journal of Biology and Medicine*, 85(4), 501–521. [/pmc/articles/PMC3516892/?report=abstract](https://pubmed.ncbi.nlm.nih.gov/23031246/)
- Millet, L. J., & Gillette, M. U. (2012b). New perspectives on neuronal development via microfluidic environments. *Trends in Neurosciences*, 35(12), 752–761. <http://www.ncbi.nlm.nih.gov/pubmed/23031246>
- Milos, F., Tullii, G., Gobbo, F., Lodola, F., Galeotti, F., Verpelli, C., Mayer, D., Maybeck, V., Offenhäusser, A., & Antognazza, M. R. (2021). High Aspect Ratio and Light-Sensitive Micropillars Based on a Semiconducting Polymer Optically Regulate Neuronal Growth. *ACS Applied Materials & Interfaces*, acsami.1c03537. <https://doi.org/10.1021/acsami.1c03537>
- Moutaux, E., Charlot, B., Genoux, A., Saudou, F., & Cazorla, M. (2018). An integrated microfluidic/microelectrode array for the study of activity-dependent intracellular dynamics in neuronal networks. *Lab on a Chip*. <https://doi.org/10.1039/C8LC00694F>
- Nam, Y., & Wheeler, B. C. (2011). In vitro microelectrode array technology and neural recordings. *Critical Reviews in Biomedical Engineering*, 39(1), 45–61.
- Narula, U., Ruiz, A., McQuaide, M., DeMarse, T. B., Wheeler, B. C., & Brewer, G. J. (2017). Narrow microtunnel technology for the isolation and precise identification of axonal communication among distinct hippocampal subregion networks. *PLOS ONE*, 12(5), e0176868. <https://doi.org/10.1371/JOURNAL.PONE.0176868>
- Nascimento, A. I., Mar, F. M., & Sousa, M. M. (2018). The intriguing nature of dorsal root ganglion neurons: Linking structure with polarity and function. *Progress in Neurobiology*, 168, 86–103. <https://doi.org/10.1016/J.PNEUROBIO.2018.05.002>

- Neto, E., Alves, C. J., Sousa, D. M., Alencastre, I. S., Lourenço, A. H., Leitão, L., Ryu, H. R., Jeon, N. L., Fernandes, R., Aguiar, P., Almeida, R. D., & Lamghari, M. (2014). Sensory neurons and osteoblasts: close partners in a microfluidic platform. *Integrative Biology: Quantitative Biosciences from Nano to Macro*, 6(6), 586–595. <https://doi.org/10.1039/c4ib00035h>
- Neto, E., Leitao, L., Mateus, J., Sousa, D., Conceicao, F., Alves, C. J., Oreffo, R. O. C., West, J., Aguiar, P., & Lamghari, M. (2020). Sensory neurons sprouting is dependent on osteoclast-derived extracellular vesicles involving the activation of epidermal growth factor receptors. *BioRxiv*. <https://doi.org/10.1101/259218>
- Neto, E., Leitão, L., Sousa, D. M., Alves, C. J., Alencastre, I. S., Aguiar, P., & Lamghari, M. (2016). Compartmentalized microfluidic platforms: The unrivaled breakthrough of in vitro tools for neurobiological research. *Journal of Neuroscience*, 36(46), 11573–11584. <https://doi.org/10.1523/JNEUROSCI.1748-16.2016>
- Niven, J. E., & Laughlin, S. B. (2008). Energy limitation as a selective pressure on the evolution of sensory systems. In *Journal of Experimental Biology* (Vol. 211, Issue 11, pp. 1792–1804). The Company of Biologists. <https://doi.org/10.1242/jeb.017574>
- O'Donnell, C., & van Rossum, M. C. W. (2014). Systematic analysis of the contributions of stochastic voltage gated channels to neuronal noise. *Frontiers in Computational Neuroscience*, 8(September), 105. <https://doi.org/10.3389/fncom.2014.00105>
- Obien, M. E. J. E. J., Deligkaris, K., Bullmann, T., Bakkum, D. J. J., & Frey, U. (2015). Revealing neuronal function through microelectrode array recordings. *Front Neurosci*, 8, 423. <https://doi.org/10.3389/fnins.2014.00423>
- Ojovan, S. M., Rabieh, N., Shmoel, N., Erez, H., Maydan, E., Cohen, A., & Spira, M. E. (2015). A feasibility study of multi-site, intracellular recordings from mammalian neurons by extracellular gold mushroom-shaped microelectrodes. *Scientific Reports*, 5, 14100. <https://doi.org/10.1038/srep14100>
- Oláh, V. J., Tarcsay, G., & Brunner, J. (2021). Small size of recorded neuronal structures confines the accuracy in direct axonal voltage measurements. *BioRxiv*, 2021.01.29.428709. <https://doi.org/10.1101/2021.01.29.428709>
- Oliva, A. A., James, C. D., Kingman, C. E., Craighead, H. G., & Banker, G. A. (2003). Patterning Axonal Guidance Molecules Using a Novel Strategy for Microcontact Printing. In

- Neurochemical Research* (Vol. 28, Issue 11, pp. 1639–1648). Springer.  
<https://doi.org/10.1023/A:1026052820129>
- Pan-Vazquez, A., Wefelmeyer, W., Gonzalez Sabater, V., Neves, G., & Burrone, J. (2020). Activity-Dependent Plasticity of Axo-axonic Synapses at the Axon Initial Segment. *Neuron*, 106(2), 265–276.e6. <https://doi.org/10.1016/j.neuron.2020.01.037>
- Pan, L., Alagapan, S., Franca, E., Brewer, G. J., & Wheeler, B. C. (2011). Propagation of action potential activity in a predefined microtunnel neural network. *Journal of Neural Engineering*, 8(4), 46031. <https://doi.org/10.1088/1741-2560/8/4/046031>
- Pan, L., Alagapan, S., Franca, E., DeMarse, T., Brewer, G. J., & Wheeler, B. C. (2014). Large extracellular spikes recordable from axons in microtunnels. *IEEE Transactions on Neural Systems and Rehabilitation Engineering: A Publication of the IEEE Engineering in Medicine and Biology Society*, 22(3), 453–459. <https://doi.org/10.1109/TNSRE.2013.2289911>
- Panaitov, G., Thiery, S., Hofmann, B., & Offenhäusser, A. (2011). Fabrication of gold micro-spine structures for improvement of cell/device adhesion. *Microelectronic Engineering*, 88(8), 1840–1844. <https://doi.org/10.1016/j.mee.2010.12.074>
- Panzera, L. C., & Hoppa, M. B. (2019). Genetically Encoded Voltage Indicators Are Illuminating Subcellular Physiology of the Axon. *Frontiers in Cellular Neuroscience*, 13, 52. <https://doi.org/10.3389/fncel.2019.00052>
- Papatheodoropoulos, C. (2008). A possible role of ectopic action potentials in the in vitro hippocampal sharp wave–ripple complexes. *Neuroscience*, 157(3), 495–501. <https://doi.org/10.1016/j.neuroscience.2008.09.040>
- Park, J. W., Vahidi, B., Taylor, A. M., Rhee, S. W., & Jeon, N. L. (2006). Microfluidic culture platform for neuroscience research. *Nature Protocols*, 1(4), 2128–2136. <https://doi.org/10.1038/nprot.2006.316>
- Park, M., Oh, E., Seo, J., Kim, M.-H., Cho, H., Choi, J. Y., Lee, H., & Choi, I. S. (2016). Control over Neurite Directionality and Neurite Elongation on Anisotropic Micropillar Arrays. *Small*, 12(9), 1148–1152. <https://doi.org/10.1002/SMLL.201501896>
- Park, M. U., Bae, Y., Lee, K.-S., Song, J. H., Lee, S.-M., & Yoo, K.-H. (2021). Collective dynamics of neuronal activities in various modular networks. *Lab on a Chip*, 17. <https://doi.org/10.1039/D0LC01106A>

- Perge, J. A., Niven, J. E., Mugnaini, E., Balasubramanian, V., & Sterling, P. (2012). Why do axons differ in caliber? *Journal of Neuroscience*, 32(2), 626–638. <https://doi.org/10.1523/JNEUROSCI.4254-11.2012>
- Peterka, D. S., Takahashi, H., & Yuste, R. (2011). Imaging Voltage in Neurons. *Neuron*, 69(1), 9–21. <https://doi.org/10.1016/J.NEURON.2010.12.010>
- Peyrin, J. M., Deleglise, B., Saias, L., Vignes, M., Gougis, P., Magnifico, S., Betuing, S., Pietri, M., Caboche, J., Vanhoutte, P., Viovy, J. L., & Brugg, B. (2011). Axon diodes for the reconstruction of oriented neuronal networks in microfluidic chambers. *Lab on a Chip*, 11(21), 3663–3673. <https://doi.org/10.1039/c1lc20014c>
- Pinault, D. (1995). Backpropagation of action potentials generated at ectopic axonal loci: hypothesis that axon terminals integrate local environmental signals. *Brain Research Reviews*, 21(1), 42–92. [https://doi.org/10.1016/0165-0173\(95\)00004-M](https://doi.org/10.1016/0165-0173(95)00004-M)
- Pinto-Costa, R., Sousa, S. C., Leite, S. C., Nogueira-Rodrigues, J., da Silva, T. F., Machado, D., Marques, J., Costa, A. C., Liz, M. A., Bartolini, F., Brites, P., Costell, M., Fässler, R., & Sousa, M. M. (2020). Profilin 1 delivery tunes cytoskeletal dynamics toward CNS axon regeneration. *Journal of Clinical Investigation*, 130(4), 2024–2040. <https://doi.org/10.1172/JCI125771>
- Popovic, M. A., Foust, A. J., McCormick, D. A., & Zecevic, D. (2011). The spatio-temporal characteristics of action potential initiation in layer 5 pyramidal neurons: A voltage imaging study. *Journal of Physiology*, 589(17), 4167–4187. <https://doi.org/10.1113/jphysiol.2011.209015>
- Potter, S. M., & DeMarse, T. B. (2001). A new approach to neural cell culture for long-term studies. *Journal of Neuroscience Methods*, 110(1–2). [https://doi.org/10.1016/S0165-0270\(01\)00412-5](https://doi.org/10.1016/S0165-0270(01)00412-5)
- Radivojevic, M., Franke, F., Altermatt, M., Müller, J., Hierlemann, A., & Bakkum, D. J. J. (2017). Tracking individual action potentials throughout mammalian axonal arbors. *ELife*, 6. <https://doi.org/10.7554/eLife.30198>
- Raj, V., Jagadish, C., & Gautam, V. (2021). Understanding, engineering, and modulating the growth of neural networks: An interdisciplinary approach. *Biophysics Reviews*, 2(2), 021303. <https://doi.org/10.1063/5.0043014>
- Rall, W. (1977). Core Conductor Theory and Cable Properties of Neurons. In *Handbook of*

- physiology, cellular biology of neurons*. Bethesda, MD: American Physiological Society.  
<https://doi.org/10.1002/cphy.cp010103>
- Rama, S., Zbili, M., & Debanne, D. (2018). Signal propagation along the axon. *Current Opinion in Neurobiology*, 51, 37–44. <https://doi.org/10.1016/J.CONB.2018.02.017>
- Ramon y Cajal, S., & May, R. M. (1928). *Degeneration and regeneration of the nervous system* (Vol. 2). Haffner Publishing Co.
- Raposo, C., & Schwartz, M. (2014). Glial Scar and Immune Cell Involvement in Tissue Remodeling and Repair Following Acute CNS Injuries. *Glia*, 62(11), 1895–1904. <https://doi.org/10.1002/glia.22676>
- Rasband, M. N. (2010). Clustered K<sup>+</sup> channel complexes in axons. In *Neuroscience Letters* (Vol. 486, Issue 2, pp. 101–106). NIH Public Access. <https://doi.org/10.1016/j.neulet.2010.08.081>
- Rey, H. G., Pedreira, C., & Quiñero, R. (2015). Past, present and future of spike sorting techniques. *Brain Research Bulletin*, 119, 106–117. <https://doi.org/10.1016/j.brainresbull.2015.04.007>
- Rezakhaniha, R., Agianniotis, A., Schrauwen, J. T. C., Griffa, A., Sage, D., Bouten, C. V. C., van de Vosse, F. N., Unser, M., & Stergiopoulos, N. (2012). Experimental investigation of collagen waviness and orientation in the arterial adventitia using confocal laser scanning microscopy. *Biomechanics and Modeling in Mechanobiology*, 11(3–4), 461–473. <https://doi.org/10.1007/s10237-011-0325-z>
- Rishal, I., & Fainzilber, M. (2014). Axon–soma communication in neuronal injury. *Nature Reviews Neuroscience*, 15(1), 32–42. <https://doi.org/10.1038/nrn3609>
- Ritzau-Jost, A., Tsintsadze, T., Krueger, M., Ader, J., Bechmann, I., Eilers, J., Barbour, B., Smith, S. M., & Hallermann, S. (2021). Large, Stable Spikes Exhibit Differential Broadening in Excitatory and Inhibitory Neocortical Boutons. *Cell Reports*, 34(2), 108612. <https://doi.org/10.1016/j.celrep.2020.108612>
- Robinson, J. T., Jorgolli, M., Shalek, A. K., Yoon, M.-H., Gertner, R. S., & Park, H. (2012). Vertical nanowire electrode arrays as a scalable platform for intracellular interfacing to neuronal circuits. *Nature Nanotechnology*, 7(3), 180–184. <https://doi.org/10.1038/nnano.2011.249>

- Rost, B. R., Schneider-Warme, F., Schmitz, D., & Hegemann, P. (2017). Optogenetic Tools for Subcellular Applications in Neuroscience. In *Neuron* (Vol. 96, Issue 3, pp. 572–603). Cell Press. <https://doi.org/10.1016/j.neuron.2017.09.047>
- Roth, S., Bisbal, M., Brocard, J., Bugnicourt, G., Saoudi, Y., Andrieux, A., Gory-Fauré, S., & Villard, C. (2012). How morphological constraints affect axonal polarity in mouse neurons. *PLoS ONE*, 7(3), 33623. <https://doi.org/10.1371/journal.pone.0033623>
- Rowan, M. J. M., & Christie, J. M. (2017). Rapid State-Dependent Alteration in Kv3 Channel Availability Drives Flexible Synaptic Signaling Dependent on Somatic Subthreshold Depolarization. *Cell Reports*, 18(8), 2018–2029. <https://doi.org/10.1016/j.celrep.2017.01.068>
- Rowan, M. J. M., DelCanto, G., Yu, J. J., Kamasawa, N., & Christie, J. M. (2016). Synapse-Level Determination of Action Potential Duration by K<sup>+</sup> Channel Clustering in Axons. *Neuron*, 91(2), 370–383. <https://doi.org/10.1016/j.neuron.2016.05.035>
- Roy, J., Kennedy, T. E., & Costantino, S. (2013). Engineered cell culture substrates for axon guidance studies: moving beyond proof of concept. *Lab on a Chip*, 13(4), 498. <https://doi.org/10.1039/c2lc41002h>
- Roy, S. (2016). Waves, rings, and trails: The scenic landscape of axonal actin. *J Cell Biol*, 212(2), 131–134. <https://doi.org/10.1083/jcb.201511016>
- Rueden, C. T., Schindelin, J., Hiner, M. C., DeZonia, B. E., Walter, A. E., Arena, E. T., & Eliceiri, K. W. (2017). ImageJ2: ImageJ for the next generation of scientific image data. *BMC Bioinformatics*, 18(1), 529. <https://doi.org/10.1186/s12859-017-1934-z>
- Rumelhart, D. E., Hinton, G. E., & Williams, R. J. (1986). Learning representations by back-propagating errors. *Nature*. <https://doi.org/10.1038/323533a0>
- Rushton, W. A. H. (1951). A theory of the effects of fibre size in medullated nerve. *The Journal of Physiology*, 115(1), 101–122. <https://doi.org/10.1113/jphysiol.1951.sp004655>
- Ryu, J. R., Jang, M. J., Jo, Y., Joo, S., Lee, D. H., Lee, B. Y., Nam, Y., & Sun, W. (2016). Synaptic compartmentalization by micropatterned masking of a surface adhesive cue in cultured neurons. *Biomaterials*, 92, 46–56. <https://doi.org/10.1016/j.biomaterials.2016.03.027>
- Ryu, J. R., Kim, J. H., Cho, H. M., Jo, Y., Lee, B., Joo, S., Chae, U., Nam, Y., Cho, I.-J., & Sun,

- W. (2019). A monitoring system for axonal growth dynamics using micropatterns of permissive and Semaphorin 3F chemorepulsive signals. *Lab on a Chip*. <https://doi.org/10.1039/C8LC00845K>
- Samhaber, R., Schottdorf, M., El Hady, A., Bröking, K., Daus, A., Thielemann, C., Stühmer, W., & Wolf, F. (2016). Growing neuronal islands on multi-electrode arrays using an accurate positioning- $\mu$ CP device. *Journal of Neuroscience Methods*, 257, 194–203. <https://doi.org/10.1016/j.jneumeth.2015.09.022>
- Santoro, F., Panaitov, G., & Andreas, O. (2014). Defined Patterns of Neuronal Networks on 3D Thiol-functionalized Microstructures. *Nano Letters*.
- Sardi, S., Vardi, R., Sheinin, A., Goldental, A., & Kanter, I. (2017). New Types of Experiments Reveal that a Neuron Functions as Multiple Independent Threshold Units. *Scientific Reports*, 7(1), 18036. <https://doi.org/10.1038/s41598-017-18363-1>
- Sasaki, T. (2013). The axon as a unique computational unit in neurons. In *Neuroscience Research* (Vol. 75, Issue 2, pp. 83–88). <https://doi.org/10.1016/j.neures.2012.12.004>
- Sasaki, T., Matsuki, N., & Ikegaya, Y. (2011). Action-potential modulation during axonal conduction. *Science*, 331(6017), 599–601. <https://doi.org/10.1126/science.1197598>
- Sasaki, T., Matsuki, N., & Ikegaya, Y. (2012a). Effects of axonal topology on the somatic modulation of synaptic outputs. *Journal of Neuroscience*, 32(8), 2868–2876. <https://doi.org/10.1523/JNEUROSCI.5365-11.2012>
- Sasaki, T., Matsuki, N., & Ikegaya, Y. (2012b). Targeted axon-attached recording with fluorescent patch-clamp pipettes in brain slices. *Nature Protocols*, 7(6), 1228–1234. <https://doi.org/10.1038/nprot.2012.061>
- Schmitz, D., Schuchmann, S., Fisahn, A., Draguhn, A., Buhl, E. H., Petrasch-Parwez, E., Dermietzel, R., Heinemann, U., & Traub, R. D. (2001). Axo-Axonal Coupling: A Novel Mechanism for Ultrafast Neuronal Communication. *Neuron*, 31(5). <http://www.ncbi.nlm.nih.gov/pubmed/11567620>
- Schroeter, M. S., Charlesworth, P., Kitzbichler, M. G., Paulsen, O., & Bullmore, E. T. (2015). Emergence of rich-club topology and coordinated dynamics in development of hippocampal functional networks In vitro. *Journal of Neuroscience*, 35(14), 5459–5470. <https://doi.org/10.1523/JNEUROSCI.4259-14.2015>

- Schröter, M., Paulsen, O., & Bullmore, E. T. (2017). Micro-connectomics: Probing the organization of neuronal networks at the cellular scale. In *Nature Reviews Neuroscience* (Vol. 18, Issue 3, pp. 131–146). Nature Publishing Group. <https://doi.org/10.1038/nrn.2016.182>
- Scott, L. L., Hage, T. A., & Golding, N. L. (2007). Weak action potential backpropagation is associated with high-frequency axonal firing capability in principal neurons of the gerbil medial superior olive. *Journal of Physiology*, 583(2), 647–661. <https://doi.org/10.1113/jphysiol.2007.136366>
- Seo, J., Kim, J., Joo, S., Choi, J. Y., Kang, K., Cho, W. K., Choi, I. S., Yu Choi, J., Kang, K., Kyung Cho, W., Choi, I. S., Seo, J., Kim, J., Joo, S., Choi, J. Y., Choi, I. S., Kang, K., & Cho, W. K. (2018). Nanotopography-Promoted Formation of Axon Collateral Branches of Hippocampal Neurons. *Small*, 1801763. <https://doi.org/10.1002/smll.201801763>
- Seymour, J. P., Wu, F., Wise, K. D., & Yoon, E. (2017). State-of-the-art MEMS and microsystem tools for brain research. *Microsystems & Nanoengineering*, 3, 16066. <https://doi.org/10.1038/micronano.2016.66>
- Sheffield, M. E. J., Best, T. K., Mensh, B. D., Kath, W. L., & Spruston, N. (2011). Slow integration leads to persistent action potential firing in distal axons of coupled interneurons. *Nature Neuroscience*, 14(2), 200–207. <https://doi.org/10.1038/nn.2728>
- Sheffield, M. E. J. J., Edgerton, G. B., Heuermann, R. J., Deemyad, T., Mensh, B. D., & Spruston, N. (2013). Mechanisms of retroaxonal barrage firing in hippocampal interneurons. *The Journal of Physiology*, 591(19), 4793–4805. <https://doi.org/10.1113/jphysiol.2013.258418>
- Shimba, K., Kotani, K., & Jimbo, Y. (2021). Microfabricated Device to Record Axonal Conduction under Pharmacological Treatment for Functional Evaluation of Axon Ion Channel. *IEEE Transactions on Biomedical Engineering*, PP, 1–1. <https://doi.org/10.1109/TBME.2021.3078473>
- Shmoel, N., Rabieh, N., Ojovan, S. M., Erez, H., Maydan, E., & Spira, M. E. (2016). Multisite electrophysiological recordings by self-assembled loose-patch-like junctions between cultured hippocampal neurons and mushroom-shaped microelectrodes. *Scientific Reports*, 6, 27110. <https://doi.org/10.1038/srep27110>
- Shirao, A. B., Kung, F. H., Omelchenko, A., Schloss, R. S., Boustany, N. N., Zahn, J. D.,

- Yarmush, M. L., & Firestein, B. L. (2018). Microfluidic platforms for the study of neuronal injury in vitro. *Biotechnology and Bioengineering*, 115(4), 815–830. <https://doi.org/10.1002/bit.26519>
- Shu, Y., Duque, A., Yu, Y., Haider, B., & McCormick, D. A. (2007). Properties of Action-Potential Initiation in Neocortical Pyramidal Cells: Evidence From Whole Cell Axon Recordings. *Journal of Neurophysiology*, 97(1), 746–760. <https://doi.org/10.1152/jn.00922.2006>
- Sileo, L., Pisanello, F., Quarta, L., Maccione, A., Simi, A., Berdondini, L., Vittorio, M. De, & Martiradonna, L. (2013). Electrical coupling of mammalian neurons to microelectrodes with 3D nanoprotusions. *Microelectronic Engineering*, 111, 384–390. <https://doi.org/10.1016/j.mee.2013.03.152>
- Simitzi, C., Ranella, A., & Stratakis, E. (2017). Controlling the morphology and outgrowth of nerve and neuroglial cells: The effect of surface topography. *Acta Biomaterialia*, 51, 21–52. <https://doi.org/10.1016/j.actbio.2017.01.023>
- Sobotzik, J. M., Sie, J. M., Politi, C., Del Turco, D., Bennett, V., Deller, T., & Schultz, C. (2009). AnkyrinG is required to maintain axo-dendritic polarity in vivo. *Proceedings of the National Academy of Sciences of the United States of America*, 106(41), 17564–17569. <https://doi.org/10.1073/pnas.0909267106>
- Sousa, D. M., Conceição, F., Silva, D. I., Leitão, L., Neto, E., Alves, C. J., Alencastre, I. S., Herzog, H., Aguiar, P., & Lamghari, M. (2016). Ablation of  $\gamma$  receptor impairs osteoclast bone-resorbing activity. *Scientific Reports*, 6, 33470. <https://doi.org/10.1038/srep33470>
- Spira, M. E., & Hai, A. (2013). Multi-electrode array technologies for neuroscience and cardiology. *Nature Nanotechnology*, 8(2), 83–94. <https://doi.org/10.1038/nnano.2012.265>
- Spira, M. E., Shmoel, N., Huang, S.-H. M., & Erez, H. (2018). Multisite Attenuated Intracellular Recordings by Extracellular Multielectrode Arrays, a Perspective. *Frontiers in Neuroscience*, 12, 212. <https://doi.org/10.3389/fnins.2018.00212>
- Sporns, O., & Betzel, R. F. (2016). Modular brain networks. *Annual Review of Psychology*, 67, 613–640. <https://doi.org/10.1146/annurev-psych-122414-033634>
- Stasheff, S. F., Hines, M., & Wilson, W. A. (1993). Axon terminal hyperexcitability associated with epileptogenesis in vitro. I. Origin of ectopic spikes. *Journal of Neurophysiology*, 70(3),

961–975. <https://doi.org/10.1152/jn.1993.70.3.961>

- Steinmetz, N. A., Aydin, C., Lebedeva, A., Okun, M., Pachitariu, M., Bauza, M., Beau, M., Bhagat, J., Böhm, C., Broux, M., Chen, S., Colonell, J., Gardner, R. J., Karsh, B., Kloosterman, F., Kostadinov, D., Mora-Lopez, C., O'Callaghan, J., Park, J., ... Harris, T. D. (2021). Neuropixels 2.0: A miniaturized high-density probe for stable, long-term brain recordings. *Science*, 372(6539). <https://doi.org/10.1126/science.abf4588>
- Stuart, G. J., & Sakmann, B. (1994). Active propagation of somatic action potentials into neocortical pyramidal cell dendrites. *Nature*, 367(6458), 69–72. <https://doi.org/10.1038/367069a0>
- Stuart, G., Schiller, J., & Sakmann, B. (1997). Action potential initiation and propagation in rat neocortical pyramidal neurons. *Journal of Physiology*, 505(3), 617–632. <https://doi.org/10.1111/j.1469-7793.1997.617ba.x>
- Susloparova, A., Halliez, S., Begard, S., Colin, M., Buée, L., Pecqueur, S., Alibart, F., Thomy, V., Arscott, S., Pallecchi, E., & Coffinier, Y. (2021). Low impedance and highly transparent microelectrode arrays (MEA) for in vitro neuron electrical activity probing. *Sensors and Actuators, B: Chemical*, 327, 128895. <https://doi.org/10.1016/j.snb.2020.128895>
- Suzuki, M., Ikeda, K., Yamaguchi, M., Kudoh, S. N., Yokoyama, K., Satoh, R., Ito, D., Nagayama, M., Uchida, T., & Gohara, K. (2013). Neuronal cell patterning on a multi-electrode array for a network analysis platform. *Biomaterials*, 34(21), 5210–5217. <https://doi.org/10.1016/J.BIOMATERIALS.2013.03.042>
- Szabadics, J., Varga, C., Molnár, G., Oláh, S., Barzó, P., & Tamás, G. (2006). Excitatory effect of GABAergic axo-axonic cells in cortical microcircuits. *Science*, 311(5758), 233–235. <https://doi.org/10.1126/science.1121325>
- Taylor, A. M., Blurton-Jones, M., Rhee, S. W., Cribbs, D. H., Cotman, C. W., & Jeon, N. L. (2005). A microfluidic culture platform for CNS axonal injury, regeneration and transport. *Nature Methods*, 2(8), 599–605. <https://doi.org/10.1038/nmeth777>
- Taylor, A. M., Rhee, S. W., Tu, C. H., Cribbs, D. H., Cotman, C. W., & Jeon, N. L. (2003). Microfluidic multicompartiment device for neuroscience research. *Langmuir*, 19(5), 1551–1556. <https://doi.org/10.1021/la026417v>
- Teixeira, H., Dias, C., Aguiar, P., & Ventura, J. (2020). Gold-Mushroom Microelectrode Arrays and the Quest for Intracellular-Like Recordings: Perspectives and Outlooks. *Advanced*

- Tervo, D. G. R., Hwang, B. Y., Viswanathan, S., Gaj, T., Lavzin, M., Ritola, K. D., Lindo, S., Michael, S., Kuleshova, E., Ojala, D., Huang, C. C., Gerfen, C. R., Schiller, J., Dudman, J. T., Hantman, A. W., Looger, L. L., Schaffer, D. V., & Karpova, A. Y. (2016). A Designer AAV Variant Permits Efficient Retrograde Access to Projection Neurons. *Neuron*, 92(2), 372–382. <https://doi.org/10.1016/j.neuron.2016.09.021>
- Thome, C., Roth, F. C., Obermayer, J., Yanez, A., Draguhn, A., & Egorov, A. V. (2018). Synaptic entrainment of ectopic action potential generation in hippocampal pyramidal neurons. *The Journal of Physiology*, 596(21), 5237–5249. <https://doi.org/10.1113/JP276720>
- Tian, B., Cohen-Karni, T., Qing, Q., Duan, X., Xie, P., & Lieber, C. M. (2010). Three-Dimensional, Flexible Nanoscale Field-Effect Transistors as Localized Bioprobes. *Science*, 329(5993), 830–834. <https://doi.org/10.1126/science.1192033>
- Tovar, K. R., Bridges, D. C., Wu, B., Randall, C., Audouard, M., Jang, J., Hansma, P. K., & Kosik, K. S. (2018). Action potential propagation recorded from single axonal arbors using multielectrode arrays. *Journal of Neurophysiology*, 120(1), 306–320. <https://doi.org/10.1152/jn.00659.2017>
- Traub, R. D., Cunningham, M. O., Gloveli, T., LeBeau, F. E. N., Bibbig, A., Buhl, E. H., & Whittington, M. A. (2003). GABA-enhanced collective behavior in neuronal axons underlies persistent gamma-frequency oscillations. *Proceedings of the National Academy of Sciences of the United States of America*, 100(19), 11047–11052. <https://doi.org/10.1073/pnas.1934854100>
- Traub, Roger D., Bibbig, A., Piechotta, A., Draguhn, A., & Schmitz, D. (2001). Synaptic and nonsynaptic contributions to giant IPSPs and ectopic spikes induced by 4-aminopyridine in the hippocampus in vitro. *Journal of Neurophysiology*, 85(3), 1246–1256. <https://doi.org/10.1152/jn.2001.85.3.1246>
- Traub, Roger D., Schmitz, D., Maier, N., Whittington, M. A., & Draguhn, A. (2012). Axonal properties determine somatic firing in a model of in vitro CA1 hippocampal sharp wave/ripples and persistent gamma oscillations. *European Journal of Neuroscience*, 36(5), 2650–2660. <https://doi.org/10.1111/j.1460-9568.2012.08184.x>
- Traub, Roger D., Whittington, M. A., Maier, N., Schmitz, D., & Nagy, J. I. (2020). Could electrical

- coupling contribute to the formation of cell assemblies? *Reviews in the Neurosciences*, 31(2), 121–141. <https://doi.org/10.1515/revneuro-2019-0059>
- Traub, Roger D, & Miles, R. (1991). *Neuronal Networks of the Hippocampus*. Cambridge University Press.
- Trigo, F. F. (2019). Antidromic Analog Signaling. *Frontiers in Cellular Neuroscience*, 13. <https://doi.org/10.3389/fncel.2019.00354>
- Tsantoulas, C., Farmer, C., Machado, P., Baba, K., McMahon, S. B., & Raouf, R. (2013). Probing Functional Properties of Nociceptive Axons Using a Microfluidic Culture System. *PLoS ONE*, 8(11), e80722. <https://doi.org/10.1371/journal.pone.0080722>
- Vandael, D., Okamoto, Y., Borges-Merjane, C., Vargas-Barroso, V., Suter, B. A., & Jonas, P. (2021). Subcellular patch-clamp techniques for single-bouton stimulation and simultaneous pre- and postsynaptic recording at cortical synapses. *Nature Protocols*, 16(6), 2947–2967. <https://doi.org/10.1038/s41596-021-00526-0>
- VanDersarl, J. J., Xu, A. M., & Melosh, N. A. (2012). Nanostraws for Direct Fluidic Intracellular Access. *Nano Letters*, 12(8), 3881–3886. <https://doi.org/10.1021/nl204051v>
- Vivekananda, U., Novak, P., Bello, O. D., Korchev, Y. E., Krishnakumar, S. S., Volynski, K. E., & Kullmann, D. M. (2017). Kv1.1 channelopathy abolishes presynaptic spike width modulation by subthreshold somatic depolarization. *Proceedings of the National Academy of Sciences of the United States of America*, 114(9), 2395–2400. <https://doi.org/10.1073/pnas.1608763114>
- Vogt, A. K., Wrobel, G., Meyer, W., Knoll, W., & Offenhäusser, A. (2005). Synaptic plasticity in micropatterned neuronal networks. *Biomaterials*, 26(15), 2549–2557. <https://doi.org/10.1016/J.BIOMATERIALS.2004.07.031>
- Vogt, K. E., Gerharz, S., Graham, J., & Canepari, M. (2011). High-resolution simultaneous voltage and Ca<sup>2+</sup> imaging. *Journal of Physiology*, 589(3), 489–494. <https://doi.org/10.1113/jphysiol.2010.200220>
- Wagenaar, D. A., Madhavan, R., Pine, J., & Potter, S. M. (2005). Controlling Bursting in Cortical Cultures with Closed-Loop Multi-Electrode Stimulation. *Journal of Neuroscience*, 25(3), 680–688. <https://doi.org/10.1523/JNEUROSCI.4209-04.2005>
- Wang, L., Riss, M., Buitrago, J. O., & Claverol-Tinturé, E. (2012). Biophysics of microchannel-

- enabled neuron–electrode interfaces. *Journal of Neural Engineering*, 9(2), 026010. <https://doi.org/10.1088/1741-2560/9/2/026010>
- Wang, T., Li, W., Martin, S., Papadopoulos, A., Joensuu, M., Liu, C., Jiang, A., Shamsollahi, G., Amor, R., Lanoue, V., Padmanabhan, P., & Meunier, F. A. (2020). Radial contractility of actomyosin rings facilitates axonal trafficking and structural stability. *Journal of Cell Biology*, 219(5). <https://doi.org/10.1083/jcb.201902001>
- Wang, W., Kim, C. K., & Ting, A. Y. (2019). Molecular tools for imaging and recording neuronal activity. *Nature Chemical Biology*, 15(2), 101–110. <https://doi.org/10.1038/s41589-018-0207-0>
- Wang, X., Wang, S., Wang, W., Duan, J., Zhang, M., Lv, X., Niu, C., Tan, C., Wu, Y., Yang, J., Hu, S., & Xing, J. (2016). A novel intrinsic analgesic mechanism: The enhancement of the conduction failure along polymodal nociceptive C-fibers. *Pain*, 157(10), 2235–2247. <https://doi.org/10.1097/j.pain.0000000000000632>
- Wang, Y., Barakat, A., & Zhou, H. (2010). Electrotonic coupling between pyramidal neurons in the neocortex. *PLoS ONE*, 5(4), 10253. <https://doi.org/10.1371/journal.pone.0010253>
- Waxman, S. G. (1980). Determinants of conduction velocity in myelinated nerve fibers. *Muscle & Nerve*, 3(2), 141–150. <https://doi.org/10.1002/mus.880030207>
- Weydert, S., Girardin, S., Cui, X., Zürcher, S., Peter, T., Wirz, R., Sterner, O., Stauffer, F., Aebersold, M. J., Tanner, S., Thompson-Steckel, G., Forró, C., Tosatti, S., & Vörös, J. (2019). A Versatile Protein and Cell Patterning Method Suitable for Long-Term Neural Cultures. *Langmuir*, 35(8), 2966–2975. <https://doi.org/10.1021/acs.langmuir.8b03730>
- Whittington, J. C. R., & Bogacz, R. (2019). Theories of Error Back-Propagation in the Brain. In *Trends in Cognitive Sciences* (Vol. 23, Issue 3, pp. 235–250). Elsevier Ltd. <https://doi.org/10.1016/j.tics.2018.12.005>
- Wijdenes, P., Ali, H., Armstrong, R., Zaidi, W., Dalton, C., & Syed, N. I. (2016). A novel bio-mimicking, planar nano-edge microelectrode enables enhanced long-term neural recording. *Scientific Reports*, 6(1), 34553. <https://doi.org/10.1038/srep34553>
- Winckler, B., Forscher, P., & Mellman, I. (1999). A diffusion barrier maintains distribution of membrane proteins in polarized neurons. *Nature*, 397(6721), 698–701. <https://doi.org/10.1038/17806>

- Xie, C., Hanson, L., Xie, W., Lin, Z., Cui, B., & Cui, Y. (2010). Noninvasive Neuron Pinning with Nanopillar Arrays. *Nano Letters*, 10(10), 4020–4024. <https://doi.org/10.1021/nl101950x>
- Xie, C., Lin, Z., Hanson, L., Cui, Y., & Cui, B. (2012). Intracellular recording of action potentials by nanopillar electroporation. *Nature Nanotechnology*, 7(3), 185–190. <https://doi.org/10.1038/nnano.2012.8>
- Xu, D., Mo, J., Xie, X., & Hu, N. (2021). In-Cell Nanoelectronics: Opening the Door to Intracellular Electrophysiology. *Nano-Micro Letters*, 13(1), 1–27. <https://doi.org/10.1007/s40820-021-00655-x>
- Xu, K., Zhong, G., & Zhuang, X. (2013). Actin, spectrin, and associated proteins form a periodic cytoskeletal structure in axons. *Science*, 339(6118), 452–456. <https://doi.org/10.1126/science.1232251>
- Xu, L., Hu, C., Huang, Q., Jin, K., Zhao, P., Wang, D., Hou, W., Dong, L., Hu, S., & Ma, H. (2021). Trends and recent development of the microelectrode arrays (MEAs). In *Biosensors and Bioelectronics* (Vol. 175, p. 112854). Elsevier Ltd. <https://doi.org/10.1016/j.bios.2020.112854>
- Yamamoto, H., Matsumura, R., Takaoki, H., Katsurabayashi, S., Hirano-Iwata, A., & Niwano, M. (2016). Unidirectional signal propagation in primary neurons micropatterned at a single-cell resolution. *Applied Physics Letters*, 109(4), 043703. <https://doi.org/10.1063/1.4959836>
- Yamamoto, Hideaki, Moriya, S., Ide, K., Hayakawa, T., Akima, H., Sato, S., Kubota, S., Tanii, T., Niwano, M., Teller, S., Soriano, J., & Hirano-Iwata, A. (2018). Impact of modular organization on dynamical richness in cortical networks. *Science Advances*, 4(11), eaau4914. <https://doi.org/10.1126/sciadv.aau4914>
- Yuan, X., Schröter, M., Obien, M. E. J., Fiscella, M., Gong, W., Kikuchi, T., Odawara, A., Noji, S., Suzuki, I., Takahashi, J., Hierlemann, A., & Frey, U. (2020). Versatile live-cell activity analysis platform for characterization of neuronal dynamics at single-cell and network level. *Nature Communications*, 11(1), 4854. <https://doi.org/10.1038/s41467-020-18620-4>
- Zbili, Mickael, & Debanne, D. (2019). Past and Future of Analog-Digital Modulation of Synaptic Transmission. *Frontiers in Cellular Neuroscience*, 13, 160. <https://doi.org/10.3389/fncel.2019.00160>
- Zbili, Mickaël, Rama, S., Yger, P., Inglebert, Y., Boumedine-Guignon, N., Fronzaroli-Moliniere,

- L., Brette, R., Russier, M., & Debanne, D. (2020). Axonal Na<sup>+</sup> channels detect and transmit levels of input synchrony in local brain circuits. *Science Advances*, 6(19), eaay4313. <https://doi.org/10.1126/sciadv.aay4313>
- Zečević, D. (1996). Multiple spike-initiation zones in single neurons revealed by voltage-sensitive dyes. *Nature*, 381(6580), 322–325. <https://doi.org/10.1038/381322a0>
- Zeck, G., Jetter, F., Channappa, L., Bertotti, G., & Thewes, R. (2017). Electrical Imaging: Investigating Cellular Function at High Resolution. *Advanced Biosystems*, 1(11), 1700107. <https://doi.org/10.1002/adbi.201700107>
- Zhang, Q. fang, Li, H., Chen, M., Guo, A., Wen, Y., & Poo, M. ming. (2018). Functional organization of intrinsic and feedback presynaptic inputs in the primary visual cortex. *Proceedings of the National Academy of Sciences of the United States of America*, 115(22), E5174–E5182. <https://doi.org/10.1073/pnas.1719711115>
- Ziv, N. E., & Spira, M. E. (1995). Axotomy induces a transient and localized elevation of the free intracellular calcium concentration to the millimolar range. *Journal of Neurophysiology*, 74(6), 2625–2637. <https://doi.org/10.1152/jn.1995.74.6.2625>
- Zorrilla de San Martin, J., Trigo, F. F., & Kawaguchi, S. Y. (2017). Axonal GABAA receptors depolarize presynaptic terminals and facilitate transmitter release in cerebellar Purkinje cells. *Journal of Physiology*, 595(24), 7477–7493. <https://doi.org/10.1113/JP275369>

## **Annex**



# Improved *in vitro* electrophysiology using 3D-structured microelectrode arrays with a micro-mushrooms islets architecture capable of promoting topotaxis

José C Mateus<sup>1,2,3</sup>, Cátia D F Lopes<sup>1,2</sup>, Mónica Cerquido<sup>4</sup>,  
Luís Leitão<sup>1,2</sup>, Diana Leitão<sup>5</sup>, Susana Cardoso<sup>5</sup>, João Ventura<sup>4</sup>  
and Paulo Aguiar<sup>1,2</sup>

<sup>1</sup> INEB—Instituto de Engenharia Biomédica, Universidade do Porto, R. Alfredo Allen, 4200-135 Porto, Portugal

<sup>2</sup> i3S—Instituto de Investigação e Inovação em Saúde, Universidade do Porto, R. Alfredo Allen, 4200-135 Porto, Portugal

<sup>3</sup> Instituto de Ciências Biomédicas Abel Salazar (ICBAS), Universidade do Porto, R. Jorge de Viterbo Ferreira, 4050-313 Porto, Portugal

<sup>4</sup> Instituto de Física dos Materiais, Faculdade de Ciências (IFIMUP), Universidade do Porto, R. do Campo Alegre, 4169-007 Porto, Portugal

<sup>5</sup> Instituto de Engenharia de Sistemas e Computadores Microsistemas e Nanotecnologias (INESC-MN), R. Alves Redol, 1000-029, Lisboa, Portugal

E-mail: [pauloaguiar@ineb.up.pt](mailto:pauloaguiar@ineb.up.pt)

Received 4 December 2018, revised 11 February 2019

Accepted for publication 28 February 2019

Published 12 April 2019



CrossMark

## Novelty and significance


A novel MEA architecture with excellent electrophysiological recordings is presented, where planar microelectrodes are replaced by localized  $3 \times 3$  arrays of mushroom-shaped microstructures. The micro-mushrooms in this islets configuration are not for membrane engulfment but rather for somata entrapment and neurites embracement. As extracellular signals have a significant contribution from axons initial segment, this MEA design also addresses the electrode-neurites electrical coupling. These islets act as strong physical cues, causing topotaxis and increasing by two-fold the probability for somata to localize in the islets. We carry this topotaxis study not only with rat cortical neurons but also with human-derived SH-SY5Y cells.

## Abstract

**Objective.** Planar microelectrode arrays are widely used in neuroscience but have relatively low electrical coupling and signal-to-noise ratio (SNR) in electrophysiology recordings. Strong efforts are therefore being made in improving microelectrode arrays (MEAs) performance, exploring both the microelectrode's shape and the array's architecture. Topographical features can be used in MEAs for promoting neuron-microelectrode contact, making 3D-microstructured MEAs an interesting design strategy for better electrophysiology measurements. **Approach.** Here, we present a novel MEA architecture, where planar microelectrodes are replaced by localized  $3 \times 3$  arrays of mushroom-shaped microstructures. Contrarily to previous studies, the purpose for the micro-mushrooms in this islets configuration is not membrane engulfment but rather entrapment, for somata, and embracement, for neurites. **Main results.** We show that these islet-like agglomerates of micro-mushrooms act as strong physical cues, causing topotaxis and increasing the probability by two-fold for somata to localize in the islets, and neurites to curl on the microelectrodes. Importantly, we carry this

topotaxis study not only with rat cortical neurons but also with human-derived SH-SY5Y cells. With recent evidence that extracellular signals have a significant contribution from axons initial segment it becomes clear that MEA designs should also address the electrode-neurites coupling. We detail the fabrication process of these chips, designed to be compatible with a standard MEA recording system, and make the computer-aided design (CAD) publically available. We also demonstrate the electrophysiological capabilities of this new MEA by electrochemical impedance spectroscopy and recordings of cortical and hippocampal neurons, showing excellent SNR. *Significance.* Overall this new MEA islets configuration has a significant impact in the array efficiency and contributes towards improved high yield and high fidelity/quality extracellular recordings from mammalian neurons.

**Keywords:** topotaxis and neuronal guidance, neurite-electrode interface, neuron-electrode interface, human-derived SH-SY5Y cells, mushroom-shaped microelectrodes, microelectrode array

 Supplementary material for this article is available [online](#)

(Some figures may appear in colour only in the online journal)

## 1. Introduction

Understanding neuronal dynamics in normal and pathological conditions requires precise electrophysiological measurements and detailed information about neuronal activity, as this is the proxy for neuronal function. Electrophysiology ‘on-a-chip’ in the form of microelectrode arrays (MEAs) allows for simultaneous, multi-site, noninvasive, long-term extracellular stimulation and recording of neuronal networks [1, 2]. Over the last decades, *in vitro* MEA recordings have helped describe fundamental properties of network activity patterns [3], plasticity [4] and have also shown promise from a clinical perspective in neurotoxicity research [5], pharmacological testing [6] or disease modelling [7]. Still, conventional MEA technology is impaired by relatively low signal-to-noise ratio (SNR) and yield of active/populated microelectrodes, which limits its potential applications [8]. Although the noise level of commercial MEAs is in the range of a few tens of  $\mu\text{V}$ , source signals are greatly attenuated (2–3 orders of magnitude) due to a very low neuron-microelectrode electrical coupling coefficient. Weak membrane potential fluctuations (e.g. subthreshold activity, slow frequency modulations, synaptic signals) are therefore not detected with planar MEAs [9, 10].

Recently, some groups have focused on improving the quality of the recorded signal by modifying the microelectrode’s topography. Of particular importance are the promising ad hoc tri-dimensional (3D)-structured microelectrodes that merge some of the advantages of both intracellular and extracellular recordings [9]. These include MEA structured with vertical micro- or nanoprotusions, e.g. nanopillars [11], nanotubes [12], nanowires [13, 14], nanostraws [15] and nanocylinders [16] (for reviews see [9, 17, 18]). In general, nanoprotusions function as cell-penetrating nanoprobe that either need spontaneous poration [12, 19], electroporation [11, 13] or plasmonic optoporation [16] to measure intracellular-like activity. The interface established between the cell and the microelectrode 3D structure has been a topic of great interest in recent reviews [20, 21]. Despite the promising

nanotechnologies proof-of-concept results [18], until now only a few studies have shown their capability to perform intracellular-like recordings from single mammalian neurons, following electroporation [13] or plasmonic optoporation [16].

The design of the 3D-structured microelectrodes has often taken inspiration from naturally occurring morphological structures dedicated to cell coupling, such as the synaptic cleft [22] or the shape (mushroom-like) and dimension of dendritic spines [23, 24]. In particular, work pioneered by Spira and collaborators have enabled intracellular-like recordings using mushroom-shaped extracellular microelectrodes (gM $\mu$ Es), due to the formation of a neuron-gM $\mu$ E high seal resistance ( $R_{\text{seal}}$ ) and an increase in the junctional membrane conductance [9]. First reported to record subthreshold synaptic signals in large invertebrate (*Aplysia californica*) neurons [23], these gM $\mu$ Es have more recently been used in ‘loose-patch-like’ configurations with rat hippocampal neurons failing to unequivocally record synaptic potentials [25]. While large *Aplysia californica* neurons (80  $\mu\text{m}$  diameter) tightly engulf gM $\mu$ Es through the formation of actin rings around the gM $\mu$ E stem [26], larger than 2–2.5  $\mu\text{m}$  mushroom-shaped caps preclude engulfment by the relatively small mammalian neurons (10–20  $\mu\text{m}$  diameter). However, producing smaller caps limits the junctional membrane conductance and significantly increases the impedance and noise level [27]. Other laboratories’ attempts to mimic the mushroom-shaped protusion at the nanoscale ( $\sim 500\text{nm}$ ) [28] have not yet succeeded in exhibiting the intracellular-like recordings, characterized by positive peaks in the mV range. Therefore, the translation of extracellular electrodes’ stable, multi-site and long-term intracellular-like recording capabilities to mammalian neurons remains challenging [10].

Low yield of active/populated microelectrodes is also a common problem in MEA experiments. Typically, conventional MEA cultures with standard cell densities register activity in less than half of the available microelectrodes [29]. As high  $R_{\text{seal}}$  is crucial for appropriate signal detection, somata and/or large neurites need to be in close vicinity with the sensing microelectrodes. Research groups tend to use high-densities

(>1000 cells mm<sup>-2</sup>) in cell plating to increase the probability of effective electrodes [1, 25], though such solution may bias the viability of the mature neuronal population. Besides, neuron-microelectrode proximity may change over time due to neuronal migration and/or death, which may impair long-term studies. An alternative approach consists in constraining neurons' localization to the electrodes recording sites through parylene small cages [30], nanopillars [31], 3D-wells made of carbon nanotubes [32], or micro-/nano-patterning techniques [33, 34]. Biochemical substrate functionalization has also been used to constrain localization, and used in both planar [33, 35–37] and 3D-structured microelectrodes [38]. None of these solutions are ideal though, as some lead to MEAs that (i) have very limited reusability, (ii) are costly, and (iii) require advanced microfabrication techniques. Biochemical substrate functionalization typically only works during the neuronal culture's initial stage, losing the ability to constrain neuron localization after some days *in vitro* (as neurons cover the remaining surface with extracellular matrix proteins).

The fact that topographical features can be used to manipulate neuron placement, growth and connectivity is supported by a growing body of knowledge demonstrating that neurons are affected by physical cues [34, 39–41]. Despite the interesting early findings that a single *Aplysia californica* neuron growth pattern is markedly altered in a highly dense (inter-interval <8  $\mu$ m) multi-gM $\mu$ Es substrate, without loss of functionality [26], no further studies have attempted to quantitatively assess how the topography of 3D-microstructured MEAs affects the localization of somata, the placement of neurites and the spatial organization of mammalian neuronal networks.

Here, we present our recent work involving the design, fabrication and performance assessment of a new MEA architecture alternative to the conventional planar MEAs. In our design, individual planar microelectrodes are replaced by islets of (3  $\times$  3) mushroom-shaped 3D microelectrodes (micro-mushrooms), in a configuration that can be seen as arrays of microelectrode arrays (AMEAs). These chips are made compatible with standard MEA commercial amplifier systems and can be adapted depending on the fabrication design and experimental needs. We describe the microfabrication procedure involved and assess the biocompatibility of the chip with mammalian neurons. We also demonstrate the topography effect on the spatial organization of individual primary embryonic rat cortical neurons and human-derived SH-SY5Y cells. The 3D microstructures influence the growth pattern, neurite guidance and somata localization in a way that enhances the coupling between cell structures and microelectrodes, with relevant improvements in the yield and quality of electrophysiological recordings. The electrophysiological properties of this chip configuration are analyzed here in terms of background noise, SNR and amplitude of the recorded signals.

## 2. Results and discussion

### 2.1. Microfabrication of 3D-microstructured MEAs

Two different configurations of 3D-microstructured arrays were developed and used in the experiments. The key new

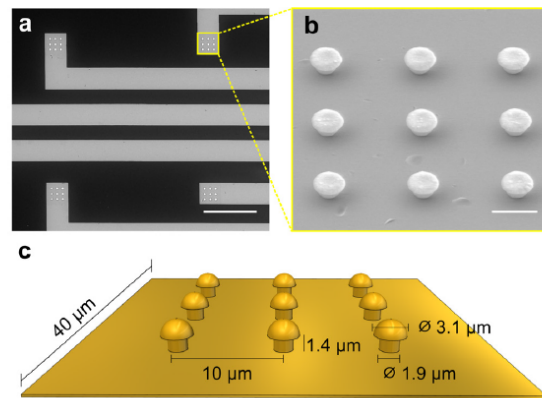


**Figure 1.** SEM images of 3D-microstructured microelectrodes. (a) Top view of the reading tracks and the islets where the micro-mushrooms are deposited (scale bar = 100  $\mu$ m). (b) Tilted image of a fabricated 3  $\times$  3 islet of micro-mushrooms (scale bar = 5  $\mu$ m). (c) Schematic diagram of one 3D-microstructured microelectrode with associated measurements.

configuration consists of a MEA where each microelectrode is composed of an islet of 3  $\times$  3 micro-mushrooms. These islets are in turn arranged in an array of roughly 8  $\times$  8 units (including ground electrodes). The optimization of the fabrication procedure which permitted fabricating well-ordered hemispherical mushroom caps has been recently reported by our teams [42]. A second, simpler, configuration was also fabricated and used in supporting experiments. In this configuration, the chip consists of a continuous large array of micro-mushrooms (2 mm  $\times$  2 mm) in a gold substrate area (figure S1, supporting information ([stacks.iop.org/JNE/16/036012/mmedia](https://stacks.iop.org/JNE/16/036012/mmedia))). These simpler chips have been recently shown by our teams to be able to record the synchronized and cooperative dynamics of astrocyte populations [43]. The inter-distance between adjacent micro-mushrooms in both configurations was kept at 10  $\mu$ m. The choice for a 3  $\times$  3 layout in the islets configuration was made to satisfy the following constraints: (a) spacing between the microelectrodes similar to mammalian neurons' cell body diameter ( $\sim$ 10  $\mu$ m); (b) base area of the islet in the same scale as conventional planar microelectrodes; and (c) potentiate that each islet would hold, on average, a single neuron.

The new developed 3D-microstructured MEA with the micro-mushroom islets was designed to be compatible with commercial MEA systems (Multi Channel Systems, Reutlingen, Germany), with contact pads in the same position as those of commercial 60-MEAs. Figure S2 in the supporting information shows the different levels of the computer aided design (CAD) diagram used for the fabrication of the MEA.

The microfabrication of the 3D-microstructured MEAs was analyzed through scanning electron microscopy (SEM), and figure 1 shows SEM images at two different magnifications. Figure 1(a) shows four different 3D-microstructured microelectrodes islets with the 3  $\times$  3 array of micro-mushrooms present in the final portion of each lead (figure 1(b)). SEM analysis revealed that the grown micro-mushrooms have

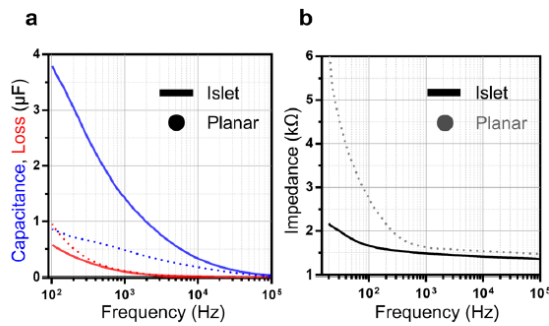


**Figure 2.** Electrical properties of the fabricated microelectrodes. (a) Capacitance and loss as a function of frequency for planar and for 3D-microstructured microelectrodes (islets), showing that the capacitance of the micro-mushrooms islets is higher in comparison to the planar microelectrodes. (b) Total impedance ( $|Z|$ ) as a function of frequency, showing that planar microelectrodes are more resistive than the 3D-microstructured microelectrodes.

an inter-distance of  $10\ \mu\text{m}$ , a cap diameter of  $3.1\ \mu\text{m}$ , a base of  $1.9\ \mu\text{m}$  and a stalk height of  $1.4\ \mu\text{m}$ , with an intrinsic variability on the dimensions below  $0.2\ \mu\text{m}$ . Figure 1(c) shows a schematic drawing of a representative 3D-microstructured microelectrode.

## 2.2. MEAs electrochemical characterization: impedance and noise level

Measurements of the planar and 3D-structured microelectrode's capacitance, impedance and electrical noise levels were performed to assess the advantages of using a micro-structured surface in comparison to a flat microelectrode (figure 2). The planar version used for comparison had the same specifications as the 3D-structured version except for the presence of the micro-mushrooms. Figure 2(a) shows the frequency dependence of the capacitance and loss components for planar and 3D-microstructured microelectrodes. The 3D-microstructured surface increases the capacitance of the electrode/electrolyte interface. Microelectrode impedance is an important characteristic for *in vitro* recordings, as low impedance values decrease the thermal noise and increase the SNR of the recorded signals. Standard commercial MEAs with  $30\ \mu\text{m}$  of diameter have impedance values in the order of hundreds of  $\text{k}\Omega$ . Figure 2(b) shows the total impedance spectrum measured in the frequency range from  $10^2$  to  $2 \times 10^5\ \text{Hz}$  for planar and 3D-microstructured microelectrodes. As expected, the impedance magnitude decreased with frequency and with the microelectrode surface area. The 3D-microstructured microelectrodes offer therefore lower impedances.

We also analyzed the power spectral density of the voltage noise (Sv), as a function of frequency for the 3D-microstructured microelectrodes. As expected, the magnitude of the noise decreases with the increase of the frequency. For frequencies above  $1\ \text{kHz}$ , the noise follows a  $1/f$ . This frequency dependence confirms that the thermal noise of the resistive elements dominates the electrical noise of the system. The voltage noise

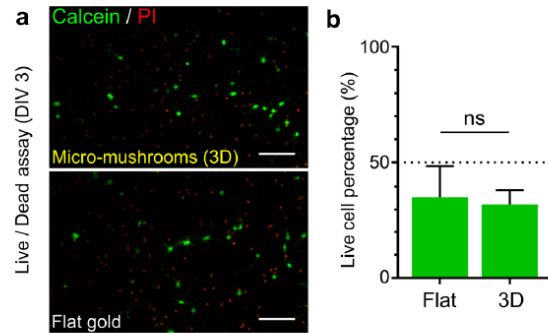


**Figure 3.** Rat cortical neurons live/dead assay at 3 d *in vitro* (DIV). (a) The number of live and dead cells was determined by a live/dead assay using the calcein-AM (live) and propidium iodide (dead) double staining (scale bars =  $100\ \mu\text{m}$ ). (b) Bar graph showing the percentage of live cells. Results are expressed as mean percentage  $\pm$  SD ( $n = 15$ ). No significant differences (ns) were observed between the flat and 3D areas of the 3D-microstructured array. Mann-Whitney  $U$  test;  $p = 0.65$ .

is  $0.15\ \mu\text{V}$  and determines the detection limit of the measuring system for signals in the frequency range of  $1\ \text{kHz}$ .

## 2.3. Cell viability

Biocompatibility was expected as the chip is composed by materials that have been previously reported as safe in the literature [44]. The viability of rat cortical neurons cultured on 3D-microstructured arrays was assessed at 3 and 13 DIV (days *in vitro*). The fluorescence microscopy images of live/dead stained cells revealed vital neurons with multiple neurites distributed over the flat and 3D-microstructured areas of the 3D-microstructured arrays (figure 3(a)). At three DIV the percentage of live cells in the 3D-microstructured area was of  $32.3 \pm 6.1\ \text{SD}$ , which is in the range of what has been previously reported in the literature [24]. The differences between the flat and 3D-microstructured areas were not significant, suggesting that the micro-mushrooms do not affect cell viability (figure 3(b)). The cultures remained viable at 13 DIV, but the extensive network formation did not allow for precise cell counting of the live cells.

## 2.4. Influence on growth pattern

The ability to guide neurite extension in the desired directions is an objective constantly sought in neuronal networks engineering. Although neurite directionality is mostly achieved by anisotropic substrate topography (e.g. grooves, ridges) [40], interspaced vertical structures have previously been shown to be able to guide neurite extensions [45, 46].

Our initial cell culturing experiments suggested that the discontinuous topographical feature of the 3D-microstructured arrays could, *per se*, influence neuronal growth pattern. To evaluate the influence of 3D-microstructured arrays in neurite guidance and growth pattern, primary rat cortical neurons as well as SH-SY5Y cells, a human neuroblastoma cell line that acquires

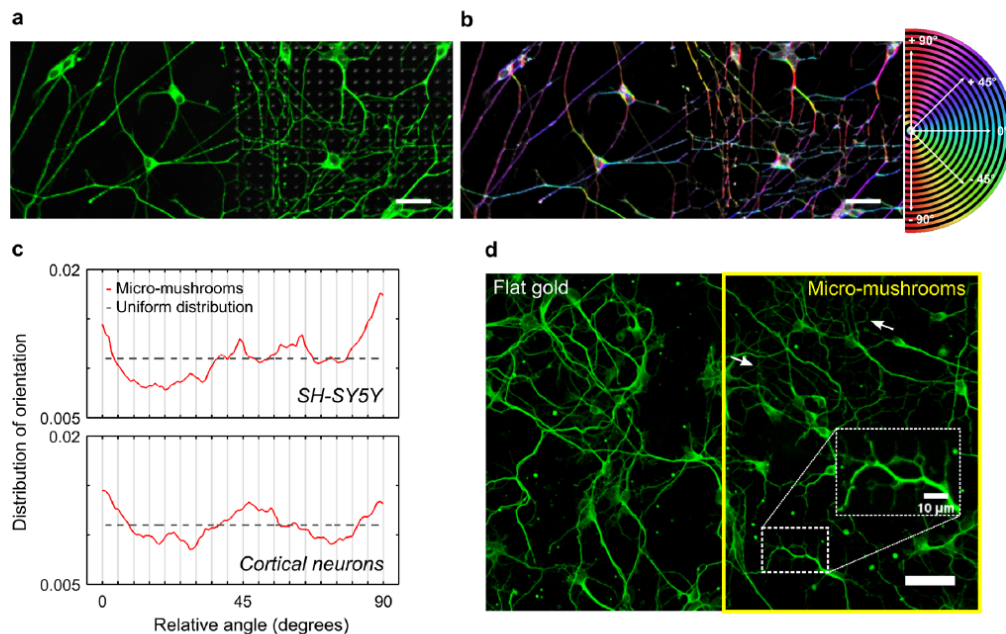


**Figure 4.** Influence of 3D-microstructured arrays in neurite guidance and growth pattern. (a) Differentiated SH-SY5Y cells reveal different growth pattern on flat gold substrate and on the large contiguous array of micro-mushrooms at eight DIV. Note the increased neurite branching complexity in the micro-mushrooms array region. (b) Color coded image of the neurite orientation. The color-orientation association is shown in the color-wheel (right side). In the micro-mushrooms array neurites tend to project in straight lines along the array main axis and diagonals, and are thus mainly colored in light blue (0°), purple/green (45°) and red (90°). It is relevant to note that neurites frequently appear as dashed lines as they extend immediately under the mushroom-like caps (scale bars = 30  $\mu$ m). (c) Orientation distribution shows that neurites of SH-SY5Y cells extend preferentially at angles around 0°, 45°, 63° and 90° ( $n = 59$ ) and that neurites of rat cortical neurons extend preferentially at angles around 0°, 45°, and 90° in the 3D-microstructured area ( $n = 47$ ). Dashed line is the reference uniform (isotropic) distribution. (d) Rat cortical neurons exhibit a different growth pattern on flat gold substrate and on the contiguous array of micro-mushrooms at three DIV (scale bar = 40  $\mu$ m). The white arrows indicate extensive secondary branching along the contiguous array of micro-mushrooms. Inset shows neurites wrapping around the micro-mushrooms. SH-SY5Y cells and neurons were immunolabelled for  $\beta$ III-tubulin (green).

many of the morphologic characteristics of primary neuronal cultures upon a sequential treatment with ATRA and BDNF [47], were cultured on top of the 3D-microstructured arrays.

Neurite orientation was isotropic on the flat gold substrate regions (without micro-mushrooms; data not shown), whereas in the continuous large arrays of micro-mushrooms neurites tended to align preferentially at 0°, 45°, and 90° (figures 4(a)–(c)). These are the angles established by near-neighbor/adjacent micro-mushrooms, which indicates a preference for neurite elongation along the array topography. This effect was particularly robust in the SH-SY5Y cells; to the best of our knowledge, this is the first report of orientation preference of human-derived cells in mushroom-shaped microelectrodes. Interestingly, in the SH-SY5Y culture, a peak around 63° is also noticeable in the orientation distributions (figure 4(c)), which could be due to a second order of proximity between micro-mushrooms, since  $\arctan(2) \approx 63^\circ$ . The obtained orientation distribution for both cortical neurons and SH-SY5Y cells could not be described by a uniform distribution (two-sample Kolmogorov–Smirnov test;  $p = 0.001$ ), thus we can state that the observed preferences are not random.

It was observed that frequently neurites visibly altered their path to contact with the micro-mushrooms and extended along

sequential microstructures. Furthermore, neurite wrapping around the micro-mushrooms was also often observed (figure 4(d)). Interestingly, this occurred both in neurites extending from the soma and in secondary branches. An increase in the network complexity was also observed at the transition from flat substrate (without micro-mushrooms) to the 3D-microstructured array, but a detailed quantification was not performed. Multiple studies have now demonstrated that topographical features which guide neurites in multiple directions, also enhance the rate and degree of neurite branching development and network interconnection [48, 49]. Thus, beyond influencing neurite directionality, topographical features could have an outgrowth-promoting effect. However, further studies are needed to explore this situation in 3D MEA chip settings.

It is important to emphasize that all these changes in growth pattern were observed in both rat cortical neurons and human-derived SH-SY5Y cells, despite their morphological differences and maturation status. Together, these results indicate that whereas the growth pattern on flat gold substrate is random, it considerably changes into a micro-mushrooms-seeking pattern in the 3D-microstructured area.

This anisotropic behavior of mammalian neurons has been shown before in other similar discontinuous isotropic

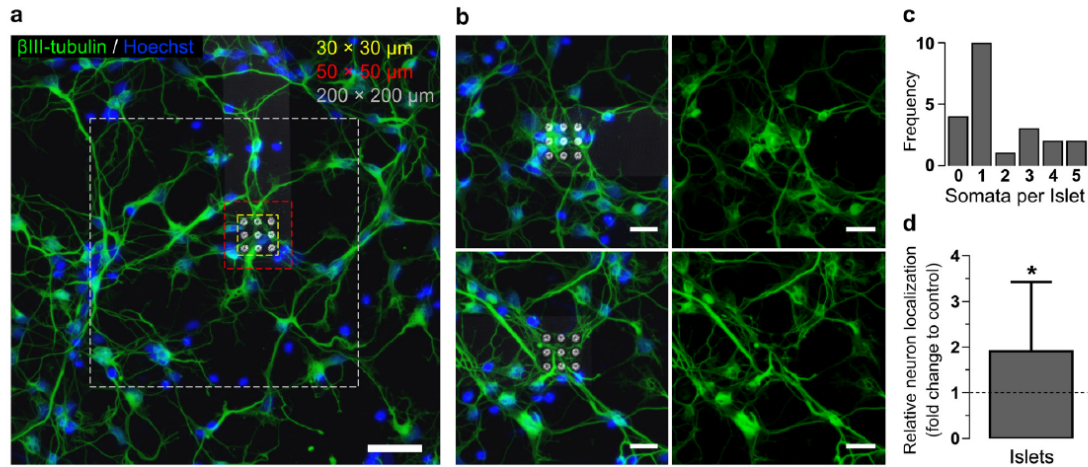


**Figure 5.** Islets of micro-mushrooms promote neuron-microelectrode co-localization and effective contact. (a) Composite fluorescence image of rat cortical neurons, at 3 d *in vitro*, cultured on an islet of micro-mushrooms. The nuclei were stained with Hoechst (blue) and the cytoskeleton with  $\beta$ III-tubulin (green). This staining allowed for quantification of the number of neurons (somata) located inside (yellow ROI) and outside (between red and gray borders) the islets. Somata located in the peripheral planar area of each microelectrode (between red and yellow borders) were excluded from the analysis (scale bar = 40  $\mu$ m). (b) Composite fluorescence images (left side) showing islets of micro-mushrooms with the most frequent situation of having at least one somata (top), and one of the few situations without somata (bottom).  $\beta$ III-tubulin single-channel (right side) show neurites and somata spatial organization in planar and 3D-microstructured substrates. Note that neurites still cross and embrace the micro-mushrooms in the bottom example where no cells co-localize (scale bars = 20  $\mu$ m). (c) Frequency plot of the number of somata co-localized with the 3D-microstructured area (islet). (d) Bar graph shows the relative increase in somata co-localization with the 3D-microstructured area to the remaining planar  $\text{SiO}_2$  substrate (control). Representative data of two independent experiments was normalized and expressed as mean  $\pm$  SD ( $n = 22$ ). Results are shown as fold change to control (indicated by the dashed line). Two tailed unpaired *t*-test with Welch's correction;  $*p < 0.05$ .

topographies of PDMS protrusions [45] and semiconductor nanowires [48] but a pitch of  $\sim 0.5\text{--}3\text{ }\mu\text{m}$  was indicated as critical for optimal alignment of neurite extension [39]. Moreover, in Hai *et al* experiments with larger *Aplysia californica* neurons, no change in growth pattern was observed when using gMuEs arrays with spacing ranges above 8  $\mu\text{m}$  [26]. In alignment with the results presented here, Panaitov *et al* reported that neurites of rat cortical neurons tended to follow the micro-mushrooms (spacing ranges of 3–5  $\mu\text{m}$ ) and wrapped around the mushroom-like caps, albeit no quantifications were shown [24]. More recently, the same group reported guiding rat cortical neurons in a grid-like pattern selectively functionalized with self-assembled monolayers [38]. However, this combination of chemical and physical cues impairs the analysis of to which extent the topography, *per se*, influenced the neuronal network organization, as 85% of the neurons grew on the pre-defined pattern. Interestingly, somata tended to agglomerate in the larger grid nodes (25  $\mu\text{m} \times 25\text{ }\mu\text{m}$ ), whereas neurites grew along the grid lines (10  $\mu\text{m}$  width). These nodes were of similar dimensions to the islets used in our 3D-MEA configuration, which influence somata localization even in the absence of a restricting biochemical pattern, as shown in the next section.

## 2.5. Influence on neuron localization

One of the key motives behind the use of micro-mushrooms is the increase in area for cell-electrode contact. But beyond increasing the area per microelectrode, the islet configuration with localized agglomerates of micro-mushrooms influenced

neuronal localization and increased the propensity for neuron-microelectrode co-localization and effective contact. To quantify the effect of the islets on neuronal localization, the density of neuronal cell bodies (somata) located in the 3D-microstructured area (islet) was calculated and compared with the planar substrate area ( $\text{SiO}_2$ ). To avoid repetition of the planar substrate area to be analyzed (due to microelectrodes proximity), each image was restricted to a region of interest (gray ROI in figure 5(a)) of  $200 \times 200\text{ }\mu\text{m}$  surrounding the  $30 \times 30\text{ }\mu\text{m}$  3D-microstructured area (yellow ROI in figure 5(a)). Somata located in the planar area of each microelectrode (red ROI of  $50 \times 50\text{ }\mu\text{m}$  in figure 5(a)) were excluded from the analysis to separate the effects of the micro-mushrooms from the effects of the surface material transition ( $\text{SiO}_2\text{--Au}$ ).

From the total number of microelectrodes analyzed ( $n = 22$ , from two independent experiments), the majority of the islets contained somata (18/22;  $\approx 82\%$ ), whereas neurites crossed and caught micro-mushrooms in the 3D-microstructured area (islet) in all of them (figure 5(b)). Figure 5(c) shows that the number of somata located in the area varied between 0 (minimum) and 5 (maximum), with one somata per islet being the most common occurrence (10/22;  $\approx 45\%$ ). The probability for somata to localize in the islets increased near two-fold ( $1.9 \pm 1.5\text{ SD}$ ) when compared to the planar substrate ( $*p = 0.0195$ , two tailed unpaired *t*-test with Welch's correction) (figure 5(d)). It was found that neuronal density in the 3D-microstructured and planar areas was of  $2.0 \times 10^{-3}$  neurons  $\mu\text{m}^{-2}$  and  $1.1 \times 10^{-3}$  neurons  $\mu\text{m}^{-2}$ , respectively.

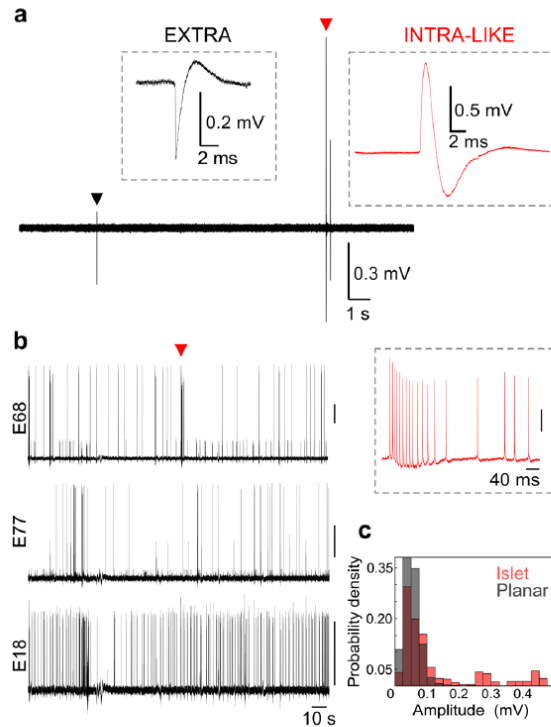


**Figure 6.** Islets of micro-mushrooms enable high-fidelity electrophysiological recordings from neurons. (a) Single-channel electrophysiological recording of spontaneous extracellular and intracellular-like firing activity of rat cortical neurons at 24 DIV. A large extracellular spike ( $384 \mu\text{V}_{\text{pp}}$ ) and two intracellular-like spikes are easily distinguishable from the baseline. The biggest intracellular-like spike (red inset) had the positive phase clipped (at  $+1 \text{ mV}$ ) by the recording software range, therefore it had an amplitude of at least  $1.49 \text{ mV}_{\text{pp}}$ . (b) Raw data traces of spontaneous activity as recorded by three different microelectrodes from rat hippocampal neurons at ten DIV. The inset shows an enlargement of a burst recorded in electrode E68. Note the relative decrease in amplitude in consecutive spikes (all amplitude scale bars =  $0.1 \text{ mV}$ ). (c) Probability distribution of spike amplitudes recorded by 3D-microstructured (islets) and planar microelectrodes at ten DIV.

Moreover, the presence of a microstructured substrate influenced neurite navigation, and every islet was covered with cellular components as early as three DIV.

### 2.6. Electrophysiological recordings

The novel islets 3D-microstructured MEAs were used for long-term recordings of rat cortical and hippocampal neurons. Spontaneous neuronal activity from 10 to 24 DIV cultures were recorded in multiple islets from three different chips. The noise level was about  $2.1\text{--}4.3 \mu\text{V}_{\text{SD}}$  (and never exceeded  $40 \mu\text{V}_{\text{pp}}$ ) so spikes were easily distinguishable over the baseline (SD: standard deviation noise scale; pp: peak-to-peak noise scale).

It is important to note that recordings by conventional planar MEAs are predominantly characterized by negative

monophasic signals with low amplitude ( $\leq 100 \mu\text{V}$ ). In the recordings with the islets configuration, mainly positive monophasic or biphasic signals with amplitudes bigger than  $100 \mu\text{V}$  were obtained. Smaller extracellular positive biphasic signals were also observed. It is well established that the spike's shape is influenced by cell geometry, size and maturation status [1], as well as by the source electrogenic cell compartment. Importantly, these small positive spikes may be axonal signals originating from axons that establish a close contact with the micro-mushrooms (embracing or curling round the 3D micro-structures).

Most interestingly, spontaneous intracellular-like activity (positive spikes in the mV range) with very high SNR were also recorded in the islet chip configuration (figure 6). Figure 6(a) shows a single-channel signal trace with both extracellular and intracellular-like recorded activity from cortical neurons.

The recorded SNR was consistently high across all islet electrodes. Figure 6(b) shows representative concurrent recording traces from three microelectrodes of the same chip, all with high amplitude positive spikes. Pooling the recorded activity of all islet electrodes, the average noise level was  $2.4 \mu\text{V}_{\text{SD}}$  and the average SNR was 52. On the other, all recordings from the equivalent planar electrodes (same electrode base, but without micro-mushrooms) showed an average noise level of  $1.9 \mu\text{V}_{\text{SD}}$  but a significantly lower average SNR of 28. Comparing the distribution of the amplitudes of the recorded spikes (using a threshold detection method at  $10 \times \text{SD}$ ), there is a clear advantage towards the micro-mushrooms islets configuration (figure 6(c)). It is important to note that the flange gold at the base of the islet electrodes is not passivated, thus the recorded signals result from a combination of the 3D and planar components of the microelectrode.

Altogether, these results show the potential of the proposed micro-mushrooms islets configuration for attaining *in vitro* MEA recordings with higher fidelity than conventional planar MEA.

### 3. Conclusion

The importance of incorporating physical cues in *in vitro* electrophysiology research is becoming more and more evident. From a biological perspective, it is clear that topography influences neuronal development and potentially helps recapitulating an *in vivo* environment. However, with rare exceptions [32], many of the recent efforts in this front have not integrated such findings into MEA devices that have been tested/validated in actual electrophysiological recordings. A novel 3D-microstructured MEA architecture was presented here, which holds promise for multisite *in vitro* electrophysiological recordings with high-yield and high-fidelity. The configuration is a hybrid between the canonical planar microelectrodes and the continuous array of 3D micro-mushrooms [43], where the planar microelectrodes are replaced by islets of  $3 \times 3$  micro-mushrooms, leading to improvements in the recordings by: (i) promoting the co-localization (topotaxis) of neuron active structures with the electrodes (somata and neurites); (ii) decreasing the impedance and increasing the

SNR; (iii) enhancing membrane-electrode coupling allowing measurement of signals with intracellular characteristics; and (iv) raising the number of useful (recording) microelectrodes in cultures with normal cell densities. Importantly, this new MEA architecture is easy to fabricate and structurally robust, allowing conventional cleaning protocols and multiple uses of the same chip.

When compared to the most recent mushroom-shaped microelectrodes reported by Spira and collaborators [25], one of the most distinctive features of our design is the size and the organization of the micro-mushrooms in islets instead of using a single micro-mushroom per sensing microelectrode. But more importantly, the approach taken here is different from the original effort for producing patch-clamp intracellular-like recordings from the engulfment of mushroom-shaped microelectrodes (caps larger than  $2.5\ \mu\text{m}$  preclude engulfment by the small mammalian neurons [27]). In the islets configuration proposed here, the objective of engulfment is replaced by entrapment, for somata, and by embracement, for neurites (axons/dendrites). The islets 3D topography greatly increases the cell-electrode contact surface and enables the acquisition of spontaneous activity with intracellular characteristics in the mV range. The high quality recordings with cortical and hippocampal neurons presented here confirm the potential of the proposed configuration.

In MEAs, in addition to excellent SNR, it is also important to promote useful microelectrodes (i.e. electrodes with active neuronal structures in their vicinity), at adequate cell densities. With recent evidence that a large contribution of the extracellular signals comes, not from the somas, but from axons initial segment [50, 51], it becomes clear that clever MEA designs should also address the electrode-neurites coupling. This is achieved with our micro-mushrooms islets configuration, with localized neurites embracement. In the configurations presented here, a spacing range of  $10\ \mu\text{m}$  in-between micro-mushrooms already produces effects on neurite guidance. Not only could we find neurites wrapped in all the islets analyzed but also the probability for somata to co-localize with the islets increased near two-fold. We show that topographical features of the islets 3D-MEAs cause directional topotaxis not only in rat cortical neurons but also in human derived SH-SY5Y cells. A plausible mechanism is that the micro-mushrooms may function as anchors, serving as focal adhesion points for the neurons, providing long-term stable interfaces.

To the best of our knowledge, this is the first study employing cultures of human-derived cells on top of mushroom-shaped microelectrodes. The here proven advantages of the islets configuration holds promise for the translation of this technology to *in vitro* drug screening applications with, for example, induced human pluripotent stem cells. Naturally, future efforts will benefit from the combination of the gold microstructures with conductive polymers (e.g PEDOT-PSS) [52, 53] or carbon nanotubes [54], as previously suggested in the literature. This combination should help to reduce further the impedance of the islets 3D-microstructured microelectrodes.

## 4. Experimental section

### 4.1. Fabrication

The fabrication process of the MEAs starts with the magnetron sputtering deposition of and electrically conductive Cr (5 nm)/Au (40 nm) layer on top of  $49 \times 49\ \text{mm}^2$  glass substrates. The dimensions of the glass substrate was chosen for compatibility with the commercial MEA2100 system (figure S2(a)). A three-level lithography process (corresponding to the three layers of the CAD design represented in different colors in figure S2(b) in the supporting information) was then used to fabricate the micro-mushrooms. The first step begins with spin-coating of PFR7790G27cP photoresist ( $1.5\ \mu\text{m}$  nominal thickness) followed by a soft bake (1 min at  $86\ ^\circ\text{C}$ ). The first level (schematized in white in figure S2(b), supporting information) of the lithography mask was then exposed using a Heidelberg DWLii direct laser writing system with a 405 nm diode laser, defining sixty electrical leads and  $2.2 \times 2.2\ \text{mm}^2$  pads for independent reading points. After post-bake for 1 min at  $110\ ^\circ\text{C}$  and development in TMA238WA for 1 min, the pattern was transferred to the Cr/Au layer by ion-milling etching. This was performed in a Nordiko 3600 system with base pressure  $1 \times 10^{-7}$  Torr, an RF forward power of 203 W, first grid voltage 724 V and current 103 mA, a second grid voltage of  $-345\ \text{V}$  and current 2.4 mA, and an Ar flow of 10.2 sccm corresponding to a working pressure of  $3 \times 10^{-5}$  Torr. The second level consists on the passivation of the electrical leads with  $800\ \text{\AA}$  of  $\text{Al}_2\text{O}_3$ . The oxide is deposited by RF sputtering with a base pressure of  $3 \times 10^{-7}$  Torr, an RF power of 200 W, Ar flow of 45 sccm leading to a working pressure of  $3 \times 10^{-3}$  Torr. Using optical lithography, the outside reading pads and  $40\ \mu\text{m} \times 40\ \mu\text{m}$  areas (the islets where mushroom-shaped protrusions are grown) were previously protected. Oxide lift-off was then performed by immersing the sample in Microstrip 3001 at  $60\ ^\circ\text{C}$  for 30 min in ultrasonic bath, leaving the leads insulated while vias to the pads and islets were opened in a planar MEA design. The final level defined the micrometric holes in  $1.5\ \mu\text{m}$  photoresist where the micro-mushrooms were to be fabricated (red layer in figure S2(b), supporting information). In each of the islets, a square array of  $3 \times 3$  holes with nominal diameters of  $2\ \mu\text{m}$  and center-to-center distance of  $10\ \mu\text{m}$  was opened. To create the mushroom shape, gold was potentiostatically electrodeposited inside the opened holes using an Orosene bath, with an applied potential of  $-1.0\ \text{V}$  during 39 min, at room temperature (RT,  $23.5\ ^\circ\text{C}$ ) [42]. Finally, at the end of the electrodeposition process the photoresist was removed using acetone and the 3D-microstructured MEA obtained. The morphology of the fabricated micro-structures was analyzed by SEM using a FEI Quanta 400FEG ESEM. In some comparison experiments, planar versions of 3D-structured microelectrodes were used, where the only difference in the specifications was the absence of the micro-mushrooms on top of the  $40\ \mu\text{m} \times 40\ \mu\text{m}$  islets areas.

#### 4.2. Impedance measurements

The electrical impedance of the  $40\ \mu\text{m} \times 40\ \mu\text{m}$  areas both with and without  $3 \times 3$  3D-microstructured microelectrodes was measured using a Precision Component Analyzer 6440B from Wayne Kerr Electronics in the  $10^2$  to  $2 \times 10^6$  Hz frequency range. This equipment uses four-terminal connections to measure with more accuracy the impedance and reduce the effect of contact resistance. To perform the measurements, the microelectrodes were emerged in a PBS (phosphate buffered saline) solution at RT.

#### 4.3. Cell culture

Before cell culture, chips were rinsed in distilled water to remove residues from fabrication. Afterwards, chips were sterilized by a brief immersion in 70% ethanol followed by UV light exposure. A sterilized silicon or PDMS ring was attached to the chip to hold the cells and culture medium. To assure a good cell attachment to the surface, chips were coated with  $0.01\ \text{mg}\ \text{ml}^{-1}$  poly(D-lysine) (PDL, 500 kDa, Corning) diluted in sterile distilled water for 1 h at RT. After three washes with sterile distilled water, they were let to air-dry before cell seeding.

Experimental procedures involving animals were carried out in accordance with current Portuguese laws on Animal Care (DL 113/2013) and with the European Union Directive (2010/63/EU) on the protection of animals used for experimental and other scientific purposes. The experimental protocol (reference 0421/000/000/2017) was approved by the ethics committee of the Portuguese official authority on animal welfare and experimentation (Direção-Geral de Alimentação e Veterinária). All efforts were made to minimize as possible the number of animals and their suffering.

Primary embryonic rat cortical and hippocampal neurons were isolated from Wistar embryo rats (E15–18). Embryos cortices were dissected in Hanks' Balanced Salt Solution (HBSS) and enzymatically digested in 0.05% (w/v) trypsin (1:250, Gibco®, Thermo Fisher Scientific) in HBSS for 15 min at 37 °C. Subsequently, tissue fragments were washed once with 10% (v/v) heat-inactivated fetal bovine serum (hiFBS, Biowest) in HBSS, to inactivate trypsin, and twice with HBSS to remove hiFBS residues from solution. Tissue fragments were then mechanically dissociated with a 5 ml serological pipette followed by a 1 ml pipette tip. Viable cells were counted using the trypan blue (0.4% (w/v), Sigma-Aldrich Co.) exclusion assay and seeded in PDL-coated 3D-microstructured arrays at a density around 1000 viable cells  $\text{mm}^{-2}$ . Cells were cultured in Neurobasal medium supplemented with 0.5 mM glutamine, 2% (v/v) B27 supplement and 1% (v/v) penicillin/streptomycin (P/S, 10000 units  $\text{ml}^{-1}$  penicillin and 10000  $\mu\text{g}\ \text{ml}^{-1}$  streptomycin) (all from Gibco®, Thermo Fisher Scientific), and kept in a humidified incubator at 37 °C supplied with 5%  $\text{CO}_2$  until use.

SH-SY5Y cells (a human neuroblastoma cell line), obtained from DSMZ (Germany) were routinely cultured in Dulbecco's Modified Eagle Medium/Hams F-12 (DMEM/F-12, 50/50

Mix, Corning), supplemented with 10% (v/v) hiFBS and 1% (v/v) P/S (Biowest). SH-SY5Y cells were subcultured in PDL-coated 3D-microstructured arrays at a density of 100 viable cells  $\text{mm}^{-2}$ , and incubated with differentiation medium I (DMEM/F-12 supplemented with 10% (v/v) hiFBS, 10  $\mu\text{M}$  all-trans-retinoic acid (ATRA) and 1% (v/v) P/S) for 5 d, followed by incubation with differentiation medium II (DMEM/F-12 supplemented with 50 ng  $\text{ml}^{-1}$  brain-derived neurotrophic factor (BDNF, PeproTech) and 1% (v/v) P/S) for an additional 2 d, as reported by Encinas *et al* [47].

After the experiments, cells were detached from the chip surface by a brief treatment with 0.25% (w/v) trypsin/ 0.05% (w/v) EDTA solution (Sigma-Aldrich, Co) at 37 °C, followed by an overnight incubation with a commercial alkaline detergent solution containing proteases (Terg-A-Zyme®, Sigma-Aldrich, Co) at RT. This procedure allowed the reuse of chips.

#### 4.4. Immunofluorescence staining

Primary cortical neurons and SH-SY5Y cells were fixed at 3 or 8 d *in vitro* (DIV), respectively, with 4% (w/v) paraformaldehyde in 0.1 M phosphate buffer (pH 7.4) for 15 min, at RT. After washing in PBS, cells were blocked and permeabilized with 0.1% (w/v) bovine serum albumin (BSA, Sigma-Aldrich Co) containing 0.3% (v/v) Triton X-100 (Sigma-Aldrich Co) for 1 h, at RT. Afterwards, cells were incubated with primary antibody solution (rabbit anti- $\beta$ III tubulin, 1:500, Abcam) overnight, at 4 °C. After washing in PBS, cells were incubated with fluorescently-labeled secondary antibody solution (anti-rabbit Alexa Fluor® 488 conjugate, 1:1000, Molecular Probes®, Thermo Fisher Scientific) for 1 h, at RT. Nuclei were stained with 0.5  $\mu\text{g}\ \text{ml}^{-1}$  Hoechst (Molecular Probes®, Thermo Fisher Scientific).

Cells were imaged using a laser scanning confocal microscope Leica TCS SP5 II (Leica Microsystems, Germany) with the HCX PL APO CS 40 $\times$ /1.3 oil objective. Laser lines at 405 or 488 nm were used for Hoechst or Alexa 488 excitation, respectively. For each condition (primary neuron or SH-SY5Y cell cultures), a total of 47 and 59 images (3D-microstructured areas) were acquired from five and six independent 3D-microstructured arrays, respectively.

#### 4.5. Cell viability

The cell viability after seeding in 3D-microstructured arrays was assessed by the live/dead assay using calcein-AM/propidium Iodide (PI). Primary cortical neurons were isolated and seeded as previously described. At 3 and 13 DIV, cells were incubated with 1 mM calcein-AM (Molecular Probes®, Thermo Fisher Scientific) for 10 min at 37 °C, followed by incubation with 2  $\mu\text{M}$  PI (Sigma-Aldrich Co) for 5 min, at RT. After incubation, cells were imaged in an inverted fluorescence microscope (Axiovert 200M, Zeiss) with a Plan NeoFluar 20 $\times$ /0.4 Ph2 Korr objective. Laser lines at 488 and 543 nm were used for calcein-AM or PI excitation, respectively. For each 3D-microstructured array, a total of five fields from 3D-microstructured or flat areas were randomly selected

for representative imaging and analysis. Images were acquired from three independent 3D-microstructured arrays, for each time point.

#### 4.6. Image processing and analysis

Image processing and quantitative analysis were performed using ImageJ software [55]. Experiments involving manual cell counting procedures were assisted by an ImageJ cell counter plug-in. For the quantitative analysis of the neurite directionality of both cortical neurons and SH-SY5Y cells, maximum intensity projection images from  $z$  stacked images were evaluated using the OrientationJ Distribution plug-in [56]. This plug-in computes the local orientation properties of structures in the image at the pixel level. The algorithm assesses local directionality in terms of two measures: coherency and energy. Distributions of orientations (directionality analysis) were built taking into account the pixels that had a coherency larger than 90% (min-coherency) and an energy larger than 10% (min-energy). The final orientation distributions were calculated and visualized using custom-made MATLAB (The MathWorks Inc., USA) scripts. The obtained distributions of orientations were tested for uniformity using the two-sample Kolmogorov–Smirnov test.

#### 4.7. Electrophysiological recordings

AC voltage electrophysiological recordings of rat cortical neuron cultures started at 13 DIV. Single-channel extracellular acquisitions were performed inside a Faraday cage at RT (22 °C). All data was analog-filtered (0.3–20 kHz) and amplified ( $\times 100$ ) with a four-channel amplifier (Model 1700, A-M Systems). The amplifier was connected to the contact pads of the chips via pogo pins held in place by manipulators. One Ag/AgCl electrode was submerged in the medium to be used as ground. Signals were digitized via an oscilloscope with 16-bit resolution at a sampling rate of 1 gigasamples  $s^{-1}$ . The recording setup capability was successfully tested with planar 256-microelectrodes MEA cultures that also exhibited spontaneous activity in a commercial MEA system (MEA2100-256-System, MultiChannel Systems, Germany). The fabricated chips' compatibility with a commercial system was confirmed by performing recordings from hippocampal neurons at ten DIV with a 60-channel MEA2100-Mini-System (MultiChannel Systems, Germany). These recordings were performed inside a humidified incubator (37 °C, 5%  $CO_2$ ) at a sampling rate of 20 kHz. The estimated SNR was calculated by dividing the peak-to-peak (pp) amplitude of the recorded spikes by the standard deviation (SD) of the noise level. Presented figures for measured electrical potential are scaled to pre-amplification values.

#### 4.8. Statistical analysis

Statistical analysis was performed using GraphPad Prism version 7.0 (GraphPad Software Inc., CA, USA). The ROUT method did not identify any outlier in all datasets. The method of D'Agostino & Pearson was used as a normality test and parametric or non-parametric tests were chosen as appropriate.

Statistical significance was considered for  $p < 0.05$ . All statistical data was presented as mean and SD.

#### Acknowledgments

This work was partly financed by FEDER—Fundo Europeu de Desenvolvimento Regional funds through the COMPETE 2020—Operational Programme for Competitiveness and Internationalisation (POCI), Portugal 2020, and by Portuguese funds through FCT—Fundação para a Ciência e a Tecnologia/ Ministério da Ciência, Tecnologia e Inovação in the framework of the project 'Institute for Research and Innovation in Health Sciences' (POCI-01-0145-FEDER-007274) and in the framework of the financed project PTDC/CTM-NAN/3146/2014. José Mateus was supported by FCT (PD/BD/135491/2018) in the scope of the BiotechHealth Program (Doctoral Program on Cellular and Molecular Biotechnology Applied to Health Sciences). Paulo Aguiar was supported by Programa Ciência—Programa Operacional Potencial Humano (POPH)—Promotion of Scientific Employment, ESF and MCTES and program Investigador FCT, POPH and Fundo Social Europeu. The SH-SY5Y cells (DSMZ, Germany), were kindly provided by the UnIGENE group at i3S.

#### Supporting information

Separate file with all figures incorporated into the text.

#### ORCID iDs

José C Mateus  <https://orcid.org/0000-0001-8058-5093>  
 Cátia D F Lopes  <https://orcid.org/0000-0002-7467-6498>  
 Luís Leitão  <https://orcid.org/0000-0001-8419-2967>  
 Paulo Aguiar  <https://orcid.org/0000-0003-4164-5713>

#### References

- [1] Nam Y and Wheeler B C 2011 *In vitro* microelectrode array technology and neural recordings *Crit. Rev. Biomed. Eng.* **39** 45–61
- [2] Obien M E J E J, Deligkaris K, Bullmann T, Bakkum D J J and Frey U 2015 Revealing neuronal function through microelectrode array recordings *Front. Neurosci.* **8** 423
- [3] Wagenaar D A, Madhavan R, Pine J and Potter S M 2005 Controlling bursting in cortical cultures with closed-loop multi-electrode stimulation *J. Neurosci.* **25** 680–8
- [4] Massobrio P, Tessadori J, Chiappalone M and Ghirardi M 2015 *In vitro* studies of neuronal networks and synaptic plasticity in invertebrates and in mammals using multielectrode arrays *Neural Plast.* **2015** 196195
- [5] Johnstone A F M, Gross G W, Weiss D G, Schroeder O H-U, Gramowski A and Shafer T J 2010 Microelectrode arrays: a physiologically based neurotoxicity testing platform for the 21st century *Neurotoxicology* **31** 331–50
- [6] Accardi M V, Pugsley M K, Forster R, Troncy E, Huang H and Authier S 2016 The emerging role of *in vitro* electrophysiological methods in CNS safety pharmacology *J. Pharmacol. Toxicol. Methods* **81** 47–59

- [7] Chong S-A et al 2011 Synaptic dysfunction in hippocampus of transgenic mouse models of Alzheimer's disease: a multi-electrode array study *Neurobiol. Dis.* **44** 284–91
- [8] Seymour J P, Wu F, Wise K D and Yoon E 2017 State-of-the-art MEMS and microsystem tools for brain research *Microsyst. Nanoeng.* **3** 16066
- [9] Spira M E and Hai A 2013 Multi-electrode array technologies for neuroscience and cardiology *Nat. Nanotechnol.* **8** 83–94
- [10] Spira M E, Shmuel N, Huang S-H M and Erez H 2018 Multisite attenuated intracellular recordings by extracellular multielectrode arrays, a perspective *Front. Neurosci.* **12** 212
- [11] Xie C, Lin Z, Hanson L, Cui Y and Cui B 2012 Intracellular recording of action potentials by nanopillar electroporation *Nat. Nanotechnol.* **7** 185–90
- [12] Duan X et al 2012 Intracellular recordings of action potentials by an extracellular nanoscale field-effect transistor *Nat. Nanotechnol.* **7** 174–9
- [13] Robinson J T, Jorgolli M, Shalek A K, Yoon M-H, Gertner R S and Park H 2012 Vertical nanowire electrode arrays as a scalable platform for intracellular interfacing to neuronal circuits *Nat. Nanotechnol.* **7** 180–4
- [14] Liu R et al 2017 High density individually addressable nanowire arrays record intracellular activity from primary rodent and human stem cell derived neurons *Nano Lett.* **17** 2757–64
- [15] VanDersarl J J, Xu A M and Melosh N A 2012 Nanostraws for direct fluidic intracellular access *Nano Lett.* **12** 3881–6
- [16] Dipalo M et al 2017 Intracellular and extracellular recording of spontaneous action potentials in mammalian neurons and cardiac cells with 3D plasmonic nanoelectrodes *Nano Lett.* **17** 3932–9
- [17] Angle M R, Cui B and Melosh N A 2015 Nanotechnology and neurophysiology *Curr. Opin. Neurobiol.* **32** 132–40
- [18] Abbott J, Ye T, Ham D and Park H 2018 Optimizing nanoelectrode arrays for scalable intracellular electrophysiology *Acc. Chem. Res.* **51** 600–8
- [19] Tian B, Cohen-Karni T, Qing Q, Duan X, Xie P and Lieber C M 2010 Three-dimensional, flexible nanoscale field-effect transistors as localized bioprobes *Science* **329** 830–4
- [20] Kwak M, Han L, Chen J J and Fan R 2015 Interfacing inorganic nanowire arrays and living cells for cellular function analysis *Small* **11** 5600–10
- [21] McGuire A F, Santoro F and Cui B 2018 Interfacing cells with vertical nanoscale devices: applications and characterization *Annu. Rev. Anal. Chem.* **11** 101–26
- [22] Wijdenes P, Ali H, Armstrong R, Zaidi W, Dalton C and Syed N I 2016 A novel bio-mimicking, planar nano-edge microelectrode enables enhanced long-term neural recording *Sci. Rep.* **6** 34553
- [23] Hai A, Shappir J and Spira M E 2010 In-cell recordings by extracellular microelectrodes *Nat. Methods* **7** 200–2
- [24] Panaitov G, Thierry S, Hofmann B and Offenhäusser A 2011 Fabrication of gold micro-spine structures for improvement of cell/device adhesion *Microelectron. Eng.* **88** 1840–4
- [25] Shmuel N, Rabieh N, Ojovan S M, Erez H, Maydan E and Spira M E 2016 Multisite electrophysiological recordings by self-assembled loose-patch-like junctions between cultured hippocampal neurons and mushroom-shaped microelectrodes *Sci. Rep.* **6** 27110
- [26] Hai A et al 2009 Changing gears from chemical adhesion of cells to flat substrata toward engulfment of micro-protrusions by active mechanisms *J. Neural Eng.* **6** 066009
- [27] Ojovan S M et al 2015 A feasibility study of multi-site, intracellular recordings from mammalian neurons by extracellular gold mushroom-shaped microelectrodes *Sci. Rep.* **5** 14100
- [28] Sileo L et al 2013 Electrical coupling of mammalian neurons to microelectrodes with 3D nanoprotusions *Microelectron. Eng.* **111** 384–90
- [29] Gertz M L, Baker Z, Jose S and Peixoto N 2017 Time-dependent Increase in the network response to the stimulation of neuronal cell cultures on micro-electrode arrays *J. Vis. Exp.* e55726
- [30] Erickson J, Tooker A, Tai Y-C and Pine J 2008 Caged neuron MEA: a system for long-term investigation of cultured neural network connectivity *J. Neurosci. Methods* **175** 1–16
- [31] Xie C, Hanson L, Xie W, Lin Z, Cui B and Cui Y 2010 Noninvasive neuron pinning with nanopillar arrays *Nano Lett.* **10** 4020–4
- [32] Cools J, Copic D, Luo Z, Callewaert G, Braeken D and De Volder M 2017 3D microstructured carbon nanotube electrodes for trapping and recording electrogenic cells *Adv. Funct. Mater.* **27** 1–9
- [33] Samhaber R et al 2016 Growing neuronal islands on multi-electrode arrays using an accurate positioning- $\mu$ CP device *J. Neurosci. Methods* **257** 194–203
- [34] Aebbersold M J et al 2016 'Brains on a chip': towards engineered neural networks *TrAC—Trends Anal. Chem.* **78** 60–9
- [35] James C D et al 2004 Extracellular recordings from patterned neuronal networks using planar microelectrode arrays *IEEE Trans. Biomed. Eng.* **51** 1640–8
- [36] Suzuki M et al 2013 Neuronal cell patterning on a multi-electrode array for a network analysis platform *Biomaterials* **34** 5210–7
- [37] Ryu J R et al 2016 Synaptic compartmentalization by micropatterned masking of a surface adhesive cue in cultured neurons *Biomaterials* **92** 46–56
- [38] Santoro F, Panaitov G and Andreas O 2014 Defined patterns of neuronal networks on 3D thiol-functionalized microstructures *Nano Lett.* **14** 6906–9
- [39] Simitzi C, Ranella A and Stratakis E 2017 Controlling the morphology and outgrowth of nerve and neuroglial cells: the effect of surface topography *Acta Biomater* **51** 21–52
- [40] Marcus M, Baranes K, Park M, Choi I S, Kang K and Shefi O 2017 Interactions of neurons with physical environments *Adv. Healthcare Mater.* **6** 1700267
- [41] Hoffman-Kim D, Mitchell J A and Bellamkonda R V 2010 Topography, cell response, and nerve regeneration *Annu. Rev. Biomed. Eng.* **12** 203–31
- [42] Cerquido M et al 2018 Tailoring the cap's morphology of electrodeposited gold micro-mushrooms *Appl. Surf. Sci.* **445** 512–8
- [43] Mestre A L G et al 2017 Ultrasensitive gold micro-structured electrodes enabling the detection of extra-cellular long-lasting potentials in astrocytes populations *Sci. Rep.* **7** 14284
- [44] Brüggemann D, Wolfrum B, Maybeck V, Mourzina Y, Jansen M and Offenhäusser A 2011 Nanostructured gold microelectrodes for extracellular recording from electrogenic cells *Nanotechnology* **22** 265104
- [45] Hanson J N, Motala M J, Heien M L, Gillette M, Sweedler J and Nuzzo R G 2009 Textural guidance cues for controlling process outgrowth of mammalian neurons *Lab Chip* **9** 122–31
- [46] Micholt L, Gärtner A, Prodanov D, Braeken D, Dotti C G and Bartic C 2013 Substrate topography determines neuronal polarization and growth *in vitro PLoS One* **8** e66170
- [47] Encinas M et al 2000 Sequential treatment of SH-SY5Y cells with retinoic acid and brain-derived neurotrophic factor gives rise to fully differentiated, neurotrophic factor-dependent, human neuron-like cells *J. Neurochem.* **75** 991–1003

- [48] Gautam V *et al* 2017 Engineering highly interconnected neuronal networks on nanowire scaffolds *Nano Lett.* **17** 3369–75
- [49] Seo J *et al* 2018 Nanotopography-promoted formation of axon collateral branches of hippocampal neurons *Small* **14** 1801763
- [50] Radivojevic M, Franke F, Altermatt M, Müller J, Hierlemann A and Bakkum D J 2017 Tracking individual action potentials throughout mammalian axonal arbors. *eLife* **6** e30198
- [51] Bakkum D J *et al* 2018 The axon initial segment is the dominant contributor to the Neuron's extracellular electrical potential landscape *Adv. Biosyst.* **3** 1800308
- [52] Abidian M R, Corey J M, Kipke D R and Martin D C 2010 Conducting-polymer nanotubes improve electrical properties, mechanical adhesion, neural attachment, and neurite outgrowth of neural electrodes *Small* **6** 421–9
- [53] Aqrawe Z, Montgomery J, Travas-Sejdic J and Svirskis D 2018 Conducting polymers for neuronal microelectrode array recording and stimulation *Sensors Actuators B* **257** 753–65
- [54] Kim G H *et al* 2017 CNT-Au nanocomposite deposition on gold microelectrodes for improved neural recordings *Sensors Actuators B* **252** 152–8
- [55] Rueden C T *et al* 2017 ImageJ2: ImageJ for the next generation of scientific image data *BMC Bioinform.* **18** 529
- [56] Rezakhaniha R *et al* 2012 Experimental investigation of collagen waviness and orientation in the arterial adventitia using confocal laser scanning microscopy *Biomech. Model Mechanobiol.* **11** 461–73



This is a License Agreement between University of Porto ("User") and Copyright Clearance Center, Inc. ("CCC") on behalf of the Rightsholder identified in the order details below. The license consists of the order details, the CCC Terms and Conditions below, and any Rightsholder Terms and Conditions which are included below.

All payments must be made in full to CCC in accordance with the CCC Terms and Conditions below.

|                  |             |             |                     |
|------------------|-------------|-------------|---------------------|
| Order Date       | 21-Jul-2021 | Type of Use | Republish in a      |
| Order License ID | 1134806-1   |             | thesis/dissertation |
| ISSN             | 1741-2552   | Publisher   | IOP Publishing      |
|                  |             | Portion     | Chapter/article     |

## LICENSED CONTENT

|                   |                                      |                  |   |
|-------------------|--------------------------------------|------------------|---|
| Publication Title | Journal of Neural Engineering        | Country          | United Kingdom of Great Britain and Northern Ireland                              |
| Author/Editor     | Institute of Physics (Great Britain) | Rightsholder     | IOP Publishing, Ltd   |
| Date              | 01/01/2004                           | Publication Type | e-Journal   |
| Language          | English                              | URL              | <a href="http://www.iop.org/EJ/journal/JNE">http://www.iop.org/EJ/journal/JNE</a> |

## REQUEST DETAILS

|                                 |                         |                             |                                  |
|---------------------------------|-------------------------|-----------------------------|----------------------------------|
| Portion Type                    | Chapter/article         | Rights Requested            | Main product                     |
| Page range(s)                   | 1-12                    | Distribution                | Worldwide                        |
| Total number of pages           | 12                      | Translation                 | Original language of publication |
| Format (select all that apply)  | Print, Electronic       | Copies for the disabled?    | No                               |
| Who will republish the content? | Academic institution    | Minor editing privileges?   | No                               |
| Duration of Use                 | Life of current edition | Incidental promotional use? | No                               |
| Lifetime Unit Quantity          | Up to 499               | Currency                    | EUR                              |

## NEW WORK DETAILS

|                 |  |                            |                     |
|-----------------|--|----------------------------|---------------------|
| Title           | Novel insights into axonal physiology through the development and use of new microelectrode array technologies | Institution name           | University of Porto |
|                 |  | Expected presentation date | 2021-07-30          |
| Instructor name | Paulo Aguiar   |                            |                     |

## ADDITIONAL DETAILS

|                        |     |   |                     |
|------------------------|-----|---|---------------------|
| Order reference number | N/A | The requesting person / organization to appear on the license | University of Porto |
|------------------------|-----|---|---------------------|

## REUSE CONTENT DETAILS

|   |                               |
|---|-------------------------------|
| Title, description or numeric reference of the portion(s) | DOI: 10.1088/1741-2552/ab0b86 |
| Editor of portion(s)                                      | N/A                           |

|                               |      |  |   |
|-------------------------------|------|--|---|
| Volume of serial or monograph | N/A  | Title of the article/chapter the portion is from | Improved in vitro electrophysiology using 3D-structured microelectrode arrays with a micro-mushrooms islets architecture capable of promoting topotaxis |
| Page or page range of portion | 1-12 | Author of portion(s)                             | Institute of Physics (Great Britain)  |
|                               |      | Issue, if republishing an article from a serial  | N/A   |
|                               |      | Publication date of portion                      | 2021-07-30  |

## RIGHTSHOLDER TERMS AND CONDITIONS

These special terms and conditions are in addition to the standard terms and conditions for CCC's Reproduction Service and, together with those standard terms and conditions, govern the use of the Works. As the User you will make all reasonable efforts to contact the author(s) of the article which the Work is to be reused from, to seek consent for your intended use. Contacting one author who is acting expressly as authorised agent for their co-author(s) is acceptable. User will reproduce the following wording prominently alongside the Work: the source of the Work, including author, article title, title of journal, volume number, issue number (if relevant), page range (or first page if this is the only information available) and date of first publication; and a link back to the article (via DOI); and if practicable, and IN ALL CASES for new works published under any of the Creative Commons licences, the words "© IOP Publishing. Reproduced with permission. All rights reserved" Without the express permission of the author(s) and the Rightsholder of the article from which the Work is to be reused, User shall not use it in any way which, in the opinion of the Rightsholder, could: (i) distort or alter the author(s)' original intention(s) and meaning; (ii) be prejudicial to the honour or reputation of the author(s); and/or (iii) imply endorsement by the author(s) and/or the Rightsholder. This licence does not apply to any article which is credited to another source and which does not have the copyright line '© IOP Publishing Ltd'. User must check the copyright line of the article from which the Work is to be reused to check that IOP Publishing Ltd has all the necessary rights to be able to grant permission. User is solely responsible for identifying and obtaining separate licences and permissions from the copyright owner for reuse of any such third party material/figures which the Rightsholder is not the copyright owner of. The Rightsholder shall not reimburse any fees which User pays for a republication license for such third party content. This licence does not apply to any material/figure which is credited to another source in the Rightsholder's publication or has been obtained from a third party. User must check the Version of Record of the article from which the Work is to be reused, to check whether any of the material in the Work is third party material. Third party citations and/or copyright notices and/or permissions statements may not be included in any other version of the article from which the Work is to be reused and so cannot be relied upon by the User. User is solely responsible for identifying and obtaining separate licences and permissions from the copyright owner for reuse of any such third party material/figures where the Rightsholder is not the copyright owner. The Rightsholder shall not reimburse any fees which User pays for a republication license for such third party content. User and CCC acknowledge that the Rightsholder may, from time to time, make changes or additions to these special terms and conditions without express notification, provided that these shall not apply to permissions already secured and paid for by User prior to such change or addition. User acknowledges that the Rightsholder (which includes companies within its group and third parties for whom it publishes its titles) may make use of personal data collected through the service in the course of their business. If User is the author of the Work, User may automatically have the right to reuse it under the rights granted back when User transferred the copyright in the article to the Rightsholder. User should check the copyright form and the relevant author rights policy to check whether permission is required. If User is the author of the Work and does require permission for proposed reuse of the Work, User should select 'Author of requested content' as the Requestor Type. The Rightsholder shall not reimburse any fees which User pays for a republication license. If User is the author of the article which User wishes to reuse in User's thesis or dissertation, the republication licence covers the right to include the Version of Record of the article, provided it is not then shared or deposited online. User must include citation details. Where User wishes to share their thesis or dissertation online, they should remove the Version of Record before uploading it. User may include a Preprint or the Accepted Manuscript (after the embargo period) in the online version of the thesis or dissertation, provided they do so in accordance with the Rightsholder's policies on sharing Preprints or Accepted Manuscripts. User may need to obtain separate permission for any third party content included within the article. User must check this with the copyright owner of such third party content. Any online or commercial use of User's thesis or dissertation containing the article, including publication via ProQuest, would need to be expressly notified in writing to the Rightsholder at the time of request and would require separate written permission from the Rightsholder. As well as CCC, the Rightsholder shall have the right to bring any legal action that it deems necessary to enforce its rights should it consider that the Work infringes those rights in any way. For content reuse requests that qualify for permission under the STM Permissions Guidelines, which may be updated from time to time, the STM Permissions Guidelines supplement the terms and conditions contained in this license.

## SPECIAL RIGHTSHOLDER TERMS AND CONDITIONS

When you transferred the copyright in your article to IOP, we granted back to you certain rights, including the right to include all or part of the Final Published Version of the article within any thesis or dissertation. Please note you may need to obtain separate permission for any third party content you included within your article. Please include citation details, "© IOP Publishing. Reproduced with permission. All rights reserved" and for online use, a link to the Version of Record. The only restriction is that if, at a later date, you wanted your thesis/dissertation to be published commercially, further permission would be required.

## CCC Terms and Conditions

1. Description of Service; Defined Terms. This Republication License enables the User to obtain licenses for republication of one or more copyrighted works as described in detail on the relevant Order Confirmation (the "Work(s)"). Copyright Clearance Center, Inc. ("CCC") grants licenses through the Service on behalf of the rightsholder identified on the Order Confirmation (the "Rightsholder"). "Republication", as used herein, generally means the inclusion of a Work, in whole or in part, in a new work or works, also as described on the Order Confirmation. "User", as used herein, means the person or entity making such republication.
2. The terms set forth in the relevant Order Confirmation, and any terms set by the Rightsholder with respect to a particular Work, govern the terms of use of Works in connection with the Service. By using the Service, the person transacting for a republication license on behalf of the User represents and warrants that he/she/it (a) has been duly authorized by the User to accept, and hereby does accept, all such terms and conditions on behalf of User, and (b) shall inform User of all such terms and conditions. In the event such person is a "freelancer" or other third party independent of User and CCC, such party shall be deemed jointly a "User" for purposes of these terms and conditions. In any event, User shall be deemed to have accepted and agreed to all such terms and conditions if User republishes the Work in any fashion.
3. Scope of License; Limitations and Obligations.
  - 3.1. All Works and all rights therein, including copyright rights, remain the sole and exclusive property of the Rightsholder. The license created by the exchange of an Order Confirmation (and/or any invoice) and payment by User of the full amount set forth on that document includes only those rights expressly set forth in the Order Confirmation and in these terms and conditions, and conveys no other rights in the Work(s) to User. All rights not expressly granted are hereby reserved.
  - 3.2. General Payment Terms: You may pay by credit card or through an account with us payable at the end of the month. If you and we agree that you may establish a standing account with CCC, then the following terms apply: Remit Payment to: Copyright Clearance Center, 29118 Network Place, Chicago, IL 60673-1291. Payments Due: Invoices are payable upon their delivery to you (or upon our notice to you that they are available to you for downloading). After 30 days, outstanding amounts will be subject to a service charge of 1-1/2% per month or, if less, the maximum rate allowed by applicable law. Unless otherwise specifically set forth in the Order Confirmation or in a separate written agreement signed by CCC, invoices are due and payable on "net 30" terms. While User may exercise the rights licensed immediately upon issuance of the Order Confirmation, the license is automatically revoked and is null and void, as if it had never been issued, if complete payment for the license is not received on a timely basis either from User directly or through a payment agent, such as a credit card company.
  - 3.3. Unless otherwise provided in the Order Confirmation, any grant of rights to User (i) is "one-time" (including the editions and product family specified in the license), (ii) is non-exclusive and non-transferable and (iii) is subject to any and all limitations and restrictions (such as, but not limited to, limitations on duration of use or circulation) included in the Order Confirmation or invoice and/or in these terms and conditions. Upon completion of the licensed use, User shall either secure a new permission for further use of the Work(s) or immediately cease any new use of the Work(s) and shall render inaccessible (such as by deleting or by removing or severing links or other locators) any further copies of the Work (except for copies printed on paper in accordance with this license and still in User's stock at the end of such period).
  - 3.4. In the event that the material for which a republication license is sought includes third party materials (such as photographs, illustrations, graphs, inserts and similar materials) which are identified in such material as having been used by permission, User is responsible for identifying, and seeking separate licenses (under this Service or otherwise) for, any of such third party materials; without a separate license, such third party materials may not be used.
  - 3.5.

Use of proper copyright notice for a Work is required as a condition of any license granted under the Service. Unless otherwise provided in the Order Confirmation, a proper copyright notice will read substantially as follows: "Republished with permission of [Rightsholder's name], from [Work's title, author, volume, edition number and year of copyright]; permission conveyed through Copyright Clearance Center, Inc. " Such notice must be provided in a reasonably legible font size and must be placed either immediately adjacent to the Work as used (for example, as part of a by-line or footnote but not as a separate electronic link) or in the place where substantially all other credits or notices for the new work containing the republished Work are located. Failure to include the required notice results in loss to the Rightsholder and CCC, and the User shall be liable to pay liquidated damages for each such failure equal to twice the use fee specified in the Order Confirmation, in addition to the use fee itself and any other fees and charges specified.

- 3.6. User may only make alterations to the Work if and as expressly set forth in the Order Confirmation. No Work may be used in any way that is defamatory, violates the rights of third parties (including such third parties' rights of copyright, privacy, publicity, or other tangible or intangible property), or is otherwise illegal, sexually explicit or obscene. In addition, User may not conjoin a Work with any other material that may result in damage to the reputation of the Rightsholder. User agrees to inform CCC if it becomes aware of any infringement of any rights in a Work and to cooperate with any reasonable request of CCC or the Rightsholder in connection therewith.
4. Indemnity. User hereby indemnifies and agrees to defend the Rightsholder and CCC, and their respective employees and directors, against all claims, liability, damages, costs and expenses, including legal fees and expenses, arising out of any use of a Work beyond the scope of the rights granted herein, or any use of a Work which has been altered in any unauthorized way by User, including claims of defamation or infringement of rights of copyright, publicity, privacy or other tangible or intangible property.
5. Limitation of Liability. UNDER NO CIRCUMSTANCES WILL CCC OR THE RIGHTSHOLDER BE LIABLE FOR ANY DIRECT, INDIRECT, CONSEQUENTIAL OR INCIDENTAL DAMAGES (INCLUDING WITHOUT LIMITATION DAMAGES FOR LOSS OF BUSINESS PROFITS OR INFORMATION, OR FOR BUSINESS INTERRUPTION) ARISING OUT OF THE USE OR INABILITY TO USE A WORK, EVEN IF ONE OF THEM HAS BEEN ADVISED OF THE POSSIBILITY OF SUCH DAMAGES. In any event, the total liability of the Rightsholder and CCC (including their respective employees and directors) shall not exceed the total amount actually paid by User for this license. User assumes full liability for the actions and omissions of its principals, employees, agents, affiliates, successors and assigns.
6. Limited Warranties. THE WORK(S) AND RIGHT(S) ARE PROVIDED "AS IS". CCC HAS THE RIGHT TO GRANT TO USER THE RIGHTS GRANTED IN THE ORDER CONFIRMATION DOCUMENT. CCC AND THE RIGHTSHOLDER DISCLAIM ALL OTHER WARRANTIES RELATING TO THE WORK(S) AND RIGHT(S), EITHER EXPRESS OR IMPLIED, INCLUDING WITHOUT LIMITATION IMPLIED WARRANTIES OF MERCHANTABILITY OR FITNESS FOR A PARTICULAR PURPOSE. ADDITIONAL RIGHTS MAY BE REQUIRED TO USE ILLUSTRATIONS, GRAPHS, PHOTOGRAPHS, ABSTRACTS, INSERTS OR OTHER PORTIONS OF THE WORK (AS OPPOSED TO THE ENTIRE WORK) IN A MANNER CONTEMPLATED BY USER; USER UNDERSTANDS AND AGREES THAT NEITHER CCC NOR THE RIGHTSHOLDER MAY HAVE SUCH ADDITIONAL RIGHTS TO GRANT.
7. Effect of Breach. Any failure by User to pay any amount when due, or any use by User of a Work beyond the scope of the license set forth in the Order Confirmation and/or these terms and conditions, shall be a material breach of the license created by the Order Confirmation and these terms and conditions. Any breach not cured within 30 days of written notice thereof shall result in immediate termination of such license without further notice. Any unauthorized (but licensable) use of a Work that is terminated immediately upon notice thereof may be liquidated by payment of the Rightsholder's ordinary license price therefor; any unauthorized (and unlicensable) use that is not terminated immediately for any reason (including, for example, because materials containing the Work cannot reasonably be recalled) will be subject to all remedies available at law or in equity, but in no event to a payment of less than three times the Rightsholder's ordinary license price for the most closely analogous licensable use plus Rightsholder's and/or CCC's costs and expenses incurred in collecting such payment.
8. Miscellaneous.
  - 8.1. User acknowledges that CCC may, from time to time, make changes or additions to the Service or to these terms and conditions, and CCC reserves the right to send notice to the User by electronic mail or otherwise for the purposes of notifying User of such changes or additions; provided that any such changes or additions shall not apply to permissions already secured and paid for.
  - 8.2. Use of User-related information collected through the Service is governed by CCC's privacy policy,

- 8.3. The licensing transaction described in the Order Confirmation is personal to User. Therefore, User may not assign or transfer to any other person (whether a natural person or an organization of any kind) the license created by the Order Confirmation and these terms and conditions or any rights granted hereunder; provided, however, that User may assign such license in its entirety on written notice to CCC in the event of a transfer of all or substantially all of User's rights in the new material which includes the Work(s) licensed under this Service.
- 8.4. No amendment or waiver of any terms is binding unless set forth in writing and signed by the parties. The Rightsholder and CCC hereby object to any terms contained in any writing prepared by the User or its principals, employees, agents or affiliates and purporting to govern or otherwise relate to the licensing transaction described in the Order Confirmation, which terms are in any way inconsistent with any terms set forth in the Order Confirmation and/or in these terms and conditions or CCC's standard operating procedures, whether such writing is prepared prior to, simultaneously with or subsequent to the Order Confirmation, and whether such writing appears on a copy of the Order Confirmation or in a separate instrument.
- 8.5. The licensing transaction described in the Order Confirmation document shall be governed by and construed under the law of the State of New York, USA, without regard to the principles thereof of conflicts of law. Any case, controversy, suit, action, or proceeding arising out of, in connection with, or related to such licensing transaction shall be brought, at CCC's sole discretion, in any federal or state court located in the County of New York, State of New York, USA, or in any federal or state court whose geographical jurisdiction covers the location of the Rightsholder set forth in the Order Confirmation. The parties expressly submit to the personal jurisdiction and venue of each such federal or state court. If you have any comments or questions about the Service or Copyright Clearance Center, please contact us at 978-750-8400 or send an e-mail to [support@copyright.com](mailto:support@copyright.com).

v 1.1